2019

Engineering Noble-metal Nanostructures for Biosensing Applications

Haihang Ye
University of Central Florida

ENGINEERING NOBLE-METAL NANOSTRUCTURES FOR BIOSENSING APPLICATIONS

by

HAIHANG YE

B.Sc., Beijing Jiaotong University, 2012

M.A., Beijing Jiaotong University, 2015

A dissertation submitted in partial fulfillment of the requirements
for the degree of Doctor of Philosophy
in the Department of Chemistry
in the College of Sciences
at University of Central Florida
Orlando, Florida

Spring Term
2019

Major Professor: Xiaohu Xia

ABSTRACT

The ability to engineer noble-metal nanostructures (NMNSs) in a controllable manner and to understand the structure-dependent properties greatly boost our knowledge in rational design of biosensing technologies. In particular, as a type of highly efficient peroxidase mimics, NMNSs hold promising potential to break through the bottleneck of conventional enzyme-based *in vitro* diagnostics.

During the time of my Ph.D. study, I have successfully: 1) directed a two-step method involving seed-mediated growth and chemical etching for the synthesis of Ru nanoframes (RuNFs) with face-centered cubic crystal phase and enhanced catalytic activities; 2) demonstrated, for the first time, the inherent peroxidase-like activity of RuNFs as a type of efficient peroxidase mimics, opening up possibilities for their bioapplications; 3) developed an enzyme-free signal amplification technique for ultrasensitive colorimetric assay of disease biomarkers by using Pd-Ir nanooctahedra encapsulated gold vesicles as labels; 4) prepared polyvinylpyrrolidone (PVP)-capped Pt nanocubes with superior peroxidase-like catalytic activity and record-high specific catalytic activity; 5) developed a facile colorimetric method for the detection of Ag(I) ions with picomolar sensitivity by using the PVP-capped Pt nanocubes as the probes; 6) developed a non-enzyme cascade amplification strategy for colorimetric assay of disease biomarkers by taking advantage of the interaction between the Ag(I) ions and PVP-capped Pt nanocubes; and 7) established a highly sensitive colorimetric lateral flow assay platform by using Au@Pt core-shell nanoparticles as the labels that possess both plasmonic and catalytic properties.

Keywords: Noble metal · nanostructures · peroxidase mimics · *in vitro* diagnostics · biosensing technique · colorimetric detection

Dedicated to My Family!

ACKNOWLEDGMENTS

I'm glad to thank all the people who made this thesis possible.

First, I'm indebted to my PhD supervisor, Prof. Xiaohu Xia. His professionality in both teaching and research inspired me from the first day I met him. Under his supervision, I learned how to do research efficiently and independently. Surviving from PhD study is never a piece of cake, I will never forget the days and nights we spent in lab together. I got so lucky to have him carry me forward!

I also would like to express my gratitude to my dissertation committee members (Prof. Stephen Kuebler, Prof. Melanie Beazley, Prof. Gang Chen, and Prof. Xiaofeng Feng) for their generous support and invaluable advice. It is fantastic to have them as my graduate committee advisors. Their insightful comments and crucial remarks greatly helped shaping my final dissertation. In addition, someone I haven't met in the graduate dissertation service helped me so much in templating the dissertation. I'm so grateful for their kind help.

With a special mention to the postdocs Dr. Zhuangqiang Gao and Dr. Jiuxing Li in our lab, Dr. Kuikun Yang and Prof. Zhihong Nie at the University of Maryland, and many other collaborators, it is so great to do research with you! Your tremendous experience in conduction research benefits me a lot.

I'm so grateful to have my entire family and friends for providing a loving environment for me.

And finally, last but by no means least, to my wife, it is my pleasure to sharing life with you.

I love you all!!!

TABLE OF CONTENTS

LIST OF FIGURES

LIST OF TABLES

CHAPTER 1 GENERAL INTRODUCTION

1.1 General Introduction

1.1.1 Viewpoints of Noble-metal: Traditional *vs*. Modern

Noble metals nowadays refer to a group of metals including gold (Au), silver (Ag), palladium (Pd), platinum (Pt), ruthenium (Ru), rhodium (Rh), iridium (Ir), and osmium (Os). The word "noble" traditionally comes from these metals' high value and rarity in the Earth's crust, as well as their highly resistance of oxidation and corrosion in moist air and being not easily attacked by acids. As such, the jewelry, coinage, and historical artifacts made of noble metals (mostly, Au and Ag) are able to maintain their glossiness for centuries without fading.

Modern scientific evaluation of noble metals could be traced back to 1850s when Michael Faraday first created a colloidal Au solution with ruby red color and conjectured that the color was generated by the light scattering property of the Au species with "finely divided metallic state".[1] Following this revolutionary discovery, Au played a prominent role in the field of colloid science, where theoretical and experimental knowledge was steadily increasing during the 20th century. As a remarkable milestone to the materials in modern era, Richard Feynman gave a famous talk entitled "There's Plenty of Room at the Bottom" at the American Physical Society meeting in 1959, wherein he foresaw a more powerful matter that could be operated at atomic and molecular level.[2] Since then, the emerging of advanced microscopy methods, such as scanning tunneling microscope (IBM's Zurich lab, 1981)[3] and atomic force microscopy (Gerd Binnig, Calvin Quate, and Christoph Gerber, 1986),[4] allowed the scientists to visually measure and manipulate individual atoms, eventually leading to the establish of *nanotechnology*.[5] Again, noble metals played a unique

role as metallic features in the evolving of "*the world of nano dimensions*"[6] due to their high stability as pure metals.

The goal of nanotechnology is to create materials with at least one dimension in the range of approximately 1-100 nm (defined as *nanomaterials*),[7] explore the fundamentally new properties and functions at that scale that are different with single atoms or molecules or bulk behavior, and build systems and devices that are applicable to cross-disciplinary domains of relevance.[8] To date, the art of handling noble-metal nanostructures (NMNSs) has fascinated mankind for centuries due to their exceptional physicochemical properties and remarkable applications in the fields of catalysis,[9] electronics,[10] and photonics.[11] For instance, Au and Ag nanostructures have been used as colorants in ancient time, typically in glass and ceramic or enamel potteries, though being unknowingly. The earliest example is the Lycurgus Cup that could be dated back to Roman times in about 290-325 AD.[12] In spite of the high price, Pd, Pt, Rh, Ru, and Ir were heavily used as catalysts in the chemical industries for almost two centuries because of their superior catalytic performance.[13] Nevertheless, in the light of nanotechnology, these old phenomena and applications have been revisited in recent decades, which advances the synthetic strategies for NMNSs, enriches the insights of their physicochemical properties, and upgrades the applications even to the sensing,[14] imaging,[15] and biomedicine.[16]

1.1.2 Enriched Insights of the Physicochemical Properties for NMNSs

When matter is divided into the nanolength, its physical features will be changed drastically, such as increased surface-to-volume-ratio, decreased coordination number of surface atoms, and quantum-confinement effects.[17] When applied to noble metals, unusual optical phenomena and catalytic activities will arise in the nanostructures.[18] These emerging properties

grant a new division for the noble metals, wherein the Au and Ag are assigned as *plasmonic metals*, while the rest as the *catalytic metals* (**Figure 1.1**).[19] Excitingly, both theoretical and experimental results indicate these physicochemical properties are chiefly dependent on the physical parameters of a noble-metal nanostructure, including size, geometric shape, internal structure (solid or hollow), and elemental composition. That is, we are able to tailor the properties of a noble-metal nanostructure by controlling one or a combination of those parameters.

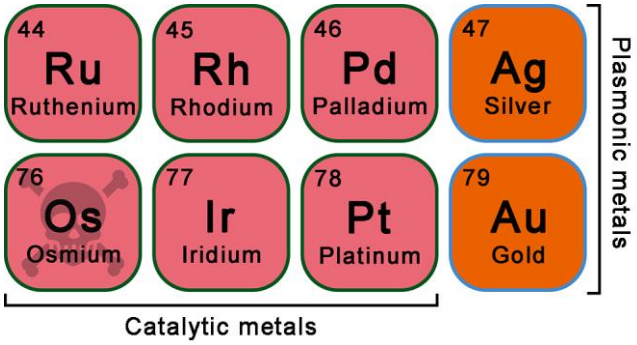

Figure 1.1 A section of the periodic table showing the noble-metals. These metals can be divided into two major groups according to their distinctive properties. Note that due to the pyrophoricity of Os nanostructure and extreme toxicity of its oxide, this metal is rarely studied.[20]

1.1.2.1 Modelling the Optical Response of the Plasmonic-metal Nanostructures

The optical properties of the plasmonic-metal nanostructures mainly arise from a phenomenon called the Localized Surface Plasmon Resonance (LSPR). In principle, when irradiated by an incident light, free electrons in metal particle will be excited and create a collective oscillation away from their equilibrium positions. Such oscillation of electrons is analogous to that of gaseous plasma so as to be defined as Surface Plasmons (SPs) and the light-particle interaction is called Surface Plasmon Resonance (SPR). Specifically, when the metal is transformed into nanostructure, the frequency of electronic oscillation will match with that of the incident light,

resulting in the absorption of photons and confinement of the SPR by the geometrical boundary of the metal nanostructure, which is furthered as LSPR (**Figure 1.2a**).[21] During the course, a portion of these absorbed photons will be coherently released in all directions that is known as *scattering*, meanwhile some of them will be transferred into phonons or vibrations of the lattice known as *absorption*. Therefore, the LSPR peak of a metal structure combines both light absorption and scattering at specific wavelength, which indeed is an extinction peak (**Figure 1.2b**).[22] By taking advantage of the LSPR, plasmonic-metal nanostructures are capable to *i*) span the extinction peak in the ultraviolet (UV), full visible (Vis), and near-infrared (NIR) regions of spectrum (**Figure 1.2c**);[23] *ii*) enhance the cross-section of extinction peak, whose molar extinction coefficient could reach at level of 10^{8}~10^{11} $M^{-1}\cdot cm^{-1}$, approximately 3~6 orders of magnitude higher than that of conventional organic dyes;[24] and *iii*) finely tune the spectral features, such as the resonant modes and peak positions, by changing the abovementioned physical parameters of a nanostructure[18, 25].

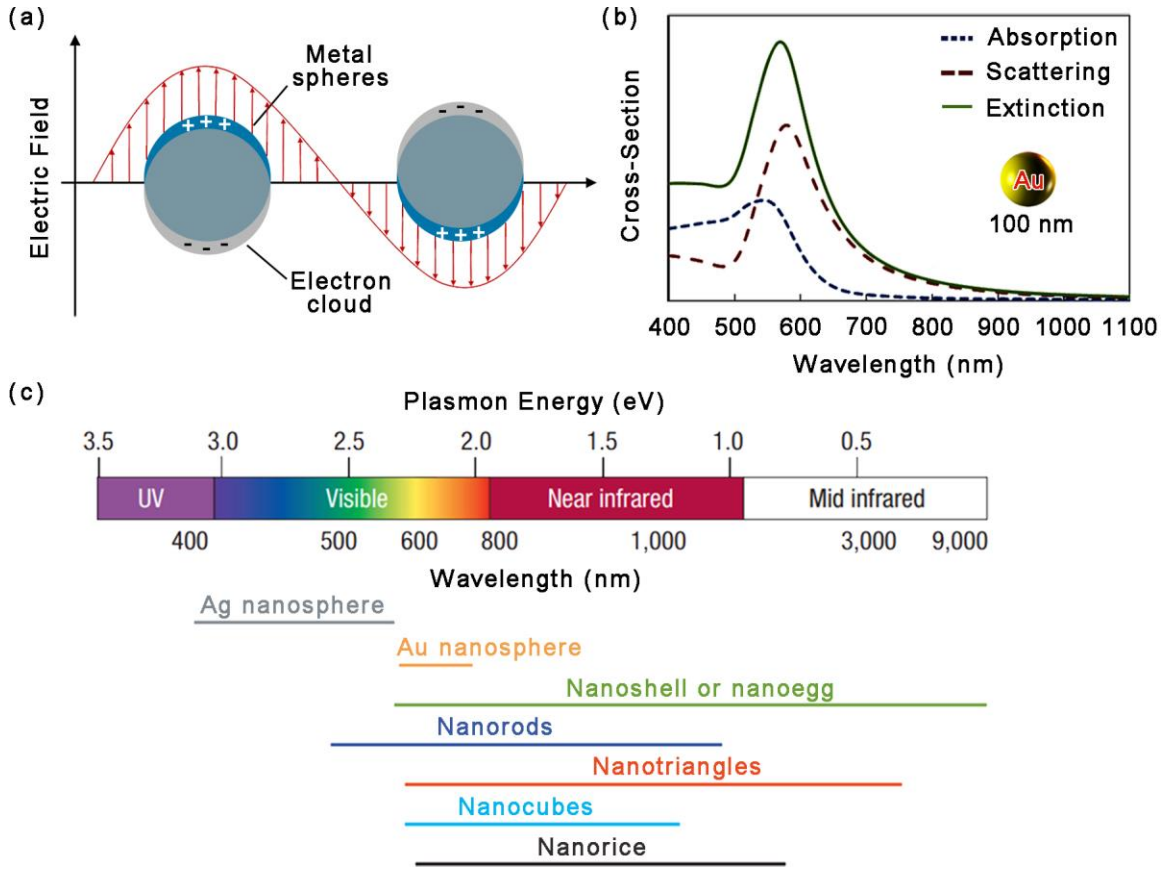

Figure 1.2 (a) Schematic illustration of LSPR for a metal nanosphere induced by an external electric field (*e.g.*, incident light). Adapted with permission from ref 21. Copyright 2003 American Chemical Society. (b) Scattering, absorption and extinction cross-section of a 100 nm Au nanosphere. Adapted with permission from ref 22. Copyright 2015 Optical Society of America. (c) The range of LSPR peaks for a variety of Au and/or Ag nanostructures. Adapted with permission from ref 23. Copyright 2007, Springer Nature.

The theoretically modelling of optical response for small metal spheres was first accomplished by Gustav Mie in 1908.[26] His solutions to the Maxwell's electromagnetic field equations described the extinction spectra of metal spheres with varied size in a homogenous medium. Following this work, Richard Gans modified the Mie's solutions for metal ellipsoids.[27] Later, "Lorenz-Mie theory" and "Lorenz-Mie-Debye theory" were also proposed to expand the calculated models.[28] However, these theories were marginalized at that time because it was hardly

to obtain metal nanostructures with regular shapes. It was until the end of last century when the advance in nanotechnology blossomed the synthetic methods for plasmonic-metal nanostructures with various sizes and shapes, theoretical calculations were recalled to understand the underlying mechanism of the spectacular colors induced by size and/or shape of a noble-metal nanostructure (**Figure 1.3**).

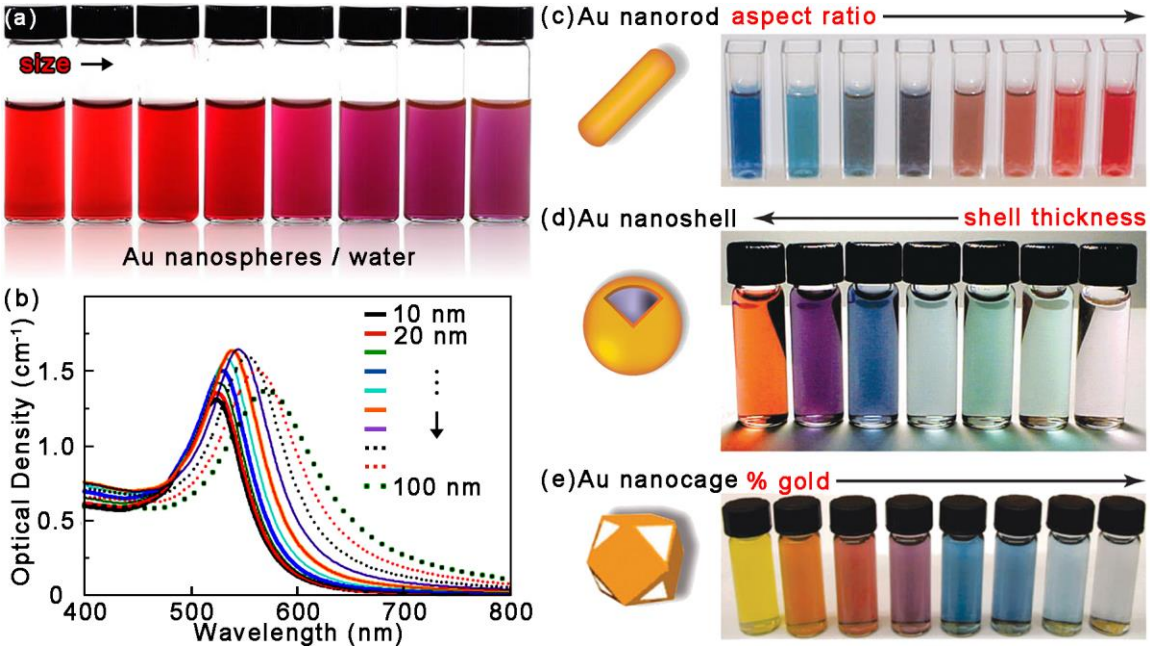

Figure 1.3 Optical properties of Au nanostructures with different size and shape. (a) Commercial Au nanospheres (AuNSs) dispersed in water. Copyright and image from *Nanocomposix*. (b) Corresponding LSPR extinction peaks of AuNSs as a function of the size. Copyright and image from *Nanocomposix*. (c) Au nanorods, (d) SiO_2-Au core-shell nanostructures, and (e) Au nanocage model and colors of aqueous solutions containing these nanostructures that have different (c) aspect ratio, (d) shell thickness, and (e) degree of galvanic replacement by Au. Adapted with permission from ref 16. Copyright 2012 Royal Society of Chemistry.

Despite the prediction of Mie's theory and its derivatives succeeded in a number of simple systems, such as spheres, ellipsoids, and infinite cylinders, they were no longer valid for other asymmetric nanostructures. Therefore, *discrete dipole approximation* (DDA) was proposed in

1973, which can be applied to nanostructures of any arbitrary shape.[29-31] In DDA calculations, a nanostructure is approximated as a three-dimensional array of polarizable elements considered as point dipoles.[21] When this array is irradiative by an incident light, a dipole moment will be induced by the external electric field and the surrounding dipoles. The contribution from each dipole can then be used to determine the overall optical response (*e.g.*, scattering and absorption cross-sections) of the metal nanostructure with respect to the wavelength. Making use of this simulation, Prof. Xia presented a series of DDA calculations for the Ag nanoparticles of 2- and 3-dimentional (2D and 3D) structures, successfully correcting the relationship between the morphology and the spectral features (**Figure 1.4**).[32] So far, methods like the *finite difference in the time domain* (FDTD) and the *boundary element method* (BEM) were also established as driven by the demanding to explain the LSPR properties of nanostructures subjected to a more complex environment.[33]

Taken together, the classical Mie's theory and modern numerical analyses are able to describe many optical properties of plasmonic-metal nanostructures of different size, shape, and etc. Theoretical modeling is of great importance to bridge the experimental observations and the physics behind plasmonics, and thus predicting unique optical responses of novel structures yet to be obtained. Nevertheless, this progress boosts our confidence in the design of spectroscopic techniques and colorimetric sensing platforms based on plasmonic-metal nanostructures that mature to both practical fabrication and theoretical guidance.[34]

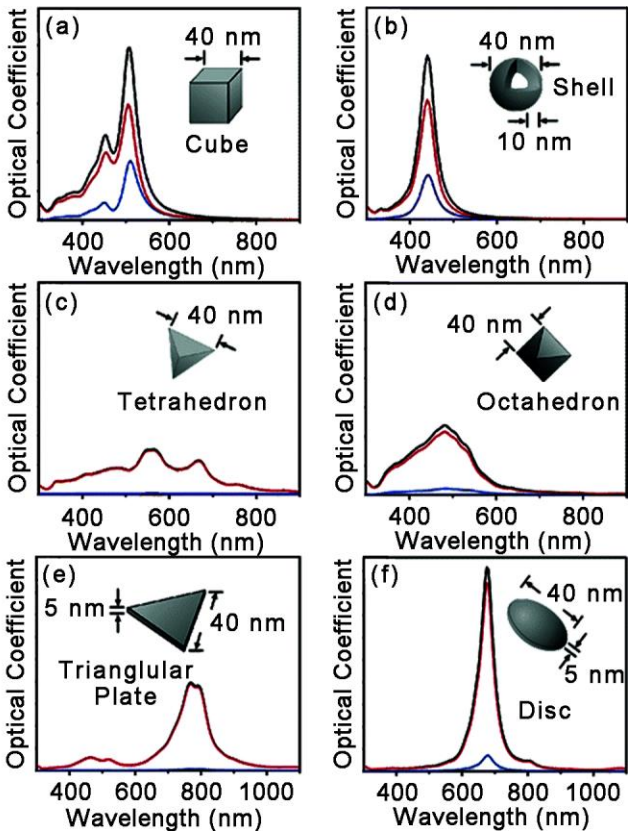

Figure 1.4 The DDA simulations of the optical response for Ag nanoparticles with a variety of shapes in water. Absorption peak is shown in red, scattering peak in blue, and LSPR extinction peak in black. Adapted with permission from ref 32. Copyright 2006 American Chemical Society.

1.1.2.2 <u>Renovating the Cost-efficiency of Catalytic-metal Nanostructures</u>

The catalytic metals locate at the second and third row of VIII group on the periodic table that possess *d*-electrons and *d*-orbital to spare as the reaction proceeding, of which the ability to transit electrons is the key for them to serve as catalysts in oxidation, cross-coupling, electron-transfer, and hydrogenation reactions.[35] In traditional industries and modern automobile, these catalytic metals used to be employed as heterogeneous catalysts, among which the Pt-based particles are the most popular candidates.[36-37] Moreover, these catalytic metals share many similarities in chemical, physical, and anatomical properties, therefore, they are also categorized

as *platinum group metals* (PGMs).[38] Not surprisingly, taking the high price and demand of PGMs as catalysts into consideration, we have to face to a foremost challenge: how to maximize the cost-efficiency of PGMs?

A promising answer was given by the nanotechnology. Recent landmark achievements in the syntheses of nanostructures, mostly on the basis of a colloidal chemistry, ensure the employment of PMG-based nanocatalysts to meet the technological demands.[18] A notable example is that the size of nanostructures can be maneuvered in the regimes of 1-10 nm with high uniformity. As a result, these extremely small nanostructures could have high fractions of the surface atoms to the whole (also called *dispersion*) along with the surface-to-volume-ratio. Considering the heterogeneous reaction occurs on the surface of a catalyst, shrinking the size of a nanostructure could ensure as many atoms to be exposed on the surface, which is a straightforward yet efficient way to improve its cost-efficiency.[39] Coincidently, the high uniformity of the PGMs nanostructures makes the surface atoms almost identical from particle to particle, enabling the reaction to be catalyzed in a consistent pathway, yielding the desired products with reduced number of byproducts. For example, Prof. Somorjai reported a study on the size effect of Pt nanoparticles (PtNPs) supported on SBA-15 silica toward the hydrogenation of pyrrole.[40] Representative transmission electron microscopy (TEM) images of PtNPs of 2 nm and 5 nm was provided in **Figure 1.5a, b**, respectively. It was found that unique selectivity came out as the PtNPs size increasing above 2 nm, favoring for the ring opening to *n*-butylamine while the formation of pyrrolidine was retarded (**Figure 1.5c**). The reason was that *n*-butylamine is a more electron-rich structure than pyrrolidine, which is more likely to poison the smaller PtNPs that possess more unsaturated surface bonds.

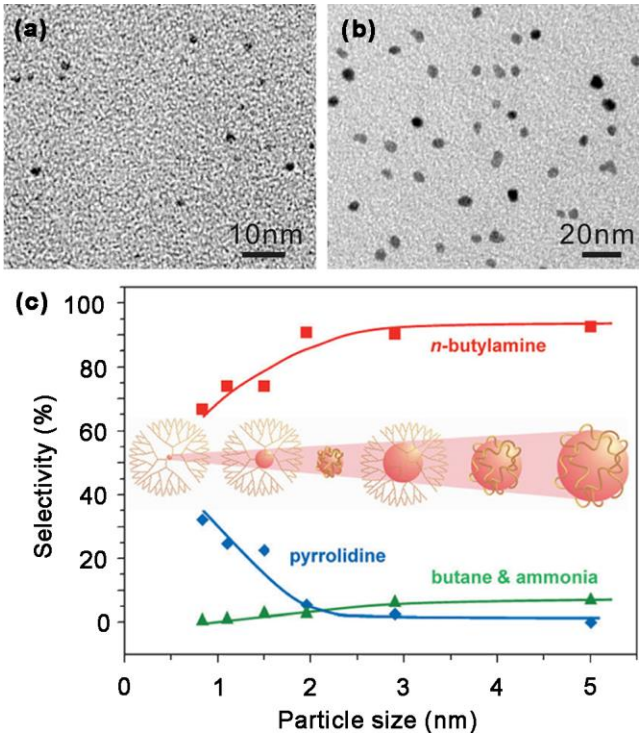

Figure 1.5 Size-dependent selectivity of Pt nanoparticles (PtNPs) toward pyrrole hydrogenation. TEM images of (a) 2.0 nm and (b) 5.0 nm PtNPs. (c) Reaction selectivity as a function of Pt size. Inset shows the strategy of size control for PtNPs. Adapted with permission from ref 38. Copyright 2008 American Chemical Society.

Now that we know the surface atoms of PGM nanostructures are the key component to a heterogeneous-catalytic process, we can also tailor both catalytic activity and selectivity by means of shape control of PGM nanostructures. For example, Prof. Yang reported a study on the benzene hydrogenation over Pt nanostructures of cubic and cuboctahedral shapes (**Figure 1.6**).[41] It has been shown that Pt nanocubes with (100) facets only could produce cyclohexene as the product, while Pt cuboctahedra with a mixture of (100) and (111) facets produced both cyclohexane and cyclohexene. The result is in consistency with the reaction selectivity catalyzed by bulk Pt (111) and Pt (100) single crystals and gives a hint on the relationship between the well-defined shape of a nanostructure and the catalytic performance. It worth pointing out that other than the facets,

edges and corners in a given shape can also serve as intrinsically active centers for catalysis due to the low coordination numbers.[42]

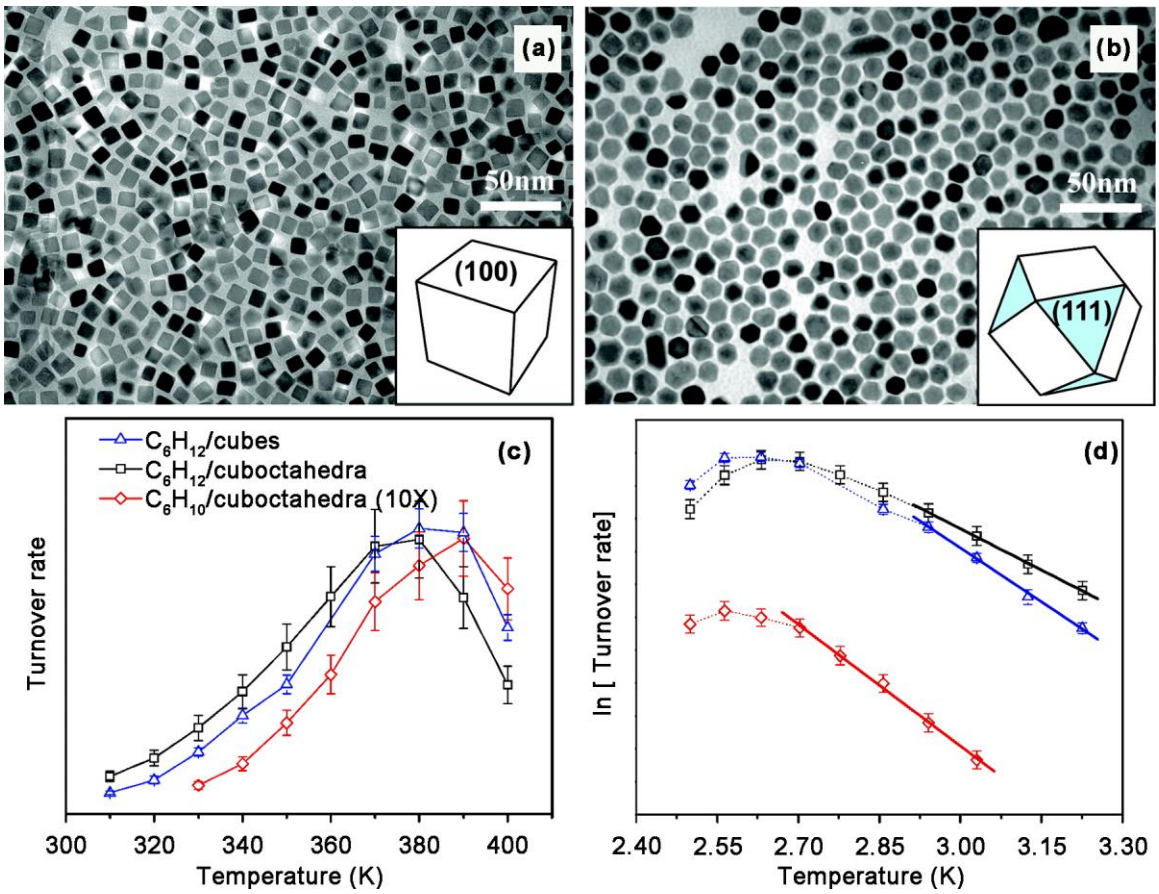

Figure 1.6 Shape-dependent selectivity of Pt nanoparticles (PtNPs) toward benzene hydrogenation. TEM images of PtNPs of (a) cubic shape and (b) cuboctahedral shape. Insets show the model of cube covered by (100) facets and cuboctahedron covered by a mixture of (100) and (111) facets. (c) Turnover rate and (d) corresponding Arrhenius plots of benzene hydrogenation reaction for cyclohexane and cyclohexene in presence of Pt cubes and Pt cuboctahedra as catalysts, wherein the Pt cubes exhibited selectivity for cyclohexane. Adapted with permission from ref 39. Copyright 2007 American Chemical Society.

In addition, depositing active metals on a supported material made of other metals that are more abundant and/or less expensive used to be a prevalence strategy. In a sense, the "ideal"

situation should be only a single layer of the active atoms is formed on the outer surface. Thanks to the substantial achievement made by Prof. Xia's group, it is now technically feasible to grow a shell within one to several atomic layers on a template. Recent examples based on Pd-Pt core-shell nanostructures have been reported, where Xia and co-workers implemented seed-mediated growth for the conformal coating of Pt layers on Pd cubes as seeds.[43] They demonstrated the growth of Pt atoms was following a layer-by-layer mode, where the thickness of Pt shell could be precisely controlled from 1 to 6 atomic layers, as shown in **Figure 1.7a**, **b**. Using the oxygen reduction reaction (ORR) as a model reaction, the Pd-Pt nanocubes showed enhancements in electrocatalytic performance (*e.g.*, specific and mass activity and durability) when compared to a commercial Pt/C catalyst (**Figure 1.7c, d**). However, it may be argued that the interior of this type of nanostructures is still occupied by the seeds (Pd, in this case), which in fact has little contribution to the catalytic reaction yet much to the material cost. To avoid this, a logical solution is to engineer a cage-like nanostructure with hollow interior. Following this idea, by selectively removal of the interior of Pd-Pt core-shell nanostructures, Pt nanocages with subnanometer-thick walls and cubic or octahedra shape could be obtained (**Figure 1.8a, b**).[44] The electrocatalytic performance of the Pt nanocages toward ORR was substantially improved, which may be originated from the shortened atomic distance in the Pt layer compared to the pure Pt nanostructures (**Figure 1.8c, d**).

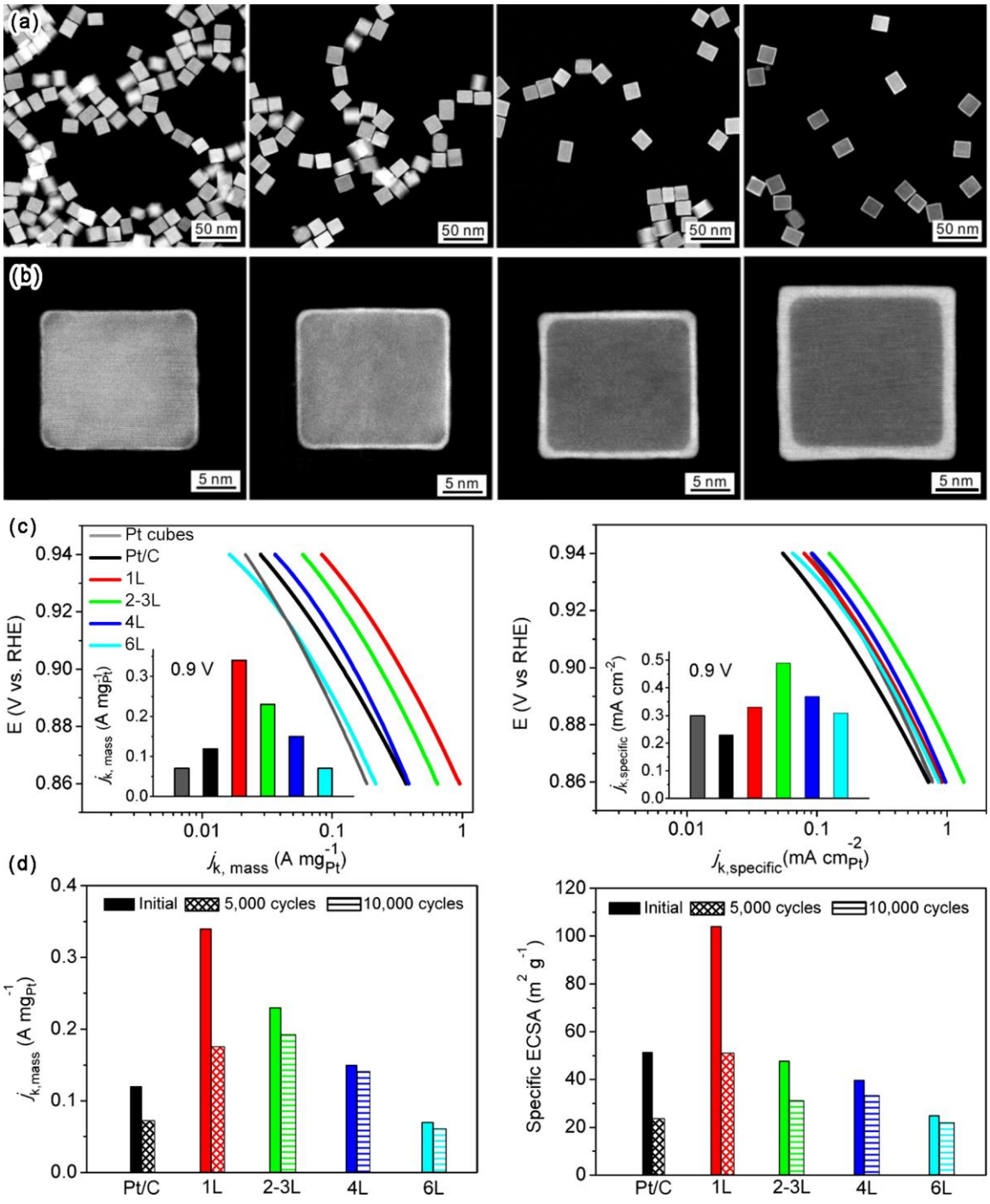

Figure 1.7 Low-magnification high-angle annular dark-field scanning TEM (HAADF-STEM) images of (a) Pd-Pt$_{n\mathrm{L}}$ core-shell nanocubes, from left to right: n=1, 2-3, 4, and 6; (b) high-magnification HAADF-STEM images of individual nanocubes corresponding to (a). Mass (left) and specific (right) ORR performance of (c) activity and (d) durability of the Pd-Pt$_{n\mathrm{L}}$/C catalysts

against a commercial Pt/C catalyst and/or Pt nanocubes of 9 nm in edge length. Adapted with permission from ref 40. Copyright 2014 American Chemical Society.

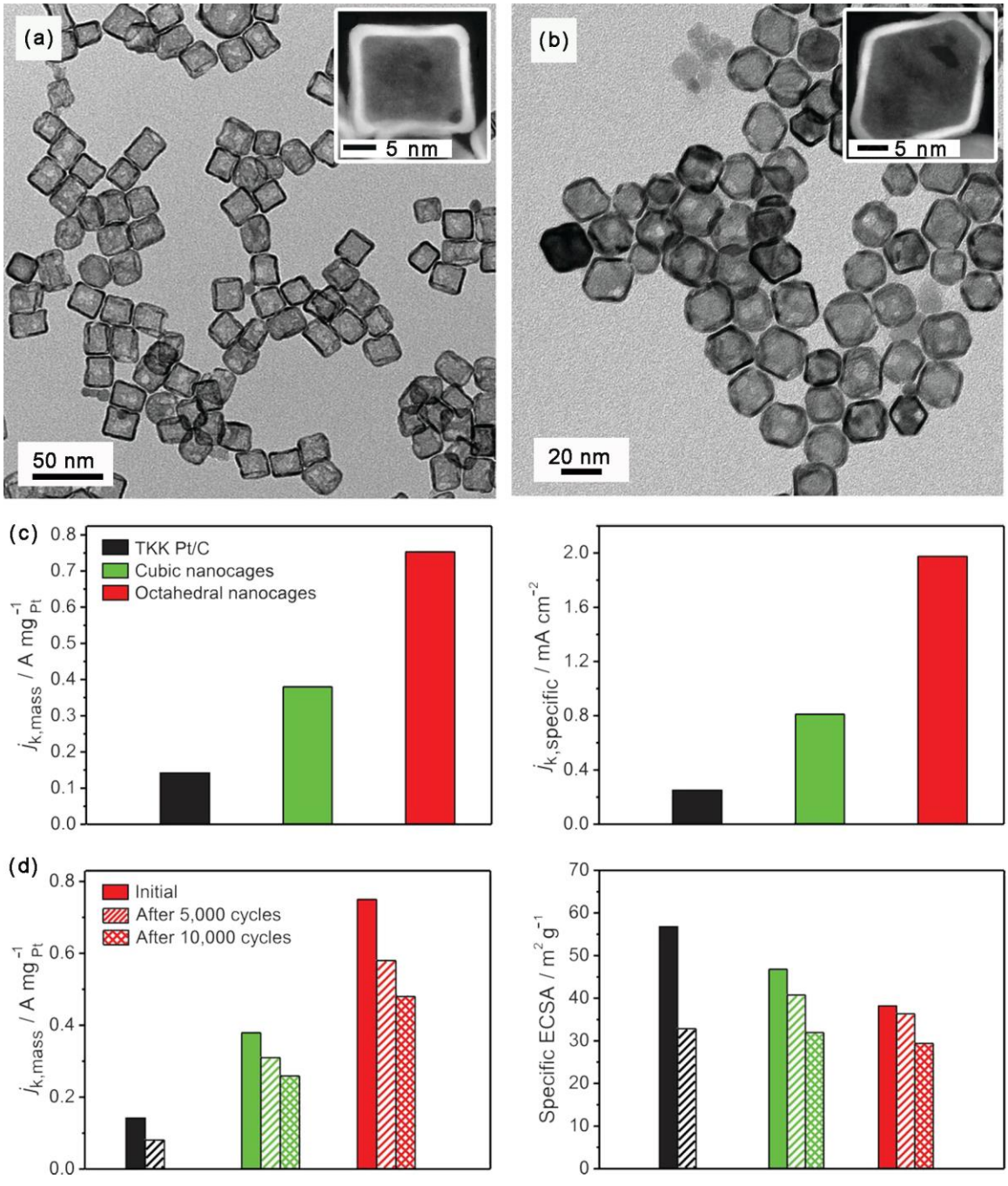

Figure 1.8 TEM images of Pt (a) cubic and (b) octahedral nanocages. Insets in (a) and (b) are the high-magnification HAADF-STEM images of an individual nanocage. Electrocatalytic properties and stability tests of the two types of Pt nanocages compared to a commercial Pt/C catalyst. Mass

(left) and specific (right) ORR performance of (c) activity and (d) durability of the cage-based catalysts against a commercial Pt/C catalyst at 0.9 V_{RHE}. Adapted with permission from ref 41. Copyright 2015, American Association for the Advancement of Science.

The rationale behind fabrication of PGM-based nanocatalysts again stems from the fact that a large portion of atoms are exposed on surface in a nanostructure and the electrons are confined to spaces (*e.g.*, edge and corner) only a few of nanometers across, giving rise to more active sites for reactions and thus greatly improve the cost-efficiency of the PGMs. Perhaps most importantly, many studies in the past decades showed that the catalytic performance (*e.g.*, activity, selectively, and durability) have strong relationship with the physical parameters and elemental composition of PGM-based nanostructures, which can be precisely controlled at atomic and molecular level.[18]

1.1.2.3 NMNSs as Artificial Enzymes[a]

The rising development of controllable syntheses of NMNSs not only maintains their dominance in traditional industries, but also raises them as appealing stars in the field of artificial enzymes as alternatives to natural enzymes.[45-46] As well known, enzymes are virtually biocatalysts of great efficiency and specificity at mild conditions (*e.g.*, room temperature, ambient pressure, and aqueous solutions), which are very important to the living systems and beyond.[47] However, these natural enzymes made of proteins or ribonucleic acids have several drawbacks like gradual denaturation, high expense, and sophisticated recycling, which inevitably limited their practical usage. To tackle these issues, artificial enzymes made of nanostructures have been developed.

[a]Under review by *ChemNanoMat*. Expected to be accepted on May 2019.

Though essentially different, nanostructure-based enzyme mimics display many advantages over the conventional artificial enzymes and natural enzymes (see **Table 1.1** for detail comparison).[45-46, 48]

Table 1.1 Comparison between artificial enzymes and natural enzymes. Reprinted with permission from ref 48. Copyright © The Author(s) 2016.

	Features
Artificial enzymes of nanostructure	Low cost Easy for mass production Robustness to harsh environments High stability Long-term storage Tunable activity Structure-dependent properties Multifunction Easy for further bioconjugation Smart response to external stimuli Self-assembly
Conventional artificial enzymes	Low cost Easy for mass production Robustness to harsh environments High stability Long-term storage Tunable activity Established methods for preparation Uniform size and defined structures Smaller size (compared with nanostructures)
Natural enzymes	High catalytic efficiency High substrate specificity High selectivity Sophisticated three-dimensional structures Wide range of catalytic reactions Tunable activity Good biocompatibility Rational design via protein engineering

Taking peroxidases as an example, they are a group of enzymes that act as catalysts to the oxidation of certain compounds with peroxides (*e.g.*, H_2O_2).[49-50] They have been found in plants and animals, where their main role is to break down the oxidizing agents into harmless substances, helping prevent damage.[51-52] Technologies for isolation and purification of peroxidases from organisms allow for their industrial applications.[53] Horseradish peroxidase (HRP), as a typical model, has been used as labels in medical diagnostic kits, where they are conjugated to antibodies and specifically produce detection signal by catalyzing substrates.[54] HRPs have also been utilized for treatment of wastewater as they are able to eliminate phenolic contaminants through catalysis.[55] Despite of these demonstrations, the intrinsic limitations of peroxidases greatly inhibit broader applications. For instance, peroxidases are relatively unstable under harsh conditions (*e.g.*, temperatures above 50 °C or pH below 4.5).[56] Their catalytic efficiencies are confined to certain levels, which are determined by the inherent molecular structures of peroxidases. Moreover, the isolation and purification of peroxidases are complicated and costly.

To circumvent those issues, much effort has been made to develop peroxidase mimics as the natural counterparts.[45-46] Since the first report of ferromagnetic nanoparticles with intrinsic peroxidase-like activity in 2007,[57] a variety of peroxidase mimics made of inorganic nanomaterials, including carbon materials,[58-59] noble metals,[48, 60] metal oxides,[61-63] and a combination of them[64-65] have been actively reported in recent years. Among them, NMNSs as peroxidase mimics are of great interest due to their higher peroxidase-like efficiencies than most other types of peroxidase mimics with similar dimensions. For example, our group reported a new type of peroxidase mimics made of Pd-Ir core-shell nanocubes, featuring record-high peroxidase-like activity at a level as high as 10^6-10^7 s^{-1}, which is approximately 1000-fold higher than that of

HRP.[57, 66] In addition, they have several other distinctive features that make them strong candidates among peroxidase mimics: *i*) they are made of inert noble metals with excellent stabilities, enabling them survive harsh environments; *ii*) their surfaces can be conveniently labeled with chemical ligands and biomolecules (*e.g.*, antibodies and nucleic acids) through physical adsorption or metal-thiolate bonding; and *iii*) they can be prepared in high quality and large quantities in common chemical laboratories,[18, 67-68] ensuring good reproducibility in certain applications.

In addition to peroxidase, the NMNSs can also mimic enzymes like RNase, DNase, superoxide dismutase, catalase, etc. Detail information can be found in many recent reviews.[45-46, 48]

1.2 Applications of NMNSs in Biomedicine

Integrating NMNSs into the fields of biomedicine is a huge breakthrough that benefits from the nanotechnology. In essential, the unique physicochemical properties of NMNSs form the basis for a variety of applications. The capacity of structural engineering for NMNSs like controllable synthesis and surface modification, indeed bridges the gap between theoretical direction and the practical use, such as *in vitro* diagnostics, *in vivo* imaging, therapy and medicine (**Figure 1.9**). For example, taking advantage of the strong electromagnetic enhancement by the LSPR of plasmonic-metal nanostructures, surface-enhanced Raman scattering (SERS) could achieve ultrasensitive detection by molecular fingerprinting.[69-70]

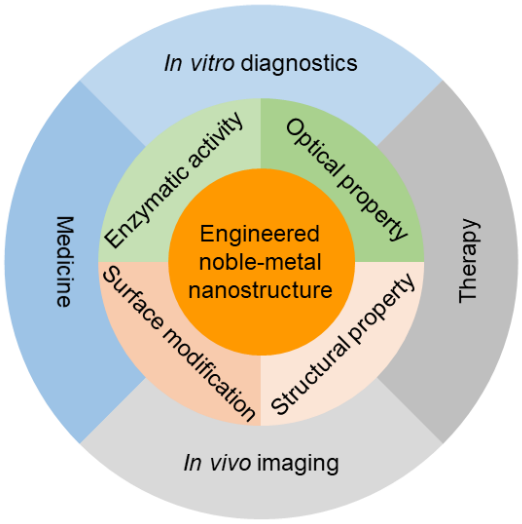

Figure 1.9 A summary of the properties of engineered NMNSs that fit for the biomedicine applications.

1.2.1 *In Vitro* Diagnostics[a]

In vitro diagnostics (IVDs) refer to tests on biological samples that are taken from the human body, including, but not limited to, blood, urine, saliva, and tissues.[71-74] IVD tests are usually performed to detect and monitor disease in an individual (in most cases, through the determination of molecular biomarkers), intending to provide valuable medical information for disease treatment, management, and prevention. IVDs represent a crucial component in modern healthcare. They influence more than 60% of clinical decision making, while accounting for only ~2% of total healthcare spending.[75] IVDs reduce cost by diminishing subsequent health issues, avoiding unnecessary treatment, and reducing hospitalization. In addition to cost-effectiveness, IVDs are featured by low patient risk. Most IVDs do not come into direct contact with the human

[a]Reprinted with permission from *Chem. Mater*. **2018**, *30*, 8391-8414.

Haihang Ye contributed the review of literature, collection of figures, and preparation of the article.

body, involving no more than minimal risk for a patient.[76-78]

Today, IVDs go far beyond simply telling a doctor whether a patient has certain diseases or not. They are able to spot early warning signs, provide quantitative data on relevant biomarkers, and evaluate individual risk factors.[79-80] This information greatly enhances doctors' ability to make an optimized decision at the right time. The versatile capabilities of IVDs make them an integral part of decision making during the entire continuum of patient care. For instance, in dealing with cancers, IVDs can guide physicians to make clinical decisions on both treatment and recovery. Prior to any invasive treatments, IVD tests (*e.g.*, blood tests for prostate cancer and core-needle biopsy for breast cancer) need to be performed to obtain detailed information about cancer, such as the exact kind of cancer, the stage of cancer, and how fast it is expanding. After treatment, IVDs help physicians monitor possible cancer recurrence by measuring the level of specific biomarkers in a patient's blood or tissue.[81-85]

The increasing demand of IVDs and their significance in biomedicine drive the development of new IVD technologies toward higher sensitivity, greater simplicity, and lower cost. In particular, high sensitivity is critical in early detection of life-threatening diseases such as cancers, infectious diseases, and cardiovascular disease, creating opportunities for early intervention and prevention.[86-88] Great simplicity and low cost allow IVDs to extend beyond the clinical laboratory and doctor's office, empowering patients to self-monitor and manage their own health conditions and ultimately achieving sustainable healthcare.[89-90]

Technological advancement is oftentimes motivated by scientific discoveries. Taking advantages of the functional nanostructures for the revolution of IVD technologies is an exciting task for scientists worldwide. However, the path from lab experiments to clinical use is long and

fraught with pitfalls. The lack of in-depth fundamental understanding and difficulties in dealing with complicated clinical samples make the translational period of these nanostructures in IVDs rather arduous. Nevertheless, a few of them have already made it through. For example, Au nanoparticles-based test strip technology has successfully been brought to the market since the 1980s and become a powerful tool to solve real-world problems (*e.g.*, tests for pregnancy and malaria).[91-93] It is worth mentioning that facile and scalable synthesis of quality colloidal Au nanoparticles can be traced back to the work by Turkevich *et al*. in the early 1950s[94-96] — only ~30 years behind their practical use. Over the past two decades, great progress has been made on both the fundamental and practical sides of nanostructures. It is now feasible to manufacture nanostructures with good uniformities and commercial scales.[97-99] Taken together, this niche field is primed to make the transition from scientific findings to clinical realities.

1.3 Engineered NMNSs for *In Vitro* Diagnostics[a]

NMNSs as a group of emerging functional materials have received increasing interest in IVDs over the past several decades due to their unique and intriguing physicochemical properties.[76, 100-103] For example, (*i*) they offer a vast of signal transduction principles that are suited for efficient IVD tests, including optical,[104] plasmonic,[105] electrochemical,[64, 106] SERS,[107-108] fluorescent,[109-110] and colorimetric signals.[111] Notably, a very small amount of NMNSs are required to yield a strong signal, allowing for sensitive detection. (*ii*) Owing to the great efforts by many research groups in the past, they can now be produced in high quality and large quantities, ensuring

[a]Reprinted with permission from *Chem. Mater*. **2018**, *30*, 8391-8414.

Haihang Ye contributed the review of literature, collection of figures, and preparation of the article.

good reproducibility for associated IVDs.[97-99] (*iii*) Their surface can be conveniently modified with functional groups such as amino and carboxyl groups by means of metal-thiolate bonding, allowing for facile labeling of biomolecules.[112-115] (*iv*) They are made of noble metals with excellent stability and mechanical flexibility, enabling them to easily survive from complex and harsh environments.[116-118] This feature is particularly desired for point-of-care IVDs, where environmental conditions such as temperature, humidity, and air quality are less predictable and controllable than those in a clinical laboratory.[119-120] Finally, it should be noted that the cost of noble metals should not be an issue in this particular application because of the tiny amount of materials usage in IVDs.

The term "engineered" refers to noble-metal nanomaterials "with controlled physical parameters, including size, shape, elemental composition, and internal structure (*e.g.*, hollow *vs.* solid)." As mentioned in **Section 1.1.2**, the physicochemical properties of a noble-metal nanostructure have strong dependence on these physical parameters.[34, 121-128] Therefore, for a given application, the engineered NMNSs would more likely to express the optimized properties, as well as the expected performance. In the past decades, many examples clearly told us the critical importance of "engineered" to the effective utilization of NMNSs. Nevertheless, compared to other fields (*e.g.*, catalysis and *in vivo* biomedicine), engineered NMNSs have not been extensively studied in IVDs. Only within the past few decades have they been applied to IVD tests. In the following couple of sections, a comprehensive literature review will be given by introducing the impacts of size, shape, elemental composition, and internal structure of a noble-metal nanoparticle on its performance in IVDs within the recent decade.

1.3.1 Impact of Size

The size of a noble-metal nanostructure not only has a great impact on signal transduction but also affects the way a nanostructure interacts with biomolecules and/or other components of an IVD platform. For example, Špringer *et al*. quantitatively investigated how the size of Au nanoparticles (AuNPs) influences their capability in enhancing the response of SPR biosensors.[129] The study involved both experimental work and theoretical simulations. As a model system (**Figure 1.10a**), neutravidin-functionalized AuNPs (N-AuNPs) were used in the last step of a sandwich assay of carcinoembryonic antigen (CEA) to enhance the SPR sensor response to biotinylated secondary antibody against CEA. AuNPs with diameters of 10, 15, 21, 33, and 52 nm were tested in this system to investigate the size effect. The sensor response (shift in the SPR wavelength, $\Delta\lambda_r$) is determined by two factors—the surface density of captured AuNPs ($\Delta\sigma$) and the sensor sensitivity to AuNP surface density (S_σ), which are related as $\Delta\lambda_r = \Delta\sigma \times S_\sigma$. Herein, the first factor ($\Delta\sigma$) is defined as the ability of the N-AuNPs to bind to the SPR sensor surface through the interaction between a biotinylated antibody and neutravidin on the AuNP surface (**Figure 1.10a**). The second factor (S_σ) is defined only by the optical properties of both the N-AuNPs and the properties of the sensor. This factor measures the ratio between changes in the sensor response to changes in the N-AuNP surface density. Significantly, $\Delta\lambda_r$ and $\Delta\sigma$ could be experimentally determined through SPR instrument readout and scanning electron microscopy (SEM) imaging, respectively. Therefore, the value of S_σ can be experimentally derived through following equation:

$$S_\sigma = {}^{\Delta\lambda_r}/_{\Delta\sigma} \qquad (1)$$

The data of $\Delta\lambda_r$ and $\Delta\sigma$ for different sized AuNPs are summarized in **Figure 1.10b**, **c**, respectively. On the basis of these data and equation 1, the values of S_σ were derived (symbol ■ in

Figure 1.10d). This set of experimental data was well correlated to the results from a theoretical model (lines in **Figure 1.10d**) that relates the enhancement generated by various characteristics of the AuNPs (*e.g.*, size, composition, and concentration). It can be concluded that, while S_σ increases with the size of the N-AuNP, the ability of the bioreceptor-functionalized surface of the sensor to bind the N-AuNPs is affected by steric effects and thus decreases with the size of N-AuNP. This study provides a quantitative understanding on the impact of particle size, allowing for the design and development of SPR biosensors with optimized analytical performance.

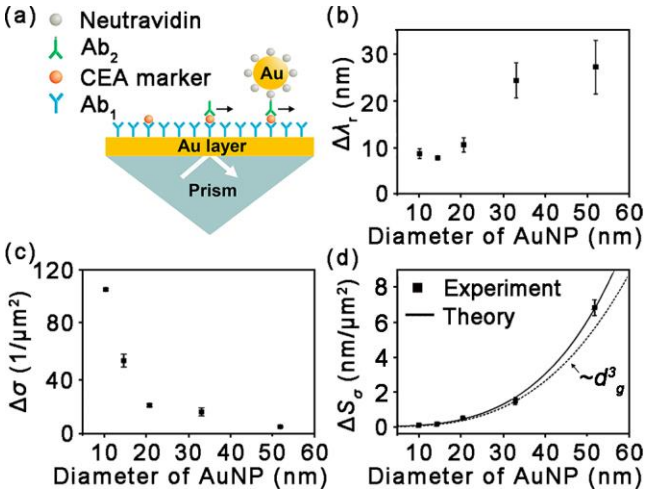

Figure 1.10 (a) Schematics showing the sandwich assay of carcinoembryonic antigen (CEA) by a neutravidin-functionalized AuNP (N-AuNP)-enhanced SPR sensor. N-AuNPs with Au cores of five different sizes are evaluated in the sensor. (b) Sensor responses ($\Delta\lambda_r$) for N-AuNPs with different sizes. (c) Surface densities ($\Delta\sigma$) for N-AuNPs with different sizes. (d) Theoretical and experimental sensor sensitivity to surface density (S_σ) as a function of N-AuNP size. The dotted line represents a cubic dependence of S_σ on the AuNP size. Adapted with permission from ref 129. Copyright 2014 American Chemical Society.

Size also plays a decisive role in other signal transduction principles. For example, AuNPs can effectively generate a color signal (through absorption/scattering of incident light) and thermal contrast signal (through the photothermal effect.[130-131] The size of AuNPs has been recognized to

have a great impact on both types of signal and associated IVD platforms. In a recent work by Zhan *et al.*, such impacts have been understood from both theoretical and experimental aspects using a lateral flow assay (LFA) as a model IVD platform.[132] In a typical sandwich LFA test (**Figure 1.11a**), analyte flows through a paper-based strip by capillary force and is first captured by detection antibody-labeled AuNPs to form a complex.[133] The complex is then captured by antibodies precoated on the test zone of the membrane. The accumulation of AuNPs at the test zone results in a visible red color, indicating a positive test. In conventional LFA, AuNPs of 30-40 nm in diameter are used as colorimetric labels. To improve the sensitivity of LFA, Zhan *et al.* carefully studied the impact of AuNP size (30, 60, and 100 nm in diameter). The nitrocellulose membrane is conceptually simplified as a bundle of cylindrical pores of radius R (**Figure 1.11a**). The Peclet number (P_e) and the Damkohler number (D_a) were scaled to assess the importance of diffusion to convection and reaction in LFA (**Figure 1.11b**). Particularly, in the formula of Da, the effective forward reaction rate constant (k_{on}') for antibody-labeled AuNP is assumed to be

$$k'_{on} = nk_{on} \qquad (2)$$

Here, k_{on} is the forward rate constant for a single antibody-antigen interaction in the LFA setting, and n is the effective number of antibodies per AuNP. A COMSOL model was developed to analyze the system and predict LFA performance prior to experiments. The model shows that reaction and convection have a higher impact on AuNP capture in the test zone than diffusion, with the reaction being the rate-limiting factor in AuNP capture. In this system, the reaction is largely determined by k_{on}'. Therefore, on the basis of equation 2, larger sized AuNPs would have greater k_{on}' due to the larger number of antibodies per AuNP (n) and thus could improve AuNP capture. **Figure 1.11c** shows the modeling results for a sandwich LFA of C-reactive protein (CRP, a

biomarker of inflammation) achieved by the COMSOL model. **Figure 1.11d** shows the modeling results-guided experimental results where both thermal and color signals were measured for the CRP LFAs. It can be seen that the modeling results agreed well with experimental results, including the observation of the "hook effect" (reduction in signal at excessively high analyte concentrations).[134-135] The two sets of data quantitatively demonstrate that larger sized AuNPs having a higher effective forward rate constant (k_{on}') could increase AuNP capture and therefore LFA sensitivity. In particular, under thermal signal detection mode, 100 nm AuNPs yield a 256-fold sensitivity enhancement relative to conventional 30 nm AuNP-based colorimetric LFA. It should be mentioned that AuNP capture will be rate-limited by diffusion when the size is beyond 100 nm. Modeling results show that larger AuNPs (*e.g.*, 400 nm) will settle in the membrane pores within 50 s, the time necessary for a AuNP to migrate from conjugate pad to test zone. Therefore, further increasing particle size will decrease AuNP capture and thus the sensitivity of LFA because larger AuNPs have slower diffusion rates.

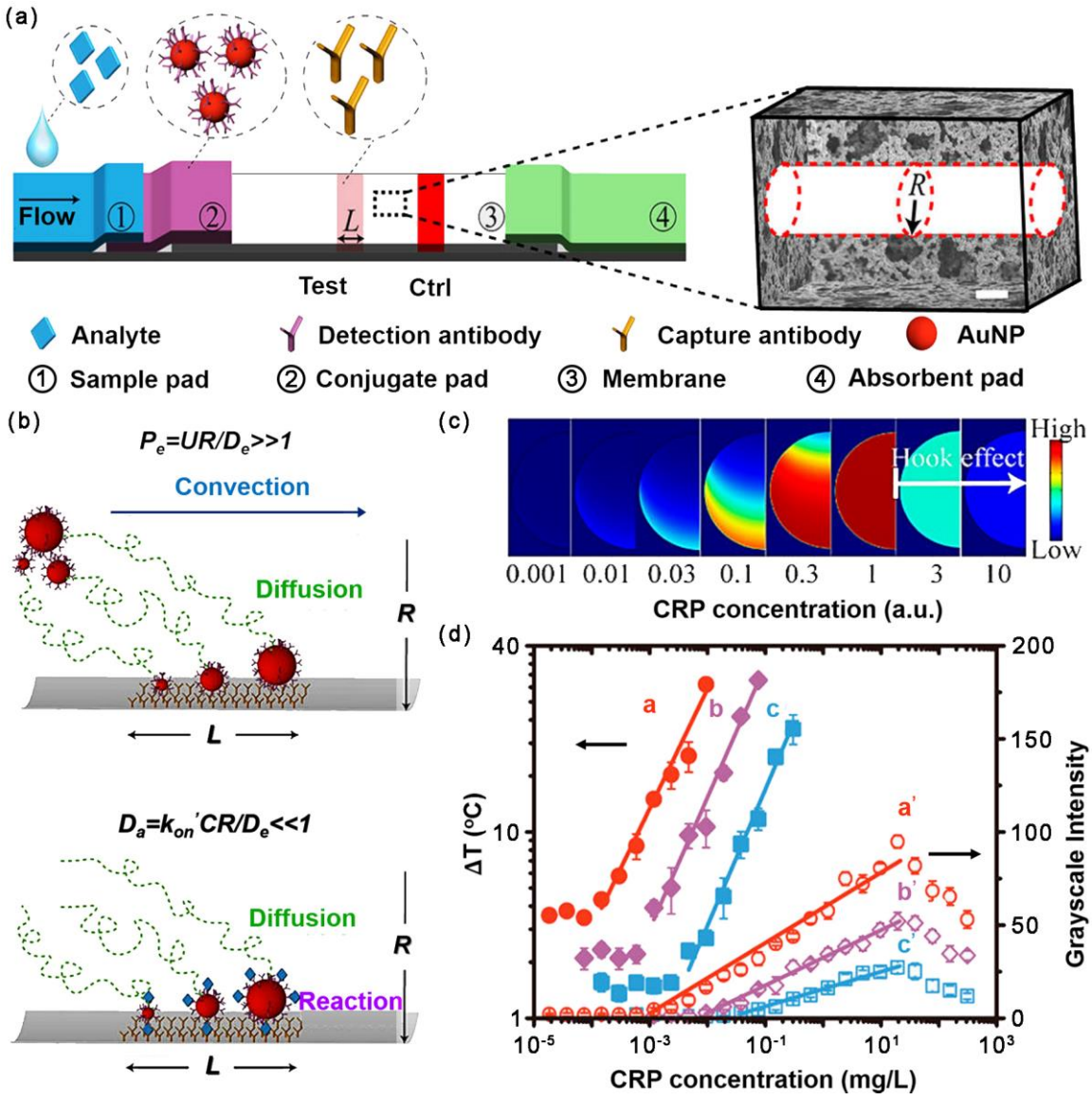

Figure 1.11 (a) Schematics showing the architecture of a typical AuNP-based LFA with test line width L, where the nitrocellulose membrane is conceptually simplified as bundles of cylindrical pores with radius R. Ctrl represents the control line of LFA. AuNPs of 30, 60, and 100 nm in diameter are studied in the LFA. (b) P_e and D_a that were used to assess the factors of convection, diffusion, and reaction in LFA. Reaction is recognized to be the rate-limiting step of AuNP capture in the test zone. (c) COMSOL modeling result showing the capture of 100 nm AuNP in the test zone of sandwich LFA of C-reactive protein (CRP). (d) Experimental thermal (solid symbols) and visual (hollow symbols) signals of CRP LFAs. a/a′, b/b′, and c/c′ denote the results for 100 nm, 60

nm, and 30 nm AuNPs, respectively. Adapted with permission from ref 132. Copyright 2017 American Chemical Society.

These examples demonstrate the importance of size control in AuNP-based IVD technologies. In fact, the profound impact of particle size on IVDs was also observed in a number of other NMNSs. For instance, for Ag nanoparticle-based SERS detection, the optimal size of Ag nanoparticles for providing a maximum SERS signal of adsorbed R6G was found to be ~50-60 nm.[136] In a Pt nanoparticle-based colorimetric assay, among Pt nanoparticles with diameters in the range of 50-280 nm, ~150 nm Pt nanoparticles gave the highest signal intensity.[137]

1.3.2 Impact of Shape

Compared to size control, shape control is even more effective and versatile in enhancing the properties of a noble-metal nanostructure and thus its performance in IVDs. For instance, the LSPR peak of a Au or Ag nanostructure is more sensitive to its shape relative to size.[126, 138] Steric effect in interaction with biomolecules caused by the increase of particle size can be minimized in the case of shape control. Moreover, shape control is more cost-efficient since it avoids the increase of materials usage.

In the SPR biosensor (see a model in **Figure 1.10a**), the signal enhancement and detection sensitivity have a strong dependence on the shape of Au nanostructures as enhancers. Kwon *et al.* studied the shape effect in the SPR biosensor by comparing the performance of Au nanostructures with quasi-spherical and rod-like shapes (**Figure 1.12a**, **b**).[139] Both Au nanostructures possess at least one dimension in the 40-50 nm range. Thrombin was chosen as a model biomarker, which was captured by the DNA aptamer probe attached to the SPR-chip surface and the specific antibody conjugated on the Au nanostructures to form a sandwich complex during an assay. As shown by

the spectra in **Figure 1.12a**, **b**, the major LSPR peaks for the Au quasi-spherical nanoparticles and nanorods were located at ~640 nm and ~530 nm, respectively. This difference in LSPR peak can be ascribed to the difference in particle shape. Under the same assay conditions, the minimum thrombin concentrations detected by the Au quasi-spherical nanoparticles and nanorods were 1 and 10 aM, respectively (see **Figure 1.12c, d**). This difference in signal generation and thus detection sensitivity originated from the changes in the real and imaginary components of the refractive index of the film at the chip-solution interface that were induced by the adsorbed Au nanostructures. The poorer detection performance of the Au nanorods relative to the Au quasi-spherical nanoparticles could be ascribed to that fact that (*i*) the nanorods induced a smaller change in the real component of the refractive index, since the volume of the nanorods is ~3-fold lower than that of the quasi-spherical nanoparticles with the same particle number, and (*ii*) near-field plasmonic coupling occurred in the case of nanorods due to the overlap between the particle LSRP profile and the wavelength of light source in the sensor device (760 nm), which affected the imaginary component of the refractive index. The shape-dependent performance of the SPR biosensor was extensively investigated in other studies, where Au nanostructures with various shapes were examined.[140-142]

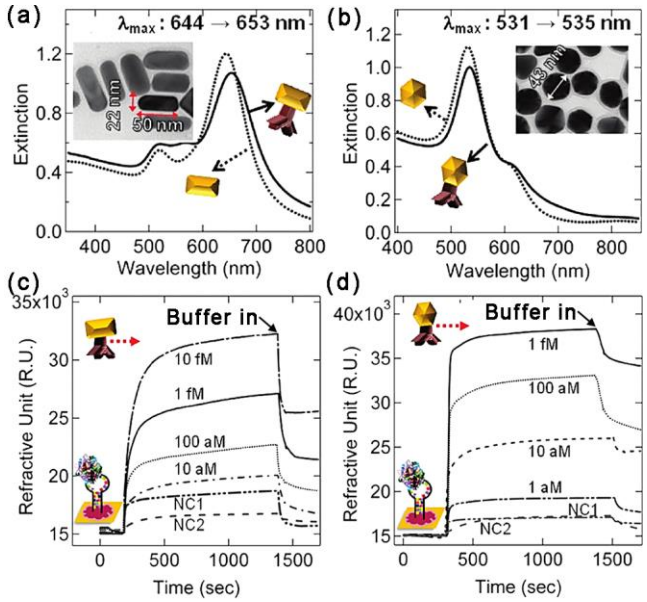

Figure 1.12 (a, b) UV-vis spectra taken from aqueous suspensions of (a) Au nanorods and (b) Au quasi-spherical nanoparticles before (dashed lines) and after (solid lines) they had been conjugated with antithrombin antibodies. Insets show TEM images of corresponding Au nanostructures. (c, d) SPR sensorgrams for the detection of thrombin using (c) Au nanorods and (d) Au quasi-spherical nanoparticles as the signal enhancers. NC1 and NC2 represent nonspecific signal recorded from antithrombin conjugated Au nanostructures in the absence of thrombin and anti-BSA conjugated Au nanostructures in the presence of thrombin, respectively. Adapted with permission from ref 139. Copyright 2012 American Chemical Society.

In recent years, artificial enzymes (or enzyme mimics) made of NMNSs have emerged as a new type of functional material for IVDs.[143-145] In a typical IVD test, the enzyme mimics are conjugated to bioreceptors and specifically generate a detection signal by catalyzing enzyme substrates. Compared to their natural counterparts, enzyme mimics are more stable owing to the excellent stabilities of noble metals. In this niche field, the major challenge is to enhance the catalytic efficiency of mimics since it largely determines the intensity of detection signal and thus the assay sensitivity. It has been demonstrated that the catalytic efficiency of an enzyme mimic has a strong dependence on the arrangement of atoms on the surface, which is correlated to the

geometric shape of the mimic. For example, the catalase-like activity (*e.g.*, decomposition of H_2O_2 into O_2) of {111}-covered Pd octahedrons was measured to be much higher than that of {100}-covered Pd nanocubes under the same conditions (**Figure 1.13a**).[146] As revealed by theoretical simulations, this difference in catalytic activity can be ascribed to the difference in reaction energy (E_r) of the rate-limiting step (E_r = -2.81 for $Pd_{\{111\}}$ *vs.* E_r = -2.64 for $Pd_{\{100\}}$). It is worth noting that the catalase-like activity of NMNSs enables the translation of molecular recognition events into easily measurable physical parameters such as volume and pressure of oxygen gas. On the basis of these signal-transducer principles, simple and sensitive point-of-care IVD tests were established.[147-148] In a recent work by Gao *et al.* (**Figure 1.13b**), Pt concave nanocubes encased by high index facets were demonstrated to possess a peroxidase-like activity that was ~1500- and 4-times higher than those of natural peroxidases and Pt nanospheres, respectively.[149] The peroxidase-like property of Pt concave cubes allowed them to generate an intense color signal by catalyzing chromogenic substrates. Using colorimetric enzyme-linked immunosorbent assay (ELISA) as a model IVD platform, antibody conjugated Pt concave nanocubes as labels were able to detect prostate-specific antigen (PSA, a biomarker of prostate cancer) with a broad linear range (20-2000 pg/mL) and a detection limit of 0.8 pg/mL, which is much lower than that of a commercial ELISA kit.

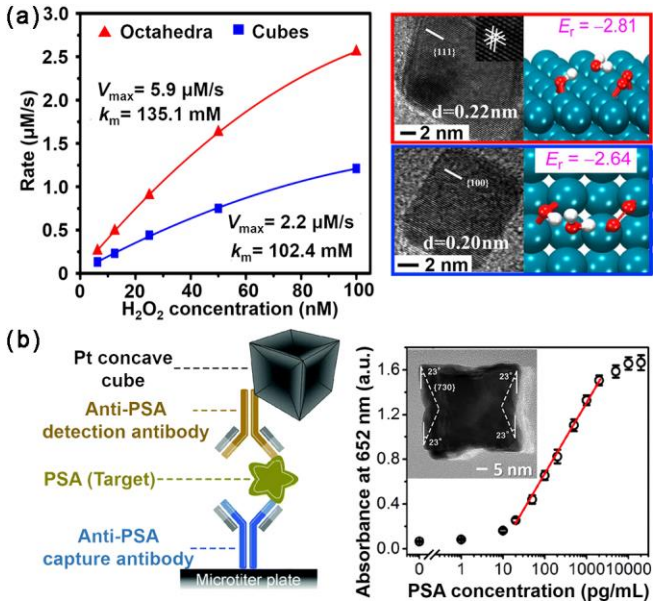

Figure 1.13 (a) Catalase-like activity of Pd octahedrons and nanocubes. The plots (left column) show the steady-state kinetic assay of Pd nanostructures with H_2O_2. V_{max} and K_m in the inset indicate the maximal reaction velocity and the Michaelis-Menten constant, respectively. The right column shows high-resolution TEM images of individual Pd octahedra (top) and nanocubes (bottom). The models show simulated atomic structures on metal surfaces after the reaction of $H_2O_2 + HO_2 \rightarrow O_2 + OH + H_2O$. Adapted with permission from ref 146. Copyright 2016 American Chemical Society. (b) ELISA of prostate specific antigen (PSA) using Pt concave nanocubes as the labels, which act as peroxidase mimics to generate a color signal by catalyzing chromogenic substrates. Left column shows the schematic illustration of the assay. Right column shows the calibration curve of the assay for PSA standards. The inset shows a TEM image of an individual Pt concave nanocube. Adapted with permission from ref 149. Copyright 2017 Royal Society of Chemistry.

Besides those above-mentioned examples, the shape of a noble-metal nanostructure also affects the generation of other types of detection signals in IVDs. For instance, in metal-enhanced fluorescence (MEF), the enhancement of the fluorescence signal has a strong dependence on the plasmonic properties that are largely determined by the shape of a nanostructure.[150-151] The color of a Au or Ag nanostructure suspension can be tuned by changing the particle shape, which allows

for multiplexed detection of the biomarker/virus with colorimetric assays.[152] The electrochemical signal of a noble-metal nanostructure can also be enhanced by carefully controlling the shape.[153-154]

1.3.3 Impact of Elemental Composition

It should be emphasized that certain properties of NMNSs within a category could be distinctively different because the inherent nature of metal is unique with each other.[19, 155] For example, the plasmonic sensitivity of Ag nanorods is up to 2 times higher than that of Au nanorods with similar resonance wavelengths.[156] Apparently, elemental composition of a noble-metal nanostructure plays an important role in determining its properties and performance in IVDs. In the following discussion, instead of a monometallic system, a bimetallic system will be used to demonstrate that the performance of a noble-metal nanostructure in IVDs can be substantially improved by incorporating a second metal. In many cases, a subtle change in elemental composition makes a dramatic difference. The ideas and strategies discussed below can be extended to multimetallic systems.

First, a second metal can enhance the detection signal generated from a nanostructure. For example, our research group has developed a novel type of peroxidase mimic—Pd@Ir_{1-2L} core@shell nanocubes (**Figure 1.14a**)—that was prepared by coating ~18 nm Pd nanocubes with a few atomic layers of Ir.[66] The Pd@Ir_{1-2L} cubes displayed a record-high catalytic efficiency with a K_{cat} at the level of 10^6 s^{-1}, which is approximately 2 and 3 orders of magnitude higher than those of the initial Pd nanocubes and HRP, respectively (**Figure 1.14b**). Obviously, the enhanced efficiency of Pd@Ir_{1-2L} cubes relative to the Pd nanocubes as the seeds can be attributed to the coat of Ir shells. To understand the impact of Ir shells on the catalytic efficiency, a set of Pd@Ir cubes

with different molar ratios of Ir to Pd were prepared, and their K_{cat} values were determined. Interestingly, it was found that the K_{cat} values showed a volcano-shaped dependence on the Ir contents, with a maximum point corresponding to approximately a monolayer of Ir on a Pd surface. Density functional theory (DFT) based theoretical calculations were conducted to gain more insights into the experimental observations, where Pd(100), Ir(100), Ir_{1L}/Pd(100), and Ir_{3L}/Pd(100) were compared. The simulation results indicated that Ir_{1L}/Pd(100) among the four surfaces was the most reactive since the adsorption energies of key species in the catalytic reaction on this surface were most exothermic, which agreed well with the experimental results. Using ELISA as a model IVD platform and PSA as a disease biomarker, the Pd@Ir_{1-2L} cube-based ELISA achieved a detection limit of 0.67 pg/mL, which is ~110-fold lower than that of the conventional HRP-based ELISA (**Figure 1.14c, d**). This substantial improvement in detection sensitivity can be ascribed to the enhanced catalytic efficiency of Pd@Ir_{1-2L} cubes relative to HRP because all the antibodies and materials used in the two ELISAs were kept the same. Enhancing the detection signal by incorporating a second metal is also evident in electrochemical biosensors.[157-158]

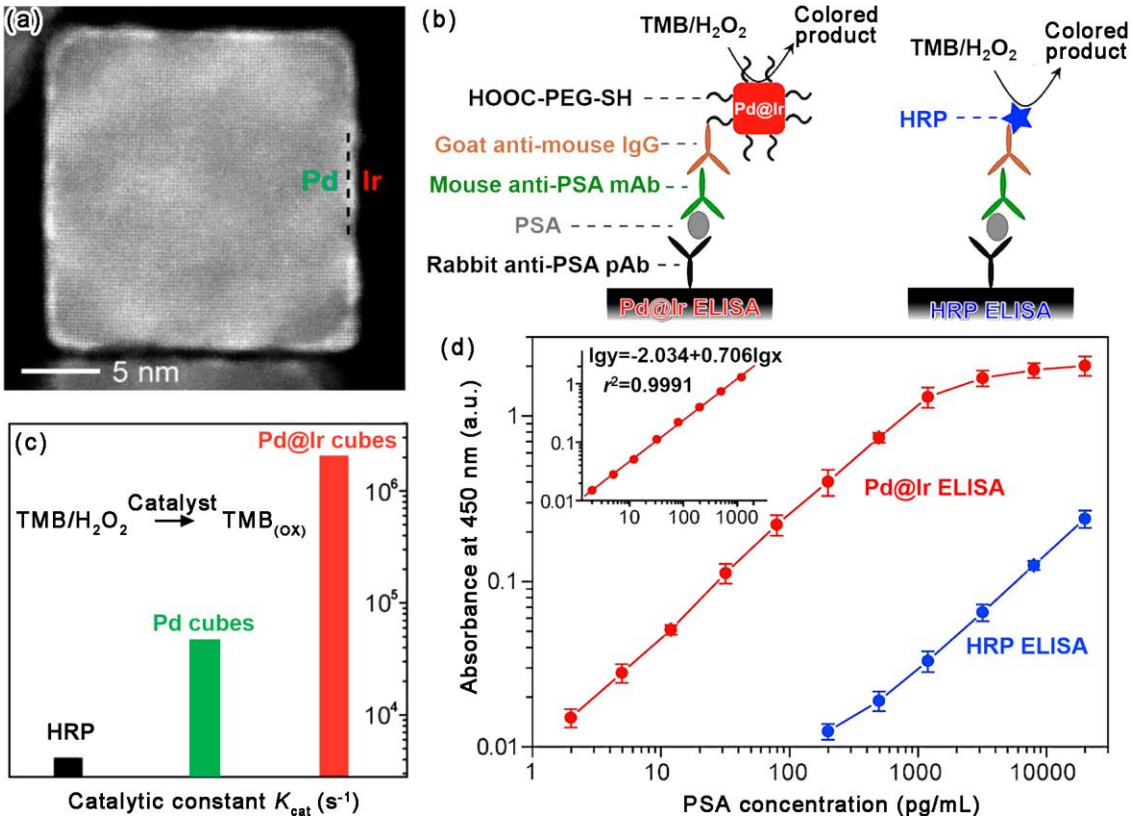

Figure 1.14 Pd@Ir$_{1\text{-}2L}$ core@shell cubes and their use in ELISA. (a) HAADF-STEM image of an individual Pd@Ir$_{1\text{-}2L}$ cube. (b) A chart comparing the peroxidase-like efficiencies (in terms of K_{cat}) of HRP, Pd cubes, and Pd@Ir$_{1\text{-}2L}$ cubes. (c) Schematics showing the principles of Pd@Ir$_{1\text{-}2L}$ cube- and HRP-based ELISAs. (d) Calibration curves of the two ELISAs for PSA standards. Inset shows the linear range region of the Pd@Ir$_{1\text{-}2L}$ cube-based ELISA. Adapted with permission from ref 66. Copyright 2015 American Chemical Society.

Second, a second metal can enhance the stability of a nanostructure, ensuring reliable IVDs. Nanostructures of Ag are known to possess the strongest plasmonic activities among noble metals owing to their appropriate electronic structure and thus dielectric function.[126, 159-161] Nevertheless, the excellent plasmonic properties of Ag nanostructures have not been fully utilized in IVDs and many other applications due to the relatively poor chemical and structural stabilities of Ag under unfavorable environments.[162-164] Therefore, development of approaches that can stabilize Ag

nanostructures without compromising their plasmonic properties is critical to the practical applications of Ag nanostructures. An effective approach is to incorporate Ag nanostructures with Au, which is much more stable and has almost the same lattice constant as Ag. For example, Yang *et al.* reported a robust synthesis of Ag@Au core@shell nanocubes by depositing Au atoms onto Ag nanocubes.[165] The key to the successful synthesis relied on the inhibition of the galvanic replacement between Ag and Au^{3+} by introducing a strong reducing agent to rapidly consume Au^{3+} ions. The conformal and ultrathin Au shells (sub-10 atomic layers, see a representative sample in **Figure 1.15a**) were able to protect the Ag nanocubes in oxidative environments. The Ag@Au nanocubes displayed surface plasmonic properties essentially identical to those of the initial Ag nanocubes. Significantly, because of the stronger adsorption of Raman probe molecules on the Au surface relative to Ag, the Ag@Au nanocubes exhibited an outstanding and stable SERS activity with an enhancement factor (EF) ~5-fold greater than that of Ag nanocubes (**Figure 1.15b**). In another study by Gao *et al.*, instead of core@shell structure, Au was mixed with Ag to form a Ag/Au alloyed structure (**Figure 1.15c**).[166] Unlike conventional methods based on co-reduction of Au and Ag precursors, the Ag/Au alloy was formed through the annealing process at elevated temperatures (~1000 °C). The high-temperature annealing promoted the complete mixing of Ag and Au at the atomic scale. The alloyed nanostructure obtained from this method is featured by homogeneous distribution of Ag and Au, minimal crystallographic defects, and the absence of structural and compositional interfaces. These features ensured outstanding plasmonic properties (*e.g.*, large extinction cross-sections and narrow bandwidths) and enhanced stabilities for the resultant Ag/Au alloyed nanostructures (see **Figure 1.15d**). Collectively, these approaches preserved the superior plasmonic properties of Ag while adopting the excellent stabilities of Au, making the Au-incorporated Ag nanostructures particularly suitable for IVDs (*e.g.*, SPR and SERS

biosensing).

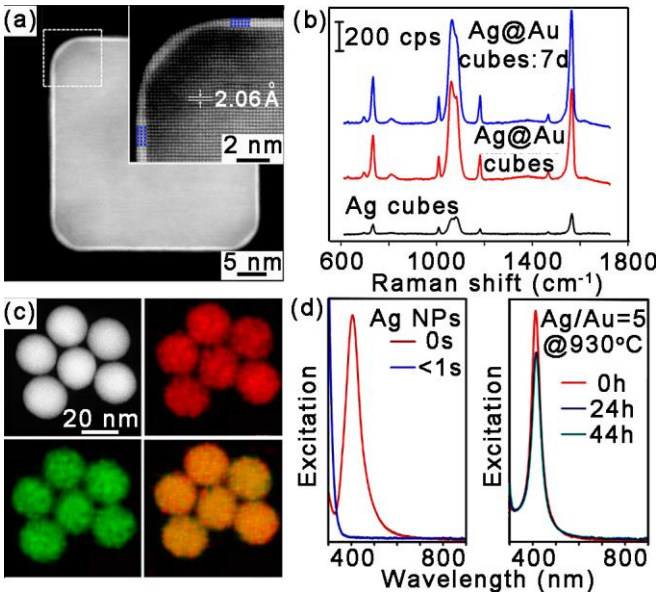

Figure 1.15 (a) HAADF-STEM image of an individual Ag@Au core@shell nanocube. Inset is a magnified image highlighting the three atomic layers of Au on the Ag core. (b) SERS spectra taken from aqueous suspensions of 1,4-benzenedithiol functionalized Ag@Au nanocubes (sample in a) and Ag nanocubes. Adapted with permission from ref 165. Copyright 2014 American Chemical Society. (c) STEM and EDX mapping images of Ag/Au alloyed NPs (Ag/Au = 5). (d) UV-vis spectra recorded from pure Ag NPs and Ag/Au alloyed NPs that were suspended in a mixed solvent of H_2O_2 and ammonia. Adapted with permission from ref 166. Copyright 2014 American Chemical Society.

1.3.4 Impact of Internal Structure

The internal structure of NMNSs in this section refers to the hollowness. Hollow NMNSs have received great interest in recent years because of the unique and useful properties that cannot be offered by their solid counterparts.[167] For example, hollow nanostructures of Au or Ag are known to have better plasmonic properties compared to their solid counterparts thanks to the interaction of plasmon fields in the inner and outer layers, in compliance with the plasmon

hybridization mechanism.[168] The hybridizations of the plasmons leads to the enhanced plasmon fields together with homogeneous distribution and a red-shift of plasmon resonances.[169-171] In a recent work, Genç *et al*. systematically investigated the plasmon resonances of Au/Ag cubic nanostructures with different extents of hollowness (including solid nanocubes, nanocubes with pinholes, nanoboxes with completely hollow interior, and nanoframes with an open structure) on the nanoscale.[172] Electron energy loss spectroscopy (EELS) was employed to obtain the spatially resolved mapping of plasmon resonances. Among those nanostructures, nanoboxes exhibited homogeneous distribution of plasmon resonances. As shown by the selected area EEL spectra obtained from different sites of a single nanobox (**Figure 1.16a**), the plasmon peaks were located in a relatively narrow range of ~2-2.5 eV and had similar energies to one another. The abundance maps clearly show the homogeneous distribution of plasmon resonance all around the nanobox. These experimental observations were accurately correlated with the simulation results based on the BEM.[33] In contrast, other nanostructures showed much fewer homogeneous distributions. This work revealed that the homogeneous distribution of plasmon resonances is the key feature for the enhanced plasmonic properties of hollow nanostructures. As a proof-of-concept demonstration, the nanoboxes were applied to label free SPR detection of bovine serum albumin (BSA) and anti-BSA antibodies, of which performance was benchmarked against solid Au nanoparticles (see **Figure 1.16b**). The adsorption of biomolecules on the plasmonic nanostructures induces refractive index changes that can be measured by a UV-vis spectrometer. Compared with solid Au nanoparticles, ~4-times stronger shifts in extinction wavelength were observed for the Au/Ag nanoboxes. This enhanced detection sensitivity could be ascribed to the enhancement of the localized electromagnetic field around the hollow nanoboxes that allowed for sensitive responses to binding events in their vicinity.

The hollow feature of a nanostructure also benefits its SERS enhancement and thus SERS biosensing. For example, in a work by Lim *et al.*, Au nanobridged nanogap particles (Au-NNPs, see **Figure 1.16c**) with ~1 nm gap between the core and shell were synthesized using dyed DNA-functionalized Au nanoparticles as the seeds.[173] Owing to the drastically enhanced electromagnetic field localized in the interior-gap region of the Au-NNP, the Raman signal from dyes trapped in the nanogap can be significantly amplified. Compared with solid Au nanoparticles, the Raman signal from the Au-NNPs was approximately 2 orders of magnitude stronger. Atomic force microscope (AFM)-correlated nano-Raman measurement was performed to determine the EF of the Au-NNPs. Random mapping of 200 individual Au-NNPs showed that their EF values were narrowly and uniformly distributed within the range of 1.0×10^8 to 5.0×10^9, making the Au-NNPs capable of single-molecule detection. Such a SERS enhancement by interior nanogap was also observed in Au/Ag double-walled nanoboxes. Notably, the size of the nanogap was found to play an important role in determining the SERS EF. Overall, the EF continuously decreased as the gap size increased from ~1 to ~16 nm.

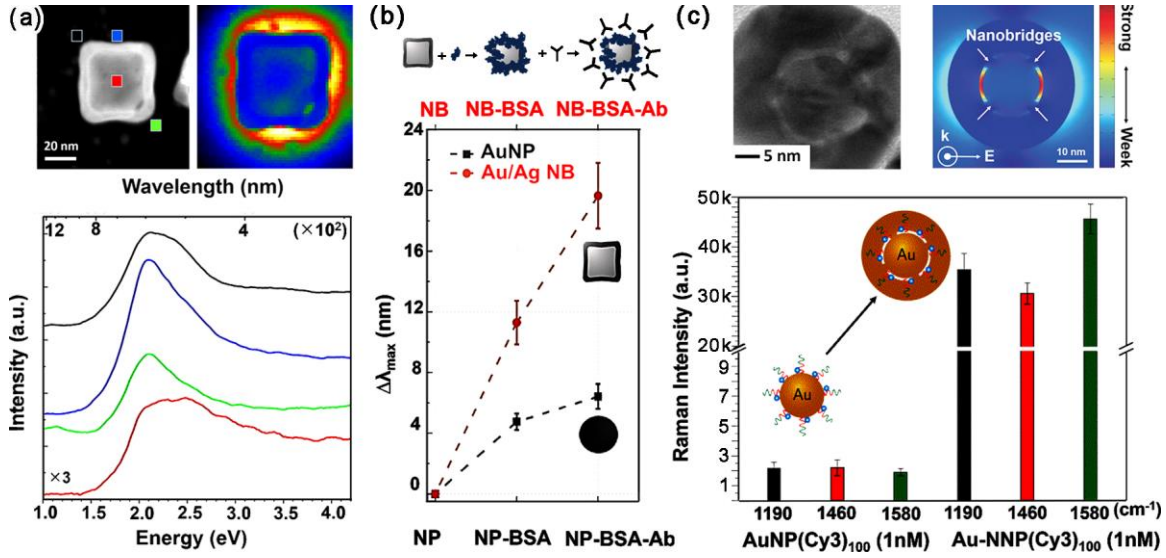

Figure 1.16 (a) Plasmonic properties of Au/Ag nanoboxes (NBs). HAADF-STEM image of a single Au/Ag NB (top left), selected area EEL spectra of the areas marked in the HAADF-STEM image (bottom), and abundance map obtained by vertex component analysis (VCA) processing (top right). (b) The shifts of major LSPR peaks ($\Delta\lambda_{max}$) for Au/Ag NB and AuNP suspensions after they had been conjugated with BSA and then anti-BSA antibody (BSA-Ab). Adapted with permission from ref 172. Copyright 2016 American Chemical Society. https://pubs.acs.org/doi/10.1021/acsphotonics.5b00667 (c) Au nanobridged nanogap particles (Au-NNPs) that were prepared using dye-DNA modified AuNPs as the seeds. TEM image of a single Au-NNP (top left), calculated near-field electromagnetic field distribution of a Au-NNP (top right), and a chart comparing the Raman intensities of Cy3 dye modified AuNPs and AuNNPs in solution. Adapted with permission from ref 173. Copyright 2011 Nature Publishing Group.

It is worth noting that most of above-mentioned enhanced performance relies on the superior plasmonic properties of hollow nanostructures. Nevertheless, hollow nanostructures have several other distinctive advantages over their solid counterparts that may be taken into consideration in future IVD development. For example, the outer and inner surfaces of a hollow nanostructure offer more flexibilities for biomolecule conjugation. The cavity in a hollow nanostructure affects its density/weight and thus transport properties (*e.g.*, diffusion and

sedimentation), which may influence its performance in IVD tests. The enlarged surface area and active surface atoms of a hollow nanostructure can boost its catalytic activities, providing enhanced detection signal.

1.4 Objective and Overview of This Thesis

Since the NMNSs serve as the signal transducers of IVDs, they are mainly responsible for the detection performance in relevance. Engineering NMNSs provides an efficient way to improve their physicochemical properties, thereby the signal generation in the IVDs. To date, many of the reported studies focused on the engineered Ag, Au, Pd, and Pt nanostructures, few attentions have been paid to the rest. Also, improvement of peroxidase-like efficiency of NMNSs-based enzyme mimics has met with limited success.

Facing with those challenges, we set up two objectives upon completion of the dissertation research: engineering NMNSs with superior peroxidase-like activity and developing ultrasensitive colorimetric IVD platforms for practical cancer detection. Inspired by our pioneer work of Pd-Ir nanocubes with record-high peroxidase-like efficient,[66] several projects were carried out. Briefly, introduction of each chapters is organized as follow:

Chapter 2 introduces the synthesis of Ru nanoframes (RuNFs) with face-centered cubic (*fcc*) crystal phase and enhanced catalytic activities. A two-step method was developed involving preferentially deposition of Ru on Pd cuboctahedra as seeds and selectively removal of Pd content, leading to the formation of RuNFs. The seed-mediated growth was believed to be responsible for the formation of *fcc* crystal phase of RuNFs.

Chapter 3 introduces a work that for the first time reports the Ru nanostructures with inherent peroxidase-like activity, of which the K_{cat} was approximately three times more active than natural peroxidases.

Chapter 4 introduces an enzyme-free signal amplification technique for ultrasensitive colorimetric assay of disease biomarkers. In this study, sub-10 nm Pd-Ir nanooctahedra encapsulated gold vesicles were employed as labels to replace the enzymes in conventional ELISA, achieving substantially enhanced detection sensitivity.

Chapter 5 introduces the facile synthesis of polyvinylpyrrolidone (PVP)-capped Pt nanocubes. The method we developed features several advantages over conventional preparation of Pt nanocubes. Also, the PVP-capped Pt nanocubes showed a superior peroxidase-like efficiency.

Chapter 6 introduces a novel strategy for colorimetric Ag(I) ions detection with high sensitivity. In this study, we found that the Ag(I) ions could significantly inhibit the peroxidase-like activity of Pt nanocubes as-prepared in Chapter 5. On the basis of this discovery, we developed a colorimetric method for Ag^+ ions detection. Also, the inhibition mechanism was investigated.

Chapter 7 introduces a non-enzyme cascade-amplification (NECA) strategy for colorimetric assay of disease biomarkers. The amplification principle was again based on the inhibition effect of Ag(I) ions to the peroxidase-like activity of Pt nanocubes. Coupling with silver enhancement, the NECA strategy could achieve a more sensitive detection of cancer biomarker than conventional ELISA.

Chapter 8 introduces a dual-mode colorimetric IVD platform based on Au@Pt core-shell nanostructures as the signal transducers. Specifically, the Au@Pt core-shell nanostructures possess

the plasmonic property of the Au cores and high peroxidase-like activity of the Pt skins, allowing them to provide "on/off-demand" detection modes: one produced by the red color of interior AuNPs as the low-sensitivity mode and the other generated by the blue color from the Pt-catalyzed oxidation of peroxidase substrate as the high-sensitivity mode.

1.5 Reference

1. Faraday, M. *Philos. Trans. R. Soc. London*, **1857**, *147*, 145-181.

2. Feynman, R. P. *Caltech. Eng. Sci.* **1960**, *23*, 22-36.

3. Binnig, G. *Helv. Phys. Acta* **1982**, *55*, 726.

4. Binnig, G. *Phys. Rev. Lett.* **1986**, *56*, 930.

5. Drexler, K. E. *Molecular machinery, manufacturing and computation.* **1992**.

6. Hutchings, G. J.; Brust, M.; Schmidbaur, H. *Chem. Soc. Rev.* **2008**, *37*, 1759-1765.

7. Fahlman, B. D. *Semiconducting materials. In Materials Chemistry*, Springer: **2007**, 153-219.

8. Roco, M. C. *The long view of nanotechnology development: the National Nanotechnology Initiative at 10 years*. Springer: 2011.

9. Somorjai, G. A. *Chem. Rev.* **1996**, *96*, 1223-1236.

10. Davey, N.; Seymour, R. *Platin. Met. Rev.* **1985**, *29*, 2-11.

11. Maier, S. A.; Brongersma, M. L.; Kik, P. G.; Meltzer, S.; Requicha, A. A.; Atwater, H. A. *Adv. Mater.* **2001**, *13*, 1501-1505.

12. Mulvaney, P. *MRS Bull.* **2001**, *26*, 1009-1014.

13. Obuchi, A.; Ohi, A.; Nakamura, M.; Ogata, A.; Mizuno, K.; Ohuchi, H. *Appl. Catal. B: Environ.* **1993**, *2*, 71-80.

14. Wang, H.; Brandl, D. W.; Nordlander, P.; Halas, N. J. *Acc. Chem. Res.* **2007**, *40*, 53-62.

15. Yang, X.; Skrabalak, S. E.; Li, Z.-Y.; Xia, Y.; Wang, L. V. *Nano Lett.* **2007**, *7*, 3798-3802.

16. Dreaden, E. C.; Alkilany, A. M.; Huang, X.; Murphy, C. J.; El-Sayed, M. A. *Chem. Soc. Rev.* **2012**, *41*, 2740-2779.

17. Ratner, M. A.; Ratner, D. *Nanotechnology: A gentle introduction to the next big idea*. Prentice Hall Professional: **2003**.

18. Xia, Y.; Xiong, Y.; Lim, B.; Skrabalak, S. E. *Angew. Chem., Int. Ed.* **2009**, *48*, 60-103.

19. Chen, M.; Wu, B.; Yang, J.; Zheng, N. *Adv. Mater.* **2012**, *24*, 862-879.

20. Smith, I. C.; Carson, B. L.; Ferguson, T. L. *Environ. Health Perspect.* **1974**, *8*, 201.

21. Kelly, K. L.; Coronado, E.; Zhao, L. L.; Schatz, G. C. *J. Phys. Chem. B* **2003**, *107*, 668-677.

22. Hatef, A.; Meunier, M. *Opt. Express* **2015**, *23*, 1967-1980.

23. Lal, S.; Link, S.; Halas, N. J. *Nat. Photonics* **2007**, *1*, 641.

24. Jain, P. K.; El-Sayed, I. H.; El-Sayed, M. A. *Nano today* **2007**, *2*, 18-29.

25. Mayer, K. M.; Hafner, J. H. *Chem. Rev.* **2011**, *111*, 3828-3857.

26. Mie, G. *Ann. Phys* **1908**, *25*, 377-445.

27. Gans, R. *Ann. Phys.(Lepzig)* **1912**, *37*, 881.

28. Wriedt, T. *Mie theory: a review. In The Mie Theory*, Springer: **2012**; 53-71.

29. Purcell, E. M.; Pennypacker, C. R. *Astrophys. J.* **1973**, *186*, 705-714.

30. Draine, B. T.; Flatau, P. J. *J. Opt. Soc. Am. A* **1994**, *11*, 1491-1499.

31. Schatz, G. C. *J. Mol. Struct.* **2001**, *573*, 73-80.

32. Wiley, B. J.; Im, S. H.; Li, Z.-Y.; McLellan, J.; Siekkinen, A.; Xia, Y. *J. Phys. Chem. B*, **2006**, *110*, 15666-15675.

33. Myroshnychenko, V.; Rodríguez-Fernández, J.; Pastoriza-Santos, I.; Funston, A. M.; Novo, C.; Mulvaney, P.; Liz-Marzan, L. M.; de Abajo, F. J. G. *Chem. Soc. Rev.* **2008**, *37*, 1792-1805.

34. Jain, P. K.; Huang, X.; El-Sayed, I. H.; El-Sayed, M. A. *Acc. Chem. Res.* **2008**, *41*, 1578-1586.

35. Sinfelt, J. H.; Yates, D. J. *J. Catal.* **1967**, *8*, 82-90.

36. Lee, I.; Morales, R.; Albiter, M. A.; Zaera, F. *Proc. Natl. Acad. Sci. U.S.A.* **2008**, *105*, 15241-15246.

37. Sinfelt, J. *Adv. Catal.* **1973**, *23*, 91-119.

38. Rao, C. R.; Trivedi, D. *Coord. Chem. Rev.* **2005**, *249*, 613-631.

39. An, K.; Somorjai, G. A. *ChemCatChem* **2012**, *4*, 1512-1524.

40. Kuhn, J. N.; Huang, W.; Tsung, C.-K.; Zhang, Y.; Somorjai, G. A. *J. Am. Chem. Soc.* **2008**, *130*, 14026-14027.

41. Bratlie, K. M.; Lee, H.; Komvopoulos, K.; Yang, P.; Somorjai, G. A. *Nano Lett.* **2007**, *7*, 3097-3101.

42. Xiong, Y.; Wiley, B. J.; Xia, Y. *Angew. Chem., Int. Ed.* **2007**, *46*, 7157-7159.

43. Xie, S.; Choi, S.-I.; Lu, N.; Roling, L. T.; Herron, J. A.; Zhang, L.; Park, J.; Wang, J.; Kim, M. J.; Xie, Z. *Nano Lett.* **2014**, *14*, 3570-3576.

44. Zhang, L.; Roling, L. T.; Wang, X.; Vara, M.; Chi, M.; Liu, J.; Choi, S.-I.; Park, J.; Herron, J. A.; Xie, Z. *Science* **2015**, *349*, 412-416.

45. Wei, H.; Wang, E. *Chem. Soc. Rev.* **2013**, *42*, 6060-6093.

46. Wu, J.; Wang, X.; Wang, Q.; Lou, Z.; Li, S.; Zhu, Y.; Qin, L.; Wei, H. *Chem. Soc. Rev.* **2019**.

47. Nelson, D. L.; Lehninger, A. L.; Cox, M. M. *Lehninger principles of biochemistry*. Macmillan: **2008**.

48. Wang, X.; Guo, W.; Hu, Y.; Wu, J.; Wei, H. *Nanozymes: next wave of artificial enzymes*. Springer: **2016**.

49. Passardi, F.; Theiler, G.; Zamocky, M.; Cosio, C.; Rouhier, N.; Teixera, F.; Margis-Pinheiro, M.; Ioannidis, V.; Penel, C.; Falquet, L. *Phytochemistry* **2007**, *68*, 1605-1611.

50. Pandey, V.; Awasthi, M.; Singh, S.; Tiwari, S.; Dwivedi, U. *Biochem. Anal. Biochem.* **2017**, *6*.

51. Hiraga, S.; Sasaki, K.; Ito, H.; Ohashi, Y.; Matsui, H. *Plant Cell Physiol.* **2001**, *42*, 462-468.

52. Gaetani, G. F.; Galiano, S.; Canepa, L.; Ferraris, A. M.; Kirkman, H. N. *Blood* **1989**, *73*, 334-339.

53. Veitch, N. C. *Phytochemistry* **2004**, *65*, 249-259.

54. Price, C. P.; Newman, D. J. *Principles and practice of immunoassay*. Springer: **1991**.

55. Klibanov, A. M.; Tu, T.-M.; Scott, K. P. *Science* **1983**, *221*, 259-261.

56. Chattopadhyay, K.; Mazumdar, S. *Biochemistry* **2000**, *39*, 263-270.

57. Gao, L.; Zhuang, J.; Nie, L.; Zhang, J.; Zhang, Y.; Gu, N.; Wang, T.; Feng, J.; Yang, D.; Perrett, S. *Nat. Nanotechnol.* **2007**, *2*, 577.

58. Song, Y.; Qu, K.; Zhao, C.; Ren, J.; Qu, X. *Adv. Mater.* **2010**, *22*, 2206-2210.

59. Sun, H.; Zhou, Y.; Ren, J.; Qu, X. *Angew. Chem., Int. Ed.* **2018**.

60. Fan, J.; Yin, J.-J.; Ning, B.; Wu, X.; Hu, Y.; Ferrari, M.; Anderson, G. J.; Wei, J.; Zhao, Y.; Nie, G. *Biomaterials* **2011**, *32*, 1611-1618.

61. André, R.; Natálio, F.; Humanes, M.; Leppin, J.; Heinze, K.; Wever, R.; Schröder, H. C.; Müller, W. E.; Tremel, W. *Adv. Funct. Mater.* **2011**, *21*, 501-509.

62. Zhao, H.; Dong, Y.; Jiang, P.; Wang, G.; Zhang, J. *ACS Appl. Mater. Interfaces* **2015**, *7*, 6451-6461.

63. Liu, S.; Lu, F.; Xing, R.; Zhu, J. *Chem. Eur. J.* **2011**, *17*, 620-625.

64. Sun, X.; Guo, S.; Chung, C. S.; Zhu, W.; Sun, S. *Adv. Mater.* **2013**, *25*, 132-136.

65. Zhang, X.; Wu, G.; Cai, Z.; Chen, X. *Talanta* **2015**, *134*, 132-135.

66. Xia, X.; Zhang, J.; Lu, N.; Kim, M. J.; Ghale, K.; Xu, Y.; McKenzie, E.; Liu, J.; Ye, H. *ACS nano* **2015**, *9*, 9994-10004.

67. Kang, Y.; Pyo, J. B.; Ye, X.; Diaz, R. E.; Gordon, T. R.; Stach, E. A.; Murray, C. B. *ACS nano* **2012**, *7*, 645-653.

68. Xia, Y.; Xia, X.; Peng, H.-C. *J. Am. Chem. Soc.* **2015**, *137*, 7947-7966.

69. Banholzer, M. J.; Millstone, J. E.; Qin, L.; Mirkin, C. A. *Chem. Soc. Rev.* **2008**, *37*, 885-897.

70. Dieringer, J. A.; Lettan, R. B.; Scheidt, K. A.; Van Duyne, R. P. *J. Am. Chem. Soc.* **2007**, *129*, 16249-16256.

71. Turner, A. P.; Chen, B.; Piletsky, S. A. *Clin. Chem.* **1999**, *45*, 1596-1601.

72. Michalet, X.; Pinaud, F.; Bentolila, L.; Tsay, J.; Doose, S.; Li, J.; Sundaresan, G.; Wu, A.; Gambhir, S.; Weiss, S. *Science* **2005**, *307*, 538-544.

73. Khlebtsov, N.; Dykman, L. *Chem. Soc. Rev.* **2011**, *40*, 1647-1671.

74. Jin, Z.; Hildebrandt, N. *Trends Biotechnol.* **2012**, *30*, 394-403.

75. Rohr, U.-P.; Binder, C.; Dieterle, T.; Giusti, F.; Messina, C. G. M.; Toerien, E.; Moch, H.; Schäfer, H. H. *PLoS One* **2016**, *11*, e0149856.

76. Zhou, W.; Gao, X.; Liu, D.; Chen, X. *Chem. Rev.* **2015**, *115*, 10575-10636.

77. Scott, M. G.; Bruns, D. E.; Boyd, J. C.; Sacks, D. B. *Clin. Chem.* **2009**, *55*, 18-20.

78. Peter, J. G.; Theron, G.; Dheda, K. *PloS one* **2013**, *8*, e54875.

79. Gottlieb, S.; Woodcock, J. *Nat. Biotechnol.* **2006**, *24*, 927.

80. Giljohann, D. A.; Mirkin, C. A. *Nature* **2009**, *462*, 461.

81. Ambrosi, A.; Airo, F.; Merkoçi, A. *Anal. Chem.* **2009**, *82*, 1151-1156.

82. Beqa, L.; Fan, Z.; Singh, A. K.; Senapati, D.; Ray, P. C. *ACS Appl. Mater. Interfaces* **2011**, *3*, 3316-3324.

83. Rundle, A.; Neugut, A. I. *Prostate* **2008**, *68*, 373-380.

84. Thaxton, C. S.; Elghanian, R.; Thomas, A. D.; Stoeva, S. I.; Lee, J.-S.; Smith, N. D.; Schaeffer, A. J.; Klocker, H.; Horninger, W.; Bartsch, G. *Proc. Natl. Acad. Sci. U.S.A.* **2009**, *106*, 18437.
85. Rissin, D. M.; Kan, C. W.; Campbell, T. G.; Howes, S. C.; Fournier, D. R.; Song, L.; Piech, T.; Patel, P. P.; Chang, L.; Rivnak, A. J. *Nat. Biotechnol.* **2010**, *28*, 595.
86. Asiago, V. M.; Alvarado, L. Z.; Shanaiah, N.; Gowda, G. N.; Owusu-Sarfo, K.; Ballas, R. A.; Raftery, D. *Cancer Res.* **2010**, 0008-5472. CAN-10-1319.
87. Turner, A. P. *Chem. Soc. Rev.* **2013**, *42*, 3184-3196.
88. Vashist, S. K.; Schneider, E. M.; Luong, J. H. *Biosens. Bioelectron.* **2015**, *67*, 73-78.
89. Jain, K. K. *Clin. Chim. Acta* **2005**, *358*, 37-54.
90. Chi, X.; Huang, D.; Zhao, Z.; Zhou, Z.; Yin, Z.; Gao, J. *Biomaterials* **2012**, *33*, 189-206.
91. Butler, S. A.; Khanlian, S. A.; Cole, L. A. *Clin. Chem.* **2001**, *47*, 2131-2136.
92. Van Amerongen, A.; Wichers, J.; Berendsen, L.; Timmermans, A.; Keizer, G.; Van Doorn, A.; Bantjes, A.; Van Gelder, W. *J. Biotechnol.* **1993**, *30*, 185-195.
93. Leuvering, J. H.; Thal, P.; Waart, M. v. d.; Schuurs, A. *J. Immunoassay. Immunochem.* **1980**, *1*, 77-91.
94. Kimling, J.; Maier, M.; Okenve, B.; Kotaidis, V.; Ballot, H.; Plech, A. *J. Phys. Chem. B* **2006**, *110*, 15700-15707.
95. Turkevich, J. *Gold Bull.* **1985**, *18*, 125-131.
96. Enustun, B.; Turkevich, J. *J. Am. Chem. Soc.* **1963**, *85*, 3317-3328.
97. Nightingale, A. M.; Bannock, J. H.; Krishnadasan, S. H.; O'Mahony, F. T.; Haque, S. A.; Sloan, J.; Drury, C.; McIntyre, R. *J. Mater. Chem. A* **2013**, *1*, 4067-4076.
98. Lohse, S. E.; Eller, J. R.; Sivapalan, S. T.; Plews, M. R.; Murphy, C. J. *ACS nano* **2013**, *7*, 4135-4150.
99. Niu, G.; Zhang, L.; Ruditskiy, A.; Wang, L.; Xia, Y. *Nano Lett.* **2018**, *18*, 3879-3884.
100. Sepúlveda, B.; Angelomé, P. C.; Lechuga, L. M.; Liz-Marzán, L. M. *nano today* **2009**, *4*, 244-251.
101. Huang, X.; Liu, Y.; Yung, B.; Xiong, Y.; Chen, X. *ACS nano* **2017**, *11*, 5238-5292.
102. Howes, P. D.; Rana, S.; Stevens, M. M. *Chem. Soc. Rev.* **2014**, *43*, 3835-3853.
103. Perfezou, M.; Turner, A.; Merkoçi, A. *Chem. Soc. Rev.* **2012**, *41*, 2606-2622.

104. Wu, X.; Xu, L.; Ma, W.; Liu, L.; Kuang, H.; Kotov, N. A.; Xu, C. *Adv. Mater.* **2016**, *28*, 5907-5915.

105. Rodríguez-Lorenzo, L.; De La Rica, R.; Álvarez-Puebla, R. A.; Liz-Marzán, L. M.; Stevens, M. M. *Nat. Mater.* **2012**, *11*, 604.

106. Zhu, H.; Sigdel, A.; Zhang, S.; Su, D.; Xi, Z.; Li, Q.; Sun, S. *Angew. Chem., Int. Ed.* **2014**, *53*, 12508-12512.

107. Hu, Y.; Cheng, H.; Zhao, X.; Wu, J.; Muhammad, F.; Lin, S.; He, J.; Zhou, L.; Zhang, C.; Deng, Y. *ACS nano* **2017**, *11*, 5558-5566.

108. Xie, J.; Zhang, Q.; Lee, J. Y.; Wang, D. I. *ACS nano* **2008**, *2*, 2473-2480.

109. Gao, L.; Liu, M.; Ma, G.; Wang, Y.; Zhao, L.; Yuan, Q.; Gao, F.; Liu, R.; Zhai, J.; Chai, Z. *ACS nano* **2015**, *9*, 10979-10990.

110. Liu, D.; Huang, X.; Wang, Z.; Jin, A.; Sun, X.; Zhu, L.; Wang, F.; Ma, Y.; Niu, G.; Hight Walker, A. R. *ACS nano* **2013**, *7*, 5568-5576.

111. Bui, M.-P. N.; Ahmed, S.; Abbas, A. *Nano Lett.* **2015**, *15*, 6239-6246.

112. Hong, R.; Fischer, N. O.; Emrick, T.; Rotello, V. M. *Chem. Mater.* **2005**, *17*, 4617-4621.

113. Latham, A. H.; Williams, M. E. *Langmuir* **2006**, *22*, 4319-4326.

114. Pale-Grosdemange, C.; Simon, E. S.; Prime, K. L.; Whitesides, G. M. *J. Am. Chem. Soc.* **1991**, *113*, 12-20.

115. Xia, X.; Yang, M.; Wang, Y.; Zheng, Y.; Li, Q.; Chen, J.; Xia, Y. *ACS nano* **2011**, *6*, 512-522.

116. Yan, Y.; Wang, T.; Li, X.; Pang, H.; Xue, H. *Inorg. Chem. Front.* **2017**, *4*, 33-51.

117. Zhang, X.; Si, S.; Zhang, X.; Wu, W.; Xiao, X.; Jiang, C. *ACS Appl. Mater. Interfaces* **2017**, *9*, 40726-40733.

118. Xia, X.; Xia, Y. *Front. Phys.* **2014**, *9*, 378-384.

119. Kim, M. S.; Kweon, S. H.; Cho, S.; An, S. S. A.; Kim, M. I.; Doh, J.; Lee, J. *ACS Appl. Mater. Interfaces* **2017**, *9*, 35133-35140.

120. Zhu, Z.; Guan, Z.; Jia, S.; Lei, Z.; Lin, S.; Zhang, H.; Ma, Y.; Tian, Z. Q.; Yang, C. J. *Angew. Chem., Int. Ed.* **2014**, *53*, 12503-12507.

121. Lee, Y. W.; Kim, M.; Kang, S. W.; Han, S. W. *Angew. Chem., Int. Ed.* **2011**, *50*, 3466-3470.

122. Sankar, M.; Dimitratos, N.; Miedziak, P. J.; Wells, P. P.; Kiely, C. J.; Hutchings, G. J. *Chem. Soc. Rev.* **2012**, *41*, 8099-8139.

123. Chen, C.; Kang, Y.; Huo, Z.; Zhu, Z.; Huang, W.; Xin, H. L.; Snyder, J. D.; Li, D.; Herron, J. A.; Mavrikakis, M. *Science* **2014**, *343*, 1339-1343.

124. Hong, J. W.; Kang, S. W.; Choi, B.-S.; Kim, D.; Lee, S. B.; Han, S. W. *ACS nano* **2012**, *6*, 2410-2419.

125. Park, J.; Joo, J.; Kwon, S. G.; Jang, Y.; Hyeon, T. *Angew. Chem., Int. Ed.* **2007**, *46*, 4630-4660.

126. Rycenga, M.; Cobley, C. M.; Zeng, J.; Li, W.; Moran, C. H.; Zhang, Q.; Qin, D.; Xia, Y. *Chem. Rev.* **2011**, *111*, 3669-3712.

127. Murphy, C. J.; Sau, T. K.; Gole, A. M.; Orendorff, C. J.; Gao, J.; Gou, L.; Hunyadi, S. E.; Li, T. *J. Phys. Chem. B*, **2005**, *109*, 13857-13870.

128. Daniel, M.-C.; Astruc, D. *Chem. Rev.* **2004**, *104*, 293-346.

129. Špringer, T.; Ermini, M. L.; Špačková, B.; Jabloňků, J.; Homola, J. *Anal. Chem.* **2014**, *86*, 10350-10356.

130. Yue, K.; Nan, J.; Zhang, X.; Tang, J.; Zhang, X. *Appl. Therm. Eng.* **2016**, *99*, 1093-1100.

131. Zeng, J.; Goldfeld, D.; Xia, Y. *Angew. Chem., Int. Ed.* **2013**, *52*, 4169-4173.

132. Zhan, L.; Guo, S.; Song, F.; Gong, Y.; Xu, F.; Boulware, D. R.; McAlpine, M. C.; Chan, W. C.; Bischof, J. C. *Nano Lett.* **2017**, *17*, 7207-7212.

133. Ye, H.; Xia, X. *J. Mater. Chem. B* **2018**, *6*, 7102-7111.

134. Bahadır, E. B.; Sezgintürk, M. K. *Trends Anal. Chem.* **2016**, *82*, 286-306.

135. Lu, C.-H.; Kalmar, B.; Malaspina, A.; Greensmith, L.; Petzold, A. *J. Neurosci. Methods* **2011**, *195*, 143-150.

136. Stamplecoskie, K. G.; Scaiano, J. C.; Tiwari, V. S.; Anis, H. *J. Phys. Chem. C* **2011**, *115*, 1403-1409.

137. Loynachan, C. N.; Thomas, M. R.; Gray, E. R.; Richards, D. A.; Kim, J.; Miller, B. S.; Brookes, J. C.; Agarwal, S.; Chudasama, V.; McKendry, R. A. *ACS nano* **2017**, *12*, 279-288.

138. Eustis, S.; El-Sayed, M. A. *Chem. Soc. Rev.* **2006**, *35*, 209-217.

139. Kwon, M. J.; Lee, J.; Wark, A. W.; Lee, H. J. *Anal. Chem.* **2012**, *84*, 1702-1707.

140. Zhang, H.; She, Z.; Su, H.; Kerman, K.; Kraatz, H.-B. *Analyst* **2016**, *141*, 6080-6086.

141. Peters, S.; Verheijen, M.; Prins, M.; Zijlstra, P. *Nanotechnology* **2015**, *27*, 024001.

142. Chen, H.; Kou, X.; Yang, Z.; Ni, W.; Wang, J. *Langmuir* **2008**, *24*, 5233-5237.

143. Jv, Y.; Li, B.; Cao, R. *Chem. Commun.* **2010**, *46*, 8017-8019.

144. He, W.; Wu, X.; Liu, J.; Hu, X.; Zhang, K.; Hou, S.; Zhou, W.; Xie, S. *Chem. Mater.* **2010**, *22*, 2988-2994.

145. He, W.; Liu, Y.; Yuan, J.; Yin, J.-J.; Wu, X.; Hu, X.; Zhang, K.; Liu, J.; Chen, C.; Ji, Y. *Biomaterials* **2011**, *32*, 1139-1147.

146. Ge, C.; Fang, G.; Shen, X.; Chong, Y.; Wamer, W. G.; Gao, X.; Chai, Z.; Chen, C.; Yin, J.-J. *ACS nano* **2016**, *10*, 10436-10445.

147. Liu, D.; Li, X.; Zhou, J.; Liu, S.; Tian, T.; Song, Y.; Zhu, Z.; Zhou, L.; Ji, T.; Yang, C. *Biosens. Bioelectron.* **2017**, *96*, 332-338.

148. Liu, D.; Jia, S.; Zhang, H.; Ma, Y.; Guan, Z.; Li, J.; Zhu, Z.; Ji, T.; Yang, C. J. *ACS Appl. Mater. Interfaces* **2017**, *9*, 22252-22258.

149. Gao, Z.; Lv, S.; Xu, M.; Tang, D. *Analyst* **2017**, *142*, 911-917.

150. Geddes, C. D.; Lakowicz, J. R. *J. Fluoresc.* **2002**, *12*, 121-129.

151. Aslan, K.; Lakowicz, J. R.; Geddes, C. D. *Anal. Bioanal. Chem.* **2005**, *382*, 926-933.

152. Yen, C.-W.; de Puig, H.; Tam, J. O.; Gómez-Márquez, J.; Bosch, I.; Hamad-Schifferli, K.; Gehrke, L. *Lab Chip* **2015**, *15*, 1638-1641.

153. Wang, Y.; Yang, X.; Bai, J.; Jiang, X.; Fan, G. *Biosens. Bioelectron.* **2013**, *43*, 180-185.

154. Huang, Y.; Ferhan, A. R.; Dandapat, A.; Yoon, C. S.; Song, J. E.; Cho, E. C.; Kim, D.-H. *J. Phys. Chem. C* **2015**, *119*, 26164-26170.

155. Gilroy, K. D.; Ruditskiy, A.; Peng, H.-C.; Qin, D.; Xia, Y. *Chem. Rev.* **2016**, *116*, 10414-10472.

156. Jakab, A.; Rosman, C.; Khalavka, Y.; Becker, J.; Trügler, A.; Hohenester, U.; Sönnichsen, C. *ACS nano* **2011**, *5*, 6880-6885.

157. Liu, A.; Geng, H.; Xu, C.; Qiu, H. *Anal. Chim. Acta* **2011**, *703*, 172-178.

158. Xu, C.; Liu, Y.; Su, F.; Liu, A.; Qiu, H. *Biosens. Bioelectron.* **2011**, *27*, 160-166.

159. Link, S.; El-Sayed, M. A. *J. Phys. Chem. B*, **1999**, *103*, 8410-8426.

160. Mulvaney, P. *Langmuir* **1996**, *12*, 788-800.

161. López Lozano, X.; Mottet, C.; Weissker, H.-C. *J. Phys. Chem. C* **2013**, *117*, 3062-3068.

162. Xiu, Z.-M.; Ma, J.; Alvarez, P. J. *Environ. Sci. Technol.* **2011**, *45*, 9003-9008.

163. Liu, J.; Sonshine, D. A.; Shervani, S.; Hurt, R. H. *ACS nano* **2010**, *4*, 6903-6913.

164. Levard, C.; Hotze, E. M.; Lowry, G. V.; Brown Jr, G. E. *Environ. Sci. Technol.* **2012**, *46*, 6900-6914.

165. Yang, Y.; Liu, J.; Fu, Z.-W.; Qin, D. *J. Am. Chem. Soc.* **2014**, *136*, 8153-8156.

166. Gao, C.; Hu, Y.; Wang, M.; Chi, M.; Yin, Y. *J. Am. Chem. Soc.* **2014**, *136*, 7474-7479.

167. Wang, X.; Feng, J.; Bai, Y.; Zhang, Q.; Yin, Y. *Chem. Rev.* **2016**, *116*, 10983-11060.

168. Prodan, E.; Radloff, C.; Halas, N. J.; Nordlander, P. *Science* **2003**, *302*, 419-422.

169. Mahmoud, M. A.; El-Sayed, M. A. *J. Am. Chem. Soc.* **2010**, *132*, 12704-12710.

170. Mahmoud, M. A.; O'Neil, D.; El-Sayed, M. A. *Chem. Mater.* **2013**, *26*, 44-58.

171. Mahmoud, M.; Snyder, B.; El-Sayed, M. *J. Phys. Chem. C* **2010**, *114*, 7436-7443.

172. Genç, A.; Patarroyo, J.; Sancho-Parramon, J.; Arenal, R.; Duchamp, M.; Gonzalez, E. E.; Henrard, L.; Bastús, N. G.; Dunin-Borkowski, R. E.; Puntes, V. F. *ACS Photonics* **2016**, *3*, 770-779.

173. Lim, D.-K.; Jeon, K.-S.; Hwang, J.-H.; Kim, H.; Kwon, S.; Suh, Y. D.; Nam, J.-M. *Nat. Nanotechnol.* **2011**, *6*, 452.

CHAPTER 2 RU NANOFRAMES WITH AN *FCC* STRUCTURE AND ENHANCED CATALYTIC PROPERTIES[a]

2.1 Introduction

Nanoframes (NFs) made of noble metals have received great attention in recent years due to their remarkable performance in many applications including catalysis, plasmonics, and biomedicine.[1-3] The highly open structure of NFs is mainly responsible for their enhanced properties and superior performance. In catalysis, for example, nanocatalysts with frame morphologies ensure increased surface area to volume ratio and reduced coordination number for atoms on the surface, thereby maximizing the catalytic activity.[4-6] In plasmonics, the localized surface plasmon resonance peaks of noble-metal (*e.g.*, Au and Ag) nanostructures could be tuned to the near-infrared region when they are engineered to be frames, making them particularly suitable for *in vivo* medical applications.[7-9]

Over the past two decades, a variety of noble-metal NFs have been actively developed, including those made of Au, Ag, Pt, Pd, Rh, and a combination of them.[4-26] Notable examples include Au-Ag cubic,[7, 13, 14] triangular,[8] octahedral,[9] and decahedral[10] NFs by the Xia, Mirkin, Li, and Kitaev groups, respectively, Pt concave cubic NFs by Lou and co-workers,[11] Pd cubic NFs by Matsui and co-workers,[12] Rh cubic NFs by Xia and co-workers,[15] and Pt-Ni rhombic dodecahedral NFs by Yang and co-workers.[4] However, to the best of our knowledge, Ru NFs have never been reported before. It should be noted that Ru nanostructures have found widespread use in many industrially important catalytic reactions such as hydrogenation, ammonia synthesis, and CO

[a]Reprinted with permission from *Nano Lett.* **2016**, *16*, 2812-2817.

oxidation,[27-29] which motivated us to explore NFs of Ru and investigate their catalytic properties. Moreover, unlike the cases of other noble metals, shape-controlled synthesis of Ru nanostructures has received very limited success.[30, 31] Herein, we report a robust approach, based on seeded growth and chemical etching, to the synthesis of Ru NFs with an octahedral shape, edge length of sub-10 nm, and thickness of only ~2 nm. Notably, the Ru NFs exhibited a face-centered cubic (*fcc*) structure that is unusual for Ru nanocrystals. Using the reduction of *p*-nitrophenol by sodium borohydride ($NaBH_4$) and the dehydrogenation of ammonia borane as model reactions, we demonstrated that the *fcc* Ru NFs showed enhanced catalytic activities compared to Ru nanowires with a hexagonal close-packed (*hcp*) structure and a similar thickness.

Figure 2.1 illustrates the two-step synthetic approach for the Ru NFs. In the first step, Ru was directed to selectively grow on the corners and edges of Pd truncated octahedra as the seeds, resulting in the formation of Pd-Ru core-frame octahedra. Here, the site-selective growth of Ru was achieved by manipulating the reaction kinetics (which will be discussed in detail later). In the second step, Ru NFs were obtained by removing Pd from the Pd-Ru core-frame octahedra using an oxidative etchant, of which strength is sufficiently strong to etch Pd while too weak to react with Ru.

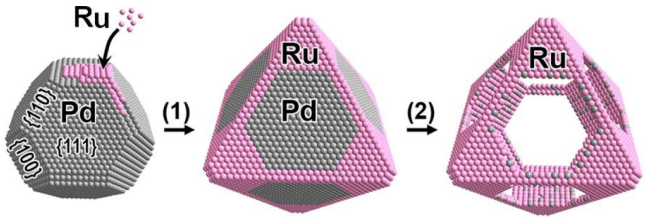

Figure 2.1 Schematic illustration showing the two steps involved in the synthesis of Ru NFs: (1) selective nucleation and growth of Ru on the corners and edges of Pd truncated octahedra, yielding Pd-Ru core-frame octahedra, and (2) formation of Ru octahedral NFs by etching away the Pd cores.

2.2 Results and Discussion

We started with the growth of Ru on Pd-truncated octahedral seeds. In a standard synthesis, a solution of $RuCl_3 \cdot xH_2O$ (precursor to Ru) in ethylene glycol was injected at a rate of 2.0 mL/h using a syringe pump into a mixture containing Pd-truncated octahedra with an average size of 5.6 nm as the seeds (**Figure S2.1** in Appendix B), L-ascorbic acid as a reductant, and poly(vinylpyrrolidone) (PVP) as a colloidal stabilizer, which had been preheated to 200 °C under magnetic stirring. The reasons why we chose Pd-truncated octahedra as the seeds are (*i*) they can be easily prepared with high purity and large quantity because they represent the most thermodynamically stable product (*i.e.*, the Wulff polyhedron)[30] and (*ii*) they expose a set of well-defined, low-index facets on the surface, {100} at corners, {110} at edges, and {111} at side faces (see the model in **Figure 2.1** and corresponding high-resolution transmission electron microscopy, HRTEM, **Figure S2.1** in Appendix B),[32] making it convenient to achieve the site-selective growth of Ru. **Figure 2.2a** shows a typical TEM image of the products obtained from a standard synthesis. It can be seen that the products took an octahedral shape with sharp corners and straight edges of ~6.1 nm, implying the successful deposition of Ru on the corners and edges of Pd seeds and thus the formation of Pd-Ru core-frame octahedra. The composition and structure of the Pd-Ru bimetallic octahedra were characterized by energy dispersive X-ray (EDX) analyses and HAADF-STEM. The line profiles of EDX analysis recorded from an individual Pd-Ru octahedron along two different directions (**Figure 2.2b**) clearly show that the corners and edges exhibited high Ru content while the core was essentially made of pure Pd, confirming that the products were Pd-Ru core-frame octahedra. The high-resolution HAADF-STEM (**Figure 2.2c**) and HRTEM (**Figure S2.2** in Appendix B) images taken from individual Pd-Ru core-frame octahedron clearly indicate that Ru was epitaxially grown on Pd seeds and replicated the *fcc* structure of Pd as indicated by

the continuous lattice from the Pd core to the Ru frame. The lattice fringe spacing of 1.9 and 2.2 Å marked on the corner and edge regions (see **Figure 2.2c**) can be indexed to the {200} and {111} reflections, respectively, of *fcc* Ru.[33] Note that Ru and Pd have similar atomic masses, and the lattice mismatch between *fcc* Ru and Pd is only 1.8% (3.82 *vs.* 3.89 Å), so it is impossible to resolve the elemental composition from the STEM image. Because the reduction potential of Pd^{2+}/Pd (0.95 V *vs.* SHE) is more positive than that of Ru^{3+}/Ru (0.60 V *vs.* SHE),[34] galvanic replacement between Pd seeds and $RuCl_3$ should not occur during the synthesis.[35] This argument was validated by the experimental observation that no characteristic pits or cavities caused by galvanic replacement reaction[35] were observed in the Pd-Ru core-frame octahedra (**Figure 2.2a, c**).

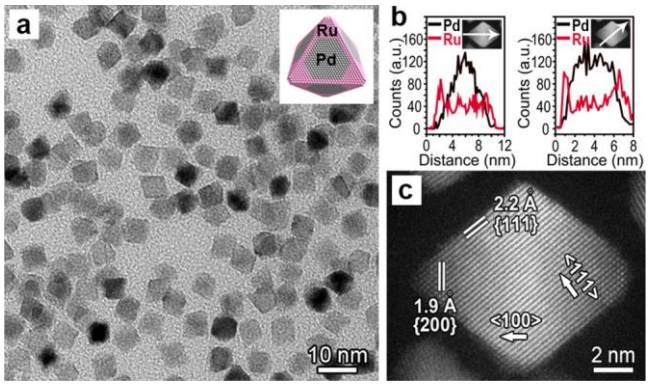

Figure 2.2 Structural and compositional analyses of the Pd-Ru core-frame octahedra that were obtained by growing Ru on the corners and edges of Pd truncated octahedra as the seeds. (a) Typical TEM image showing the octahedral shape and good uniformity of the sample. Inset shows corresponding atomic model. (b) Line-scan EDX spectra of elemental Pd and Ru that were acquired from an individual octahedron (inset) along a corner-to-corner and an edge-to-edge directions as indicated by the white arrows. (c) High-resolution HAADF-STEM image of an individual octahedron orientated along ⟨110⟩ direction.

It is worth pointing out that in most cases Ru tends to take an *hcp* structure during the synthesis of Ru nanocrystals.[36-38] Despite *fcc* Ru nanocrystals being occasionally observed,[33, 39] the mechanism of *fcc* structure formation is still unclear. In a sense, the epitaxial overgrowth of Ru on an *fcc* Pd seed reported here provides a simple and effective method to synthesize *fcc* Ru nanocrystals. To further demonstrate this method, we also used Pd nanocubes (**Figure 2.3a**) that were mainly covered by {100} facets as the seeds for the overgrowth of Ru. Because all the side faces of these Pd cubes were blocked by Br ions,[40] the overgrowth of Ru was forced to occur on the corner sites, leading to the formation of Pd-Ru octapods (**Figure 2.3b**). In this case, the growth direction of Ru was along the ⟨111⟩ directions that is completely different from the previous case of Pd truncated octahedral seeds (*e.g.*, ⟨100⟩ and ⟨110⟩ directions). Nevertheless, as indicated by the HRTEM image in **Figure 2.3c, d**, Ru at the out-extending corners of a Pd-Ru octapod still took the *fcc* structure regardless of the growth direction. In the absence of Pd seeds and under the similar reaction conditions, however, Ru wavy nanowires (NWs) of ~2 nm in thickness (**Figure 2.4a**) were obtained as the products. Interestingly, these Ru NWs took an *hcp* structure that was confirmed by the HRTEM image in **Figure 2.4b** and the X-ray diffraction (XRD) data in **Figure 2.4c**. These results demonstrated the versatility of this seeded-growth method to the synthesis of *fcc* Ru nanocrystals.

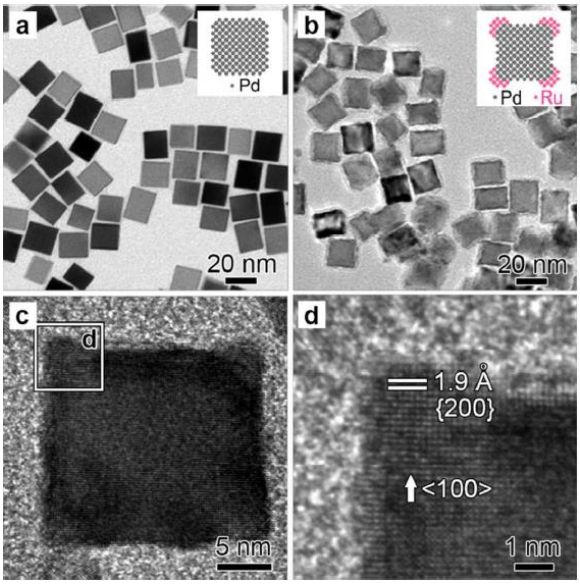

Figure 2.3 Overgrowth of Ru on the corners of 18 nm Pd nanocubes as the seeds. (a) TEM image of the 18 nm Pd cubic seeds; (b) TEM image of the Pd-Ru octapods that were grown from the 18 nm Pd cubic seeds; (c) HRTEM of an individual Pd-Ru octapod orientated along the <100> direction; (d) magnified HRTEM image of the region marked by a white box in (c), showing the *fcc* structure of Ru at the corners. Insets in (a, b) show corresponding atomic models of the samples.

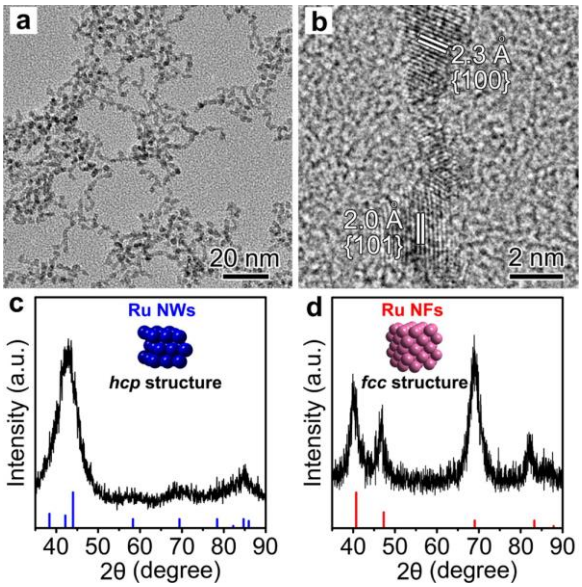

Figure 2.4 (a) Typical TEM image of Ru wavy NWs that were prepared in the absence of Pd seeds. (b) HRTEM image recorded from part of an individual Ru NW, showing the *hcp* structure. (c) XRD pattern recorded from the Ru NWs shown in (a). (d) XRD pattern recorded from the Ru

NFs shown in **Figure 2.6**. Insets in (c, d) show corresponding models of the crystal structures. Blue bars in (c): JCPDS no. 06-0663 (*hcp* Ru). Red bars in (d): JCPDS no. 88-2333 (*fcc* Ru).

The key to the successful synthesis of Pd-Ru core-frame octahedra is to induce preferential overgrowth of Ru at the corners and edges of a Pd truncated octahedral seed by controlling the reaction kinetics. On the basis of our recent mechanistic understanding on kinetic control,[41, 42] we assume that the growth pathway for the current system could be summarized in **Figure 2.5a**: the newly generated Ru atoms from the reduction of $RuCl_3 \cdot xH_2O$ were initially deposited on the corners of a Pd truncated octahedral seed due to their higher reactivity relative to the edges and side faces.[43] Upon deposition, the Ru adatoms could migrate to the edges and side faces through surface diffusion. The growth pathway of the seed was determined by the ratio between the rates for atom deposition and surface diffusion ($V_{deposition}/V_{diffusion}$). When $V_{deposition}/V_{diffusion} >> 1$, surface diffusion can be ignored and thereby the growth will be largely confined to the corner sites of seeds, resulting in the formation of Pd-Ru hexapods. On the contrary, when $V_{deposition}/V_{diffusion} << 1$ the growth will be dominated by surface diffusion, facilitating the conformal coating of Ru and thus the formation of Pd-Ru truncated octahedra as the final product. When $V_{deposition}$ and $V_{diffusion}$ are comparable, a portion of the Ru adatoms at the corners will migrate to the edges (which are relatively active than the side faces)[43] of seeds, leading to the formation of Pd-Ru core-frame octahedra. To validate this assumption, we adjusted $V_{deposition}$ by controlling the injection rate for $RuCl_3 \cdot xH_2O$ solution using a syringe pump, while kept $V_{diffusion}$ unchanged by fixing the reaction temperature at 200 °C.[42] In this way, $V_{deposition}/V_{diffusion}$ should increase as the injection rate for $RuCl_3 \cdot xH_2O$ solution increases. If the proposed mechanism is reasonable, Pd-Ru hexapods and truncated octahedra should be obtained when the injection rate in the standard synthesis (*e.g.*, 2.0 mL/h) is increased and decreased, respectively. As expected, the final product took a hexapod-like

morphology (**Figure 2.5b**) when the injection rate was increased to 10 mL/h; truncated octahedra (**Figure 2.5c**) with a slightly enlarged size compared to the initial seeds were obtained when the injection rate was decreased to 0.5 mL/h.

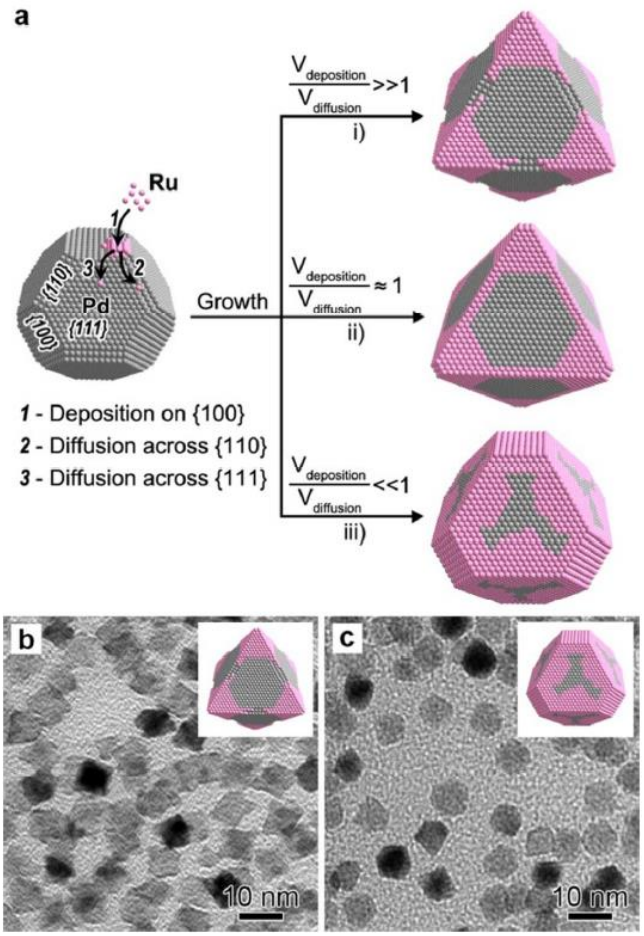

Figure 2.5 (a) Schematic illustrations summarizing the different pathways and the corresponding morphologies expected for the overgrowth of Ru on a Pd truncated octahedral seed under three different conditions; (b) TEM image of Pd-Ru hexapods corresponding to the case *i*) in (a), which were obtained by increasing the injection rate for $RuCl_3 \cdot xH_2O$ in a standard synthesis of Pd-Ru core-frame octahedra from 2.0 mL/h to 10 mL/h; (c) TEM image of Pd-Ru truncated octahedra corresponding to the case *iii*) in (a), which were obtained by decreasing the injection rate for $RuCl_3 \cdot xH_2O$ in a standard synthesis of Pd-Ru core-frame octahedra from 2.0 mL/h to 0.5 mL/h.

Note that the TEM images of Pd-Ru core-frame octahedra corresponding to the case *ii*) in (a) are shown in **Figure 2.2**.

In order to obtain Ru NFs from the Pd-Ru core-frame octahedra shown in **Figure 2.2**, Pd cores need to be selectively removed. It is known that the chemical stabilities of Ru and Pd are quite different.[44] Specifically, Ru is highly resistant to oxidative corrosion and can hardly be dissolved by aqua regia.[45] In contrast, Pd is much more vulnerable to chemical oxidation. On the basis of this difference in chemical stability, we chose chemical etching to selectively remove the Pd cores from the Pd-Ru core-frame octahedra. The etching was conducted in an aqueous solution at 90 °C using an etchant based on the Fe^{3+}/Br^{-} pair, where Pd was etched through reaction: $Pd + 2\ Fe^{3+} + 4\ Br^{-} \rightarrow PdBr_4^{2-} + 2Fe^{2+}$.[15] As shown by the TEM and HAADF-STEM images in **Figure 2.6a-c**, most of the Pd cores were successfully removed, leaving only Ru NFs with an overall octahedral shape. This result further confirms that Ru was preferentially grown on the corners and edges on a Pd-truncated octahedral seed. It should be pointed out that most of the products had an imperfect octahedral shape with some edges and/or corners undeveloped (HAADF-STEM images of representative samples are shown in **Figure S2.3** of Appendix B). For simplicity, we refer to the products as "octahedral NFs" in this study. The undeveloped edges/corners of Ru octahedral NFs might be ascribed to the incomplete diffusion of Ru adatoms across the edges of Pd seeds. This assumption was supported by the observation that Ru octahedral NFs with more missing edges/corners (**Figure S2.4** in Appendix B) were obtained as the final products when Ru precursor was halved during the overgrowth of Ru on Pd seeds. The additional low-magnification TEM image in **Figure S2.5** (Appendix B) demonstrated that the Ru NFs could be obtained with a high purity and good uniformity. From the magnified TEM image in **Figure 2.6b**, the average edge length and thickness of the Ru NFs were measured to be 6.1 and 1.8 nm, respectively. This edge

length of Ru NFs was essentially the same as that of the initial Pd-Ru core-frame octahedra, indicating that Ru was intact during the etching. We also analyzed the chemical composition of the NFs by inductively coupled plasma-optical emission spectrometry (ICP-OES) in which the molar ratio of Ru to Pd was determined to be ~4.5:1. According to previous studies,[46, 47] the small portion of Pd in Ru NFs likely exists in the form of Ru/Pd alloy due to the interdiffusion between Ru and Pd. Significantly, the *fcc* structure and lattice spacing of Ru were maintained during the etching as indicated by the HRTEM image in the inset of **Figure 2.6d**. The *fcc* structure of the Ru NFs was also confirmed by the XRD data in **Figure 2.4d**.

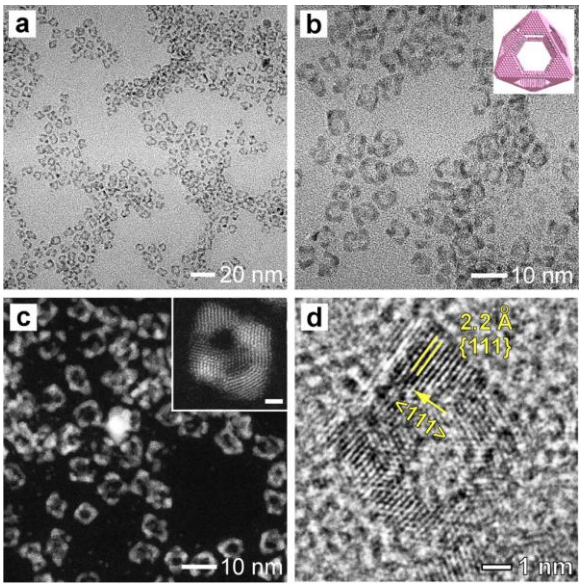

Figure 2.6 Characterization of the Ru NFs that were obtained by etching away Pd cores from the Pd-Ru core-frame octahedra shown in **Figure 2.2**. (a) Low-magnification TEM image showing the good uniformity. (b) TEM image at a higher magnification showing the overall octahedral shape. Inset shows an ideal atomic model of the sample. (c) HAADF-STEM image. Inset shows a high-resolution HAADF-STEM image of an individual Ru NF (scale bar = 1 nm). (d) HRTEM image of an individual Ru NF orientated along ⟨110⟩ direction.

Finally, the *fcc* Ru NFs were evaluated as catalysts for model catalytic reactions. We started with the reduction of *p*-nitrophenol by $NaBH_4$. We chose this reaction because it has been widely used for evaluating the catalytic properties of noble-metal catalysts and its reaction kinetics can be conveniently determined with a UV-vis spectrophotometer.[48-51] Because the *hcp* Ru NWs (**Figure 2.4a)** have a similar thickness with the *fcc* Ru NFs, we benchmarked the catalytic activity of the *fcc* Ru NFs against the *hcp* Ru NWs. For all experiments, the initial concentrations of *p*-nitrophenol and $NaBH_4$ were kept at 0.15 mM and 10 mM, respectively. The concentrations of both Ru-based catalysts were 2.2 μM in Ru element. The *p*-nitrophenol solution exhibited a major absorption peak at 317 nm under neutral or acidic condition. Upon the addition of $NaBH_4$, the absorption peak shifted to 400 nm due to the increase of alkalinity of the solution and the dominance of *p*-nitrophenolate ions.[52, 53] After Ru-based catalyst was added, the absorption peak at 400 nm gradually dropped in intensity as the reduction reaction proceeded (**Figure 2.7a, b**). The reaction kinetics was monitored by measuring the concentration of *p*-nitrophenolate ions based on the absorbance at 400 nm. **Figure 2.7c** shows the plots of extinction intensity at 400 nm (I_{ext}) as a function of time (t) for both Ru NFs and Ru NWs. It is clear that Ru NFs catalyzed reaction was much faster than Ru NWs catalyzed one. In our reaction system, the concentration of $NaBH_4$ was far more in excess than that of *p*-nitrophenol, so its concentration can be considered as a constant during the reaction. As such, the pseudo-first-order kinetics with respect to *p*-nitrophenol could be applied to the reaction.[53] This assumption was supported by the approximately linear shape of the plot of -ln I_{ext} versus time as shown in **Figure 2.7d**. On the basis of this linear relationship, the average reaction rate constant (k) from three independent experiments for the Ru NFs and Ru NWs were calculated to be 0.022 ± 0.001 and 0.005 ± 0.0002 min^{-1}, respectively, indicating a higher catalytic activity for Ru NFs relative to Ru NWs.

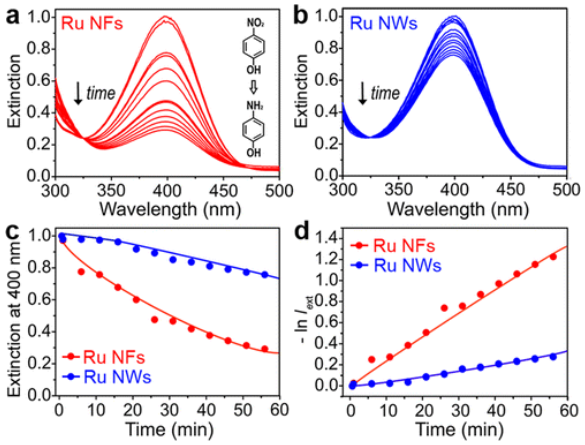

Figure 2.7 Comparison of the catalytic activities of *fcc* Ru NFs (red) and *hcp* Ru NWs (blue) toward the reduction of *p*-nitrophenol by $NaBH_4$. (a, b) The extinction spectra of reaction solutions at different times, indicating the decrease of peak intensity at 400 nm for p-nitrophenol due to the reduction of $-NO_2$ group into $-NH_2$ group (see the inset in panel a). (c) Normalized extinction (against the initial point) at the 400 nm peak for *p*-nitrophenol as a function of time. (d) Plots of $-\ln I_{ext}$ against time that were generated from (c), where I_{ext} denotes the normalized extinction at the 400 nm peak.

We also evaluated the catalytic performance of Ru NFs in dehydrogenation of ammonia borane (H_3N-BH_3, which will be referred to as "AB" in the following discussion for simplicity). AB is an attractive hydrogen storage material because of its high hydrogen content (19.6 *wt* %) and good stability in solid form at room temperature.[54-56] Hydrogen can be conveniently generated from AB through dehydrogenation in the presence of a suitable catalyst. Ru nanoparticles have been proven to be an effective type of catalysts for this reaction.[57-59] In our tests, the catalytic reaction was initiated by adding an aqueous suspension of Ru NFs (**Figure 2.6**) or Ru NWs (**Figure 2.4a**) to an aqueous solution of AB held in a flask. The amount of generated H_2 was measured by a gas buret. As indicated by the plots of H_2 production against time (**Figure 2.8**), Ru NFs showed higher catalytic activity in terms of turnover frequency[58] compared with Ru NWs (19.7 *vs.* 13.2 mol H_2 sec^{-1} $(mol\ Ru)^{-1}$). The enhanced catalytic activities for Ru NFs toward these

reactions might be ascribed to their unique *fcc* crystal structure (note that other factors such as the small portion of Pd-Ru alloy in Ru NFs have not yet been ruled out). Further studies including theoretical calculations are needed to understand the catalytic mechanism for the *fcc* Ru NFs.

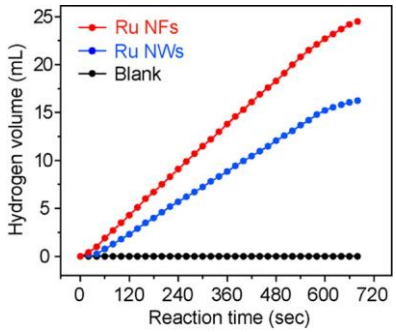

Figure 2.8 Plots of hydrogen evolution versus time during AB dehydrogenation catalyzed by *fcc* Ru NFs (red), *hcp* Ru NWs (blue), and deionized water (black, referred to as "blank") at room temperature (~22 °C) and under 1 atm of pressure. The final concentrations of AB and Ru catalysts in the reaction solution were 49 and 0.0075 mM (in Ru element), respectively. Volume of reaction solution = 10 mL.

2.3 Conclusion

In summary, we have demonstrated a two-step method based on seeded growth and chemical etching for the synthesis of Ru NFs. The key was to direct the overgrowth of Ru to selectively occur on the corner and edge sites of Pd truncated octahedral seeds in the first step by kinetic control. In this way, Ru NFs could be easily obtained in the second step by removing Pd cores from the resultant Pd-Ru core-frame octahedra through chemical etching. Significantly, the *fcc* structure of Pd seeds was replicated by Ru that usually takes an hcp structure. This work not only represents the first successful attempt for the synthesis of Ru NFs but also provides a general route to *fcc* Ru nanocrystals. We believe the synthetic strategy reported here can also be extended

to the synthesis of nanoframes of other metals and the development of nanostructures with unusual crystal structures.

2.4 Materials and Experiment

2.4.1 Chemicals and Materials

Ruthenium (III) chloride hydrate ($RuCl_3 \cdot xH_2O$, MW=207.4), sodium tetrachloropalladate(II) (Na_2PdCl_4, 98%), potassium bromide (KBr, ≥99%), L-ascorbic acid (AA, ≥99%), poly(vinyl pyrrolidone) (PVP, MW≈55,000), hydrochloric acid (HCl, 37%), iron(III) chloride ($FeCl_3$, 97%), p-nitrophenol, borane-ammonia complex ($H_3N\text{-}BH_3$, 90%), and sodium borohydride ($NaBH_4$, ≥99%) were all obtained from Sigma-Aldrich. Ethylene glycol (EG) was obtained from J. T. Baker. All aqueous solutions were prepared using deionized (DI) water with a resistivity of 18.0 MΩ·cm.

2.4.2 Preparation of Pd Nanocrystals to be Used as Seeds

1) *5.6 nm Pd truncated octahedra.* In a typical synthesis, 2 mL of an EG solution containing 40 mg of PVP was hosted in a vial and preheated to 160 °C in an oil bath under magnetic stirring for 10 min. 1 mL of an EG solution containing 16 mg of Na_2PdCl_4 was then quickly injected into the reaction solution using a pipette. The reaction was allowed to continue at 160 °C for 3 h. After being washed with acetone once and ethanol twice via centrifugation, the final product was re-dispersed in 1 mL of EG for future use.

2) *18 nm Pd nanocubes*. 8.0 mL of an aqueous solution containing 105 mg of PVP, 60 mg of AA, and 600 mg of KBr was hosted in a vial and pre-heated to 80 °C in an oil bath under

magnetic stirring. Subsequently, 3.0 mL of an aqueous solution containing 57 mg of Na_2PdCl_4 was added with a pipette. The reaction was allowed to continue at 80 ^oC for 3 h. After being washed with DI water twice via centrifugation, the final product was re-dispersed in 2 mL of EG for future use.

2.4.3 Standard Procedure for the Overgrowth of Ru on Pd Truncated Octahedral Seeds

In a standard procedure, 8 mL of an EG solution containing 100 mg of PVP and 50 mg of AA was hosted in a 50-mL three-neck flask and preheated to 200 ^oC in an oil bath under magnetic stirring for 5 min. Then, 0.5 mL of the 5.6 nm truncated octahedral Pd seeds was added to the flask using a pipette. After 5 min, 8.0 mL of $RuCl_3 \cdot xH_2O$ solution (0.5 mg/mL, in EG) was injected to the flask at a rate of 2.0 mL/h using a syringe pump. The reaction was allowed to proceed for an additional 10 min after the $RuCl_3 \cdot xH_2O$ precursor had been completed injected. The products (*e.g.*, Pd-Ru core-frame octahedra) were collected by centrifugation, washed once with acetone, two times with water, and finally redispersed in 0.5 mL of DI water. The procedure for the overgrowth of Ru on 18 nm Pd cubic seeds was the same as the procedure above except for the substitution of 0.5 mL truncated octahedral seeds with 0.5 mL cubic seeds.

2.4.4 Removal of Pd Cores from Pd-Ru Core-frame Octahedra by Chemical Etching

KBr (150 mg), PVP (25 mg), $FeCl_3$ (25 mg), HCl (0.15 mL, 37%), DI water (2.85 mL), and an aqueous suspension of the as-prepared Pd-Ru core-frame octahedra (0.5 mL) were mixed together in a 20-mL glass vial under magnetic stirring at room temperature for 10 min. Then, the solution was heated to 80 ^oC in an oil bath under magnetic stirring. After 3 h, the solution was cooled down with a water bath to room temperature and the product was collected by

centrifugation, washed once with ethanol, twice with water, and finally re-dispersed in 0.5 mL of DI water for future use.

2.4.5 Synthesis of Ru Nanowires

The Ru nanowires shown in **Figure 2.4** were synthesized through a one-pot method. In a typical synthesis, 8 mL EG containing 100 mg of PVP was hosted in a 20-mL glass vial and preheated to 200 ^{o}C in an oil bath under magnetic stirring for 10 min. Then, 3 mL of an EG solution containing 45 mg of $RuCl_3 \cdot xH_2O$ was quickly added to the reaction solution using a pipette. The reaction was allowed to continue at 200 ^{o}C for 3 h. After being washed with acetone once and ethanol twice via centrifugation, the final product was re-dispersed in 5 mL of DI water for future use.

2.4.6 Evaluation of Catalytic Activities

1) *Reduction of p-nitrophenol by $NaBH_4$.* The reaction was conducted in aqueous suspension and under room temperature. In a typical process, both aqueous suspensions of Ru nanocatalysts (*e.g.*, Ru nanoframes and Ru nanowires) were first diluted to 0.218 mM in terms of Ru element (based on the result of inductively coupled plasma-optical emission spectroscopy, ICP-OES). Meanwhile, aqueous solutions of p-nitrophenol (0.5 mM) and $NaBH_4$ (2 M) were freshly prepared. Then, 0.690 mL of DI water was mixed with 0.295 mL *p*-nitrophenol solution in a cuvette. The color of the solution changed from colorless to yellow immediately after the addition of 0.005 mL of the $NaBH_4$ solution. Finally, 0.010 mL Ru nanocatalysts was injected into the system and quickly mixed well using a pipette. The reaction time (*t*) was recorded immediately thereafter and the intensity of the absorption at 400 nm for the reaction solution was monitored

from t = 20 s to t = 60 min. The final concentrations of p-nitrophenol, $NaBH_4$, and Ru catalysts in the reaction solution were about 0.15 mM, 10 mM, and 2.2 μM (in Ru element), respectively.

2) *Dehydrogenation of ammonia borane*. The reaction was conducted in aqueous suspension, at room temperature, and under one atmosphere of pressure. In a typical process, 9.8 mL of ammonia borane aqueous solution (50 mM) and 0.2 mL of an aqueous suspension of Ru catalyst (nanoframes or nanowires, 0.375 mM in Ru element) or deionized water (blank) were sequentially added into a 50 mL three-neck flask kept at room temperature (~ 22 ^{o}C) under magnetic stirring, with one of the openings connected to a gas burette. The volume of hydrogen produced from the flask at different reaction time was recorded using the gas burette. The number of moles of hydrogen (n) could be calculated from the volume of hydrogen (V) according to the ideal gas law $PV = nRT$ (P: absolute pressure of gas; R: ideal gas constant; T: absolute temperature). n will then be used to calculate the turnover frequency (mol H_2 sec^{-1} (mol Ru)$^{-1}$).

2.5 Characterizations

The TEM images were taken using a JEOL JEM-2010 microscope operated at 200 kV. HAADF-STEM and the energy dispersive X-ray (EDX) analyses were performed using a JEOL ARM200F with STEM Cs corrector operated at 200 kV. The UV-vis spectra of the catalytic reaction solution were recorded using an Agilent Cary 60 UV-vis spectrophotometer. XRD patterns were taken using a Scintag XDS2000 powder diffractometer. The concentrations of Pd and Ru ions were determined using an inductively coupled plasma-optical emission spectroscopy (ICP-OES, Perkin Elmer Optima 7000DV).

2.6 Reference

1. Fang, Z.; Wang, Y.; Liu, C.; Chen, S.; Sang, W.; Wang, C.; Zeng, J. *Small* **2015**, *11*, 2593-2605.

2. Mahmoud, A. M.; El-Sayed, A. M. *J. Am. Chem. Soc.* **2010**, *132*, 12704-12710.

3. Zhu, C.; Du, D.; Eychmüller, A.; Lin, Y. *Chem. Rev*. **2015**, *115*, 8896-8943.

4. Chen, C.; Kang, Y.; Huo, Z.; Zhu, Z.; Huang, W.; Xin, H. L.; Snyder, J. D.; Li, D.; Herron, J. A.; Mavrikakis, M. *Science* **2014**, *343*, 1339-1343.

5. Chen, S.; Su, H.; Wang, Y.; Wu, W.; Zeng, J. *Angew. Chem., Int. Ed.* **2015**, *54*, 108-113.

6. Wu, Y.; Wang, D.; Zhou, G.; Yu, R.; Chen, C.; Li, Y. *J. Am. Chem. Soc.* **2014**, *136*, 11594-11597.

7. Lu, X. M.; Au, L.; McLellan, J.; Li, Z. Y.; Marquez, M.; Xia, Y. *Nano Lett.* **2007**, *7*, 1764-1769.

8. Métraux, G. S.; Cao, Y. C.; Jin, R.; Mirkin, C. A. *Nano Lett.* **2003**, *3*, 519-522.

9. Hong, X.; Wang, D.; Cai, S.; Rong, H.; Li, Y. *J. Am. Chem. Soc.* **2012**, *134*, 18165-18168.

10. McEachran, M.; Keogh, D.; Pietrobon, B.; Cathcart, N.; Gourevich, I.; Coombs, N.; Kitaev, V. *J. Am. Chem. Soc.* **2011**, *133*, 8066-8069.

11. Xia, B.; Wu, H.; Wang, X.; Lou, X. *Angew. Chem., Int. Ed.* **2013**, *52*, 12337-12340.

12. Wei, Z.; Matsui, H. *Nat. Commun*. **2014**, *5*, 3870.

13. Au, L.; Chen, Y.; Zhou, F.; Camargo, P. H. C.; Lim, B.; Li, Z.-Y.; Ginger, D. S.; Xia, Y. *Nano Res.* **2008**, *1*, 441-449.

14. Wan, D.; Xia, X.; Wang, Y.; Xia, Y. *Small* **2013**, *9*, 3111-3117.

15. Xie, S.; Lu, N.; Xie, Z.; Wang, J.; Kim, M. J.; Xia, Y. *Angew. Chem., Int. Ed.* **2012**, *51*, 10266-10270.

16. Zhang, L.; Liu, T.; Liu, K.; Han, L.; Yin, Y.; Gao, C. *Nano Lett*. **2015**, *15*, 4448-4454.

17. Sun, X.; Qin, D. *J. Mater. Chem. C* **2015**, *3*, 11833-11841.

18. Ye, W.; Kou, S.; Guo, X.; Xie, F.; Sun, H.; Lu, H.; Yang, J. *Nanoscale* **2015**, *7*, 9558-9562.

19. Oh, A.; Baik, H.; Choi, D. S.; Cheon, J. Y.; Kim, B.; Kim, H.; Kwon, S. J.; Joo, S. H.; Jung, Y.; Lee, K. *ACS Nano* **2015**, *9*, 2856-2867.

20. Jang, H.-J.; Ham, S.; Acapulco, J. A., Jr; Song, Y.; Hong, S.; Shuford, K. L.; Park, S. *J. Am. Chem. Soc.* **2014**, *136*, 17674-17680.

21. Jang, H.-J.; Hong, S.-C.; Park, S. *J. Mater. Chem.* **2012**, *22*, 19792-19797.

22. Nosheen, F.; Zhang, Z. C.; Zhuang, J.; Wang, X. *Nanoscale* **2013**, *5*, 3660-3663.

23. González, E.; Arbiol, J.; Puntes, V. F. *Science* **2011**, *334*, 1377-1380.

24. Fan, N.; Yang, Y.; Wang, W.; Zhang, L.; Chen, W.; Zou, C.; Huang, S. *ACS Nano* **2012**, *6*, 4072-4082.

25. Zhang, Z.; Zhu, W.; Yan, C.; Zhang, Y. *Chem. Commun*. **2015**, *51*, 3997-4000.

26. Ham, S.; Jang, H. J.; Song, Y.; Shuford, K. L.; Park, S. *Angew. Chem., Int. Ed.* **2015**, *54*, 9025-9028.

27. Xiao, C. X.; Cai, Z. P.; Wang, T.; Kou, Y.; Yan, N. *Angew. Chem., Int. Ed.* **2008**, *47*, 746-749.

28. Qadir, K.; Joo, S. H.; Mun, B. S.; Butcher, D. R.; Renzas, J. R.; Aksoy, F.; Liu, Z.; Somorjai, G. A.; Park, J. Y. *Nano Lett.* **2012**, *12*, 5761-5768.

29. Su, F.; Lv, L.; Lee, F. Y.; Liu, T.; Cooper, A. I.; Zhao, X. S. *J. Am. Chem. Soc.* **2007**, *129*, 14213-14223.

30. Xia, Y.; Xiong, Y.; Lim, B.; Skrabalak, S. E. *Angew. Chem., Int. Ed.* **2009**, *48*, 60-103.

31. Chen, G.; Zhang, J.; Gupta, A.; Rosei, F.; Ma, D. *New J. Chem.* **2014**, *38*, 1827-1833.

32. Xiong, Y.; Xia, Y. *Adv. Mater.* **2007**, *19*, 3385-3391.

33. Gu, J.; Guo, Y.; Jiang, Y. Y.; Zhu, W.; Xu, Y. S.; Zhao, Z. Q.; Liu, J. X.; Li, W. X.; Jin, C. H.; Yan, C. H.; Zhang, Y. W. *J. Phys. Chem. C* **2015**, *119*, 17697-17706.

34. Harris, D. C. *Quantitative Chemical Analysis, 9th ed*.; W. H. Freeman: New York, **2015**.

35. Xia, X.; Wang, Y.; Ruditskiy, A.; Xia, Y. *Adv. Mater.* **2013**, *25*, 6313-6333.

36. Yin, A. X.; Liu, W. C.; Ke, J.; Zhu, W.; Gu, J.; Zhang, Y. W.; Yan, C. H. *J. Am. Chem. Soc.* **2012**, *134*, 20479-20489.

37. Watt, J.; Yu, C.; Chang, S. L. Y.; Cheong, S.; Tilley, R. D. *J. Am. Chem. Soc.* **2013**, *135*, 606-609.

38. Viau, G.; Brayner, R.; Poul, L.; Chakroune, N.; Lacaze, E.; Fiévet-Vincent, F.; Fiévet, F. *Chem. Mater.* **2003**, *15*, 486-494.

39. Kusada, K.; Kobayashi, H.; Yamamoto, T.; Matsumura, S.; Sumi, N.; Sato, K.; Nagaoka, K.; Kubota, Y.; Kitagawa, H. *J. Am. Chem. Soc.* **2013**, *135*, 5493-5496.

40. Peng, H.-C.; Xie, S.; Park, J.; Xia, X.; Xia, Y. *J. Am. Chem. Soc.* **2013**, *135*, 3780-3783.

41. Xia, Y.; Xia, X.; Peng, H.-C. *J. Am. Chem. Soc.* **2015**, *137*, 7947-7966.

42. Xia, X.; Xie, S.; Liu, M.; Peng, H.-C.; Lu, N.; Wang, J.; Kim, M. J.; Xia, Y. *Proc. Natl. Acad. Sci. U. S. A.* **2013**, *110*, 6669-6673.

43. Zhang, H.; Li, W.; Jin, M.; Zeng, J.; Yu, T.; Yang, D.; Xia, Y. *Nano Lett.* **2011**, *11*, 898-903.

44. Romanenko, A. V.; Tyschishin, E. A.; Moroz, E. M.; Likholobov, V. A.; Zaikovskii, V. I.; Jhung, S. H.; Park, Y. S. *Appl. Catal. A* **2002**, *227*, 117-123.

45. Balcerzak, M.; Kaczmarczyk, M. *Anal. Sci.* **2001**, *17*, 1321-1324.

46. Zhang, L.; Roling, L. T.; Wang, X.; Vara, M.; Chi, M.; Liu, J.; Choi, S. I.; Park, J.; Herron, J. A.; Xie, Z.; Mavrikakis, M.; Xia, Y. *Science* **2015**, *349*, 412-416.

47. Heggen, M.; Oezaslan, M.; Houben, L.; Strasser, P. *J. Phys. Chem. C* **2012**, *116*, 19073-19083.

48. Zeng, J.; Zhang, Q.; Chen, J. Y.; Xia, Y. *Nano Lett.* **2010**, *10*, 30-35.

49. Mahmoud, M. A.; Saira, F.; El-Sayed, M. A. *Nano Lett.* **2010**, *10*, 3764-3769.

50. Schrinner, M.; Ballauff, M.; Talmon, Y.; Kauffmann, Y.; Thun, J.; Møller, M.; Breu, J. *Science* **2009**, *323*, 617-620.

51. Lee, J.; Park, J. C.; Song, H. *Adv. Mater.* **2008**, *20*, 1523-1528.

52. Praharaj, S.; Nath, S.; Ghosh, S. K.; Kundu, S.; Pal, T. *Langmuir* **2004**, *20*, 9889-9892.

53. Hayakawa, K.; Yoshimura, T.; Esumi, K. *Langmuir* **2003**, *19*, 5517-5521.

54. Staubitz, A.; Robertson, A. P. M.; Manners, I. *Chem. Rev.* **2010**, *110*, 4079-4124.

55. Chua, Y. S.; Wu, G.; Xiong, Z.; He, T.; Chen, P. *Chem. Mater.* **2009**, *21*, 4899-4904.

56. Guo, Y.; He, X.; Li, Z.; Zou, Z. *Inorg. Chem.* **2010**, *49*, 3419-3423.

57. Chandra, M.; Xu, G. *J. Power Sources* **2007**, *168*, 135-142.

58. Chen, G.; Desinan, S.; Nechache, R.; Rosei, R.; Rosei, F.; Ma, D. *Chem. Commun.* **2011**, *47*, 6308-6310.

59. Chen, G.; Desinan, S.; Rosei, R.; Rosei, F.; Ma, D. *Chem. - Eur. J.* **2012**, *18*, 7925-7930.

CHAPTER 3 PEROXIDASE-LIKE PROPERTIES OF RUTHENIUM NANOFRAMES[a]

3.1 Introduction

Peroxidase mimics of inorganic nanomaterials hold great potential for replacing natural peroxidases in diagnostic, sensing, and imaging applications, providing enhanced performance.[1-8] Since the first demonstration of ferromagnetic nanoparticles as peroxidase mimics,[9] a vast variety of inorganic nanomaterials have been reported to show peroxidase-like properties, including nanostructures made of metal oxides,[10-14] noble metals,[15-21] carbon materials,[22-24] and a combination of them.[25, 26] Among them, noble-metal mimics are particularly intriguing because: (*i*) they are ultra-stable owing to their chemical inertness, enabling them to survive harsh environments; and (*ii*) their surfaces can be conveniently functionalized with biomolecules by means of physical adsorption or metal-thiolate bonding,[27] facilitating biomedical applications. While peroxidase-like properties have been demonstrated for NMNSs of Au, Pt, Pd, Ir and their alloys,[15-21] to the best of our knowledge, there is no literature report on Ru nanostructure-based peroxidase mimics. Ru is quite unique compared to other noble metals. For example, Ru is chemically super stable and is even invulnerable to aqua regia;[28] Ru is the only noble metal that normally takes the hexagonal close-packed (*hcp*) crystal structure.[29] These unique features of Ru inspired us to explore Ru nanostructure-based peroxidase mimics.

In this work, we demonstrate the peroxidase-like properties of Ru nanoframes (RuNFs) with an octahedral shape and size <10 nm. Specifically, uniform RuNFs were first synthesized

[a]Reprint with permission from *Sci. Bull*. **2016**, *61*, 1739-1745

using a method as reported as **Chapter 2**.[29] The peroxidase-like activity of the frames was then demonstrated by the catalytic reactions between hydrogen peroxide and different peroxidase substrates. Using 3,3',5,5'-tetramethylbenzidine (TMB)[30] as a model substrate, we have quantified the catalytic efficiency of the RuNFs. Finally, superior stabilities of the RuNFs as peroxidase mimics were demonstrated. This work represents the first attempt to explore Ru-based peroxidase mimics and, in a sense, offers a promising prospect for the application of Ru nanomaterials in biomedicine.

3.2 Results and Discussion

Figure 3.1 shows the TEM images of the RuNFs produced from a standard synthesis. As indicated by the low magnification TEM image (**Figure 3.1a**), the RuNFs were obtained with a high purity (>95 %) and good uniformity. The magnified TEM image in **Figure 3.1b** clearly reveals the frame structure with an octahedral shape for the products. By randomly analyzing 200 individual particles, the average edge length and thickness of the RuNFs equaled 6.2 and 1.8 nm, respectively. The high-resolution TEM (HRTEM) and high-angle annular dark-field scanning TEM (HAADF-STEM) images shown in **Figure 3.1c**, **d** clearly reveal the face-centered cubic (*fcc*) crystal structure and octahedral frame morphology for the RuNFs. The lattice spacing of RuNFs in **Figure 3.1c** was determined to be 0.22 nm, which could be indexed to the {111} plane of *fcc* Ru crystal structure. Since the RuNFs were grown from the ~5.6 nm Pd seeds with a well-defined truncated octahedral shape,[29] the total amount of the frames produced from a standard synthesis should be equal to that of the initial Pd seeds, which was estimated to be 4.7×10^{15} particles/mL based on the inductively coupled plasma-optical emission spectrometry (ICP-OES) analysis. Therefore, the particle concentration for the RuNFs suspension obtained from a standard

synthesis was estimated to be 4.7×10^{15} particles/mL or 3.9×10^{-6} M. This data is essential to quantitative understanding of the peroxidase-like activity of the RuNFs (see more discussions below).

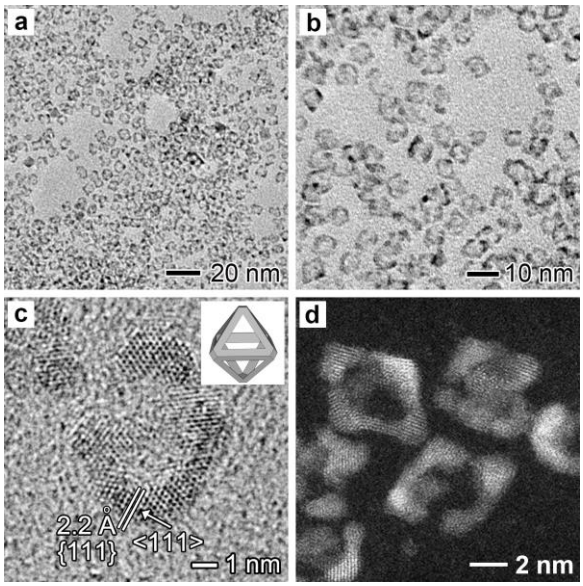

Figure 3.1 Typical TEM images of RuNFs obtained in a standard synthesis. (a) Low magnification TEM image showing the high yield and good uniformity of the sample. (b) TEM image at a higher magnification showing the frame structure with hollow interiors. (c) HRTEM image of an individual Ru frame orientated along <110> direction. The inset shows a 3D model of the sample. (d) HAADF-STEM image showing the 3D octahedral frame morphology of the sample.

The peroxidase-like property of the RuNFs was demonstrated by catalyzing the oxidation of peroxidase substrates with hydrogen peroxide (H_2O_2). As shown in **Figure 3.2**, RuNFs efficiently catalyze the oxidation of TMB (a typical peroxidase substrate)[34] by H_2O_2, generating blue-colored oxidized TMB with characteristic absorption peaks at 371, 653, and 892 nm (**Figure 3.2b**).[34] The reaction rate was directly proportional to the particle concentration of RuNFs in the reaction solution (**Figure 3.2c**). In addition to TMB, the RuNFs could also rapidly catalyze the oxidation of other peroxidase substrates such as 3,3'-diaminobenzidine (DAB) and *o*-

phenylenediamine (OPD),[9, 35] yielding brown- and light orange-colored products, respectively (**Figure 3.2a**). These observations clearly demonstrate the peroxidase-like activity of the RuNFs.

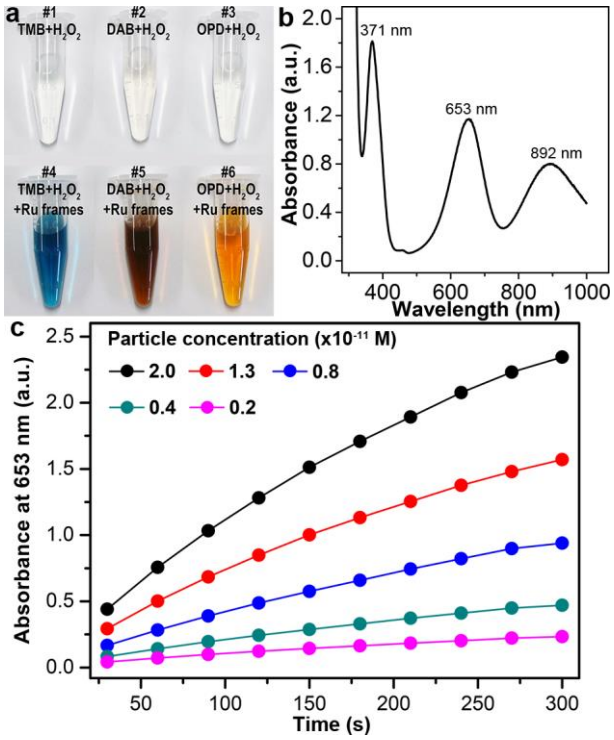

Figure 3.2 Peroxidase-like activity of RuNFs. (a) A digital photograph taken at the reaction time t = 5 min, demonstrating the capability of RuNFs as peroxidase mimics in catalyzing the oxidation of different substrates (*e.g.*, TMB, DAB, and OPD) by H_2O_2. (b) UV-Vis spectrum of the TMB-H_2O_2 reaction system catalyzed by RuNFs (1.0×10^{-11} M). (c) Time- and particle concentration-dependent absorbance at 653 nm measured from the reaction solutions containing TMB (0.8 mM), H_2O_2 (2.0 M), and RuNFs with different concentrations in 0.2 M HOAc/NaOAc buffer (pH 4.0) at room temperature.

We also evaluated the effects of various reaction conditions on the catalytic activity of the RuNFs using the oxidation of TMB by H_2O_2 as a model reaction. We chose to focus on this reaction because its mechanism has been well understood in previous studies and TMB is less toxic compared to other substrates.[34] As shown in **Figure 3.3**, the catalytic efficiency of the RuNFs

(1.0×10^{-11} M in particle concentration) had a strong dependent on pH, temperature, and concentrations of TMB and H_2O_2. Taken all the factors together, the optimal conditions for maximized reaction rate were found to be roughly pH 4.0, 40 ^oC, 0.8 mM TMB, and 6.0 M H_2O_2. Since no significant change of catalytic efficiency for temperatures at 20-40 ^oC (**Figure 3.3b**) and H_2O_2 concentrations at 2.0-8.0 M (**Figure 3.3d**), for simplicity, we adopted pH 4.0, room temperature (~22 ^oC), 0.8 mM TMB, 2.0 M H_2O_2, and 1.0×10^{-11} M RuNFs as the standard conditions for subsequent experiments.

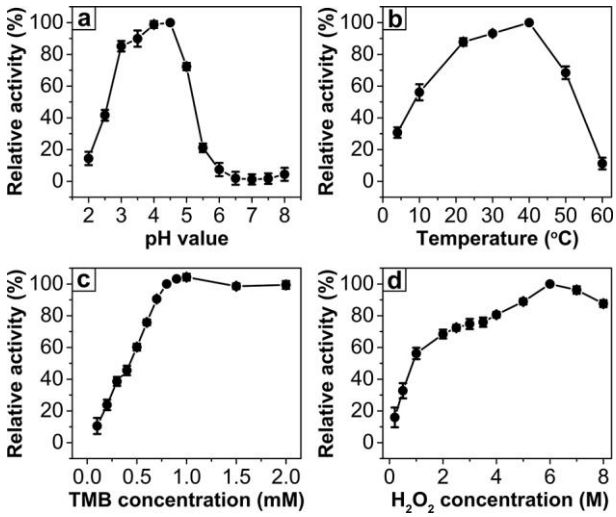

Figure 3.3 The effects of (a) pH, (b) temperature, (c) TMB concentration, and (d) H_2O_2 concentration on the catalytic activity of RuNFs. The experiments were carried out in aqueous solution in the presence of 1.0×10^{-11} M RuNFs as the catalysts. Other reaction conditions were 0.2 M HOAc/NaOAc buffer (pH 4.0), 2.0 M H_2O_2, 0.8 mM TMB, and room temperature, unless otherwise stated. The maximum absorbance at 653 nm of reaction solutions at t = 5 min in each plot (a-d) was set as 100%.

To quantitatively understand the catalytic activity of the RuNFs, we determined the apparent steady-state kinetic parameters for the catalytic reaction between TMB and H_2O_2.[34] Basically, the initial reaction velocity was determined by quantifying the concentration of colored

product (*e.g.*, oxidized TMB with a maximum absorbance at 653 nm)[34, 36] as a function of time with the aid of a spectrophotometer (experimental details were provided in **Section 3.4.3**). As shown in **Figure 3.4**, typical Michaelis-Menten curves were observed for both TMB (**Figure 3.4a**) and H_2O_2 (**Figure 3.4c**) when the initial reaction velocities were plotted against the concentrations of H_2O_2 and TMB, respectively. The curves could then be fitted to the double-reciprocal or Lineweaver-Burk plots[33] (**Figure 3.4b, d**). From the double-reciprocal plots, the kinetic parameters for RuNFs were determined and summarized in **Table 3.1**. For comparison, we also determined the kinetic parameters of initial 5.6 nm Pd octahedral seeds and listed those of HRP from Ref. 9 in **Table 3.1**. It can be seen that the catalytic efficiencies (in terms of catalytic constant, K_{cat}, which is defined as the maximum number of chemical conversions of substrate molecules per second per catalyst)[37] of the RuNFs toward TMB and H_2O_2 were approximately three and two times higher than those of HRP, respectively. Note that the catalytic efficiencies of RuNFs were also several times higher than initial Pd octahedral seeds (**Table 3.1**). Since colored products are originated from TMB, it can be concluded that the RuNFs are about three times more efficient in generating a detectable color signal. The Michaelis constant K_m (which measures the substrate concentration at which the reaction velocity is half of the maximum velocity, V_{max})[37] toward TMB for RuNFs was seven times lower than that for HRP, implying that RuNFs had a higher affinity for TMB than HRP. In contrast, the K_m toward H_2O_2 for RuNFs was eighty-six times higher than that for HRP, suggesting a lower affinity for RuNFs in binding to H_2O_2 as compared to HRP.

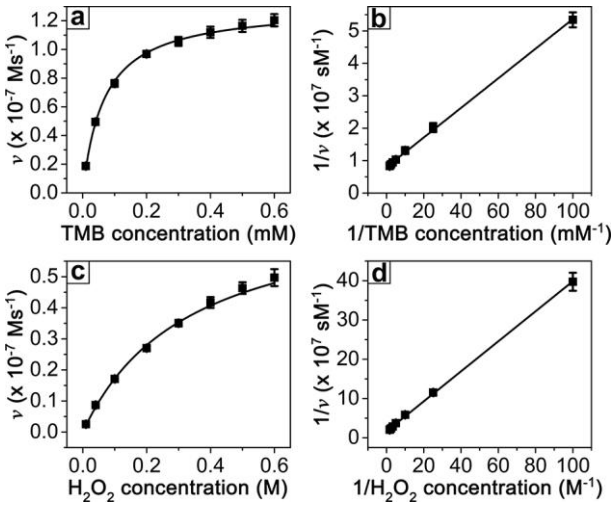

Figure 3.4 Kinetic assays of RuNFs as catalysts for the oxidation of TMB by H_2O_2. The initial reaction velocity (*v*) was measured under standard conditions. Error bars indicate the standard deviations of three independent measurements. (a) Plot of *v* against TMB concentration, in which H_2O_2 concentration was fixed at 2.0 M; (b) double-reciprocal plot generated from (a); (c) plot of *v* against H_2O_2 concentration, in which TMB concentration was fixed at 0.8 mM; (d) double-reciprocal plot generated from (c).

Table 3.1 Comparison of kinetic parameters of RuNFs and HRP toward the oxidation of TMB by H_2O_2.

Catalyst	E (M)	Substrate	K_m (M)	V_{max} (M·s^{-1})	K_{cat} (s^{-1})
RuNFs	1.06×10^{-11}	TMB	6.03×10^{-5}	1.34×10^{-7}	1.26×10^{4}
	1.06×10^{-11}	H_2O_2	3.18×10^{-1}	7.41×10^{-8}	6.98×10^{3}
Pd seeds	1.06×10^{-11}	TMB	4.7×10^{-5}	3.8×10^{-7}	3.6×10^{3}
	1.06×10^{-11}	H_2O_2	7.3×10^{-1}	1.4×10^{-7}	1.3×10^{3}
HRP[9]	2.50×10^{-11}	TMB	4.3×10^{-4}	1.0×10^{-7}	4.0×10^{3}
	2.50×10^{-11}	H_2O_2	3.7×10^{-3}	8.7×10^{-8}	3.5×10^{3}

E represents the catalyst concentration, K_m is the Michaelis constant, V_{max} is the maximal reaction velocity, and K_{cat} is the catalytic constant that equals V_{max}/E

To examine possible changes of crystal structure for the RuNFs during the catalytic reaction, we analyzed individual frames before and after the catalysis by HRTEM. As indicated by the HRTEM images and corresponding Fourier transform patterns shown in **Figure 3.5**, the *fcc* crystal structure for RuNFs was well retained after the catalytic reaction. Finally, we evaluated the stability for the RuNFs as peroxidase mimics. It should be noted that stability is a key parameter for a peroxidase mimic because it largely determines the durability and reproducibility of the mimic in certain applications.

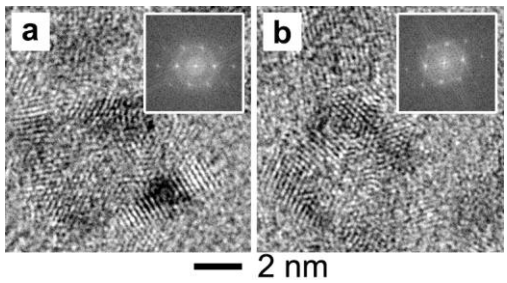

Figure 3.5 Representative HRTEM images of individual RuNFs a before and b after they had been used as catalysts for the oxidation of TMB by H_2O_2. Insets are corresponding Fourier transform patterns.

To test the chemical stability, we incubated RuNFs in solutions of different pH ranging from 0 to 12 for a period of 2h prior to the measurement of their catalytic activities. As shown in **Figure 3.6a**, the catalytic activity of the RuNFs was fairly stable even though they had been treated with strong acid or base, indicating their outstanding chemical stabilities. We also evaluated the thermal stability of RuNFs by heating them at different temperatures. As shown in **Figure 3.6b**, their catalytic activity essentially kept unchanged after they had been heated for 2h at temperatures up to 200 ^{o}C. The observed stable catalytic performance of the RuNFs might be attributed to their inherent inertness (*e.g.*, ultrahigh resistance to oxidative etching) and the excellent thermal stability of elemental Ru (*e.g.*, with an ultrahigh melting point of >2,000 ^{o}C).[28,38]

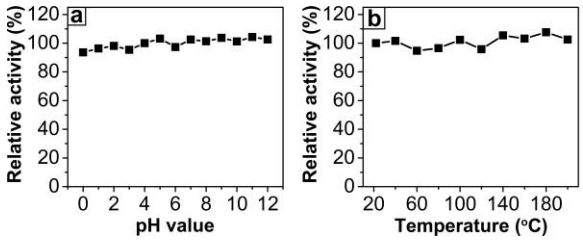

Figure 3.6 (a) Chemical and (b) thermal stability tests for the RuNFs in catalyzing the oxidation of TMB by H_2O_2. In a, RuNFs (3.9×10^{-8} M, in deionized water) were first incubated in solutions with pH of 0 to 12 for 2h. Their relative catalytic activities (*e.g.*, absorbance at 653 nm of reaction solutions at t = 5 min, standard conditions) were then measured, in which the activity at pH 4.0 was set as 100 %; In (b), RuNFs (3.9×10^{-8} M, in ethylene glycol) were heated at temperatures of 40 to 200 ^{o}C for 2 h. Their relative catalytic activities were then measured under standard conditions, in which the activity at room temperature (~22 ^{o}C) was set as 100%.

3.3 Conclusion

In conclusion, we have demonstrated a new kind of peroxidase mimic— RuNFs of sub-10 nm in size. The RuNFs could be produced in a high purity and good uniformity. The catalytic efficiency of the RuNFs was found to be higher than that of natural peroxidase. In addition, the frames displayed excellent chemical and thermal stabilities. This work represents the first demonstration of Ru nanostructure-based peroxidase mimics, and thus opens a new avenue for exploring the bioapplications of Ru nanomaterials.

3.4 Materials and Experiment

3.4.1 Chemicals and Materials

Ruthenium (III) chloride hydrate ($RuCl_3\cdot xH_2O$, MW=207.4), sodium tetrachloropalladate(II) (Na_2PdCl_4, 98%), potassium bromide (KBr, ≥99%), L-ascorbic acid (AA, ≥99%), poly(vinyl pyrrolidone) (PVP, MW≈55,000), hydrochloric acid (HCl, 37%), iron(III)

chloride ($FeCl_3$, 97%), 3,3',5,5'-tetramethylbenzidine (TMB, >99 %), 3,3'-diaminobenzidine (DAB, >99 %), *o*-phenylenediamine (OPD, > 98 %), hydrogen peroxide solution (30 wt. % in H_2O), sodium chloride (NaCl, 99.5 %), sodium phosphate dibasic (Na_2HPO_4, 99 %), potassium phosphate monobasic (KH_2PO_4, 99 %), tris base (99.9 %), citric acid (99 %), acetic acid (HOAc, 99.7 %), and sodium acetate (NaOAc, 99 %) were all obtained from Sigma-Aldrich. Ethylene glycol (EG) was obtained from J. T. Baker. All aqueous solutions were prepared using deionized (DI) water with a resistivity of 18.0 M Ω·cm.

3.4.2 Preparation of RuNFs

The standard preparation of Ru nanoframes could be found in **Section 2.4.3** and **2.4.4** in Chapter 2.

3.4.3 Evaluation of the Peroxidase-like Activities of RuNFs

The experiments were performed at room temperature in 1.5 mL tubes. The catalytic reactions were carried out in different buffer solutions (*e.g.*, 1.0 mL 0.2 M NaOAc/HOAc buffer solution pH 4.0 for TMB, 1.0 mL 0.2 M Na_2HPO_4 + 0.1 M citric acid buffer solution pH 7.8 for DAB, and 1.0 mL Tris-HCl + 0.15 M NaCl buffer solution pH 7.8 for OPD). Each contained ~1 × 10^{-11} M RuNFs, 2 M H_2O_2, and 0.8 mM TMB, DAB, or OPD. Control experiments were conducted under the same conditions except for the absence of RuNFs.

3.4.4 Kinetic Assays

The steady-state kinetic assays[9, 20] were performed at room temperature (~22 ºC) in 1.0 mL 0.2 M NaOAc/HOAc solution (pH 4.0). Upon the addition of substrates (TMB and H_2O_2) in the

buffer system containing RuNFs (1.06×10^{-11} M), the absorbance at 653 nm of the reaction solution as a function of time were recorded using a spectrophotometer for 2 min (interval of 6 s). The initial reaction velocity (v) was derived through $v = \text{Slope}_{\text{Initial}}/ (\varepsilon_{\text{TMB-653 nm}}\times l)$, where $\text{Slope}_{\text{Initial}}$ was obtained from the first derivation of each ''absorbance *vs.* time'' plots, $\varepsilon_{\text{TMB-653 nm}}$ was the molar extinction coefficient of TMB at 653 nm that equals 3.9×10^4 $M^{-1}\cdot cm^{-1}$,[32] and l is the length of cuvettes that equals 1.0 cm. The "*v vs.* substrate concentrations" plots were then fitted with the Michaelis-Menten equation $v = V_{max}\times[S]/(K_m + [S])$, where V_{max} represents the maximal reaction velocity, [S] is the substrate concentration, and K_m is the Michaelis constant. Kinetic parameters K_m and V_{max} were determined from the double reciprocal plot (or Lineweaver-Burk plot[33]).

3.5 Characterizations

TEM images were taken using a JEOL JEM-2010 microscope. HRTEM and HAADF-STEM images were performed using a JEOL ARM200F with STEM Cs corrector operated at 200 kV. The UV-Vis spectra of the catalytic reaction solutions were recorded using an Agilent Cary 60 UV-Vis spectrophotometer. The concentrations of Ru ions were determined using an inductively coupled plasma-optical emission spectroscopy (ICP-OES, Perkin Elmer Optima 7000DV), which could be converted to the particle concentration of Pd once the particle shape and size had been resolved through TEM imaging. pH values of solutions were measured using an Oakton pH 700 Benchtop Meter. Photographs of samples in tubes were taken using a Canon EOS Rebel T5 digital camera.

3.6 Reference

1. Wei, H.; Wang, E. *Chem. Soc. Rev*. **2013**, *42*, 6060-6093.

2. Kotov, N. A. *Science* **2010**, *330*, 188-189.

3. Lin, Y.; Ren, J.; Qu, X. *Acc. Chem. Res*. **2014**, *47*, 1097-1105.

4. Breslow, R. *Acc. Chem. Res*. **1995**, *28*, 146-153.

5. Li, W.; Qu, X. *Chem. Soc. Rev*. **2015**, *44*, 2963-2997.

6. Xianyu, Y.; Wang, Z.; Jiang, X. *ACS Nano* **2014**, *8*, 12741-12747.

7. Cheng, H.; Zhang, L.; He, J.; Guo, W.; Zhou, Z.; Zhang, X.; Nie, S.; Wei, H. *Anal. Chem*. **2016**, *88*, 5489-5497.

8. Wang, X.; Hua, Y.; Wei, H. *Inorg. Chem. Front*. **2016**, *3*, 41-60.

9. Gao, L.; Zhuang, J.; Nie, L.; Zhang, J.; Zhang, Y.; Gu, N.; Wang, T.; Feng, J.; Yang, D.; Perrett, S.; Yan, X. *Nat. Nanotechnol*. **2007**, *2*, 577-583.

10. Zhang, X.; Gong, S.; Zhang, Y.; Yang, T.; Wang, C.; Gu, N. *J. Mater. Chem.* **2010**, *20*, 5110-5116.

11. Liu, X.; Wang, Q.; Zhao, H.; Zhang, L.; Su, Y.; Lv, Y. *Analyst* **2012**, *137*, 4552-4558.

12. André, R.; Natálio, F.; Humanes, M.; Leppin, J.; Heinze, K.; Wever, R.; Schröder, H. C.; Müller, W. E.; Tremel, W. *Adv. Funct. Mater.* **2011**, *21*, 501-509.

13. Xiao, X.; Luan, Q.; Yao, X.; Zhou, K. *Biosens. Bioelectron*. **2009**, *24*, 2447-2451.

14. Wei, H.; Wang, E. *Anal. Chem*. **2008**, *80*, 2250-2254.

15. Su, H.; Liu, D.; Zhao, M.; Hu, W.; Xue, S.; Cao, Q.; Le, X.; Ji, L.; Mao, Z. *ACS Appl. Mater. Inter*. **2015**, *7*, 8233-8242.

16. Gao, Z.; Hou, L.; Xu, M.; Tang, D. *Sci. Rep*. **2014**, *4*, 3966.

17. He, W.; Wu, X.; Liu, J.; Hu, X.; Zhang, K.; Hou, S.; Zhou, W.; Xie, S. *Chem. Mater*. **2010**, *22*, 2988-2994.

18. Jv, Y.; Li, B.; Cao, R. *Chem. Commun.* **2010**, *46*, 8017-8019.

19. Fan, J.; Yin, J.; Ning, B.; Wu, X.; Hu, Y.; Ferrari, M.; Anderson, G. J.; Wei, J.; Zhao, Y.; Nie, G. *Biomaterials* **2011**, *32*, 1611-1618.

20. Xia, X.; Zhang, J.; Lu, N.; Kim, M. J.; Ghale, K.; Xu, Y.; McKenzie, E.; Liu, J.; Ye, H. *ACS Nano* **2015**, *9*, 9994-10004.

21. Manea, F.; Houillon, F. B.; Pasquato, L.; Scrimin, P. *Angew. Chem.; Int. Ed*. **2004**, *43*, 6165-6169.

22. Shi, W.; Wang, Q.; Long, Y.; Cheng, Z.; Chen, S.; Zheng, H.; Huang, Y. *Chem. Commun*. **2011**, *47*, 6695-6697.

23. Wang, X.; Qu, K.; Xu, B.; Ren, J.; Qu, X. *Nano Res*. **2011**, *4*, 908-920.

24. Song, Y.; Qu, K.; Zhao, C.; Ren, J.; Qu, X. *Adv. Mater.* **2010**, *22*, 2206-2210.

25. Cui, R.; Huang, H.; Yin, Z.; Gao, D.; Zhu, J. *Biosens. Bioelectron*. **2008**, *23*, 1666-1673.

26. Lei, C.; Hu, S.; Shen, G.; Yu, R. *Talanta* **2003**, *59*, 981-988.

27. Love, J. C.; Estroff, L. A.; Kriebel, J. K.; Nuzzo, R. G.; Whitesides, G. M.; *Chem. Rev*. **2005**, *105*, 1103-1169.

28. Balcerzak, M.; Kaczmarczyk, M. *Anal. Sci.* **2001**, *17*, 1321-1324.

29. Ye, H.; Wang, Q.; Catalano, M.; Lu, N.; Vermeylen, J.; Kim, M. J.; Liu, Y.; Sun, Y.; Xia, X. *Nano Lett.* **2016**, *16*, 2812-2817.

30. Josephy, P. D.; Eling, T.; Mason, R. P. *J. Biol. Chem.* **1982**, *258*, 9913-9924.

31. Xia, X.; Figueroa-Cosme, L.; Tao, J.; Peng, H. C.; Niu, G.; Zhu, Y.; Xia, Y. *J. Am. Chem. Soc.* **2014**, *136*, 10878-10881.

32. Karaseva, E. I.; Losev, Y. P.; Metelitsa, D. I. *Russ. J. Bioorg. Chem*. **2002**, *28*, 128.

33. Lineweaver, H.; Burk, D. *J. Am. Chem. Soc.* **1934**, *56*, 658-666.

34. Josephy, P. D.; Eling, T.; Mason, R. P. *J. Biol. Chem*. **1982**, *257*, 3669-3675.

35. Cai, Q.; Lu, S.; Liao, F.; Li, Y.; Ma, S.; Shao, M. *Nanoscale* **2014**, *6*, 8117-8123.

36. Frey, A.; Meckelein, B.; Externest, D.; Schmidt, M. A. *J. Immunol. Methods* **2000**, *233*, 47-56.

37. Hagen, J. *Industrial Catalysis, A Practical Approach*. Weinheim, Germany, Wiley-VCH, **2006**.

38. Pan, C.; Pelzer K.; Philippot, K. *J. Am. Chem. Soc*. **2001**, *123*, 7584-7593.

CHAPTER 4 AN ENZYME-FREE SIGNAL AMPLIFICATION TECHNIQUE FOR ULTRASENSITIVE COLORIMETRIC ASSAY OF DISEASE BIOMARKERS[a]

4.1 Introduction

Simple and affordable technologies for detection of disease biomarkers are essential to the improvement of standard of living, especially for resource-constrained areas or countries. Enzyme-based colorimetric assays (*e.g.*, enzyme-linked immunosorbent assay (ELISA), immunohistochemistry, and Western blot) are broadly recognized as such kind of technology because they can be performed by less-trained personnel with an inexpensive spectrophotometer, ordinary light microscope, or even naked eyes.[1-5] Nevertheless, the major drawback for these colorimetric assays is the relatively low detection sensitivity compared to other technologies such as those based on fluorescence and plasmonics.[6-9]

In conventional colorimetric assays, the detectable color signal is generated from enzymes (in many cases, HRP), which are conjugated to antibodies and specifically convert substrates to colored molecules.[1-5] Therefore, their detection sensitivity is largely determined by the performance of enzymes. Accordingly, a general strategy for enhancing the sensitivity is to amplify color signal by assembling as many enzyme molecules as possible on certain carriers (*e.g.*, avidin, polymers, and nanoparticles).[10-16] For example, Merkoçi *et al.* conjugated HRPs to gold nanoparticles (GNPs) as carriers and applied these conjugates as labels to ELISA of breast cancer biomarker, of which detection sensitivity was several times higher than conventional ELISA using

[a]Reprinted with permission from *ACS Nano* **2017**, *11*, 2052-2059.

HRP as label.[14] Qian *et al.* further increased HRP loading amount by employing a combination of GNPs and graphene oxide sheets as carriers, achieving a 64-fold improvement of sensitivity.[15] Despite these demonstrations, the detection sensitivity is ultimately limited by the catalytic efficiency of enzymes and the loading amount of enzymes on a carrier.

Herein, we report an enzyme-free signal amplification technique to break the intrinsic limitations of enzymes, achieving substantially enhanced detection sensitivity. In this technique, sub-10 nm Pd-Ir nanoparticles (NPs) encapsulated gold vesicles (referred to as "Pd-Ir NPs@GVs") are employed as alternatives to enzymes. In this study, we used ELISA as a model platform to demonstrate the enzyme-free technique, because ELISA has been the gold standard for detection and quantification of protein biomarkers for decades.[2] As shown in **Figure 4.1**, at elevated temperature, gold vesicles (GVs) captured by analytes liberate thousands of individual Pd-Ir NPs because of the heat-induced breakup of the GV membrane.[17-19] The released Pd-Ir NPs act as peroxidase mimics and generate intense color signal by catalyzing the oxidation of TMB by H_2O_2.[20] It should be pointed out that we have recently demonstrated the peroxidase-like property of Pd-Ir NPs and controlled release of GVs.[17-20] However, to date, there has been no report yet on the development of a signal amplification platform based on the combination of these two systems. The ultralow detection limit of this enzyme-free ELISA arises from the following distinctive features of the amplification technique: (*i*) Pd-Ir NPs as enzyme mimics possess much higher catalytic efficiency than natural enzymes, providing enhanced color signal; (*ii*) the loading capacity of enzyme mimics is maximized by taking advantage of the large interior 3D space of the GVs as carriers.[21, 22] in contrast, the loading of enzymes on carriers in current designs of ELISA is limited by the surface area that allows for the conjugation of enzymes; (*iii*) the loading of label-

free enzyme mimics of Pd-Ir NPs in the pocket of GVs avoids the loss of catalytic efficiency caused by chemical conjugation; and (*iv*) Pd-Ir NPs could disperse in catalytic reaction solution upon release, making them more active than immobilized catalysts on solid surfaces, which is the case for conventional ELISAs.

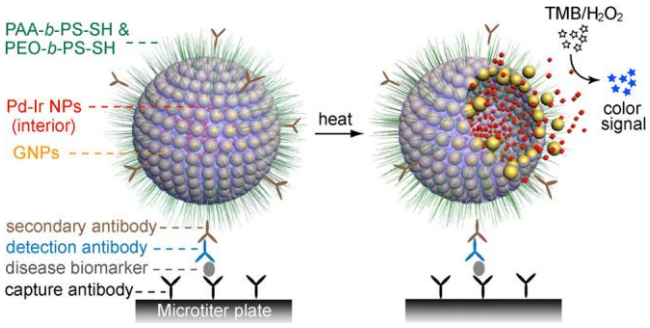

Figure 4.1 Schematic illustration of utilizing Pd-Ir NPs@GVs based ELISA for detection of disease biomarkers. The Pd-Ir NPs released from captured GVs act as effective peroxidase mimics to catalyze chromogenic substrates.

In addition to the high detection sensitivity, our enzyme-free ELISA is featured by good stability and simplicity. The Pd-Ir NPs@GVs are mainly made of inert noble metals with excellent stabilities, enabling them to survive harsh environments. In particular, we have demonstrated in our recent work that the peroxidase-like activity of Pd-Ir NPs was well retained at high temperature (up to 200 °C) and in strong acidic/basic conditions.[20] In this regard, our platform is more suitable for detection at some extreme conditions compared to natural enzyme-based amplification techniques even though their detection sensitivities may be comparable.[23] As shown in **Figure 4.1**, the principle of our enzyme-free ELISA is essentially the same as the conventional HRP-based colorimetric ELISA except for the substitution of HRP with Pd-Ir NPs@GVs. The adoption of existing ELISA platform ensures the simplicity of the assay without the involvement of additional materials and equipment other than the Pd-Ir NPs@GVs. In contrast, other enzyme-free signal

amplification systems (*e.g.*, those based on quantum dots[24, 25]) may require special materials and/or equipment.

4.2 Results and Discussion

4.2.1 Synthesis and Characterization of Pd-Ir NPs

We started with the synthesis of Pd-Ir NPs by coating an ultrathin layer of Ir on preformed sub-10 nm Pd seeds. In a standard synthesis, a solution of Na_3IrCl_6 was injected slowly into a mixture containing Pd truncated octahedra with an average size of 5.6 nm as the seeds (**Figure S4.1** in Appendix C), L-ascorbic acid as a reductant, and poly(vinylpyrrolidone) as a colloidal stabilizer. **Figure 4.2a, b** show typical TEM images of the produced Pd-Ir NPs. The Pd-Ir NPs exhibit a high purity (>95%) and good uniformity (**Figure 4.2a** and **S4.2** in Appendix C). A close inspection of the NPs shows that the Pd seeds retained their truncated octahedral shape after the deposition of Ir, indicating a conformal coating of Ir (**Figure 4.2b**). The average size of the Pd-Ir NPs was measured to be 6.1 nm, which was 0.5 nm greater than that of the initial Pd seeds. Therefore, the average thickness of the deposited Ir shells was about 0.25 nm, indicating an approximate monolayer coating of Ir on Pd(111) surfaces.[26, 27] The molar ratio of Ir to Pd for these Pd-Ir NPs was measured to be 0.28:1 by inductively coupled plasma-optical emission spectrometry (ICP-OES). On the basis of this data, the morphology of Pd seeds, and the unit cell parameters of Ir,[22] the average number of Ir atomic layers was estimated to be 1 for the Pd-Ir NPs, further confirming the overall monolayer coating of Ir. We also characterized the structure and composition of the Pd-Ir NPs by XRD, HRTEM, HAADF-STEM, energy-dispersive X-ray (EDX) mapping/scanning, and X-ray photoelectron spectroscopy (XPS). The XRD patterns of initial Pd seeds and Pd-Ir NPs were shown in **Figure S4.3** (Appendix C). It can be seen that the peaks for

Pd-Ir NPs were broadened and slightly shifted to the standard face-centered cubic (*fcc*) Ir peak positions as compared to the peaks for *fcc* Pd seeds, suggesting the successful deposition of Ir on Pd seeds and the retention of *fcc* crystal structure for the final Pd-Ir NPs. The typical HRTEM image of an individual Pd-Ir NP reveals the continuous lattice fringes from Pd core to Ir shell, indicating an epitaxial relationship between these two metals (**Figure 4.2c**).[28] The color difference between the core (green = Pd) and the shell (red = Ir) of an individual Pd-Ir NP in the EDX maps (**Figure 4.2d**) confirmed the Pd-Ir core-shell structures of the final products. The line-scan EDX profile shown in along a corner-to-edge direction of an individual Pd-Ir NP (see **Figure S4.4** in Appendix C) verified that the corners and edges were dominated by Ir, whereas the core was made of pure Pd. In addition, XPS was used to identify the oxidation state of the Ir layers. The XPS survey spectrum of the Pd-Ir NPs clearly showed the appearance of Ir 4f peaks (**Figure S4.5a** in Appendix C) as compared to the initial Pd seeds, confirming the existence of Ir layers on the Pd cores. The high-resolution spectra of the Ir 4f peaks (**Figure S4.5b** in Appendix C) revealed two chemical states for Ir species: (*i*) $Ir^0$4f7/2 and 4f5/2 peaks at 60.24 and 63.23 eV, and (*ii*) Ir^{x+} 4f7/2 and 4f5/2 at 61.25 and 64.46 eV, where the Ir^0 was dominant. This data suggests that the shell of the Pd-Ir NPs is mainly composed of Ir(0).

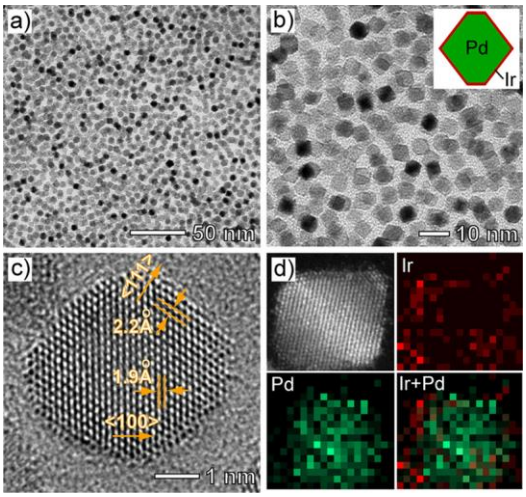

Figure 4.2 Structural and compositional analyses of Pd-Ir NPs prepared by depositing Ir atoms on 5.6 nm Pd truncated octahedral seeds. (a,b) low (a) and high (b) magnification TEM image of Pd-Ir NPs. The inset is a 2D schematic model. (c) HRTEM image of an individual Pd-Ir NP; (d) HAADF-STEM image and EDX mapping of an individual Pd-Ir NP (red = Ir, green = Pd).

4.2.2 Peroxidase-like Activity of Pd-Ir NPs

We quantitatively evaluated the peroxidase-like activity of as-synthesized Pd-Ir NPs by apparent steady-state kinetic assay as shown in **Figure 4.3**.[20, 29] Oxidation of TMB by H_2O_2 was chosen as a model catalytic reaction. The catalytic efficiency, in terms of catalytic constant (K_{cat}, which measures the maximum number of colored products generated per enzyme/mimic per second), for the Pd-Ir NPs was measured to be 1.1×10^5 s^{-1} (**Table 4.1**). In comparison, the values of K_{cat} for initial Pd seeds and HRP[29] were 4.8×10^3 and 4.0×10^3 s^{-1}, respectively. This data suggests that (*i*) The Pd-Ir NPs are ~28 times more efficient than HRP in generating color products (*e.g.*, oxidized TMB with maximum absorbance at 653 nm[30, 31]); and (*ii*) the enhanced catalytic efficiency for Pd-Ir NPs was ascribed to the coating of Ir monolayer on Pd seeds.

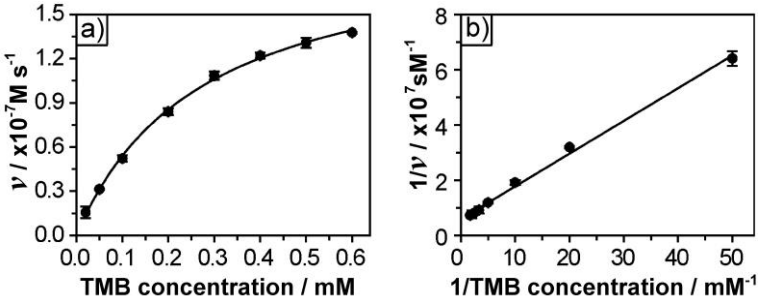

Figure 4.3 Kinetic assays of using Pd-Ir NPs as peroxidase mimics for the oxidation of TMB by H_2O_2. The reactions were conducted in 0.2 M HOAc/NaOAc buffer, pH 4.0 containing Pd-Ir NPs (1.5×10^{-12} M), 2 M H_2O_2 and TMB that was held in cuvettes at room temperature. (a) Plot of initial reaction velocity (v) as a function of TMB concentration. (b) Double-reciprocal plot generated from (a), from which the kinetics parameters in **Table 4.1** were derived. Error bars in the plots indicate standard deviations of three independent measurements.

Table 4.1 Comparison of the kinetic parameters of Pd seeds (**Figure S4.1** in Appendix C), Pd-Ir NPs (**Figure 4.2**), and HRP as catalysts towards the oxidation of TMB by H_2O_2.

Catalyst	[*E*] (M)	Substrate	K_m (M)	V_{max} (M·s^{-1})	K_{cat} (s^{-1})
Pd-Ir NPs	1.5×10^{-12}	TMB	2.0×10^{-4}	1.7×10^{-7}	1.1×10^{5}
Pd seeds	3.0×10^{-11}	TMB	8.8×10^{-5}	1.4×10^{-7}	4.8×10^{3}
HRP	2.5×10^{-11}	TMB	4.3×10^{-4}	1.0×10^{-7}	4.0×10^{3}

4.2.3 Encapsulation of Pd-Ir NPs to GVs

We then encapsulated the Pd-Ir NPs into GVs that were achieved by assembling block copolymers (BCPs)-tethered GNPs in an aqueous suspension of Pd-Ir NPs. GNPs with a diameter of 33.0±4.7 nm were first modified with thiol-terminated BCPs of poly(ethylene oxide)-*b*-polystyrene (PEO_{45}-*b*-PS_{260}-SH, **Figure 4.4a**) and poly(acrylic acid)-*b*-polystyrene (PAA_{23}-*b*-PS_{250}-SH, **Figure 4.4b**) at a molar ratio of 20:1.[32] It should be mentioned that we chose these GNPs of ~33 nm for the assemble of vesicles mainly because (*i*) the ease in the functionalization of

GNPs with polymers *via* Au-S bond, in order to trigger the formation of GVs and to conjugate biological moieties for sensing; (*ii*) the good stability of resultant GVs and their capability in retaining molecules (or nanoparticles) without noticeable leakage for a long time; our previous studies showed that GVs remain stable for months and minimal leakage of small organic molecules (or drugs) was observed from GVs after weeks, presumably owing to the jamming of particles in the vesicular membranes;[19, 33] in contrast, small molecules tend to leak out from liposomes or polymersomes within a few hours, which makes them less attractive for the present application;[34] (*iii*) these GNPs are relatively uniform and monodisperse;[17] (*iv*) the GNP size of 33 nm is greatly larger than that of Pd-Ir NPs (*e.g.,* 6.1 nm), making it convenient to distinguish Pd-Ir NPs from GNPs under electron microscope that is critical for monitoring the heat-induced NP release process.

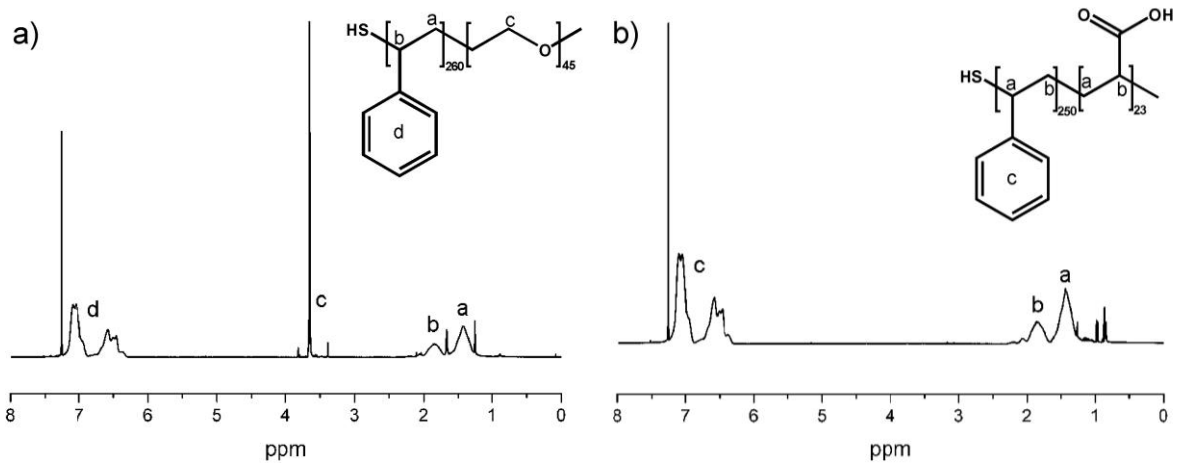

Figure 4.4 ^{1}H NMR spectra of (a) PEO_{45}-*b*-PS_{260}-SH and (b) PAA_{23}-*b*-PS_{250}-SH.

A film rehydration method, which is widely used for scalable fabrication of liposomes in pharmaceutic industry, was used to fabricate the GVs.[17] Specifically, pristine GVs were prepared by rehydrating a film of BCP-tethered GNPs in water under sonication, according to our previously

published procedures.[17-19] To encapsulate Pd-Ir NPs into GVs, an aqueous suspension of Pd-Ir NPs at a high concentration (~4.5×10^{16} particles/mL) was used for the rehydration. As indicated by the TEM and SEM images shown in **Figure 4.5a, b**, the Pd-Ir NPs@GVs showed an overall spherical shape. The low-magnification SEM image (**Figure 4.5c**) demonstrated that the Pd-Ir NPs@GVs could be obtained with a high purity and a good uniformity. Our analyses on 100 random particles indicated that the products had an average diameter of ~400 nm with a standard deviation of 48 nm. As shown by **Figure 4.5d**, the vesicular membranes of the GVs were composed of a monolayer of densely packed GNPs, which is consistent with our previous studies.[17, 32, 35] On the basis of the packing density and size of GV, the average number of GNPs in an individual GV was roughly estimated to be 339 (**Figure S4.6a** in Appendix C). The loading amount of Pd-Ir NPs in individual GVs was estimated to be 1232 by quantifying elemental Pd and Au in GVs using ICP-OES (see **Figure S4.6b** in Appendix C for detailed estimation).

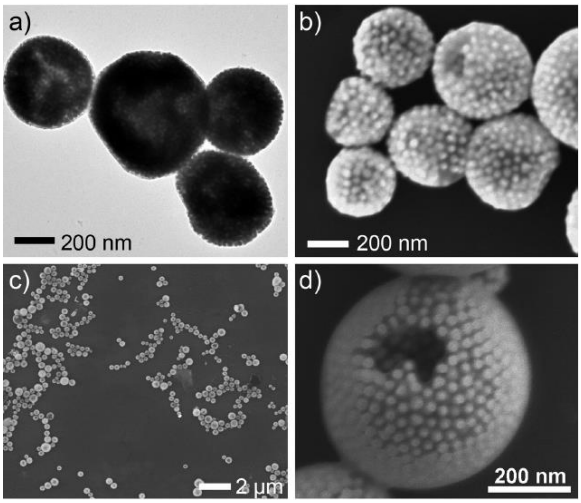

Figure 4.5 (a, b) magnified TEM and SEM images, respectively, showing the overall spherical shape of the products. (c) low-magnification SETM image showing the yield and size distribution of the products. (d) SEM image of an individual particle with a cavity on the GV surface, showing that the GVs were composed of a monolayer of GNPs.

4.2.4 Heat-triggered Release of Pd-Ir NPs

To demonstrate the heat-triggered release of Pd-Ir NPs from GVs, we incubated aqueous suspensions of Pd-Ir NPs@GVs (~0.5 mg/mL in terms of Au element) at different temperatures for 1h. The morphological change of samples caused by heat treatment was monitored by TEM and SEM. We found that the assembled GVs gradually collapsed as the temperature increased (**Figure 4.6**). Compared to the initial Pd-Ir NPs@GVs (**Figure 4.6a, e**), small holes started to appear in the membranes of GVs when the temperature was set to 70 °C (**Figure 4.6b, f**). At 80 °C, the holes in GVs became more evident and fragments began to fall off of the vesicles (**Figure 4.6c, g**). Finally, most of the GVs completely collapsed after 90 °C treatment (**Figure 4.6d, h**). We presume that the dissociation of GNPs is attributed to the breakup of Au-S bonds due to the thermal instability of the bonds at a temperature above 70 °C.[36, 37] The disassembly of GVs is associated with the release of encapsulated Pd-Ir NPs (**Figure 4.6b-d**). A number of Pd-Ir NPs can be observed outside the GVs. The heat-triggered release of Pd-Ir NPs is further confirmed by dynamic light scattering (DLS) analysis. Pristine GVs and Pd-Ir NPs were used as control groups. As shown in **Figure 4.7a**, after heating at 90 °C for 1 h, the major size distribution peak of Pd-Ir NPs@GVs suspension shifted from 380 nm (solid, blue) to 260 nm (dashed, blue). In addition, two shoulder peaks at ~8.5 nm and ~32 nm were observed. The 8.5 nm peak matched well with the peak of pristine Pd-Ir NPs (solid, red), indicating the successful release of Pd-Ir NPs from GVs. The 32 nm peak could be assigned to the dissociated GNPs from GVs since this peak was also observed for pristine GVs after they had been heated (dashed, black). Thermal treatment at 90 °C for 1 h was adopted for subsequent ELISA experiments. We are aware that heating for 1 h may limit the practical application of the platform for assays. The operation

time of assays can be drastically reduced by speeding up the release of payload from GVs *via* the irradiation of near-infrared light or the use of thermoresponsive polymer tethers.[19, 33]

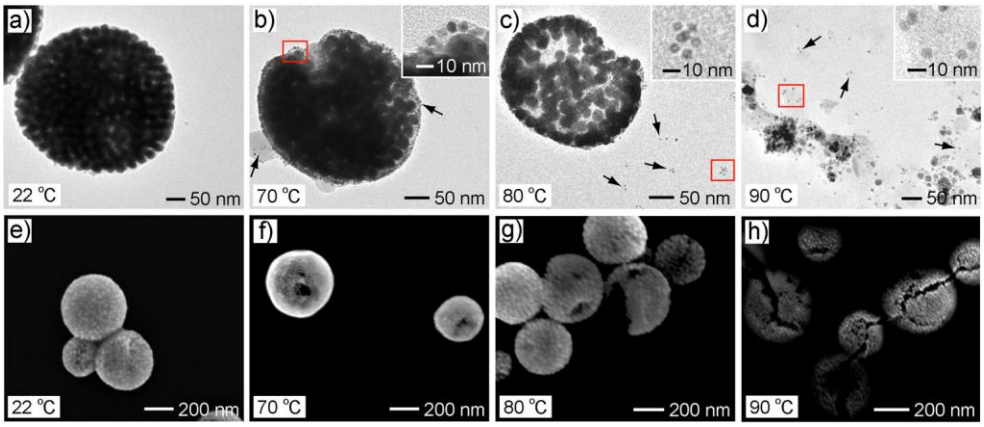

Figure 4.6 Heat-triggered release of Pd-Ir NPs from GVs. Representative (a-d) TEM and (e-h) SEM images of the Pd-Ir NPs@GVs treated at different temperatures (marked in each image) for 1 h. In (b-d), insets show magnified TEM images of corresponding regions marked by red boxes. Some of the released Pd-Ir NPs are indicated by black arrows.

4.2.5 Demonstration of Signal Amplification

We also designed a set of experiments to demonstrate the color signal amplification mechanism shown in **Figure 4.1**. Briefly, aliquots were taken from an aqueous suspension of Pd-Ir NPs@GVs before and after it had been heated at 90 °C for 1 h and were employed as catalysts for the oxidation of TMB by H_2O_2. Colored products were quantified by measuring the absorbance at 653 nm (A_{653nm}), t = 2 min. For comparison, aqueous suspensions of pristine GVs and Pd-Ir NPs with the same amounts of GVs and Pd-Ir NPs (determined by ICP-OES), respectively, as those in Pd-Ir NPs@GVs were also tested. As shown in **Figure 4.7b**, before heat treatment, the reaction solution with the presence of Pd-Ir NPs@GVs was nearly colorless with $A_{653nm} \approx 0.04$. After heat treatment, the catalytic activity of Pd-Ir NPs@GVs was dramatically enhanced, generating an intense blue color (A_{653nm} = 1.6, see the inset of **Figure 4.7b**). Since almost no absorbance at 653

nm was observed for GVs catalyzed reaction solutions, the enhanced catalytic activity for heat treated Pd-Ir NPs@GVs could be ascribed to the free Pd-Ir NPs released from GVs. It should be mentioned that, before heat treatment, the absorbance of Pd-Ir NPs@GVs catalyzed reaction solution was similar to that of GVs catalyzed reaction solution. This observation demonstrated that the GVs could effectively prevent the leakage of encapsulated Pd-Ir NPs when there is no heating. On the basis of the values of A_{653nm}, heat treated Pd-Ir NPs@GVs was as active as pristine Pd-Ir NPs, indicating that most of the Pd-Ir NPs had been released from GVs and their catalytic efficiency was well retained. Taken together, these results clearly demonstrated the signal amplification mechanism described in **Figure 4.1**.

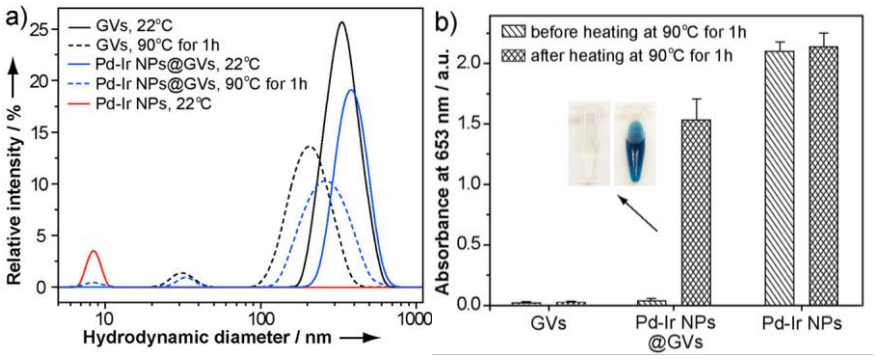

Figure 4.7 Comparison of the properties of Pd-Ir NPs@GVs before and after heat treatment (90 ^{o}C, 1 h). (a) DLS analysis of different samples: GVs (black), Pd-Ir NPs@GVs (blue), and Pd-Ir NPs (red); (b) Absorbance at 653 nm measured from catalytic reaction solutions containing different particles (marked under the bars) at t = 2 min. Concentrations of GVs were kept the same for suspensions of GVs and Pd-Ir NPs@GVs, while the concentrations of Pd-Ir NPs were kept the same for suspensions of Pd-Ir NPs@GVs and Pd-Ir NPs. Inset shows photographs of reaction solutions corresponding to Pd-Ir NPs@GVs. All tests in (a) and (b) were conducted at room temperature (~22 ^{o}C).

4.2.6 Immunoassay of Disease Biomarker

Finally, we applied the Pd-Ir NPs@GVs to ELISA of human prostate surface antigen (PSA), according to the principle shown in **Figure 4.1**. PSA was chosen because it has been recognized as the key biomarker responsible for prostate cancer recurrence in patients who have undergone radical prostatectomy.[38] It is vital to detect minute concentrations of PSA at the earliest stage possible to improve the survival rates of those patients.[39, 40] Herein, antibodies were conjugated to Pd-Ir NPs@GVs through the EDC/NHS-mediated coupling reaction between the -COOH groups of PAA_{23}-*b*-PS_{250}-S- on GVs and the -NH_2 groups on antibodies (**Figure 4.8**).[41, 42] PSA standards with a series of concentrations in dilution buffer were monitored in a 96-well microtiter plate (**Figure 4.9a**) and quantified using a PerkinElmer Victor 3 1420 multilabel plate reader. The yellow color of the wells arose from the two-electron oxidation products of TMB (*e.g.*, diimine with $\lambda_{max} \approx 450$ nm) that were formed when the catalytic reaction was quenched by H_2SO_4.[30, 43] As shown in **Figure 4.9b**, a sigmoid curve regression between the logarithms of absorbance and PSA concentration was obtained. The linear range of detection was found to be 0.2-200 pg/mL with a linear regression value of $r^2 = 0.997$. The coefficient of variations ($n = 8$) across the entire concentration range were 2.15-12.24%, indicating a good reproducibility of the assay. The limit of detection (defined as the PSA concentration corresponding to a signal that is 3 times the standard deviation above zero calibrator[44, 45]) was calculated to be 31 fg/mL. To evaluate the nonspecific binding between antibodies conjugated Pd-Ir NPs@GVs and the 96-well microtiter plate/capture antibodies, we have performed a control experiment by excluding antibodies conjugated Pd-Ir NPs@GVs from the blank well (*e.g.*, 0 pg/mL PSA) while keeping all other conditions unchanged. The absorbance at 450 nm for the control group was measured to be 0.024, whereas the absorbance for the blank was 0.036 (both values of absorbance represent the averages

from 8 independent measurements). Therefore, on average, the absorbance at 450 nm of each well caused by nonspecific binding of antibodies conjugated Pd-Ir NPs@GVs was approximately 0.012. This value is relatively low compared to the absorbance measured from the wells of PSA standards (**Figure 4.9b**), suggesting a good specificity of the antibodies conjugated Pd-Ir NPs@GVs.

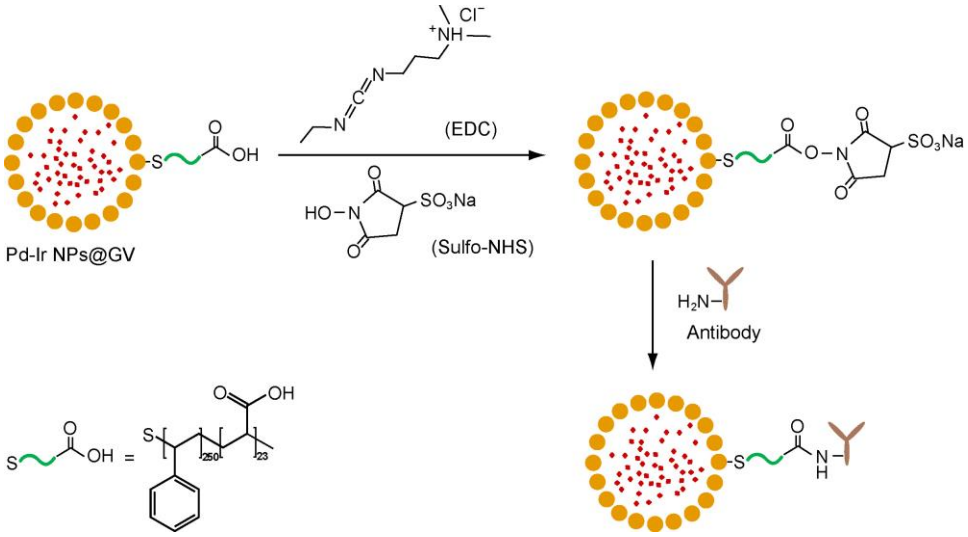

Figure 4.8 Schematic illustration showing the procedure for conjugation of antibodies (*e.g.*, goat anti-mouse IgG) onto Pd-Ir NPs@GVs.

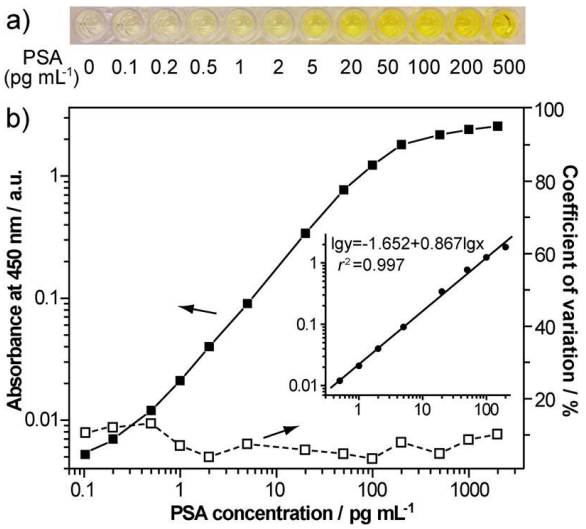

Figure 4.9 Pd-Ir NPs@GVs based ELISA of PSA. (a) Representative photographs taken from the ELISA of PSA standards; (b) Corresponding calibration curve (■) and imprecision profile (□) of the detection results shown in (a). Note that absorbance of the blank (*e.g.*, 0 pg/mL PSA) was subtracted from those of PSA standards. Inset shows the linear range region of the calibration curve.

We benchmarked the Pd-Ir NPs@GVs based ELISA against the conventional HRP based ELISA by using the same set of antibodies and procedures except for the exclusion of heat treatment. On the basis of the calibration curve shown in **Figure 4.10**, the linear detection range and overall coefficient of variations for the HRP based ELISA were found to be 0.2-100 ng/mL and 4.21-14.31%, respectively. The limit of detection was determined to be 48 pg/mL, which was ~1500-fold higher than our enzyme-free ELISA. This significantly enhanced detection sensitivity for the enzyme-free ELISA could be attributed to the signal amplification by Pd-Ir NPs@GVs, because other conditions of both ELISAs were kept identical. We also evaluated the correlation between the enzyme-free ELISA with conventional HRP based ELISA by quantifying the same 12 PSA standards of concentrations in 0.5-50 ng/mL using the two ELISAs. For the quantification with enzyme-free ELISA, the standards were diluted with dilution buffer to ensure that the

concentrations of PSA were located in the linear range. The final quantitative data was obtained based on the detected PSA concentrations and the dilution factors. As shown in **Figure 4.11**, a good correlation between the two ELISAs was found with a correlation coefficient $r = 0.998$ ($n = 12$). Taken together, these results demonstrate that our enzyme-free ELISA is three-orders-of-magnitude more sensitive than conventional ELISA, while its reliability and quantitativity are as good as those of conventional ELISA.

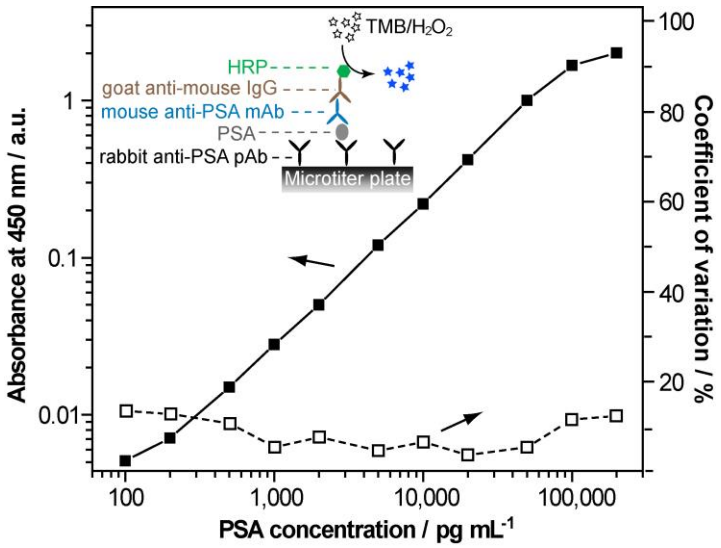

Figure 4.10 Calibration curve (■) and imprecision profile (□) of conventional HRP based colorimetric ELISA of PSA, in which PSA standards and antibodies were kept the same as what had been used for the Pd-Ir NPs@GVs based ELISA (**Figure 4.9**). Inset shows the detection principle.

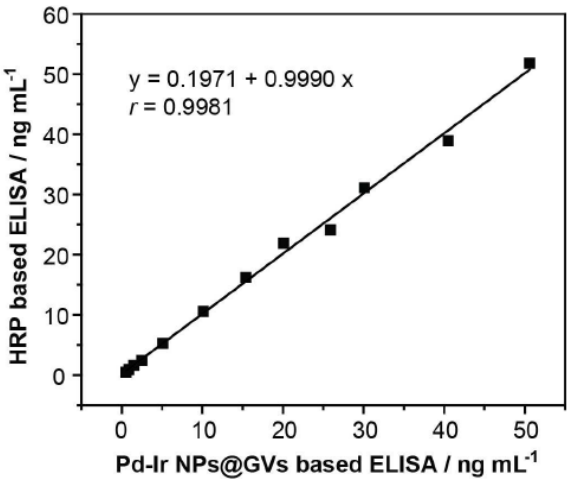

Figure 4.11 Correlation analysis between the Pd-Ir NPs@GVs based ELISA (*e.g.*, enzyme-free ELISA) and HRP based ELISA in quantification of PSA from 12 standards. Each data point in the plot represents the average from three independent measurements.

To demonstrate the potential application of the Pd-Ir NPs@GVs based ELISA in clinical scenarios, we spiked human plasma samples (from a healthy female donor, provided by the UP-Health System-Portage, Houghton, Michigan, United States) with PSA standard at different concentrations in range of 0.4-50 pg/mL and detected the concentrations of PSA. As summarized in **Table 4.2**, the analytical recoveries (defined as measured amount of PSA divided by the amount of PSA in original spiked samples)[46] for the four PSA spiked human plasma samples were determined to be in the range of 93.25-105.85%. The coefficient of variation (n = 8) for all samples was below 10.14%. This data implies that the performance of Pd-Ir NPs@GVs based ELISA was not compromised by the complex components in plasma, suggesting the feasibility of this technique in detecting clinical samples.

Table 4.2 Analytical recoveries of Pd-Ir NPs@GVs based ELISA in detecting PSA spiked human plasma samples.

PSA amount spiked (pg/mL)	PSA amount measured (pg/mL)	Coefficient of variations (%, n = 8)	Recovery (%)
0.40	0.37	10.14	93.25
2.00	2.12	7.71	105.85
10.00	9.87	3.92	98.72
50.00	51.71	6.85	103.41

4.3 Conclusion

In summary, we have demonstrated an enzyme-free signal amplification technique based on Pd-Ir NPs@GVs for colorimetric assay with substantially enhanced detection sensitivity. To the best of our knowledge, such an enzyme-free signal amplification strategy using enzyme-like NPs encapsulated responsive GVs has never been demonstrated elsewhere. The enzyme-free technique we developed can be potentially extended to a variety of other enzymes-based diagnostic technologies beyond ELISA such as immunohistochemistry, Western blot, and point-of-care tests. Importantly, this technique is compatible with equipment and procedures of existing sensing technologies, making it practically useful for clinical diagnostics. Further optimization of the Pd-Ir NPs@GVs system (*e.g.*, size of GV, loading amount of Pd-Ir NPs, particle release time, and catalytic efficiency) and detection of clinical samples are the subjects of our future research.

4.4 Materials and Experiment

4.4.1 Chemicals and Materials

Sodium hexachloroiridate(III) hydrate ($Na_3IrCl_6 \cdot xH_2O$, M_W=473.9), sodium tetrachloropalladate(II) (Na_2PdCl_4, 98%), gold(III) chloride trihydrate ($HAuCl_4 \cdot 3H_2O$, ≥99.9%), potassium bromide (KBr, ≥99%), L-ascorbic acid (AA, ≥99%), poly(vinylpyrrolidone) (PVP, MW≈55,000), 3,3',5,5'-tetramethylbenzidine (TMB, >99%), hydrogen peroxide solution (30 wt. % in H_2O), acetic acid (HOAc, ≥99.7%), sodium acetate (NaOAc, ≥99%), human prostate surface antigen (PSA, ≥99%), Tween 20, bovine serum albumin (BSA, ≥98%), sodium chloride (NaCl, ≥99.5%), potassium chloride (KCl, ≥99%), N-hydroxysulfosuccinimide sodium salt (NHS, ≥98%), N-Ethyl-N′-(3-dimethylaminopropyl)carbodiimide hydrochloride (EDC, ≥99%), sodium phosphate dibasic (Na_2HPO_4, ≥99%), potassium phosphate monobasic (KH_2PO_4, ≥99%), tris base (≥99.9%), sodium citrate, dimethylformamideand (DMF), tetrahydrofuran (THF), sodium azide (NaN_3, ≥99.5%), and sulfuric acid (H_2SO_4, 95-98%) were all obtained from Sigma-Aldrich. Ethylene glycol (EG) was obtained from J. T. Baker. Mouse anti-PSA monoclonal antibody (mouse anti-PSA mAb) and rabbit anti-PSA polyclonal antibody (rabbit anti-PSA pAb) were obtained from Abcam plc. Goat anti-mouse IgG and HRP-goat anti-mouse IgG conjugate were obtained from Thermo Fisher Scientific, Inc.. 96-well microtiter plates (polystyrene, clear, flat bottom) was obtained from Corning Inc.. All aqueous solutions were prepared using deionized (DI) water with a resistivity of 18.0 MΩ·cm.

4.4.2 Preparation of 5.6 nm Pd Truncated Octahedra to be Used as Seeds

In a typical synthesis, 30 mL of an EG solution containing 600 mg of PVP was hosted in a glass vial and preheated to 160 ^oC in an oil bath under magnetic stirring for 10 min. Then, 15 mL

of an EG solution containing 240 mg of Na_2PdCl_4 was quickly injected into the reaction solution using a pipette. The reaction was allowed to continue for 3 h. After being washed with acetone once and ethanol twice *via* centrifugation, the final product was redispersed in 10 mL of EG for future use. The concentration of Pd element in the final product was determined to be 7.5 mg/mL by ICP-OES, which could be converted to a particle concentration of ~5×10^{15} particles/mL (assuming that the particles were perfect octahedra).

4.4.3 Preparation of Pd-Ir Core-shell Nanoparticles (Pd-Ir NPs)

Pd-Ir NPs were prepared by coating a monolayer of Ir on Pd seeds according to our previously published procedure with some modifications.[20] In a standard procedure, 100 mg of PVP and 60 mg of AA were mixed with the 10 mL Pd seeds in EG and were hosted in a 50-mL three-neck flask. The mixture was preheated to 200 ºC in an oil bath under magnetic stirring for 10 min. Then, 8.0 mL of $Na_3IrCl_6\cdot xH_2O$ solution (7.0 mg/mL, in EG) was injected to the flask at a rate of 1.5 mL/h using a syringe pump. The reaction was allowed to proceed for an additional 10 min after the $Na_3IrCl_6\cdot xH_2O$ precursor had been completed injected. The products (*e.g.,* Pd-Ir NPs) were collected by centrifugation, washed once with acetone, two times with water, and finally redispersed in 1 mL of DI water for future use. Particle concentration for the suspension of Pd-Ir NPs was estimated to be 4.5×10^{16} by ICP-OES.

4.4.4 Evaluation of the Peroxidase-like Activities

Peroxidase-like activity was measured by the steady-state kinetic assays.[20, 24] All assays were carried out at room temperature in 1.0-ml cuvettes (path length, l = 1.0 cm), with 0.2 M NaOAc/HOAc solution, pH 4.0 being used as the reaction buffer. The rest procedure for collection

of V_{max} and K_m can be found in **Chapter 3**, **Section 3.4.4**.

4.4.5 Synthesis of Amphiphilic Block Copolymers (BCPs) and Gold Nanoparticles (GNPs)

Amphiphilic BCPs of poly(ethylene oxide)-*b*-polystyrene and poly(acrylic acid)-*b*-polystyrene terminated with a thiol group at polystyrene end (PEO-*b*-PS-SH and PAA-*b*-PS-SH) were synthesized following the reversible addition-fragmentation chain-transfer (RAFT) polymerization procedures reported previously.[17] The BCPs samples were designed with similar polystyrene (PS) lengths (PEO_{45}-*b*-PS_{260}-SH and PAA_{23}-*b*-PS_{250}-SH) as verified by proton nuclear magnetic resonance (^{1}H NMR) as shown in **Figure 4.4**.

GNPs with diameters of 33.0±4.7 nm were prepared by sodium citrate reduction method.[46] Briefly, a 10 mg of $HAuCl_4$ was dissolved in 500 mL H_2O and heated to boiling under stirring. A 3 mL of sodium citrate (1 wt. %) solution was then quickly injected. The reaction mixture was refluxed for 30 min and then used as seeds for the further growth of GNPs in the presence of sodium citrate at 80 ºC. The resultant 33.0 nm GNPs were collected by centrifugation.

4.4.6 Preparation of Gold Vesicles (GVs) and Pd-Ir NPs@GVs

GVs and Pd-Ir NPs@GVs were prepared by assembling GNPs tethered with BCPs in the presence of DI water and aqueous suspension of Pd-Ir NPs, respectively, according to our previously reported procedure with minor modifications.

The surface of GNPs was modified with BCPs using the ligand exchange method.[32] A 5 mg BCPs of PEO_{45}-*b*-PS_{260}-SH and PAA_{23}-*b*-PS_{250}-SH with a molar ratio of 20:1 were dissolved in 10 mL DMF. Then, a concentrated solution of GNPs (~2 mg/mL) was slowly added into the BCP solution under vigorous shaking. The mixture was subsequently sonicated for 1 h to avoid

the aggregation of GNPs and was then kept static without stirring overnight. The BCP-tethered GNPs were purified by removing free polymers through centrifugation (6-8 times) and were finally redispersed in THF at a concentration of ~0.05 mg/mL.

Self-assembly of BCP-tethered GNPs was conducted by the film rehydration method as reported previously.[19] Briefly, a solution of BCP-modified GNPs in THF was first dried under nitrogen flow to form a thin film on a glass substrate, followed by rehydration in DI water (for pristine GVs) or an aqueous suspension of Pd-Ir NPs at 4.5×10^{16} particles/mL (for Pd-Ir NPs@GVs) with sonication for 1 min. The resultant GVs and Pd-Ir NPs@GVs were collected by centrifugation (5000 rpm, 5 min), washed 8 times with DI water, and finally re-dispersed in water for future use.

4.4.7 Preparation of Pd-Ir NPs@GVs-goat Anti-mouse IgG Conjugates

Anti-mouse IgG was conjugated to Pd-Ir NPs@GVs using EDC and NHS as coupling agents (see **Figure 4.8**).[20,39,40] In brief, 50 μL of Pd-Ir NPs@GVs (~0.5 mg/mL in terms of Au element, in DI water) was added to a 450 μL of 10 mM phosphate buffered saline (PBS, pH 7.4) buffer at room temperature under stirring. Then, 5 μL of EDC (25 mM, in DI water) and 5 μL of NHS (50 mM, in DI water) were added. After 15 min, the particles were washed with DI water twice and redispersed in 50 μL PBS. Subsequently, 50 μL of goat anti-mouse IgG (2 mg/mL, in PBS) was added to the particle suspension. After incubation at room temperature for 30 min, the reaction solution was put in a refrigerator overnight at 4 ºC. Then, 100 μL of blocking solution (5% BSA in PBS) was added to the reaction solution. After 2 h, the final products were collected by centrifugation, washed twice with PBS, and redispersed in 50 μL of PBS containing 1% BSA and 0.05% NaN_3 for future use.

4.4.8 Pd-Ir NPs@GVs-based ELISA of PSA

First, 96-well microtiter plates were coated with rabbit anti-PSA pAb (100 μL per well, 5 μg/mL in carbonate/bicarbonate buffer, pH=9.6) at 4 ºC overnight. After washing the plates three times with washing buffer (10 mM PBS pH 7.4 containing 0.5% tween 20, PBST), the plates were blocked with 200 μL blocking buffer (3% BSA in PBST) for 2 h at room temperature. The plates were then washed three times with washing buffer, followed by the addition of 100 μL PSA standards or human plasma sample in dilution buffer (1% BSA in PBST). Note that plasma was pre-diluted 2 folds by dilution buffer prior to spiking of PSA and detection. After shaking at room temperature for 2 h, the plates were washed three times with washing buffer, and 100 μL mouse anti-PSA mAb (2 μg/mL, in dilution buffer) was added. After 1 h shake at room temperature, the plates were washed three times, and 100 μL Pd-Ir NPs@GVs-goat anti-mouse IgG conjugates (1:2000, in dilution buffer) was added, followed by 30 min shake at room temperature. After washing four times, 60 μL DI water was added. After being sealed with a plastic film, the plate was put in an oven set to 90 ºC for 1 h. After the plate had been cooled down to room temperature, 50 μL freshly prepared substrate solution (1.6 mM TMB and 4.0 M H_2O_2 in 0.4 M HOAc/NaOAc buffer, pH 4.0) was added to each well. After 30 min incubation at room temperature, 50 μL of 2 M H_2SO_4 as a stopping solution was added. The absorbance of each well at 450 nm was read using a microplate reader.

The procedure of HRP based ELISA was the same as the Pd-Ir NPs@GVs-based ELISA except for the substitutions of Pd-Ir NPs@GVs-goat anti-mouse IgG conjugates with 100 μL HRP-goat anti-mouse IgG conjugates (1 μg/mL, in dilution buffer), the difference in the components of substrate solution (0.8 mM TMB and 5 mM H_2O_2 in citric acid-Na_2HPO_4 buffer, pH 5.0), and the

exclusion of heat treatment step.

4.5 Characterizations

The UV-vis spectra were recorded using an Agilent Cary 60 UV-vis spectrophotometer. TEM images were taken using a JEOL JEM-2010 microscope operated at 200 kV. HRTEM images, HAADF-STEM images and energy dispersive X-ray (EDX) mapping were acquired using a double Cs-corrected JEOL ARM200F TEM at Brookhaven National Laboratory. The concentration of Pd, Ir, and Au ions were determined using an inductively coupled plasma-optical emission spectroscopy (ICP-OES, Perkin Elmer Optima 7000DV), which could be converted to the particle concentration of Pd seeds, Pd-Ir NPs, and Au NPs once the particle sizes and shapes had been resolved by TEM imaging. The X-ray photoelectron spectroscopy (XPS) measurements were performed on an SSX-100 system (Surface Science Laboratories, Inc.) equipped with a monochromated Al Kα X-ray source, a hemispherical sector analyzer (HSA) and a resistive anode detector. X-ray diffraction (XRD) pattern was taken using a Scintag XDS2000 powder diffractometer. Dynamic light scattering (DLS) analysis was conducted using a Photocor-FC light scattering instrument. ^{1}H NMR spectra were recorded on a Bruker AV-400 MHz high-resolution NMR spectrometer in $CDCl_3$. The absorbance of samples in microtiter plates was read using a Perkin Elmer Victor 3 1420 Multilabel Plate Reader. Microtiter plates were shaken using a Corning LSE Digital Microplate Shaker. pH values of buffer solutions were measured using an Oakton pH 700 Benchtop Meter. Photographs of samples in tubes and microplates were taken using a Canon EOS Rebel T5 digital camera.

4.6 Reference

1. Price, C. P., Newman, D. J. *Principles and practice of immunoassay, 2nd ed.*; Stockton: New York, 1997.
2. Wild, D. *The Immunoassay Handbook, 4th ed.*; Elsevier: Amsterdam, 2013.
3. Lequin, R. M. *Clin. Chem.* **2005**, *51*, 2415-2418.
4. Wick, M. R. *Ann. Diagn. Pathol.* **2012**, *16*, 71-78.
5. Cheng, C.-M.; Martinez, A. W.; Gong, J.; Mace, C. R.; Phillips, S. T.; Carrilho, E.; Mirica, K. A.; Whitesides, G. M. *Angew. Chem., Int. Ed.* **2010**, *49*, 4771-4774.
6. Chinen, A. B.; Guan, C. M.; Ferrer, J. R.; Barnaby, S. N.; Merkel, T. J.; Mirkin, C. A. *Chem. Rev.* **2015**, *115*, 10530-10574.
7. Tabakman, S. M.; Lau, L.; Robinson, J. T.; Price, J.; Sherlock, S. P.; Wang, H.; Zhang, B.; Chen, Z.; Tangsombatvisit, S.; Jarrell, J. A.; et al. *Nat. Commun.* **2011**, *2*, 466.
8. Su, L.-C.; Chen, R.-C.; Li, Y.-C.; Chang, Y.-F.; Lee, Y.-J.; Lee, C.-C.; Chou, C. *Anal. Chem.* **2010**, *82*, 3714-3718.
9. Soukka, T.; Paukkunen, J.; Härmä, H.; Lönnberg, S.; Lindroos, H.; Lövgren, T. *Clin. Chem.* **2001**, *47*, 1269-1278.
10. Kendall, C.; Ionescu-Matiu, I.; Dreesman, G. R *J. Immunol. Methods* **1983**, *56*, 329-339.
11. Leith, A. G.; Griffiths, G. D.; Green, M. A. *J. Forensic. Sci. Soc.* **1988**, *28*, 227-236.
12. Gao, Z.; Xu, M.; Hou, L.; Chen, G.; Tang, D. *Anal. Chem.* **2013**, *85*, 6945-6952.
13. Zhang, Q.; Zhao, B.; Yan, J.; Song, S.; Min, R.; Fan, C. *Anal. Chem.* **2011**, *83*, 9191-9196.
14. Ambrosi, A.; Airo, F.; Merkoçi, A. *Anal. Chem.* **2010**, *82*, 1151-1156.
15. Lin, J.; Liu, Y.; Huo, J.; Zhang, A.; Pan, Y.; Bai, H.; Jiao, Z.; Fang, T.; Wang, X.; Cai, Y.; et al. *Anal. Chem.* **2013**, *85*, 6228-6232.
16. Liu, D.; Wang, Z.; Jin, A.; Huang, X.; Sun, X.; Wang, F.; Yan, Q.; Ge, S.; Xia, N.; Niu, G.; et al. *Angew. Chem., Int. Ed.* **2013**, *52*, 14065-14069.
17. He, J.; Liu, Y.; Babu, T.; Wei, Z.; Nie, Z. *J. Am. Chem. Soc.* **2012**, *134*, 11342-11345.
18. Huang, P.; Lin, J.; Li, W.; Rong, P. F.; Wang, Z.; Wang, S.; Wang, X.; Sun, X.; Aronova, M.; Niu, G.; et al. *Angew. Chem., Int. Ed.* **2013**, *52*, 13958-13964.
19. Lin, J.; Wang, S.; Huang, P.; Wang, Z.; Chen, S.; Niu, G.; Li, W.; He, J.; Cui, D.; Lu, G.; et al. *ACS Nano* **2013**, *7*, 5320-5329.

20. Xia, X.; Zhang, J.; Lu, N.; Kim, M. J.; Ghale, K.; Xu, Y.; McKenzie, E.; Liu, J.; Ye, H. *ACS Nano* **2015**, *9*, 9994-10004.
21. Yang, T.; Ling, H.; Lamonier, J.-F.; Jaroniec, M.; Huang, J.; Monteiro, M. J.; Liu, J. *NPG Asia Materials* **2016**, *8*, e240.
22. Liu, J.; Hartono, S. B.; Liu, T.; Kantharidis, P.; Middelberg, A. P. J.; Lu, G. X.; He, L.; Qiao, S. *Biomaterials* **2012**, *33*, 970-978.
23. Mani, V.; Chikkaveeraiah, B. V.; Patel, V.; Gutkind, J. S.; Rusling, J. F. *ACS Nano* **2009**, *3*, 585-594.
24. Qian, J.; Zhang, C.; Cao, X.; Liu, S. *Anal. Chem.* **2010**, *82*, 6422-6429.
25. Grinyte, R.; Barroso, J.; Möller, M.; Saa, L.; Pavlov, V. Microbead QD-ELISA: *ACS Appl. Mater. Interfaces* **2016**, *8*, 29252-29260.
26. Xia, X.; Figueroa-Cosme, L.; Tao, J.; Peng, H.-C.; Niu, G.; Zhu, Y.; Xia, Y. *J. Am. Chem. Soc.* **2014**, *136*, 10878-10881.
27. Arblaster, J. W. *Platinum Metals Rev.* **2010**, *54*, 93-102.
28. Habas, S. E.; Lee, H.; Radmilovic, V.; Somorjai, G. A.; Yang, P. *Nat. Mater.* **2007**, *6*, 692-697.
29. Gao, L.; Zhuang, J.; Nie, L.; Zhang, J.; Zhang, Y.; Gu, N.; Wang, T.; Feng, J.; Yang, D.; Perrett, S.; et al. *Nat. Nanotechnol.* **2007**, *2*, 577-583.
30. Josephy, P. D.; Eling, T.; Mason, R. P. *J. Biol. Chem.* **1982**, *257*, 3669-3675.
31. Frey, A.; Meckelein, B.; Externest, D.; Schmidt, M. A. *J. Immunol. Methods* **2000**, *233*, 47-56.
32. He, J.; Huang, X.; Li, Y.-C.; Liu, Y.; Babu, T.; Aronova, M. A.; Wang, S.; Lu, Z.; Chen, X.; Nie, Z. *J. Am. Chem. Soc.* **2013**, *135*, 7974-7984.
33. Liu, J.; Li, Y.; He, J.; Duelge, K. J.; Lu, Z.; Nie, Z. *J. Am. Chem. Soc.* **2014**, *136*, 2602-2610.
34. Bhatt, N.; Huang, P. J.; Dave, N.; Liu, J. *Langmuir* **2011**, *27*, 6132-6137.
35. Li, F.; Zhang, H.; Dever, B.; Li, X.-F.; Le, X. C. *Bioconjugate Chem.* **2013**, *24*, 1790-1797.
36. Rissin, D. M.; Kan, C. W.; Campbell, T. G.; Howes, S. C.; Fournier, D. R.; Song, L.; Piech, T.; Patel, P. P.; Chang, L.; Rivnak, A. J.; et al. *Nat. Biotechnol.* **2010**, *28*, 595-599.
37. Laxman, B.; Morris, D. S.; Yu, J.; Siddiqui, J.; Cao, J.; Mehra, R.; Lonigro, R. J.; Tsodikov, A.; Wei, J. T.; Tomlins, S. A.; et al. *Cancer Res.* **2008**, *68*, 645-649.

38. Rica, R.; Stevens, M. M. *Nat. Nanotechnol.* **2012**, *7*, 821-824.
39. Qian, X.; Peng, X.-H.; Ansari, D. O.; Yin-Goen, Q.; Chen, G. Z.; Shin, D. M.; Yang, L.; Young, A. N.; Wang, M.; Nie, S. *Nat. Biotechnol.* **2008**, *26*, 83-90.
40. Hermanson, G. T. *Bioconjugate Techniques*; Academic Press: San Diego, CA, **1996**.
41. Porter, D. J.; Bright, H. J. *J. Biol. Chem.* **1982**, *258*, 9913-9924.
42. Armbruster, D. A.; Tillman, M. D.; Hubbs, L. M. *Clin. Chem.* **1994**, *40*, 1233-1238.
43. Armbruster, D. A.; Pry, T. *Clin. Biochem. Rev.* **2008**, *29*, S49-S52.
44. Burns, D. T.; Danzer, K.; Townshend, A. *Pure Appl. Chem.* **2002**, *74*, 2201-2205.
45. Lineweaver, H.; Burk, D. *J. Am. Chem. Soc.* **1934**, *56*, 658-666.
46. Frens, G. *Nature-Phys. Sci.* **1973**, *241*, 20-22.

CHAPTER 5 POLYVINYLPYRROLIDONE (PVP)-CAPPED PT NANOCUBES WITH SUPERIOR PEROXIDASE-LIKE ACTIVITY[a]

5.1 Introduction

Peroxidases (in many cases, HRP) are the key components in various colorimetric diagnostic and imaging technologies such as ELISA, immunohistochemistry, and western blots.[1-4] Since peroxidases are the inherent driving force for the generation of detectable color signal, their essential issues such as the poor stability and low catalytic efficiency largely limit the development and evolution of corresponding analytical technologies. To break this confinement of peroxidases, peroxidase mimics made of nanoscale particles have been actively developed over the past decade as alternatives.[5-7] Notable examples include inorganic nanomaterials made of metal oxides (*e.g.*, Fe_3O_4, CeO_2, MnO_2, and V_2O_5),[8-11] noble metals (*e.g.*, Au, Pt, Pd, and Ir),[12-15] and carbon materials (*e.g.*, carbon dots and graphene).[16-18] In contrast to their natural counterparts, peroxidase mimics are invulnerable to denaturation and protease digestion and therefore are much more stable.[5] Despite the remarkably enhanced stability, improvement in catalytic efficiency for peroxidase mimics has been met with very limited success.

The catalytic efficiencies, in terms of catalytic constant (K_{cat}, defined as the maximum number of colored molecules produced per second per catalyst[8]) of most previously reported peroxidase mimics is limited to the regime of 10^4 s^{-1}, which is only up to one order of magnitude more efficient than HRP as a model natural peroxidase ($K_{cat} = 10^3$ s^{-1}).[5, 8, 19] It is worth pointing out that, in general, the dimensions of peroxidase mimics (typically tens to hundreds nanometers in

[a]Reprinted with permission from *ChemNanoMat* **2017**, *3*, 33-38.

size) are greater than those of HRP (several nanometers in diameter[20]). In a sense, the specific catalytic efficiency ($K_{cat\text{-}specific}$, defined as the normalized K_{cat} to the total surface area of an individual catalyst) of peroxidase mimics is even lower than that of natural peroxidases. Taken together, substantially improving the catalytic efficiency of peroxidase mimics remains a grand challenge and deserves further investigation.

In this work, we report a type of highly efficient peroxidase mimic—polyvinylpyrrolidone (PVP)-capped Pt nanocubes of sub-10 nm in size. These Pt cubes show a superior peroxidase-like efficiency with K_{cat} and $K_{cat\text{-}specific}$ at the regimes of 10^5 s^{-1} and 10^3 $s^{-1}\cdot nm^{-2}$, respectively. To the best of our knowledge, this $K_{cat\text{-}specific}$ represents the record-high specific efficiency among all the existing peroxidase mimics (see **Table S5.2** in the Appendix D and the discussion below). Owing to the usage of inert Pt element, the cubes also showed excellent catalytic stabilities. The Pt cubes could be conveniently synthesized in good uniformity, controllable sizes, and large quantity. Mechanisms of nanocrystal formation and the surface properties were carefully investigated.

5.2 Results and Discussion

In a standard synthesis of the Pt cubes, a solution of $Na_2PtCl_6\cdot 6\ H_2O$ in ethylene glycol was rapidly injected (with a pipet) into a mixture containing PVP_{55} ($M_W \approx 55\ 000$) and KBr that had been preheated to 180 °C under magnetic stirring. After the addition of $Na_2PtCl_6\cdot 6\ H_2O$ for 20 min, the reaction was immediately quenched with an ice/water batch (see **Section 5.4.2** for details). **Figure 5.1a** shows typical TEM image of the Pt nanocrystals prepared with the standard procedure. It can be seen that the products were pretty uniform and showed an overall cubic shape with an average edge length of 7.35 nm. A close examination of the sample (**Figure 5.1b**) revealed that some of the nanocrystals were imperfect cubes with anisotropic truncations at the corners (the

growth mechanism will be discussed later). **Figure 5.1c** shows HRTEM image of an individual Pt cube, from which periodic lattice fringes could be clearly resolved. The lattice spacing of each group of parallel fringes was about 1.94 Å, which corresponded to the {200} planes, indicating the exposure of six {100} facets on the cube surface.[21] **Figure 5.1d** shows an X-ray diffraction (XRD) pattern of the sample. All the diffraction peaks could be indexed to the face-centered cubic (*fcc*) Pt (JCPDS no. 04-0802), confirming the elemental Pt and *fcc* crystal structure.

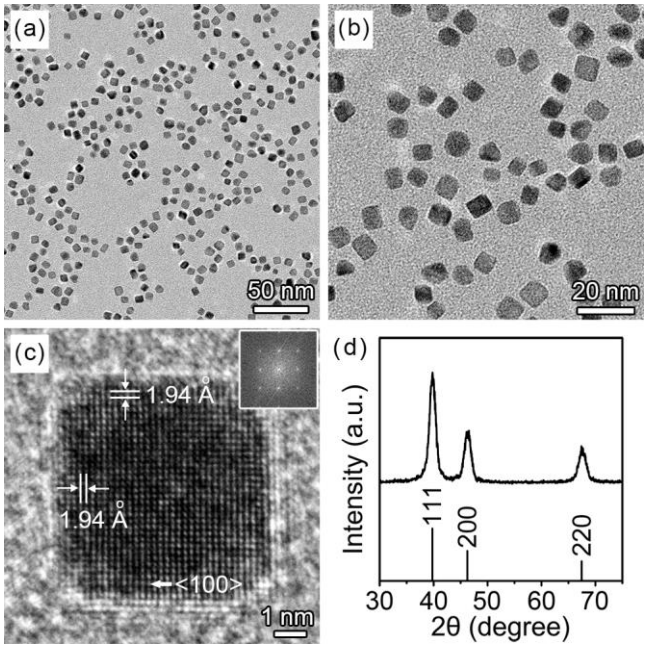

Figure 5.1 Structural analyses of PVP_{55}-capped Pt cubes prepared in a standard synthesis. (a, b) TEM images, (c) HRTEM image, and (d) XRD pattern. Inset in (c) shows the corresponding Fourier transform pattern. Black bars in (d): JCPDS no. 04-0802 (Pt).

It should be emphasized that, in previous studies, Pt cubes were typically synthesized in the presence of cetyltrimethylammonium bromide (CTAB) or tetradecyltrimethylammonium bromide (TTAB) as both the stabilizer and Pt{100} facet specific capping agent.[22-24] In this work, we used PVP_{55} as the stabilizer and ionic Br^- (from KBr) as the capping agent for Pt{100}.

Therefore, the surface property of our Pt cubes should be different from that of conventional CTAB/TTAB-capped Pt cubes. To examine chemical ligands on the surface, we conducted X-ray photoelectron spectroscopy (XPS) analysis for the Pt cubes shown in **Figure 5.1**. **Figure 5.2a** shows the XPS survey spectra of the sample deposited on silicon wafer. The observation of peaks for O 1s, N 1s, Pt 4d, C 1s and Pt 4f indicated the adsorption of PVP molecules on the surface.[25] In addition, the Br 3p peak (inset of **Figure 5.2a**) could also be seen, suggesting the presence of Br^- ions on the surfaces. **Figure 5.2b** shows high-resolution XPS spectra of the Pt 4f region, from which weak peaks of Pt^{2+} were resolved. The existence of Pt^{II} species on the surface can be ascribed to the chemisorption of Br^- ions.[26] To further confirm the adsorption of PVP on the surface of the Pt cubes, we also carried out Fourier transform infrared spectroscopy (FTIR) analysis for both the Pt cubes and pure PVP powder. As shown by **Figure S5.1** in the Appendix D, FTIR spectrum taken from the Pt cubes matched well with that of pure PVP powder. In particular, peaks for C=O and C-N stretch at 1660 cm^{-1}, C-H deformation of cyclic C-H group at 1400 cm^{-1}, and C-N stretch at 1280 cm^{-1}could be clearly observed, indicating the presence of pyrrolidone species on the Pt surface.[25, 27] In addition, the O-H stretch at 3500 cm^{-1} could be ascribed to the hydroxyl group at the terminal end of the commercially PVP.[28] Taken together, these observations demonstrate the adsorption of PVP on the Pt cube surfaces. To be more specific, we refer to these Pt cubes as the "PVP_{55}-capped Pt cubes" in the following discussion.

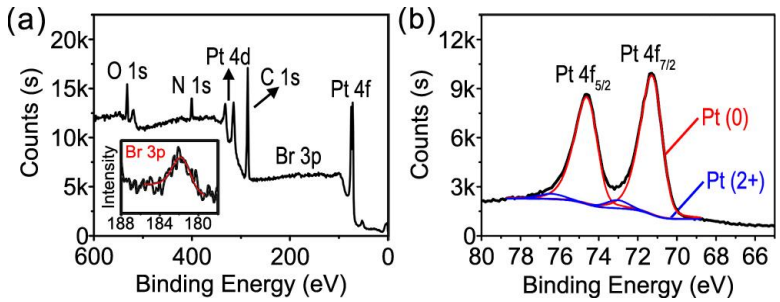

Figure 5.2 XPS analysis of the PVP_{55}-capped Pt cubes. (a) XPS survey spectra, and (b) high resolution XPS spectra of the Pt 4f region. Inset in (a) highlights the Br 3p region.

To understand the formation mechanism of the PVP_{55}-capped Pt cubes, aliquots of the reaction solution were taken from a standard synthesis at different stages and examined by TEM. In the initial stage of the reaction (t = 1.5 min, **Figure 5.3b**), nanoparticles with sizes of several nanometers were formed. HRTEM analysis (inset of **Figure 5.3b**) indicated that these nanoparticles were single-crystal Pt particles with an overall spherical shape. At t = 2.5 min (**Figure 5.3c**), the size of the nanoparticles had increased to 4-5 nm. Meanwhile, a nearly truncated octahedral or cuboctahedral shape was observed for the sample. As the reaction had proceeded to t = 5 min (**Figure 5.3d**), anisotropically truncated cubes with sizes of 5-6 nm were formed. Eventually, cubes and a small portion of anisotropically truncated cubes of ≈7 nm as the final products were obtained at t = 20 min (**Figure 5.3e**). Further extension of reaction time did not result in any obvious changes in both the size and shape. **Figure 5.3a** summarized the shape evolution during synthesis in an ideal situation: Pt atoms from the reduction of precursor first nucleated and grew into truncated octahedra or cuboctahedra enclosed by both {100} and {111} facets. The selective binding of Br^- ions to the {100} facets made these facets thermodynamically more stable than {111} facets.[29] As a result, the addition of consequent Pt atoms preferentially occurred on {111} facets, resulting in the shrinkage of {111} facets and eventually the formation

of Pt cubes mainly covered by {100} facets. The {100}-specific binding of Br^- ions was demonstrated by the result that the final product became cuboctahedra with an overall spherical shape in the absence of Br^- ions (**Figure S5.2** in Appendix D). The anisotropically truncated cubes as the byproducts might be ascribed to the relatively low rate of surface diffusion relative to atom deposition.[30-32] Since the reduction of Pt precursor and thus the deposition of Pt atoms on growing seeds was very fast in this case,[33] the Pt adatoms had no sufficient time to migrate to all the {111} facets of a seed. Those {111} facets that received fewer Pt atoms would eventually form the truncations at the corners of a cube.

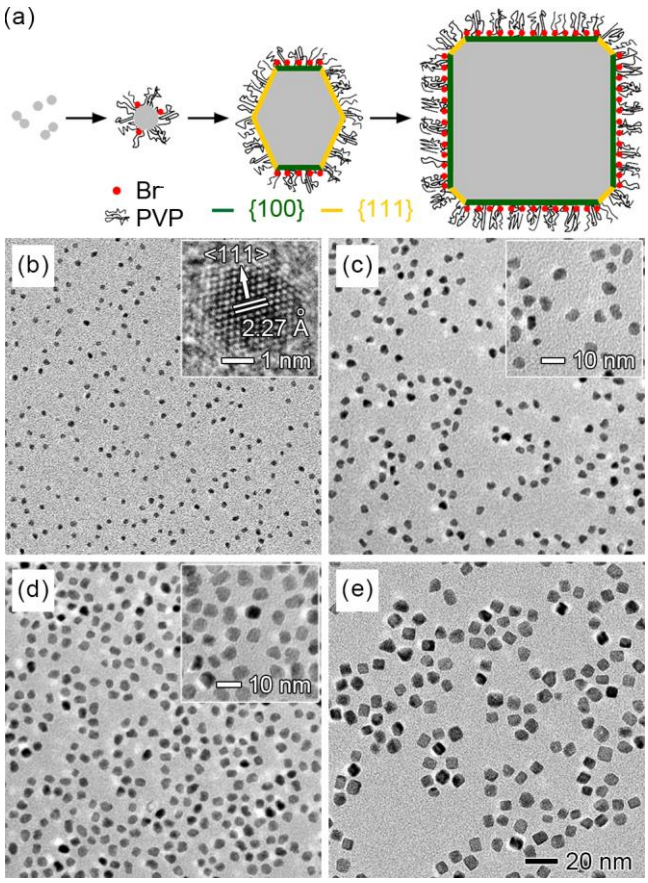

Figure 5.3 (a) Schematics illustrating the formation of PVP_{55}-capped Pt cubes. (b-e) TEM images of Pt nanocrystals obtained at different stages of a standard synthesis for the PVP_{55}-capped Pt cubes: (b) 1.5, (c) 2.5, (d) 5, and (e) 20 min. Inset in (b) is the HRTEM image of an individual Pt particle. Insets in (c) and (d) are TEM images of the same samples at higher magnification.

It is worth noting that our PVP_{55}-capped Pt cubes have several distinctive advantages over conventional CTAB/TTAB-capped Pt cubes, making them extremely suitable for industrial use: *i*) they can be synthesized in a short period. The reaction time of the PVP_{55}-capped Pt cubes is much shorter than that of CTAB/TTAB-capped Pt cubes (20 min *vs.* 6-7 hours[22-24]); *ii*) they can be produced in large quantities. As quantified by inductively coupled plasma-optical emission spectroscopy (ICP-OES), ≈ 6.7 mg of Pt cubes could be obtained in a standard synthesis. We have also demonstrated that the synthesis can be easily scaled up by ten times to reach a production of

≈67 mg per batch. As shown by the TEM images in **Figure 5.4**, sample quality was not compromised by the scale-up. In contrast, conventional CTAB/TTAB cubes could be only produced at the scale of a few milligram or less per batch;[22-24] *iii*) their size can be tuned by simply varying the amount of PVP_{55} added in the standard synthesis. For example, the sizes of PVP_{55}-capped Pt cubes could be changed to 8.16 and 6.45 nm, respectively, when 8 and 200 mg PVP_{55} (instead of 40 mg PVP_{55}) were added to the reaction solution (see **Figure 5.5**). We believe the size control is related to the reducibility of PVP molecule at high temperature.[28, 34] The reduction rate of Pt precursor and thus the number of Pt seeds formed in the initial stage will be increased by adding more PVP. Accordingly, when the amount of Pt precursor is kept the same, the size of final product will be smaller (vice versa).

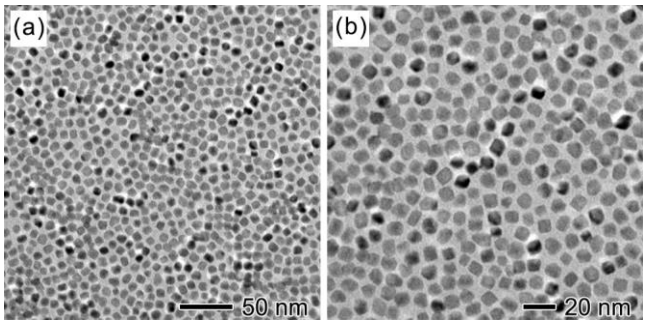

Figure 5.4 10-fold scale up synthesis of the PVP_{55}-capped Pt cubes. (a) low-magnification TEM image showing the yield and uniformity of the sample; (b) TEM image at a higher magnification showing detailed morphology of the sample.

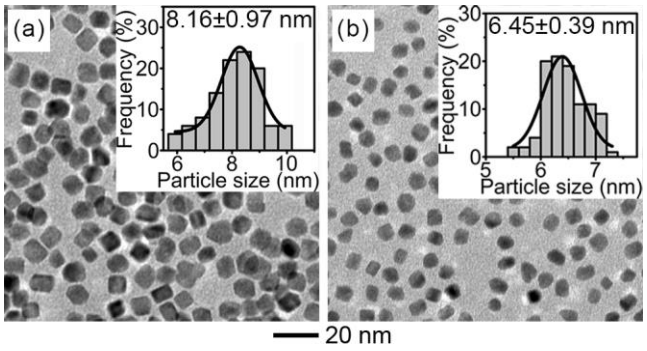

Figure 5.5 TEM images of Pt nanocrystals that were prepared using the standard procedure for PVP_{55}-capped Pt cubes shown in **Figure 5.1**, except for the variation in amount of PVP_{55}: (a) 8 and (b) 200 mg.

Peroxidase-like activity of the PVP_{55}-capped Pt cubes was determined by the apparent steady-state kinetic assay,[8, 19] in which the oxidation of TMB[35] by H_2O_2 was employed as a model catalytic reaction. All the kinetic assays were carried out at room temperature in cuvettes with path length of 1.0 cm. A UV/Vis spectrophotometer was used for determining the concentration of colored products (*e.g.*, oxidized TMB with λ_{max}=653 nm[8]) and thereby the initial reaction velocities. By plotting the initial reaction velocities against TMB concentration, a typical Michealis-Menten curve was observed (**Figure 5.4a**). This curve was then fitted to the double-reciprocal plot[36] (**Figure 5.4b**), from which the kinetic parameters listed in **Table 5.1** were derived. For comparison, we also synthesized and determined the kinetic parameters of CTAB-capped Pt cubes with an average edge length of 8.62 nm (see **Figure S5.3** in Appendix D for TEM image and FTIR analysis of these cubes). As summarized in **Table 5.1**, the K_{cat} value of the PVP_{55}-capped Pt cubes is as high as 8.16×10^5 s^{-1}, which is approximately 2 and 200-fold higher than those of CTAB-capped Pt cubes and HRP, respectively. Significantly, these PVP_{55}-capped Pt cubes exhibited a record-high specific efficiency of $K_{cat\text{-}specific}=2.52\times10^3$ $s^{-1}\cdot nm^{-2}$ among all the existing peroxidase mimics with sizes of 1-100 nm (see **Table S5.1** in Appendix D for detailed

comparison). The Michaelis constant (K_m) of the PVP_{55}-capped cubes toward TMB was close to that of HRP, suggesting that these cubes had similar binding affinity to TMB compared to HRP. It should be mentioned that the Pt cuboctahedra or spheres shown in **Figure S5.2** (Appendix D) showed a similar $K_{cat\text{-}specific}$ compared to that of the PVP_{55}-capped Pt cubes, implying that Pt(111) surface is as active as Pt(100) surface toward this catalytic reaction. In addition to the ultrahigh catalytic efficiency, we have also demonstrated the excellent chemical and thermal stabilities for the PVP_{55}-capped Pt cubes as peroxidase mimics by treating them with strong acid/base and heat up to 200 °C (**Figure 5.7**). Moreover, the catalytic activity only decreased by 6.8 % when these PVP_{55}-capped cubes had been stored in aqueous solution at room temperature for 45 days, suggesting a good storage stability of the cubes.

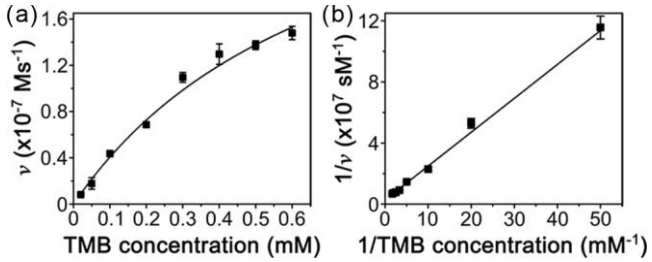

Figure 5.6 Kinetic assays of the PVP_{55}-capped Pt cubes as catalysts for the oxidation of TMB by H_2O_2. The initial reaction velocity (v) was measured in 0.2 m HOAc/NaOAc buffer, pH 4.0, containing 2.0 m H_2O_2, 4.1×10^{-13} m cubes, and TMB of different concentrations at room temperature. (a) Plot of v against TMB concentration; (b) the double-reciprocal plot generated from (A). Error bars indicate the standard deviations of three independent measurements.

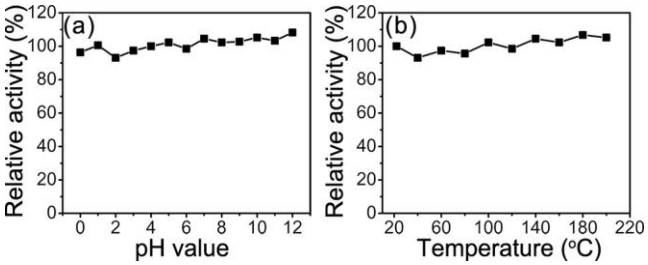

Figure 5.7 Stability test for the PVP_{55}-capped Pt cubes shown in **Figure 5.1** in catalyzing the oxidation of TMB by H_2O_2. (a) Pt cubes (4.1×10^{-13} M, in DI water) were first incubated at a range of values of pH from 0 to 12 for 2 h and then their relative catalytic activities (*e.g.*, absorbance at 653 nm of reaction solutions at t = 5min, standard conditions) were measured, in which the activity at pH 4.0 was set as 100%; (b) Pt cubes (3.1×10^{-13} M, in ethylene glycol) were first heated at a range of temperatures for 2 h and then their relative catalytic activities were measured under standard conditions, in which the activity at 22 °C was set as 100%.

Table 5.1 Comparison of kinetic parameters of various catalysts toward the oxidation of TMB by H_2O_2.

Catalyst	**Size (nm)**	**[*E*] (M)**	**K_m (M)**	**V_{max} ($M\cdot s^{-1}$)**	**K_{cat} (s^{-1})**	**$K_{cat\text{-}specific}$ ($s^{-1}\cdot nm^{-2}$)**
PVP_{55}-Pt cubes	7.35	4.1×10^{-13}	7.3×10^{-4}	3.3×10^{-7}	8.2×10^{5}	2.5×10^{3}
CTAB-Pt cubes	8.62	2.4×10^{-13}	4.2×10^{-4}	1.1×10^{-7}	4.6×10^{5}	1.0×10^{3}
PVP_{10}-Pt cubes	6.69	5.4×10^{-13}	5.2×10^{-4}	2.4×10^{-7}	4.4×10^{5}	1.6×10^{3}
PVP_{360}-Pt cubes	8.24	2.6×10^{-13}	8.1×10^{-4}	$3.0\times1^{0-7}$	1.2×10^{6}	2.8×10^{3}
HRP[8]	-	2.5×10^{-11}	4.3×10^{-4}	1.0×10^{-7}	4.0×10^{3}	-

Even though the explicit mechanism behind the superior peroxidase-like activity of the PVP_{55}-capped Pt cubes is unclear, we believe surface capping plays an important role. It has been demonstrated that CTAB tends to form a compact bilayer on the surface of Pt cubes.[37] As such,

the capping of CTAB may make the Pt surface less accessible to TMB, a large aromatic compound. In contrast, PVP is more loosely packed on Pt surface,[38] resulting in the exposure of a more active surface and thus enhanced catalytic efficiency. In this vein, we also investigated the effect of PVP chain length on the catalytic efficiency. Specifically, we evaluated both PVP_{10}- and PVP_{360}-capped Pt cubes (**Figure 5.8**) that were prepared using the standard protocol except for the substitution of PVP_{55} with PVP_{10} (M_W≈10 000) and PVP_{360}(M_W≈360 000) with the same concentration in terms of PVP repeating unit. As shown in **Table 5.1**, the values of $K_{\text{cat-specific}}$ for different PVP-capped cubes increased in the order of: PVP_{10}-capped Pt cubes<PVP_{55}-capped Pt cubes<PVP_{360}-capped Pt cubes. This trend of $K_{\text{cat-specific}}$ might be related to the packing density of PVP[39,40] on Pt cube surfaces. Specifically, the packing densities of PVP_{10}, PVP_{55}, and PVP_{360} were estimated to be 1.30, 1.19, and 0.87 nm^{-2}, respectively (**Figure 5.9** and **Table 5.2**), according to TGA analysis.[41] As PVP packing density increases, the accessibility of TMB molecules to Pt surface is expected to decrease, leading to the decrease of catalytic efficiency. Interestingly, we found that PVP packing density could barely be changed by varying the amount of certain PVP added to the reaction solution. For example, PVP packing densities of the 8.16, 7.35, and 6.45 nm PVP_{55}-Pt cubes, which were synthesized in the presence of 8, 40, and 200 mg PVP_{55}, were almost the same (**Table 5.2**). The specific catalytic activities ($K_{\text{cat-specific}}$) for these three types of PVP_{55}-Pt cubes were close to each other (**Table S5.1** in Appendix D). Taken together, these results implied that PVP packing density has a direct impact on the peroxidase-like catalytic efficiency of the PVP-capped cubes, while the effect of particle size in range of ≈6-8 nm on catalytic efficiency could be ignored. Given that the effect of surface capping on peroxidase-like activity is rarely investigated, these initial findings may serve as a foundation for inspiring future work in the field.

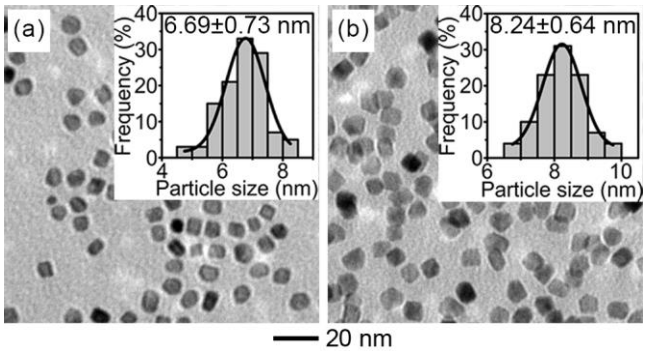

Figure 5.8 TEM images of Pt nanocrystals that were prepared using the standard procedure for PVP_{55}-capped Pt cubes shown in **Figure 5.1**, except for substitution of PVP_{55} with: (a) PVP_{10} and (b) PVP_{360}. The concentrations of different PVP in terms of repeating unit were kept the same.

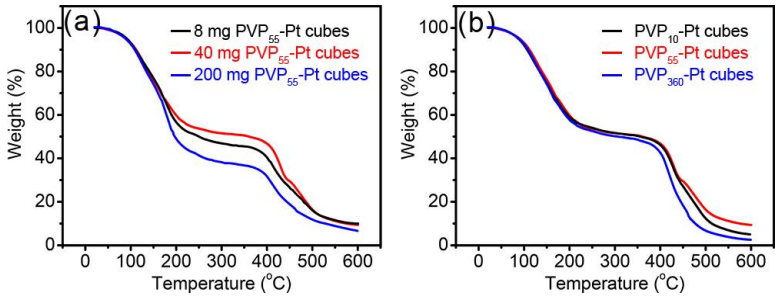

Figure 5.9 Normalized TGA curves of different (A) PVP amount and (B) PVP species capped Pt cubes. To calculate the packing density, the weight percentages (w%) at the temperature of 350, 550, and 600 °C were used.

Using the PVP_{55}-Pt cubes as an example, the w%(600 °C) = 9.50%, the w%(550 °C) = 11.30%, and w%(350 °C) =50.54%. Therefore, the mass percentage of Pt cubes is 9.50% and PVP_{55} is 39.24%. The PVP packing density (nm^{-2}) could be expressed in following equation:

$$\text{Packing density } (nm^{-2}) = \frac{\frac{\Delta w\%}{M_{PVP}} \cdot N_A}{6a^2 \cdot \frac{w_{Pt}\%}{\rho a^3}} = \frac{\frac{\Delta w\%}{M_{PVP}} \cdot N_A \cdot \rho \cdot a}{6 w_{Pt}\%}$$

where the M_{PVP} is the molecular weight (55,000 g/mol), N_A is the Avogadro's number (6.02×10^{23} mol^{-1}), ρ is the density of Pt (21.45 g/cm^3), and a is the average length of the cubes (7.35 nm). Substituting each parameter, we get the packing density for PVP_{55}-Pt cubes is 1.19 nm^{-2}.

Table 5.2 List of the TGA parameters of PVP species and Pt for different PVP-capped Pt cubes.

Sample	Size (nm)	w% (350 °C)	w% (550 °C)	Δw% (550 °C-350 °C)	w% (600 °C)	Packing density (nm^{-2})
8 mg PVP_{55}-Pt cubes	8.16	46.24%	11.39%	34.85%	9.62%	1.16
40 mg PVP_{55}-Pt cubes	7.35	50.54%	11.30%	39.24%	9.50%	1.19
200 mg PVP_{55}-Pt cubes	6.45	38.75%	8.97%	29.78%	6.44%	1.17
40 mg PVP_{10}-Pt cubes	6.69	50.23%	6.34%	43.89%	4.87%	1.30
40 mg PVP_{360}-Pt cubes	8.24	48.20%	3.63%	44.57%	2.42%	0.91

5.3 Conclusion

In summary, we have demonstrated a type of highly efficient peroxidase mimic—PVP-capped Pt cubes of sub-10 nm sizes. Distinctive features of this new mimic include record-high specific catalytic efficiency, excellent stability, good uniformity, controllable size, and facile and large quantity production. We believe that the PVP-capped Pt cubes presented here may be promising candidate of enzyme mimic for a range of applications including sensing, imaging, and detection.

5.4 Materials and Experiment

5.4.1 Chemicals and Materials

Sodium hexachloroplatinate(IV) hexahydrate ($Na_2PtCl_6 \cdot 6H_2O$, 98%), potassium tetrachloroplatinate(II) (K_2PtCl_4, 99%), potassium bromide (KBr, 99%), sodium borohydride ($NaBH_4$, ≥99%), polyvinylpyrrolidone (PVP, M_W≈10,000, 55,000, and 360,000), cetyltrimethylammonium bromide (CTAB), 3,3',5,5'-tetramethylbenzidine (TMB, >99%), hydrogen peroxide solution (wt=30% in H_2O), acetic acid (HOAc, ≥99.7%), and sodium acetate (NaOAc, ≥99%) were all obtained from Sigma-Aldrich. Ethylene glycol (EG) was obtained from J. T. Baker. All aqueous solutions were prepared using deionized (DI) water with a resistivity of 18.0 MΩ·cm.

5.4.2 Preparation of PVP_{55}-capped Pt Cubes

In a standard procedure, 3 mL of an EG solution containing 40 mg of PVP_{55} and 20 mg of KBr was hosted in a 20-mL vial and preheated to 180 °C in an oil bath under magnetic stirring for 10 min. Then, 1.0 mL of $Na_2PtCl_6 \cdot 6H_2O$ solution (20 mg/mL, in EG) was pipetted into the vial. The reaction was allowed to proceed for 20 min and cooled down immediately with an ice/water bath. The products were collected by centrifugation, washed once with acetone, twice with water, and finally redispersed in 3.2 mL of DI water for future use. The concentration of Pt element in the final product was measured to be 2.1 mg/mL by inductively coupled plasma-optical emission spectroscopy (ICP-OES).

5.4.3 Scaled-up Synthesis of the PVP_{55}-capped Pt Cubes

The 10-fold scaled up synthesis was conducted in 30 mL EG solution with 400 mg of PVP and 200 mg of KBr that was hosted in a 100-mL flask and preheated to 180 ºC in an oil bath under magnetic stirring for 10 min. Then, 10 mL of $Na_2PtCl_6 \cdot 6H_2O$ solution (20 mg/mL, in EG) was pipetted into the vial. The reaction was allowed to proceed for 20 min and cooled down immediately with an ice/water bath. The products were collected by centrifugation, washed once with acetone, twice with water, and finally redispersed in 10 mL of DI water. The concentration of Pt element in the final product was measured to be 6.7 mg/mL by ICP-OES.

5.4.4 Preparation of CTAB-capped Pt Cubes

CTAB-capped Pt cubes were prepared using a previously reported method with slight modifications.[24] In brief, 4 mL of aqueous solution containing 10 mg K_2PtCl_4 and 0.73 g CTAB was hosted in a 20-ml vial and preheated to 50 ºC in an oil bath for 5 min (the solution became clear). Then, 0.5 mL ice-cold aqueous solution of 1.35 M $NaBH_4$ was added to the vial, and the reaction was allowed to proceed for 7 h. The products were collected by centrifugation, washed twice with water, and finally redispersed in 4.0 mL of DI water.

5.4.5 Steady-state Kinetic Assays[8, 19]

All the kinetic assays were carried out at room temperature (~22 ºC) in 1.0 mL cuvettes with path length (L) of 1.0 cm. A 0.2 M NaOAc/HOAc solution (pH 4.0) was used as the reaction buffer. Final concentrations of all the PVP-capped cubes and the CTAB-capped cubes were listed in the **Tables 5.1** and **S5.1**. The rest procedure for collection of V_{max} and K_m can be found in **Chapter 3**, **Section 3.4.4**.

5.5 Characterizations

The TEM images were taken using a JEOL JEM-2010 microscope operated at 200 kV. The UV-vis spectra of the catalytic reaction solution were recorded using an Agilent Cary 60 UV-vis spectrophotometer. The X-ray photoelectron spectroscopy (XPS) measurements were performed on an SSX-100 system (Surface Science Laboratories, Inc.) equipped with a monochromated Al K_α X-ray source, a hemispherical sector analyzer (HSA) and a resistive anode detector. Fourier transform infrared spectroscopy (FTIR) spectra were measured with a Perkin Elmer, Spectrum One spectrophotometer. X-ray diffraction (XRD) pattern was taken using a Scintag XDS2000 powder diffractometer. The concentrations of Pt element from the Pt cubes were determined using an inductively coupled plasma-optical emission spectroscopy (ICP-OES, Perkin Elmer Optima 7000DV), in which Pt cubes were dissolved to Pt ions with aqua regia. Thermal Gravimetric Analysis (TGA) was carried out by using Shimadzu's TGA-50 series thermogravimetric analyzers. The thermal decomposition experiment was carried out from room temperature to 600°C at a heating rate of 10°C/min and remain at 600 °C for 30 min under N_2 flow at 20 mL/min.

5.6 Reference

1. Price, C. P.; Newman, D. J. in *Principles and Practice of Immunoassay, 2nd ed.;* Stockton, New York, **1997**.
2. Lequin, R. M. *Clin. Chem.* **2005**, *51*, 2415-2418.
3. Mahmood, T.; Yang, P.-C. *North Am. J. Med. Sci.* **2012**, *4*, 429-434.
4. Wick, M. R. *Ann. Diagn. Pathol.* **2012**, *16*, 71-78.
5. Wei, H.; Wang, E. *Chem. Soc. Rev.* **2013**, *42*, 6060-6093.
6. Lin, Y.; Ren, J.; Qu, X. *Acc. Chem. Res.* **2014**, *47*, 1097-1105.
7. Wang, X.; Guo, W.; Hu, Y.; Wu, J.; Wei, H. in *Nanoenzymes: Next Wave of Artificial Enzymes, 1st ed.;* Springer, **2016**.

8. Gao, L.; Zhuang, J.; Nie, L.; Zhang, J.; Zhang, Y.; Gu, N.; Wang, T.; Feng, J.; Yang, D.; Perrett, S.; Yan, X. *Nat. Nanotechnol.* **2007**, *2*, 577-583.
9. Mu, J.; Wang, Y.; Zhao, M.; Zhang, L. *Chem. Commun.* **2012**, *48*, 2540-2542.
10. Liu, X.; Wang, Q.; Zhao, H.; Zhang, L.; Su, Y.; Lv, Y. *Analyst* **2012**, *137*, 4552-4558.
11. André, R.; Natálio, F.; Humanes, M.; Leppin, J.; Heinze, K.; Wever, R.; Schröder, H. C.; Müller, W. E.; Tremel, W. *Adv. Funct. Mater.* **2011**, *21*, 501-509.
12. Jv, Y.; Li, B.; R. Cao, *Chem. Commun.* **2010**, *46*, 8017-8019.
13. He, W.; Wu, X.; Liu, J.; Hu, X.; Zhang, K.; Hou, S.; Zhou, W.; Xie, S. *Chem. Mater.* **2010**, *22*, 2988-2944.
14. He, W.; Liu, Y.; Yuan, J.; Yin, J.; Wu, X.; Hu, X.; Zhang, K.; Liu, J.; Chen, C.; Ji, Y.; Guo, Y. *Biomaterials* **2011**, *32*, 1139-1147.
15. Su, H.; Liu, D.; Zhao, M.; Hu, W.; Xue, S.; Cao, Q.; Le, X.; Ji, L.; Mao, Z. *ACS Appl. Mater. Inter.* **2015**, *7*, 8233-8242.
16. Shi, W.; Wang, Q.; Long, Y.; Cheng, Z.; Chen, S.; Zheng, H.; Huang, Y. *Chem. Commun.* **2011**, *47*, 6695-6697.
17. Song, Y.; Qu, K.; Zhao, C.; Ren, J.; Qu, X. *Adv. Mater.* **2010**, *22*, 2206-2210.
18. Liu, M.; Zhao, H.; Chen, S.; Yu, H.; Quan, X. *ACS Nano* **2012**, *6*, 3142-3151.
19. Xia, X.; Zhang, J.; Lu, N.; Kim, M. J.; Ghale, K.; Xu, Y.; McKenzie, E.; Liu, J.; Ye, H. *ACS Nano* **2015**, *9*, 9994-10004.
20. Gajhede, M.; Schuller, D. J.; Henriksen, A.; Smith, A. T.; Poulos, T. L. *Nat. Struct. Biol.* **1997**, *4*, 1032-1038.
21. Wang, C.; Daimon, H.; Lee, Y.; Kim, J.; Sun, S. *J. Am. Chem. Soc.* **2007**, *129*, 6974-6975.
22. Lee, H.; Habas, S. E.; Kweskin, S. J.; Butcher, D.; Somorjai, G. A.; Yang, P. *Angew. Chem.; Int. Ed.* **2006**, *45*, 7824-7828.
23. Bratlie, K. M.; Lee, H.; Komvopoulos, K.; Yang, P.; Somorjai, G. A. *Nano Lett.* **2007**, *7*, 3097-3101.
24. Ming, M.; Zhang, Y.; Gu, N. *Colloid Surf. A* **2011**, *373*, 6-10.
25. Aliaga, C.; Park, J. Y.; Yamada, Y.; Lee, H. S.; Tsung, C.-K.; Yang, P.; Somorjai, G. A. *J. Phys. Chem. C* **2009**, *113*, 6150-6155.
26. Peng, H.-C.; Xie, S.; Park, J.; Xia, X.; Xia, Y. *J. Am. Chem. Soc.* **2013**, *135*, 3780-3783.

27. Borodko, Y.; Jones, L.; Lee, H.; Frei, H.; Somorjai, G. A. *Langmuir* **2009**, *25*, 6665-6671.
28. Xiong, Y.; Washio, I.; Chen, J.; Cai, H.; Li, Z.; Xia, Y. *Langmuir* **2006**, *22*, 8563-8570.
29. Xia, X.; Zeng, J.; Zhang, Q.; Moran, C. H.; Xia, Y. *J. Phys. Chem. C* **2012**, *116*, 21647-21656.
30. Xia, X.; Xie, S.; Liu, M.; Peng, H.-C.; Lu, N.; Wang, J.; Kim, M. J.; Xia, Y. *Proc. Natl. Acad. Sci. U.S.A.* **2013**, *110*, 6669-6673.
31. Xia, Y.; Xia, X.; Peng, H.-C. *J. Am. Chem. Soc.* **2015**, *137*, 7947-7966.
32. Peng, H.-C.; Park, J.; Zhang, L.; Xia, Y. *J. Am. Chem. Soc.* **2015**, *137*, 6643-6652.
33. Xie, S.; Choi, S.-I.; Lu, N.; Roling, L. T.; Herron, J. A.; Zhang, L.; Park, J.; Wang, J.; Kim, M. J.; Xie, Z.; Mavrikakis, M. *Nano Lett.* **2014**, *14*, 3570-3576.
34. Kan, C.; Cai, W.; Li, C.; Zhang, L. *Mater. Res.* **2005**, *20*, 320-324.
35. Josephy, P. D.; Eling, T. E.; Mason, R. P. *J. Biol. Chem.* **1982**, *257*, 3669-3675.
36. Lineweaver, H.; Burk, D. *J. Am. Chem. Soc.* **1934**, *56*, 658-666.
37. Nikoobakht, B.; El-Sayed, M. A. *Langmuir* **2001**, *17*, 6368-6374.
38. Xia, X.; Yang, M.; Wang, Y.; Zheng, Y.; Li, Q.; Chen, J.; Xia, Y. *ACS Nano* **2012**, *6*, 512-522.
39. Qi, X.; Balankura, T.; Zhou, Y.; Fichthorn, K. A. *Nano Lett.* **2015**, *15*, 7711-7717.
40. Xia, X.; Zeng, J.; Otejen, L. K.; Li, Q.; Xia, Y. *J. Am. Chem. Soc.* **2012**, *134*, 1793-1801.
41. Kuhn, J. N.; Tsung, C. K.; Huang, W.; Somorjai. G. A. *J. Catal.* **2009**, *265*, 209-215.
42. Du, Y.; Yang, P.; Mou, Z.; Hua, N.; Jiang, L. *J. Appl. Ploym. Sci.* **2006**, *99*, 23-26.

CHAPTER 6 FACILE COLORIMETRIC DETECTION OF SILVER IONS WITH PICOMOLAR SENSITIVITY[a]

6.1 Introduction

With the extensive use of metallic silver (Ag) and its compounds in industries and in our daily life (*e.g.*, antimicrobial agents, catalysis, electronics, photography, and jewelry), Ag-ion-(Ag^+-) containing wastewaters have been continuously discharged into the environment over the past several decades, especially in developing countries.[1-3] As one of the most hazardous heavy-metal pollutants, Ag^+ are extremely toxic to humans at high doses.[1, 2, 4] In particular, Ag^+ can inactivate enzymes by binding to thiol, amino, and carboxyl groups and/or displacing other essential metal ions in functional enzymes, thereby seriously disrupting biological systems.[2-4] According to the Secondary Drinking Water Standards of the U.S. Environmental Protection Agency (EPA), the maximum permissible level of Ag^+ in drinking water systems is 0.1 $mg \cdot L^{-1}$ (or 0.93 μM). Consequently, the development of sensitive analytical methods for accurately detecting trace Ag^+ is of paramount importance for water quality control, public health, and environmental monitoring.

Typical sensitive techniques for Ag^+ detection include atomic absorption spectrometry (AAS), inductively coupled plasma-mass spectrometry and -optical emission spectrometry (ICP-MS and -OES, respectively), fluorescence spectroscopy, and voltammetry.[1-5] Nevertheless, these

[a]Reprinted with permission from *Anal. Chem.* **2017**, *89*, 3622-3629

Haihang Ye contributed the conception and design of the related work, acquisition and interpretation of data, and preparation of the article.

techniques generally require sophisticated instruments, complicated protocols, and skilled operators. Such requirements greatly limit practical applications of these techniques, especially in resource-limited areas such as remote villages. In contrast, colorimetric methods are broadly recognized as a type of simple and cost-effective technique for Ag^+ detection because they can be easily performed by less-trained personnel with an inexpensive spectrophotometer or even the naked eye.[6-18] The most notable approach in the colorimetric detection of Ag^+ is to utilize plasmonic Au or Ag nanoparticles because of their relatively high detection sensitivity.[9, 12-14, 16, 18] Owing to their large extinction coefficients (which are several orders of magnitude higher than those of conventional organic dyes),[19, 20] Au and Ag nanoparticles can display distinct color changes through Ag^+-triggered changes in interparticle distance or morphology and thereby achieve relatively sensitive detection of Ag^+. For instance, Tseng and co-workers modified the surface of citrate-capped Au nanoparticles with Tween 20 as a stabilizer.[9] The reduction of Ag^+ by the citrate ions led to the deposition of Ag on the Au particle surfaces, displacing the Tween 20. The displacement of Tween 20 triggered a red-to-blue color change of the Au nanoparticles because the particles tended to aggregate without the stabilization provided by Tween 20. This colorimetric method could detect Ag^+ at concentrations as low as 100 nM. Using the same Tween 20-stabilized Au nanoparticles, Chen and co-workers designed a reverse color change system (*e.g.*, blue-to-red) for Ag^+ detection by harnessing the ion-redox-modulated surface chemistry, achieving a detection limit of 10 nM.[13] Similarly to Tween 20, Ag^+-responsive cytosine- (C-) enriched single-stranded DNA was also used to stabilize Au nanoparticles.[18] In the presence of Ag^+ , double-stranded structures of C-Ag^+-C base pairs formed that compromised the stability of the Au nanoparticles, leading to a red-to-blue color change. Despite these demonstrations, the

bottleneck for current colorimetric methods remains the low detection sensitivity (confined to the nanomolar level) relative to that of the aforementioned sophisticated instrument-based techniques.

In this work, we demonstrate a novel strategy to break this restriction of low detection sensitivity for colorimetric Ag^+ detection. In this strategy, instead of relying on the plasmonic properties of Au or Ag nanoparticles, we take advantage of the excellent peroxidase-like activity of a unique type of Pt nanoparticles (PVP-capped Pt cubes[21]) as reported in **Chapter 5**. Specifically, Ag^+ were found to be able to specifically and strongly bind to the surfaces of such PVP-capped Pt cubes, leading to the inhibition of their peroxidase-like activity that could be easily monitored with a UV-vis spectrophotometer. This new strategy could push the detection limit of colorimetric methods into the picomolar (pM) range, which is even lower than those of fluorescent methods (see **Table S6.1** in Appendix E). Significantly, the method reported herein is quite simple and rapid. The detection was conducted at room temperature in an aqueous system, and the entire procedure required only ~6 min. These distinctive features make this approach extremely suitable for on-site Ag^+ detection.

6.2 Results and Discussion

6.2.1 Detection Principle

As shown in **Figure 6.1a**, the detection method relies on the high peroxidase-like catalytic activity of PVP-capped Pt cubes and the specific inhibition toward the catalytic activity by Ag^+. As demonstrated, the PVP-capped Pt cubes exhibit excellent peroxidase-like activity with an area-specific catalytic efficiency (in terms of $K_{\text{cat-specific}}$, which is defined as the maximum number of reaction products generated per second per unit surface area of catalyst[23]) as high as 2.5×10^3 s^-

[1]·nm[-2].[21] These cubes can efficiently catalyze the oxidation of TMB[24, 25] by H_2O_2, generating an intense blue-colored signal. In the presence of Ag^+, the surfaces of the cubes are specifically and strongly passivated by Ag^+ through adsorption, thereby inhibiting the generation of the colored signal. The more Ag^+ in the system, the weaker the colored signal generated by the catalytic reaction. As such, the concentration of Ag^+ can be conveniently determined by measuring the absorbance of the catalytic reaction solution using a UV-vis spectrometer. Alternatively, qualitative detection can be achieved with the naked eye.

6.2.2 Characterization of PVP-Capped Pt Cubes

Figure 6.1b shows a representative TEM image of the PVP-capped Pt cubes from a standard synthesis. Our analyses of 200 random particles indicated that ~80% of particles displayed well-defined cubic shapes, and the average edge length of the cubes was measured to be 7.3 nm with a narrow size distribution (0.6-nm standard deviation). The high-resolution TEM image of an individual cube (inset in **Figure 6.1b**) clearly shows the corresponding lattice fringes and {100}-covered side faces. The lattice fringe spacing of 1.9 Å can be indexed to the {200} reflections of face-centered-cubic (*fcc*) Pt.[26] These TEM results demonstrate the successful preparation, with a relatively high yield and good uniformity, of PVP-capped Pt cubes, which formed the basis for the subsequent design and experiments.

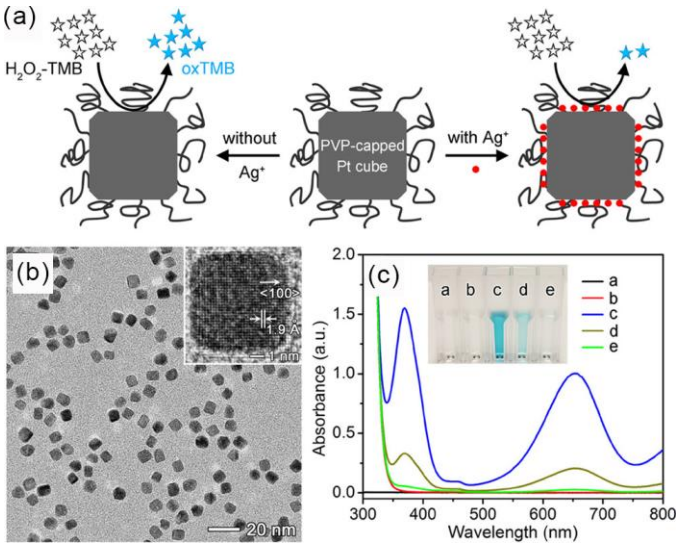

Figure 6.1 PVP-capped Pt cubes for the colorimetric detection of Ag^+. (a) Schematic of the detection principle. (b) TEM image of PVP-capped Pt cubes. Inset: HRTEM image of an individual Pt cube. (c) Photographs and corresponding UV-vis spectra of solutions in cuvettes containing **a**) PVP-capped Pt cubes (~3.78×10^{10} particles/mL), **b**) TMB-H_2O_2, **c**) PVP-capped Pt cubes + TMB-H_2O_2, **d**) 50 nM $AgNO_3$ + PVP-capped Pt cubes + TMB-H_2O_2, and **e**) 10 μM $AgNO_3$ + PVP-capped Pt cubes + TMB-H_2O_2.

6.2.3 Demonstration of Detection Feasibility

We started with the feasibility demonstration of as-proposed colorimetric method for Ag^+ detection by involving Ag^+ into the PVP-capped Pt cubes catalyzed reaction (*e.g.*, oxidation of TMB by H_2O_2). As shown in **Figure 6.1c**, neither the PVP-capped Pt cubes as catalysts at a low concentration (*e.g.*, 3.78×10^{10} particles/mL, trace **a**) nor the TMB-H_2O_2 solution (trace **b**) exhibited a distinguishable color. Only a mixture of the PVP-capped Pt cubes with the TMB-H_2O_2 solution yielded a blue-colored solution with a maximum absorbance at 653 nm ($A_{653\,nm} \approx 1.0$, trace **c**), which is the characteristic peak of oxidized TMB.[24, 25] These observations confirmed the high peroxidase-like activity of the PVP-capped Pt cubes. Interestingly, when PVP-capped Pt cubes were incubated with a colorless Ag^+ solution of 50 nM for 40 s before being mixed with the

TMB-H_2O_2 solution, the intensity of the blue color of the final reaction solution decreased significantly ($A_{653\,nm} \approx 0.21$, trace **d**). Increasing the Ag^+ concentration further decreased the intensity of the blue color. At 10 μM Ag^+, the reaction solution was almost colorless ($A_{653\,nm} \approx 0.026$, trace **e**). These results imply that Ag^+ can effectively inhibit the peroxidase-like activity of PVP-capped Pt cubes. To single out the role of the Ag^+, we conducted additional control experiments by replacing 50 nM $AgNO_3$ in the trace **c** experiment with 50 nM $NaNO_3$ and CF_3COOAg. As shown in **Figure 6.2**, the peroxidase-like activity of the PVP-capped Pt cubes remained unchanged ($A_{653\,nm} = 0.99$) after they had been treated with $NaNO_3$. In contrast, the activity of the PVP-capped Pt cubes decreased to a significant extent similar to what was observed for 50 nM $AgNO_3$ ($A_{653\,nm} = 0.19$) after the cubes were mixed with CF_3COOAg. These data verified that the inhibition of the catalytic activity of Pt cubes was specifically attributable to the Ag^+. Taken together, this set of experiments demonstrated the feasibility of the proposed colorimetric method for Ag^+ detection.

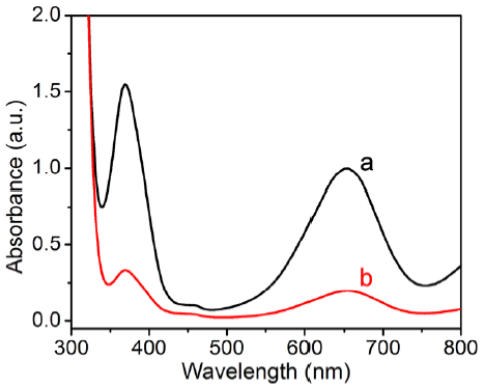

Figure 6.2 UV-vis spectra taken from reaction solutions in cuvettes containing: (a) 50 nM $NaNO_3$ + PVP-capped Pt cubes + (H_2O_2-TMB); and (b) 50 nM CF_3COOAg + PVP-capped Pt cubes + (H_2O_2-TMB). Reaction conditions were kept the same as those in standard Ag^+ detection procedure except for the substitution of $AgNO_3$ with $NaNO_3$ or CF_3COOAg.

6.2.4 Sensitivity and Reproducibility

We then evaluated the detection sensitivity and reproducibility of the proposed colorimetric method. The detection was quite simple and straightforward. In a standard procedure, the PVP-capped Pt cubes were incubated with Ag^+ standard or sample in a buffer solution held in a cuvette for a short period of time before being mixed with TMB-H_2O_2 solution. After several minutes of reaction, the final reaction solution was subjected to examination with a UV-vis spectrometer, a camera, or the naked eye. Based on the systematic examination of various experimental parameters (**Figure 6.3**), the optimal conditions for Ag^+ detection were found to be (*i*) room temperature (~22 °C) for the entire process, (*ii*) a pH value of 6.0 and an incubation time of 40 s for the incubation of Ag^+ standards/samples with Pt cubes, (*iii*) 0.8 mM TMB plus 2.0 M H_2O_2 for the TMB-H_2O_2 solution,[21, 23] and (*iv*) t = 5 min for the catalytic reaction. Under these conditions, the detection was conducted at room temperature and in aqueous solution, and the entire procedure required only ~6 min.

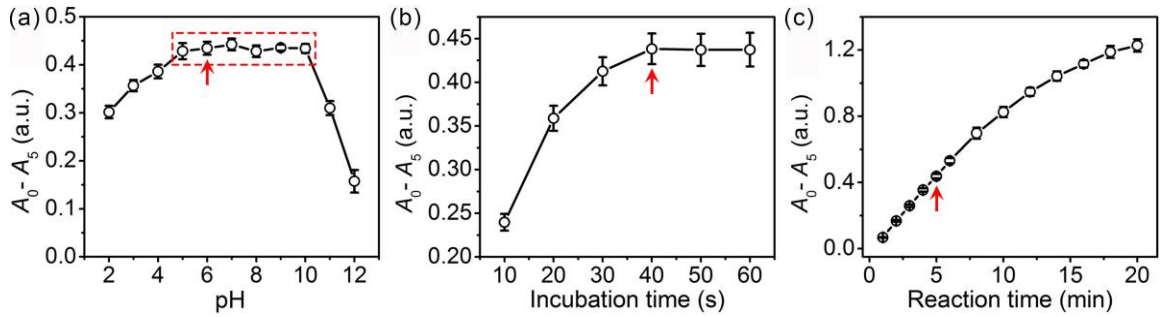

Figure 6.3 Optimization of experimental conditions for the detection of Ag^+ ions with the proposed colorimetric method. Effects of: (a) buffer pH value for the solution system in which Ag^+ and PVP-capped Pt cubes were mixed; (b) incubation time for Ag^+ and PVP-capped Pt cubes, and (c) reaction time for the PVP-capped Pt cubes catalyzed reaction (e.g., oxidation of TMB by H_2O_2). In all experiments, 5 nM Ag^+ standard was chosen as a model sample for optimization of the detection system. To make the proposed method more applicable for environmental scenarios, room temperature (~22 °C) was selected as the operational temperature for all measurements and incubations throughout the experiment. All other conditions were kept the same as those in the standard detection procedure. Error bars represent the standard deviations of six independent measurements (n = 6). Red arrows indicate the optimized parameters.

Figure 6.4a shows photographs of cuvettes containing final reaction solutions with Ag^+ standards ranging in concentration from 0 to 10000 nM. It can be seen that the solutions displayed a continuous color change from deep blue to light blue and eventually to nearly colorless. Qualitative analysis with the naked eye could achieve a detection limit of ~5 nM Ag^+. The detection results could be conveniently quantified with the aid of an ordinary UV-vis spectrometer. As shown in **Figure 6.4b**, **c**, a proportional decrease in the absorbance of the reaction solutions at 653 nm as a function of the concentration of Ag^+ was clearly seen. By plotting the decrease in absorbance ($A_0 - A_x$, where A_0 and A_x denote the absorbances at 653 nm of the blank solution and the Ag^+ standard of x nM, respectively) against the Ag^+ concentration, calibration curves for Ag^+ were generated (see **Figure 6.4d, e**). As indicated by **Figure 6.4d**, the colored signal could be

differentiated for Ag^+ in the range of 0.01-10000 nM (6 orders of magnitude), suggesting a wide response range of the colorimetric method toward Ag^+. As shown in **Figure 6.4e**, a high-quality linear relationship (R^2 = 0.998) in the range of 0.1-1 nM Ag^+ was observed. The limit of detection (LOD, defined as the concentration corresponding to a signal that is 3 times the standard deviation above the zero-calibration point[27]) was calculated to be 80 pM. The coefficients of variation across the entire concentration range were between 0.13% and 7.64% (n = 6), indicating a good reproducibility of the method.

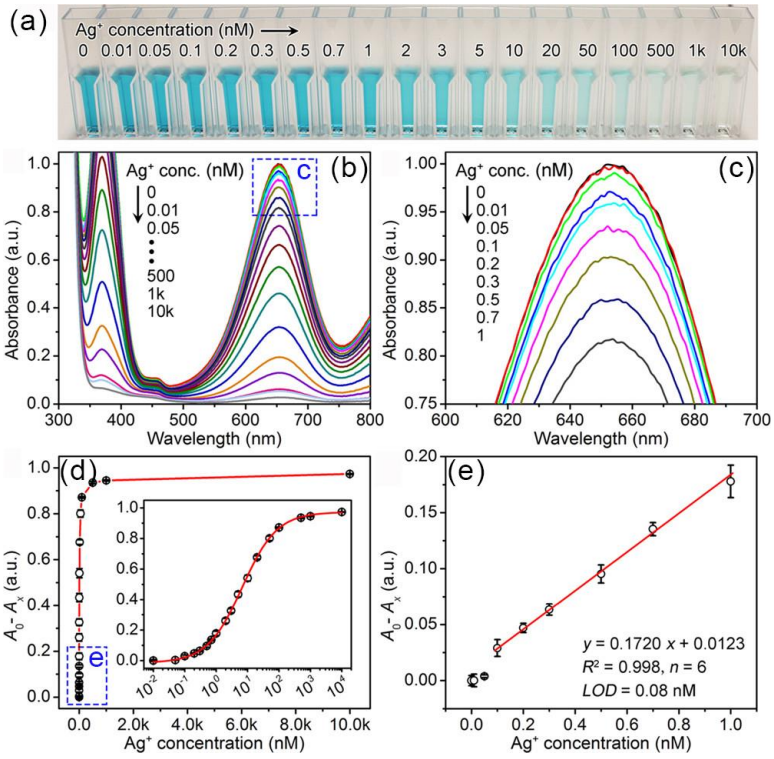

Figure 6.4 (a) Photographs showing the final reaction solutions with different Ag^+ standards in cuvettes. (b) Corresponding UV-vis spectra of the samples shown in panel a. (c) Magnified UV-vis spectra of the region marked by a blue box in panel b. (d) Calibration curve generated by plotting the decrease of the absorbance at 653 nm relative to that of the blank for the reaction solutions ($A_0 - A_x$) as a function of the Ag^+ concentration. Inset: Same plot on a logarithmic scale.

(e) Linear region of the calibration curve shown in panel d. In panel d and e, the error bars represent the standard deviations of six independent

We also investigated the effect of particle size on the detection performance. To this end, in addition to the 7.3-nm Pt cubes shown in **Figure 6.1**, we prepared PVP-capped Pt cubes of two other sizes (*e.g.*, 6.2 and 9.5 nm; see **Figure 6.5a**, **b**) by simply varying the amount of PVP in the standard synthesis. As shown in **Figure 6.5c**, we found that particle size in range of ~6.2-9.5 nm has no distinct impact on the detection performance.

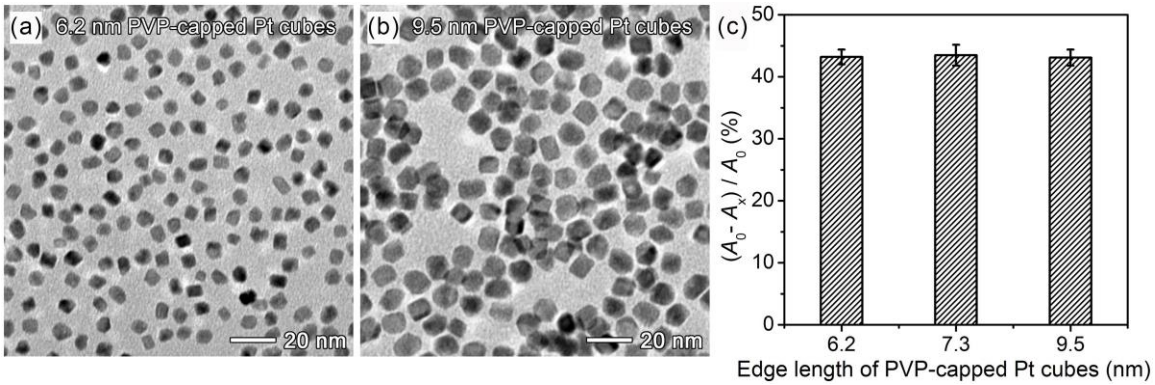

Figure 6.5 (a, b) TEM images of PVP-capped Pt cubes with average edge lengths of (a) 6.2 nm and (b) 9.5 nm. (c) Inhibition efficiencies of Ag^+ toward the peroxidase-like activities of PVP-capped Pt cubes of various edge lengths: 6.2 nm, 7.3 nm (sample in **Figure 6.1**), and 9.5 nm. In (c), A_0 and A_x are the absorbances at 653 nm of reaction solutions catalyzed by certain Pt cubes before and after incubation with 5 nM Ag^+, respectively. The concentrations of Pt cubes were set to certain values at which A_0 for all the cubes was normalized to ~1.0. Error bar represents the standard deviation of three independent measurements (n = 3).

To highlight the distinctive advantages of our method, we compared its analytical performance with those of previously reported methods for Ag^+ detection. As summarized in **Table 6.1**, our method exhibited a record-high detection sensitivity (LOD = 80 pM) among all of the existing colorimetric methods. Significantly, it was even more sensitive than most

fluorescence methods reported in the literature (**Table S6.1** in Appendix E). In addition, the entire detection time of our method was only ~6 min, making it faster than most of the reported methods. Moreover, our method is cost-effective because of the use of a tiny amount of Pt cubes (~3×10^{-9} g of Pt per test) and ordinary reagents such as TMB and H_2O_2. The materials cost for each test was estimated to be less than US$0.1.

The ultrahigh detection sensitivity of our colorimetric method can be ascribed to the outstanding catalytic activity of the Pt cubes and the efficient inhibition of Ag^+ toward the catalysis (as discussed later), which together led to an amplified signal diminishment process. The magnitude of signal diminishment of the system could be quantified by comparing the amount of Ag^+ in the system with the extent of the decrease of colored products relative to the amount in the blank sample (*e.g.*, without Ag^+). Taking the detection of 0.5 nM Ag^+ (in a volume of 590 μL) as an example, the presence of 2.95×10^{-13} mol of Ag^+ was found to correspond to a decrease of 2.45×10^{-9} mol of oxidized TMB molecules (which was calculated based on their absorbance and molar absorption coefficient[25]), suggesting a signal amplification of approximately 4 orders of magnitude by the detection system.

Table 6.1 Comparison of analytical performances of various colorimetric methods for Ag^+ detection

Detection probes	LOD (nM)	Assay time (min)	Ref
BSA-stabilized Au clusters	204	10	8
Tween 20-Au nanoparticles	100	5	9
G-quadruplex-hemin DNAzyme	64	110	10
3,3′,5,5′-tetramethylbenzidine	50	30	11
Core-shell Au nanoparticles	10	15	12
Tween 20-Au nanoparticles	10	33	13
Au-Ag core-shell nanoparticles	8.76	4	14
G-quadruplex-hemin DNAzyme	6.3	110	15
N-1-(2-mercaptoethyl)adenine-Au nanoparticles	3.3	20	16
DNAzyme switch	2.5	4	17
DNA-Au nanoparticles	0.59	32	18
PVP-capped Pt cubes	0.08	6	This work

[a]LOD = limit of detection.

6.2.5 Specificity Test

We also evaluated the specificity of our method toward other ionic species. Common cations (NH_4^+, Na^+, K^+, Li^+, Ba^{2+}, Ca^{2+}, Cd^{2+}, Co^{2+}, Cu^{2+}, Fe^{2+}, Mg^{2+}, Mn^{2+}, Ni^{2+}, Pb^{2+}, Zn^{2+}, Al^{3+}, Cr^{3+}, Fe^{3+}, Cu^+, Pd^{2+}, and Hg^{2+}) and anions ($F^–$, $Cl^–$, $Br^–$, $NO_3^–$, $Ac^–$, $SO_3^{2–}$, $SO_4^{2–}$, $CO_3^{2–}$, and $PO_4^{3–}$) as interfering ions were tested using the standard procedure. Note that Ag^+ was not included among these interfering ions. DI water and 5 nM Ag^+ solution as the blank and control,

respectively, were also tested. As shown in **Figure 6.6**, a significant decrease in absorbance at 653 nm relative to the blank was observed with Ag^+, whereas no distinct change in the absorbance was seen for any of the interfering ions except for Pd^{2+} and Hg^{2+}. Nevertheless, the extents to which the absorbance was decreased for Pd^{2+} and Hg^{2+} were much lower than that for Ag^+. These results indicate the relatively good specificity of the colorimetric method for detecting Ag^+.

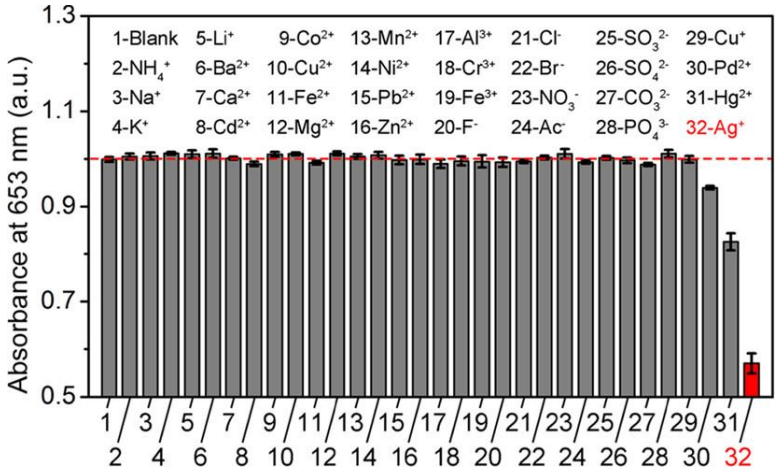

Figure 6.6 Specificity test of the developed colorimetric method. Intensities of the absorbance at 653 nm were recorded from reaction solutions containing various ionic species using the standard procedure for Ag^+ detection. The numbers under each bar correspond to the ions indicated by the same numbers. Blank (sample 1) denotes DI water. The ionic concentrations for samples 2-28 and samples 29-32 were 50 and 5 nM, respectively. The error bars represent the standard deviations of three independent measurements (n = 3).

6.2.6 Demonstration of Real Sample Detection

To demonstrate the potential use of the proposed method in environmental scenarios, tap-water samples (from the faucet in our laboratory) spiked with Ag^+ were analyzed. It should be mentioned that the original tap water was free of Ag^+, as confirmed by ICP-OES analysis. Specifically, 12 Ag^+-spiked tap-water samples with Ag^+ concentrations in the range of 0.4-100 nM

were analyzed using the standard procedure. The Ag^+ in each sample were quantified based on the calibration curve shown in **Figure 6.2e**. Note that samples with high Ag^+ concentrations were diluted to fall within the linear detection range (*e.g.*, 0.1-1 nM). The detection results are summarized in **Figure 6.7** and **Table 6.2**. A strong positive correlation between the spiked Ag^+ concentrations and the found Ag^+ concentrations was observed, with a slope of 0.9720 and an intercept of 0.0225, which are close to the ideal values of 1 and 0, respectively. The recoveries of all of the samples were between 93.7% and 108.6%. The coefficients of variation for the quantification were in the range of 5.8-12.6% (n = 3). These data demonstrate the capability of the proposed method to detect Ag^+ in real-life samples.

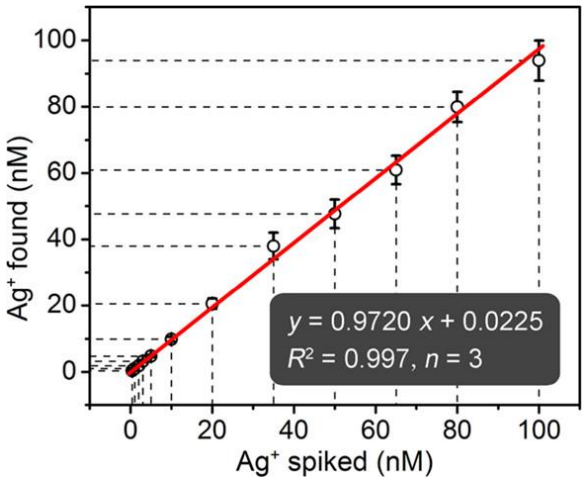

Figure 6.7 Correlation analysis between the Ag^+ concentrations in 12 Ag^+-spiked tap-water samples and the Ag^+ concentrations found by the developed colorimetric method. The error bars represent the standard deviations of three independent measurements (n = 3). Quantitative data and the recovery of each sample are summarized in **Table 6.2**.

Table 6.2 Summary of the detection of Ag^+ from spiked tap-water samples as shown in **Figure 6.7**.

Sample no.	Spiked concentration (nM)	Found concentration [mean ± SD[a] (*n* = 3)] (nM)	CV[b] (%)	Recovery[c] (%)
1	0.4	0.41 ± 0.04	9.8	104.1
2	1	1.03 ± 0.13	12.6	103.4
3	2	1.91 ± 0.12	6.3	95.5
4	3	3.26 ± 0.32	9.8	108.6
5	5	4.80 ± 0.39	8.1	95.9
6	10	9.86 ± 0.71	7.2	98.6
7	20	20.6 ± 1.5	7.3	102.8
8	35	38.0 ± 4.0	10.5	108.4
9	50	47.6 ± 4.3	9.0	95.2
10	65	60.9 ± 4.3	7.1	93.7
11	80	79.9 ± 4.6	5.8	99.9
12	100	93.9 ± 6.0	6.4	93.9

[a]SD = standard deviation. [b]CV = coefficient of variation.

[c]Recovery is defined as the amount of Ag^+ found divided by the amount of Ag^+ originally spiked in the sample.

6.2.7 Mechanistic Understanding

Finally, we designed and conducted a set of experiments in an attempt to gain insight into the mechanism behind the detection. Because the peroxidase-like catalytic property of PVP-capped Pt cubes was elaborated in our recent work,[21] the focus in this case was on understanding how Ag^+ inhibits the catalytic activity. We first performed XPS analysis to characterize the surfaces of the PVP-capped Pt cubes before and after they had been incubated with Ag^+. It should be noted that, after incubation with an excess amount of Ag^+, the Pt cubes were centrifuged and washed with DI water 10 times to remove free Ag^+ in the solution. **Figure 6.8a** shows XPS survey spectra of the Pt cubes before and after Ag^+ incubation. The peaks for Pt 4f, C 1s, Pt 4d, N 1s, and O 1s at specific positions can be seen in the spectrum of the initial Pt cubes, confirming the presence of PVP molecules on the Pt cube surface.[28] For the cubes after incubation with Ag^+, in addition to the characteristic peaks of PVP and Pt, peaks for Ag 3d were clearly observed,[29] indicating the adsorption of Ag^+ on the surface. Therefore, we assume that the binding of Ag^+ prevented TMB and/or H_2O_2 from accessing the Pt surfaces and, thus, inhibited the catalytic activity of the Pt cubes. It should be pointed out that the peak positions and relative intensities of the peaks for PVP and Pt remained essentially unchanged after Ag^+ adsorption, implying that the Ag^+ did not extensively react with or replace PVP molecules on the cube surface. **Figure 6.8b, c** show high-resolution XPS spectra of the Pt 4f region for both Pt cube samples. No significant difference can be observed between the two spectra, indicating a very weak chemical interaction between the adsorbed Ag^+ ions and Pt surface. **Figure 6.8d** shows a high-resolution XPS spectrum of the Ag 3d region for the cubes after Ag^+ incubation, in which only Ag^+ peaks can be resolved.[29] This observation indicates the presence of only Ag(I) species

on the surface and further confirmed that almost no chemical reactions occurred between Ag^+ and PVP/Pt during the adsorption of the Ag^+.

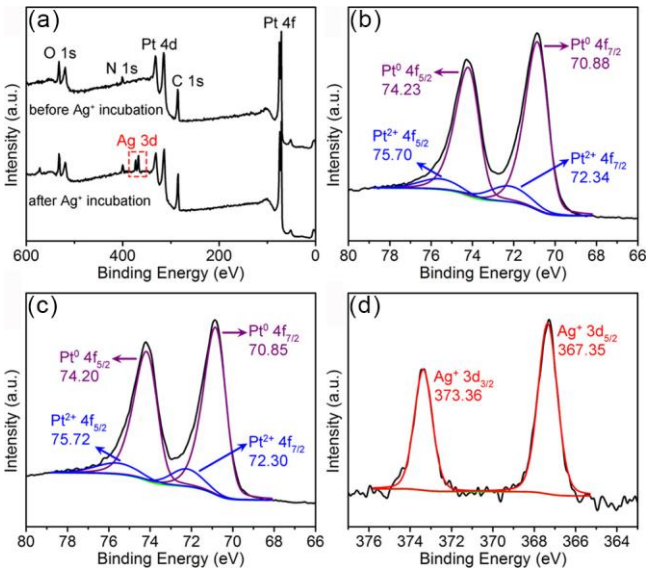

Figure 6.8 XPS analyses of the PVP-capped Pt cubes before and after incubation with Ag^+. (a) XPS survey spectra of both samples. (b, c) Pt 4f XPS spectra of the Pt cubes (b) before and (c) after incubation with Ag^+. (d) Ag 3d XPS spectrum of the Pt cubes after incubation with Ag^+.

To better understand the adsorption of Ag^+ on the PVP-capped Pt cubes, we conducted a comparison study by testing the efficiencies of Ag^+ ions in inhibiting the peroxidase-like activities of several other sub-10-nm nanostructures. These nanostructures included 6.5-nm PVP-capped Pt nanospheres (**Figure 6.9a**), 5.0-nm citrate-capped Pt nanospheres (**Figure 6.9b**),[22] 5.9-nm PVP-capped Pd nanocubes (**Figure 6.9c**),[23] and 4.5-nm PVP-capped Au nanospheres (**Figure 6.9d**). The nanostructures were first incubated with Ag^+ and then utilized as catalysts for the oxidation of TMB by H_2O_2 using the standard procedure for PVP-capped Pt cubes, in which the ratio of Ag^+ to total surface area of each nanostructure was kept the same. The inhibition efficiency of Ag^+ toward the catalytic activity was calculated as $(A_0 - A_x)/A_0$, where A_0 and A_x are the absorbances at 653 nm of the reaction solutions catalyzed by the nanostructures before and after

incubation with Ag^+, respectively. Herein, the concentrations of the nanostructures were set to certain values such that A_0 for all of the nanostructures was normalized to ~1.0. **Figure 6.9e** compares the inhibition efficiencies of Ag^+ toward the various nanostructures. It can be seen that the inhibition efficiency of Ag^+ toward the PVP-capped Pt spheres was almost the same as that toward the PVP-capped Pt cubes. This result indicates that the Pt{100} facet of the Pt cubes is not the determinative factor in the adsorption of Ag^+ because the Pt spheres were encased by a combination of Pt{100} and Pt{111} facets.[30, 31] In this regard, the performance of the PVP-capped Pt spheres is expected to be as good as that of the PVP-capped Pt cubes in practical detection. In the present study, we focused on Pt cubes for demonstration mainly because they are more uniform in terms of both shape and size than Pt spheres, which makes it convenient to gain a quantitative understanding of the detection mechanism. In contrast, the inhibition efficiency toward the citrate-capped Pt spheres was much lower than that toward the PVP-capped Pt cubes or spheres (see **Figure 6.9e**), suggesting that PVP plays an important role in facilitating the adsorption of Ag^+.[32-35] Based on these results, we hypothesize that the strong adsorption of Ag^+ on the PVP-capped Pt cubes can be ascribed to the synergistic effect of the *fcc* crystal structure of Pt and PVP. In particular, a good match in geometry between Ag^+ and the *fcc* structure of Pt might promote the Ag^+ adsorption.[36] This argument is supported by the facts that (*i*) a similar inhibition efficiency of Ag^+ was observed for PVP-capped cubes made of Pd (**Figure 6.9e**), whose lattice constant is almost the same as that of Pt (<1% in lattice mismatch[37, 38]), and (*ii*) Ag^+ did not inhibit the peroxidase-like activity of PVP-capped Au nanospheres (**Figure 6.9e**). Note that the lattice mismatch between Pt and Au is as large as 3.8%.[39] In addition, this argument is, to some extent, also supported by the data shown in **Figure 6.6**. In particular, Hg^{2+} could also inhibit the peroxidase-like activity of PVP-capped Pt cubes even though its inhibition efficiency was lower

than that of Ag^+. This observation might be due to the fact that the ionic radius of Hg^{2+} is similar to that of Ag^+ (0.126 nm *vs.* 0.110 nm),[40, 41] which ensures a relatively good match between Hg^{2+} and the Pt *fcc* structure. To further demonstrate this synergistic effect, we carried out another control experiment in which the same amount of Ag^+ was preincubated with excess PVP and then used to inhibit the catalytic activity of PVP-capped Pt cubes (**Figure 6.9f**). Interestingly, the inhibition efficiency of Ag^+ was almost the same as that of the case without the preincubation with free PVP. This result suggests that free PVP barely binds to Ag^+ and that only the combination of PVP and the Pt surface can induce the strong adsorption of Ag^+.

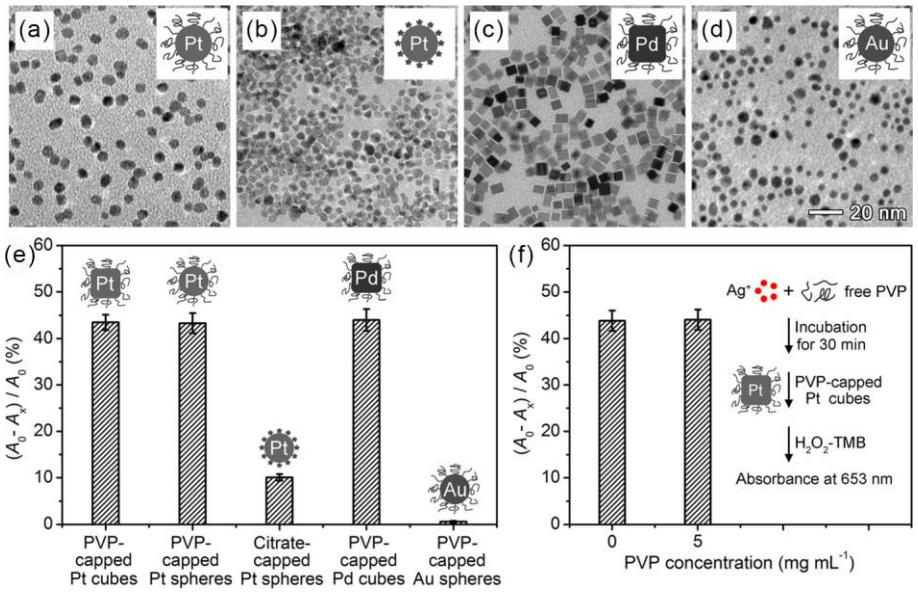

Figure 6.9 Inhibition of Ag^+ toward the peroxidase-like activities of various nanostructures. (a-d) TEM images of (a) 6.5-nm PVP-capped Pt spheres, (b) 5.0-nm citrate-capped Pt spheres, (c) 5.9-nm PVP-capped Pd cubes, and (d) 4.5-nm PVP-capped Au spheres. (e) Inhibition efficiencies of Ag^+ toward the peroxidase-like activities of different nanostructures. (f) Inhibition efficiencies of Ag^+ toward the peroxidase-like activities of two PVP-capped Pt cube samples (from the same synthesis batch) that were preincubated with 0 or 5 mg/mL PVP aqueous solution. In panel e and f, A_0 and A_x are the absorbances at 653 nm of reaction solutions catalyzed by certain nanostructures before and after incubation with Ag^+, respectively. The concentrations of the nanostructures were

set to certain values at which A_0 for all of the nanostructures was normalized to ~1.0. The error bars represent the standard deviations of three independent measurements (n = 3).

To achieve a quantitative analysis, we determined the coverage density of Ag^+ on the PVP-capped Pt cubes using ICP-OES. The cubes were first incubated with an excess amount of Ag^+ and washed 10 times with DI water by centrifugation. The resultant Ag^+-adsorbed Pt cubes were digested with aqua regia and then subjected to ICP-OES analysis. The molar ratio of Ag to Pt was quantified to be 0.074:1. Based on this result, the size of the Pt cubes, and the unit-cell parameters of Ag,[42, 43] the average number of Ag atomic layers adsorbed on the Pt cubes was estimated to be 0.972. This result suggests the nearly monolayer adsorption of Ag^+ on the Pt cube surface and further demonstrates that the Ag^+ absorbed at the interface between Pt and PVP rather than the repeat units of the polymeric PVP molecules. In a sense, the unique interface of Pt and PVP is specific to Ag^+ binding. Taken together, the synergistic adsorption effect of the Pt *fcc* crystal structure and PVP is believed to be responsible for the specific and strong adsorption of Ag^+ on the surface of PVP-capped Pt cubes. This adsorption of Ag^+ blocks the active sites for catalysis and eventually inhibits the peroxidase-like catalytic activity of the Pt cubes.

6.3 Conclusion

In summary, we have demonstrated a facile colorimetric method for the detection of Ag^+ with picomolar sensitivity. The high detection sensitivity relies on the ultrahigh peroxidase-like catalytic activity of PVP-capped Pt cubes and the specific, efficient inhibition toward this catalytic activity by Ag^+. In addition to a high sensitivity, this colorimetric method also features simple operation, rapid execution, and cost effectiveness. We believe that the method presented here will find widespread use in monitoring and quantifying Ag^+ in environmental scenarios. The concept

of taking advantage of the superior catalytic activities of nanoscale artificial peroxidases can also be extended to the detection and sensing of other critical ionic species.[44, 45]

6.4 Materials and Experiment

6.4.1 Chemicals and Materials

Silver nitrate ($AgNO_3$, ≥99.0%), sodium hexachloroplatinate(IV) hexahydrate ($Na_2PtCl_6 \cdot 6H_2O$, 98%), potassium bromide (KBr, ≥99%), poly(vinylpyrrolidone) (PVP, $M_w \approx$ 55000), hydrogen peroxide solution (30 wt % in H_2O), 3,3′,5,5′-tetramethylbenzidine (TMB, > 99%), sodium acetate (NaOAc, ≥99%), acetic acid (HOAc, ≥99.7%), L-ascorbic acid (≥99%), gold(III) chloride trihydrate ($HAuCl_4 \cdot 3H_2O$, ≥99.9%), sodium nitrate ($NaNO_3$, ≥99%), silver trifluoroacetate (CF_3COOAg, ≥99.9%), sodium citrate dihydrate (≥99%), citric acid (≥99.5%), sodium borohydride ($NaBH_4$, ≥98%), and potassium chloride (KCl, ≥99%) were all obtained from Sigma-Aldrich. Ethylene glycol (EG) was obtained from J. T. Baker. All other reagents and chemicals were of at least analytical grade. All aqueous solutions were prepared using deionized (DI) water with a resistivity of 18.0 MΩ·cm. Tap-water samples were collected from a household water pipe in our laboratory.

6.4.2 Synthesis of PVP-Capped Pt Cubes

The synthesis of Pt nanocubes was the same as in **Chapter 5**. The concentration of final products in terms of Pt element was determined to be 1.68 mg/mL by inductively coupled plasma-optical emission spectroscopy (ICP-OES). This Pt element concentration was converted to a Pt particle concentration of $\sim 2.01 \times 10^{14}$ particles/mL or $\sim 3.34 \times 10^{-7}$ M given that the shape and size of Pt particles (*e.g.*, cubes with an edge length of 7.3 nm) had been resolved by TEM

(see **Figure 6.1b**). PVP-capped Pt cubes with average edge lengths of 6.2 and 9.5 nm (shown in **Figure 6.5**) were obtained by using the same procedure as for 7.3-nm Pt cubes except for changes in the amount of PVP from 40 mg to 8 and 200 mg, respectively.

6.4.3 Standard Procedure for the Detection of Ag^+ Using PVP-Capped Pt Cubes

Before detection, Ag^+ standards with various concentrations were prepared using $AgNO_3$ as the source and 1.0 mM HOAc/NaOAc buffer (pH 6.0) as the sample matrix. Afterward, 590 μL of Ag^+standard or sample was mixed with 10 μL of PVP-capped Pt cubes (~3.78×10^{10} particles/mL) in a disposable plastic cuvette, and the mixture was incubated for 40 s at room temperature. Subsequently, 400 μL of substrate solution (5.0 M H_2O_2 and 2.0 mM TMB in 1.0 M HOAc/NaOAc buffer, pH 4.0) was added. After incubation of the reaction solution for 5 min at room temperature, its UV-vis spectrum, photograph, or both were taken.

6.4.4 Synthesis of Other Nanostructures Shown in Figure 6.9

6.5-nm PVP-Capped Pt Spheres

The 6.5-nm PVP-capped Pt spheres were synthesized using the same procedure as for the 7.3-nm PVP-capped Pt cubes except for the exclusion of KBr from the reaction solution. The final products were stored in 4 mL of DI water at a particle concentration of ~5.38×10^{14} particles/mL or ~8.94×10^{-7} M.

5.0-nm Citrate-Capped Pt Spheres

The 5.0-nm citrate-capped Pt spheres were synthesized according to a previously reported procedure with minor modifications.[22] Briefly, 100 mL of 0.01% (w/v) $Na_2PtCl_6 \cdot 6H_2O$ aqueous solution was heated to boiling under vigorous stirring, and then 2 mL of a solution containing 1%

sodium citrate and 0.05% citric acid was added. After 30 s, 1 mL of a freshly prepared solution containing 0.08% $NaBH_4$ and 1% sodium citrate was quickly added to the above solution. The resultant mixture was kept boiling and stirring for 10 min and was then cooled to room temperature. The final products were stored in 10 mL of 0.1% sodium citrate solution at a particle concentration of ~2.21×10^{14} particles/mL or ~3.67×10^{-7} M.

5.9-nm PVP-Capped Pd Cubes

The 5.9-nm PVP-capped Pd cubes were synthesized using our previously published procedure with slight changes.[23] In brief, 8.0 mL of an aqueous solution containing 105 mg of PVP, 60 mg of AA, 4 mg of KBr, and 186 mg of KCl was hosted in a vial and preheated to 80 °C in an oil bath under magnetic stirring for 10 min. Subsequently, 3.0 mL of an aqueous solution containing 57 mg of Na_2PdCl_4 was injected with a pipet. After the reaction had proceeded for 3 h, the products were collected by centrifugation. The final PVP-capped Pd cubes were stored in 5.0 mL of DI water at a particle concentration of ~1.56×10^{15} particles/mL or ~2.59×10^{-6} M.

4.5-nm PVP-Capped Au Spheres

Precisely 10.0 mL of an aqueous solution containing 1.05% (w/v) PVP and 0.25 mM $HAuCl_4$ was hosted in a vial and stirred at room temperature. Subsequently, 0.5 mL of a freshly prepared solution containing 0.08% $NaBH_4$ and 1% ascorbic acid was quickly added to the above solution. After the reaction had proceeded for 10 min, the products were collected by centrifugation. The final PVP-capped Au spheres were stored in 5.0 mL of DI water at a particle concentration of ~9.71×10^{13} particles/mL or ~1.61×10^{-7} M.

6.4.5 Estimation of the Magnitude of Signal Diminishment (N) for the Proposed Method

Here, detection of 0.5 nM Ag^+ was chosen as a model for the estimation. The magnitude of signal diminishment of the detection system was estimated by comparing the amount of Ag^+ in the system with the amount of colored products diminished relative to the blank (*e.g.,* 0 nM Ag^+).

Known parameters:

1) The Ag^+ concentration: C_{Ag+} = 0.5 nM

2) The volume of Ag^+ sample: V_{Ag+}= 590 μL

3) The amount of Ag^+ ions (n_{Ag+}): 590 μL × 0.5 nM = 2.95×10^{-13} mole

4) The decrease of the absorbance at 653 nm of the detection solution: $A_0 - A_{0.5} = 0.0954$ (see **Figure 6.4e**), where $A_{0.5}$ and A_0 denote the absorbance recorded from reaction solutions containing 0.5 and 0 (blank) nM Ag^+

5) The total volume of final reaction solution: V = 1000 μL

6) The molar absorption coefficient of oxidized TMB at 653 nm: $\varepsilon = 3.9 \times 10^4$ $M^{-1} \cdot cm^{-1}$

Results:

The path length of cuvette: b = 1.0 cm. The decreased concentration of oxidized TMB (ΔC_{oxTMB}, relative to the blank) in 1000 μL solution toward 0.5 nM Ag^+ could be calculated based on the Beer-Lambert law ($A = \varepsilon bC$): $\Delta C_{oxTMB} = (A_0 - A_{0.5})/ (\varepsilon b) = 0.0954 / (3.9 \times 10^4$ $M^{-1} \cdot cm^{-1} \times 1$ cm) = 2.4462×10^{-6} M.

Therefore, the amount of diminished oxidized TMB molecules (n_{oxTMB}) was estimated to be 2.45×10^{-9} mole (*e.g.,* 2446.2 nM × 1000 μL). Finally, the magnitude of signal diminishment (N) could be estimated: $N = n_{oxTMB} / n_{Ag+} = 2.45 \times 10^{-9}$ mole / 2.95×10^{-13} mole = 8.3×10^3.

6.4.6 Preparation of the Ionic Solutions

The ionic solutions labeled with #2-#31 in **Figure 6.6** were prepared by dissolving NH_4Cl, NaCl, KCl, LiCl, $BaCl_2 \cdot 2H_2O$, $CaCl_2 \cdot 2H_2O$, $CdCl_2$, $Co(NO_3)_2 \cdot 6H_2O$, $CuCl_2 \cdot 2H_2O$, $FeSO_4 \cdot 7H_2O$, $Mg(NO_3)_2 \cdot 6H_2O$, $MnSO_4 \cdot H_2O$, $NiCl_2 \cdot 6H_2O$, $Pb(NO_3)_2$, $Zn(NO_3)_2 \cdot 6H_2O$, $Al(NO_3)_3 \cdot 9H_2O$, $CrCl_3 \cdot 6H_2O$, $Fe(NO_3)_3 \cdot 9H_2O$, NaF, NaCl, NaBr, $NaNO_3$, NaAc, Na_2SO_3, Na_2SO_4, K_2CO_3, Na_3PO_4, CuCl, $PdCl_2$, and $HgCl_2$, respectively, in DI water. All the chemicals were analytical grade and were used as received without further purification.

6.5 Characterizations

UV-vis spectra were measured using an Agilent Cary 60 UV-vis spectrophotometer. TEM images were recorded using a JEOL JEM-2010 microscope operated at 200 kV. The concentrations of Pt, Ag, and Pd ions were determined by ICP-OES (Perkin-Elmer Optima 7000 DV spectrometer) and could be converted into particle concentrations of Pt and Pd nanoparticles by coupling with TEM imaging data. X-ray photoelectron spectroscopy (XPS) measurements were performed on an SSX-100 system (Surface Science Laboratories, Inc.) equipped with a monochromated Al K_α X-ray source, a hemispherical sector analyzer (HSA), and a resistive anode detector. The pH values of buffer solutions were recorded using an Oakton pH 700 benchtop meter. Photographs of the samples in cuvettes were taken using a Canon EOS Rebel T5 digital camera.

6.6 Reference

1. Howe, P. D.; Dobson, S. *Silver and Silver Compounds*, World Health Organization: Geneva, Switzerland, **2002**.
2. Drake, P. L.; Hazelwood, K. J. *Ann. Occup. Hyg.* **2005**, 49, 575-585.
3. Saran, R.; Liu, J. *Anal. Chem.* **2016**, 88, 4014-4020.

4. Ratte, H. T. *Environ. Toxicol. Chem.* **1999**, 18, 89-108.
5. Barriada, J. L.; Tappin, A. D.; Evans, E. H.; Achterberg, E. P. *TrAC, Trends Anal. Chem*. **2007**, *26*, 809-817.
6. Song, Y.; Wei, W.; Qu, X. *Adv. Mater*. **2011**, 23, 4215-4236.
7. Gao, Z.; Deng, K.; Wang, X.; Miró, M.; Tang, D. *ACS Appl. Mater. Interfaces* **2014**, *6*, 18243-18250.
8. Chang, Y.; Zhang, Z.; Hao, J.; Yang, W.; Tang, J. *Sens. Actuators, B* **2016**, 232, 692-697.
9. Lin, C.; Yu, C.; Lin, Y.; Tseng, W. *Anal. Chem.* **2010**, 82, 6830-6837.
10. Zhou, X.; Kong, D.; Shen, H. *Anal. Chem.* **2010**, 82, 789-793.
11. Liu, S.; Tian, J.; Wang, L.; Sun, X. *Sens. Actuators, B* **2012**, 165, 44-47.
12. Huang, H.; Qu, C.; Liu, X.; Huang, S.; Xu, Z.; Liao, B.; Zeng, Y.; Chu, P. K. *ACS Appl. Mater. Interfaces* **2011**, *3*, 183-190.
13. Lou, T.; Chen, Z.; Wang, Y.; Chen, L. *ACS Appl. Mater. Interfaces* **2011**, 3, 1568-1573.
14. Liu, Y.; Dai, J.; Xu, L.; Liu, X.; Liu, J.; Li, G. *Sens. Actuators, B* **2016**, 237, 216-223.
15. Zhou, X.; Kong, D.; Shen, H. *Anal. Chim. Acta* **2010**, 678, 124-127.
16. Sung, Y.; Wu, S. *Sens. Actuators, B* **2014**, 197, 172-176.
17. Li, T.; Shi, L.; Wang, E.; Dong, S. *Chem. - Eur. J.* **2009**, 15, 3347-3350.
18. Li, B.; Du, Y.; Dong, S. *Anal. Chim. Acta* **2009**, 644, 78-82.
19. Rycenga, M.; Cobley, C.M.; Zeng, J.; Li, W.; Moran, C. H.; Zhang, Q.; Qin, D.; Xia, Y. *Chem. Rev*. **2011**, *111*, 3669-3712.
20. Jain, P. K.; Lee, K. S.; El-Sayed, I. H.; El-Sayed, M. A. *J. Phys. Chem. B* **2006**, 110, 7238-7248.
21. Ye, H.; Liu, Y.; Chhabra, A.; Lilla, E.; Xia, X. *ChemNanoMat* **2017**, 3, 33-38.
22. Bigall, N. C.; Hartling, T.; Klose, M.; Simon, P.; Eng, L. M.; Eychmuller, A. *Nano Lett*. **2008**, *8*, 4588-4592.
23. Xia, X.; Zhang, J.; Lu, N.; Kim, M. J.; Ghale, K.; Xu, Y.; McKenzie, E.; Liu, J.; Ye, H. *ACS Nano* **2015**, 9,9994-10004.
24. Josephy, P. D.; Eling, T. E.; Mason, R. P. *J. Biol. Chem.* **1982**, 257, 3669-3675.
25. Gao, L.; Zhuang, J.; Nie, L.; Zhang, J.; Zhang, Y.; Gu, N.; Wang, T.; Feng, J.; Yang, D.; Per rett, S. *Nat. Nanotechnol.* **2007**, 2, 577-583.

26. Wang, C.; Daimon, H.; Lee, Y.; Kim, J.; Sun, S. *J. Am. Chem. Soc.* **2007**, 129, 6974-6975.
27. Armbruster, D. A.; Tillman, M. D.; Hubbs, L. M. *Clin. Chem.* **1994**, 40, 1233-1238.
28. Aliaga, C.; Park, J. Y.; Yamada, Y.; Lee, H. S.; Tsung, C.-K.; Yang, P.; Somorjai, G. A. *J. Phys. Chem. C* **2009**, *113*, 6150-6155.
29. Yin, L.; Wang, Z.; Lu, L.; Wan, X.; Shi, H. *New J. Chem.* **2015**, 39, 4891-4900.
30. Xia, Y.; Xia, X.; Peng, H.-C. *J. Am. Chem. Soc.* **2015**, 137, 7947-7966.
31. Xia, Y.; Xiong, Y.; Lim, B.; Skrabalak, S. E. *Angew. Chem., Int. Ed.* **2009**, 48, 60-103.
32. Pastoriza-Santos, I.; Liz-Marzán, L. M. *Langmuir* **2002**, 18, 2888-2894.
33. Koczkur, K. M.; Mourdikoudis, S.; Polavarapu, L.; Skrabalak, S. E. *Dalton Trans*. **2015**, *44*, 17883-17905.
34. Silvert, P.-Y.; Herrera-Urbina, R.; Duvauchelle, N.; Vijayakrishnan, V.; Elhsissen, K. T. *J. Mater. Chem.* **1996**, *6*, 573-577.
35. Huang, H.; Ni, X.; Loy, G. L, Chew, C. H.; Tan, K.; Loh, F. C.; Deng, J.; Xu, G. *Langmuir* **1996**, *12*, 909-912.
36. Xia, X.; Zeng, J.; Zhang, Q.; Moran, C. H.; Xia, Y. *J. Phys. Chem. C* **2012**, *116*, 21647-21656.
37. Habas, S. E.; Lee, H.; Radmilovic, V.; Somorjai, G. A.; Yang, P. *Nat. Mater*. **2007**, *6*, 692-697.
38. Zhang, Y.; Bu, L.; Jiang, K.; Guo, S.; Huang, X. *Small* **2016**, 12, 706-712.
39. Feng, L.; Wu, X.; Ren, L.; Xiang, Y.; He, W.; Zhang, K.; Zhou, Y.; Xie, S. *Chem. - Eur. J.* **2008**, *14*, 9764-9771.
40. Tan, G.; Shi, F.; Doak, J. W.; Sun, H.; Zhao, L.; Wang, P.; Uher, C.; Wolverton, C.; Dravid, V. P.; Kanatzidis, M. G. *Energy Environ. Sci*. **2015**, *8*, 267-277.
41. Huang, S.; Wen, Z.; Zhu, X.; Gu, Z. *Electrochem. Commun.* **2004**, 6, 1093-1097.
42. Yang, Y.; Liu, J.; Fu, Z.; Qin, D. *J. Am. Chem. Soc.* **2014**, 136, 8153-8156.
43. Cathcart, N.; Coombs, N.; Gourevich, I.; Kitaev, V. *Nanoscale* **2016**, 8, 18282-18290.
44. Wu, G.-W.; He, S.-B.; Peng, H.-P.; Deng, H.-H.; Liu, A.-L.; Lin, X.-H.; Xia, X. H.; Chen, W. *Anal. Chem*. **2014**, *86*, 10955-10960.
45. Li, W.; Chen, B.; Zhang, H.; Sun, Y.; Wang, J.; Zhang, J.; Fu, Y. *Biosens. Bioelectron*. **2015**, *66*, 251-258.

CHAPTER 7 A NON-ENZYME CASCADE AMPLIFICATION STRATEGY FOR COLORIMETRIC ASSAY OF DISEASE BIOMARKERS[a]

7.1 Introduction

Diagnostic technologies for the detection of disease biomarkers have become a critical component in biomedical research and clinical care.[1-4] Over the past several decades, a variety of technologies based on different signal-transducer principles have been actively explored, with notable examples including fluorescent,[5-7] chemiluminescent,[8,9] colorimetric,[10-12] electrochemical,[13,14] Raman,[15-17] and plasmonic[18,19] assays. Among them, enzyme-based colorimetric assays (in which the enzymes are pre-conjugated to bioreceptors and specifically generate a color signal by catalyzing chromogenic substrates) continue to attract increasing attention because of their simplicity and cost-effectiveness.[20-22] In particular, they could be performed by less-trained personnel with low-cost devices, making them extremely desirable for diagnostics in resource-limited settings.

Nevertheless, extensive application of colorimetric assays in clinical diagnosis is largely limited by their relatively low detection sensitivity. A general strategy to enhance the sensitivity is to amplify the color signal by assembling as many enzymes as possible on carriers (*e.g.*, polymers and nanoparticles).[23, 24] However, this strategy is ultimately confined by the loading amount of enzymes on a carrier with limited space and the steric hindrance.[25] Recently, enzyme

---

[a]Reprinted with permission from *Chem. Commun.* **2017**, *53*, 9055-9058

Haihang Ye contributed the conception and design of the related work, acquisition and interpretation of data, and preparation of the article.

cascade amplification has emerged to be a novel and efficient signal amplification strategy for sensitivity enhancement.[26-32] A typical mechanism involves sequential cascade reactions catalyzed by enzymes – the products generated from a primary enzyme associated with bioreceptors catalyze the activation of a secondary enzyme, which in turn yields another product with a drastically increased amount. While this amplification technique is highly efficient, it is subject to a number of variables such as the enzymatic activity, stability, and activation conditions. In particular, the relatively poor stability of enzymes makes the enzyme cascade amplification system hardly survive in harsh environments, which is oftentimes the case for field work and point-of-care tests.[33]

In this work, we report a non-enzyme cascade amplification (NECA) strategy for enhancing the sensitivity of a colorimetric assay. This strategy lies in the dense atom packing in silver (Ag) nanoparticles and the ultrahigh catalytic activity of platinum (Pt) nanocatalysts. The NECA assay adopts the classic ELISA platform,[20] ensuring the simplicity of the assay without the involvement of additional equipment. Specifically, as shown in **Figure 7.1**, after antibody-conjugated Ag nanoparticles are captured by biomarkers in a 96-well microtiter plate and the uncaptured ones removed, the nanoparticles are dissolved into individual Ag^+ through chemical etching by H_2O_2.[34] The Ag^+ could then effectively inhibit the catalytic activity of Pt nanocubes as artificial peroxidases, thereby largely eliminating the generation of blue colored product – oxidized TMB.[35,36] Despite being miniature in size, Ag nanoparticles consist of thousands to millions of Ag atoms that can be conveniently released in the form of Ag^+. For example, the Ag nanosphere of 20 nm we used in this study (will be specified later) contains $\sim 2.5 \times 10^5$ Ag atoms. On the other hand, as demonstrated in our recent study,[36] a single Ag^+ could inhibit the generation of $\sim 10^4$ oxidized TMB within several minutes owing to the superior catalytic activity of Pt nanocubes and the

efficient inhibition of Ag^+ towards the catalytic reaction. Notably, the oxidized TMB possesses a large molar extinction coefficient (ε) at a level of 10^4 $M^{-1}\cdot cm^{-1}$,[37] ensuring a distinct change in the color signal. Considering these two cascade processes together, the detection signal (refers to as the diminished color signal relative to a control) in the NECA system could be amplified by orders of magnitude. Significantly, both Ag nanoparticles and Pt nanocubes are made of inert noble metals with good stabilities, making the NECA system less vulnerable to the environment.

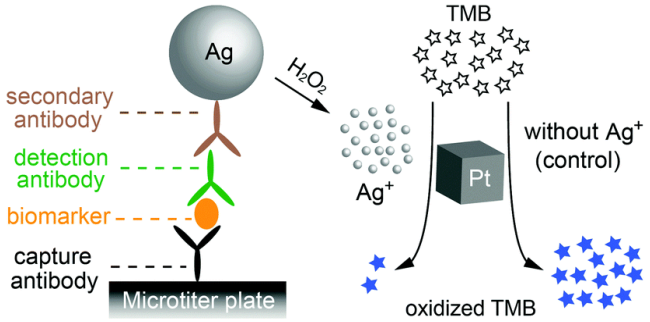

Figure 7.1 Schematics showing the non-enzyme cascade amplification (NECA) strategy for the detection of disease biomarkers.

7.2 Results and Discussion

We first conducted a set of experiments to demonstrate the feasibility and optimize the conditions of the NECA system, in which the response of Ag nanoparticles with various amounts was investigated. Specifically, 50 μL of aqueous suspensions of citrate-capped Ag nanospheres with an average diameter of ~20 nm (Sigma Aldrich, **Figure 7.2a**) were etched with 50 μL of H_2O_2 to form a Ag^+ solution. Then, to the etching solution, 20 μL of Pt nanocubes with an average edge length of 7.3 nm (100 pM in particle concentration, **Figure 7.2b**) and 100 μL of the TMB substrate solution were sequentially added. Here, the Pt nanocubes were synthesized the same as **Chapter 5**.[35] The catalytic reaction was finally quenched by H_2SO_4, in which oxidized TMB was

converted to yellow-colored diimine with $\lambda_{max} \approx 450$ nm and $\varepsilon = 5.9\times10^4$ $M^{-1}\cdot cm^{-1}$.[38] We chose these Ag nanospheres for demonstration because (*i*) they could be easily functionalized with antibodies through electrostatic interactions;[39] (*ii*) they could be prepared with good uniformities in terms of both shape and size, ensuring good reproducibility of the assay; and (*iii*) they are commercially available, making it convenient to assemble the assay system for practical use. After the systematic examination of various parameters (**Figure 7.3**), the optimal conditions for etching of Ag nanospheres were found to be 0.1 M H_2O_2, 37 °C, and 20 minute incubation, under which Ag atoms in the nanospheres were almost completely converted to Ag^+. It should be emphasized that, while we adopted etching at 37 °C as a standard condition in this study, the etching efficiency at 22 °C was similar to the case of 37 °C (**Figure 7.3c**), indicating the potential use of the present system at room temperature. As shown in **Figure 7.2c**, the intensity of the color signal from the system decreased as the concentration of the Ag nanospheres increased. A linear relationship was found between the decrease of absorbance at 450 nm relative to the control (A_0 - A_x) and the concentration of Ag nanospheres in the range of 0.5-8.0 fM (**Figure 7.2d**). It is worth noting that the decrease of the color signal was even evident when the concentration of Ag nanospheres was as low as 0.5 fM (corresponding to only $\sim1.5\times10^4$ particles in a 50 μL suspension). In other words, a small amount of Ag nanospheres could induce a detectable color change, implying a high sensitivity of the system. These results clearly demonstrated the capabilities of signal amplification and quantification for the proposed NECA strategy.

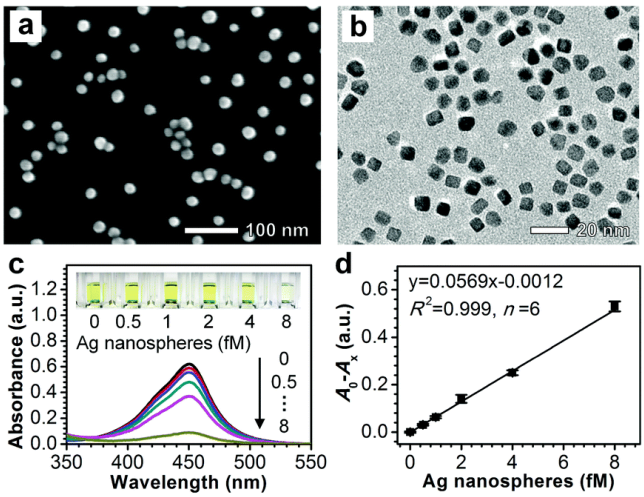

Figure 7.2 Demonstration of the NECA system by varying the amount of Ag nanospheres in an aqueous suspension. (a) Scanning electron microscopy (SEM) image of the 20 nm Ag nanospheres; (b) TEM image of the 7.3 nm Pt nanocubes; (c) UV-vis spectra taken from the reaction solutions containing Pt cubes, TMB substrates, and Ag nanospheres of various concentrations after they had been etched by H_2O_2. The group of "0 fM Ag nanospheres" is referred to as "control". The inset shows a typical photograph of the corresponding samples in cuvettes; (d) calibration curve of (c) that was generated by plotting the decrease of the absorbance at 450 nm relative to the control (A_0 - A_x) as a function of the Ag nanosphere concentration.

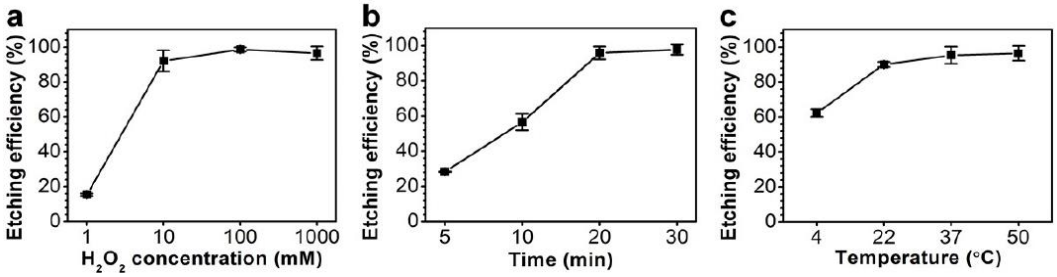

Figure 7.3 The effects of (a) H_2O_2 concentration, (b) etching time, and (c) temperature on the etching efficiency of Ag nanospheres by H_2O_2. The experiments were carried out by etching 50 μL aqueous suspensions of 20 nm Ag nanospheres (~10 fM) with 50 μL of H_2O_2. The H_2O_2 concentration was 0.1 M, etching time was 20 minutes, temperature was 37 °C, unless otherwise stated. The etching efficiency is defined as the amount of released Ag^+ as a percentage of the amount of total Ag element in initial Ag nanospheres.

We then applied the NECA system to the detection of human PSA according to the principle shown in **Figure 7.1**. PSA is the key biomarker that indicates the recurrence of prostate cancer after treatment.[40] It is pivotal to detect minute concentrations of PSA at early stages to improve the survival rates of patients who have undergone radical prostatectomy.[40, 41] For comparison, we benchmarked the NECA assay against the conventional HRP based ELISA by using the same set of antibodies and materials. Herein, antibodies were conveniently functionalized on Ag nanospheres through a simple incubation process (see **Section 7.4.4**), ensuring the simplicity of the NECA assay.

PSA standards of various concentrations were tested by both assays and quantified using a microtiter plate reader. For the NECA assay (**Figure 7.4**, blue), a quality linear relationship (R^2 = 0.999) in the range of 2-64 pg·mL^{-1} of PSA was found by plotting the decrease of absorbance relative to the control (A_0 - A_x) against PSA concentration. The coefficients of variation (n = 6) across the entire concentration range were determined to be <10%, indicating a good reproducibility of the assay. The limit of detection (LOD),[42, 43] defined as the concentration corresponding to a signal that is three times the standard deviation of a zero calibrator, was calculated to be 0.165 pg·mL^{-1}. In comparison, a linear range of 200-6400 pg·mL^{-1} and a LOD of 16.0 pg·mL^{-1} of PSA were determined for the conventional HRP ELISA based on its calibration curve (**Figure 7.4**, black). These results suggest that the NECA system could enhance the detection sensitivity by approximately 2 orders of magnitude as compared to conventional ELISA. Significantly, this substantial enhancement of the sensitivity does not compromise the simplicity of the colorimetric assay since the NECA system shares the same platform and a similar procedure with conventional ELISA. It is worth mentioning that the utilized amounts of Ag nanospheres and

Pt nanocubes were tiny based on the detection procedure (*e.g.*, ~2.0×10^{-6} and ~1.0×10^{-8} gram per test, respectively). Therefore, even though precious noble metals are used in the NECA system, their costs in individual tests are negligible.

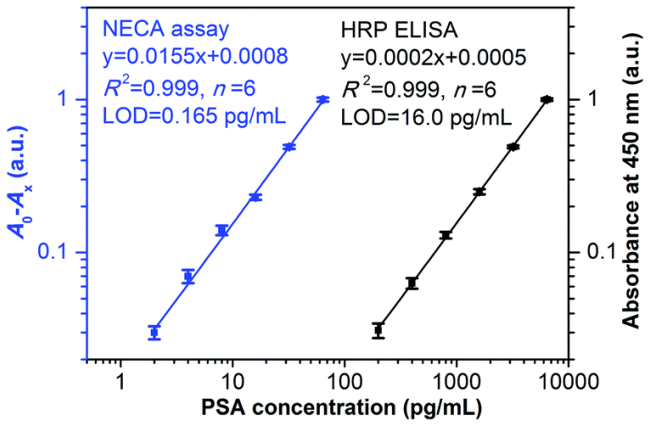

Figure 7.4 Calibration curves of the NECA assay and HRP ELISA for PSA detection. The error bars indicate the standard deviations of six independent measurements.

We also investigated the effect of Ag nanosphere size on the detection sensitivity of NECA for PSA. Specifically, we have examined the performance of two additional batches of Ag nanospheres from Sigma Aldrich (with average diameters of 10 nm and 40 nm, see **Figure 7.5a**, **b**) in detecting the PSA standards. The detection procedures were kept the same as the standard procedure used for the 20 nm Ag sphere, except for the substitution of 20 nm Ag spheres with the same amount of 10 nm or 40 nm Ag spheres. As shown in **Figure 7.5c, d**, the detection sensitivities of 10 nm and 40 nm Ag spheres were determined to be 0.195 pg·mL^{-1} and 0.549 pg·mL^{-1}, respectively (*vs.* 0.165 pg·mL^{-1} for 20 nm Ag spheres). It can be concluded that (*i*) decreasing the size of the Ag sphere from 20 to 10 did not cause an apparent change in the detection sensitivity. This observation might be explained by the argument that a 10 nm Ag sphere was more efficient in binding to the analytes. Therefore, even though a 10 nm Ag sphere contains smaller amount of

Ag element (**Figure 7.1**) compared to a 20 nm Ag sphere in the standard assay, their performances (*e.g.*, detection sensitivities) in the NECA system were comparable. The decrease of sensitivity may be ascribed to the enhanced steric hindrance of antibodies labeled on Ag spheres.[44,45]

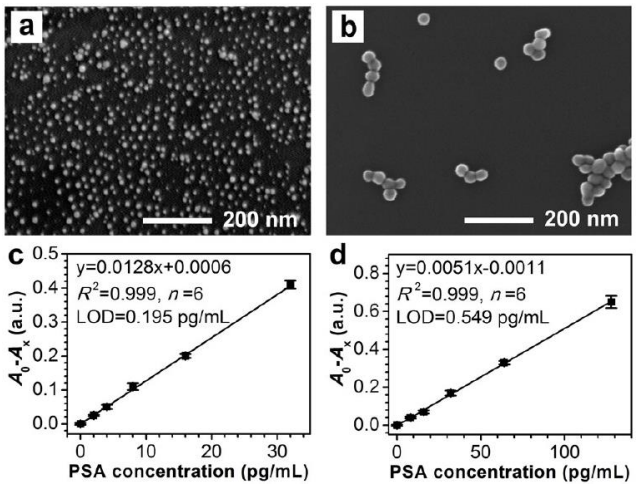

Figure 7.5 Effect of Ag nanosphere size on the detection sensitivity of NECA for PSA. SEM images of Ag nanospheres with average diameters of (a) 10 nm and (b) 40 nm. Calibration curves of NECA assays when (c) 10 nm and (d) 40 nm Ag nanospheres shown in (a, b) were used. Error bars in (c, d) indicate the standard deviations of six independent measurements.

To evaluate the stability of the NECA system, we heated the two critical components – Ag nanospheres and Pt nanocubes – at a high temperature (up to 90 °C) for 6 hours prior to the assay of a 10 pg·mL^{-1} PSA standard. As shown in **Figure 7.6**, no significant change in both the detection sensitivity and reproducibility was observed for the NECA assay after the Ag and Pt particles had been treated with heat. This superior stability might be ascribed to the inherent inertness of noble metals.[25] In this regard, the NECA system is expected to be more reliable for detection under extreme conditions compared to enzyme-based signal amplification techniques.

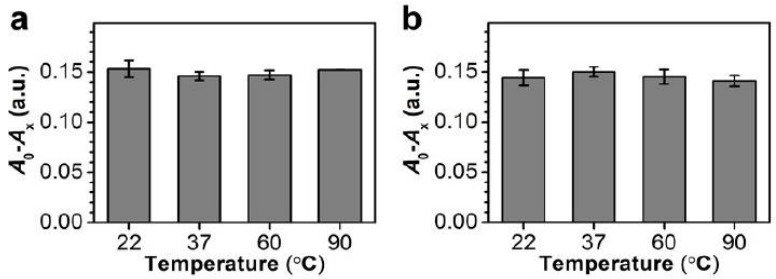

Figure 7.6 Stability test for the NECA system, in which the 20 nm Ag nanospheres (a) and 7.3 nm Pt nanocubes (b) were heated at different temperatures for 6 hours before they had been utilized for the NECA assay of 10 pg/mL PSA standards.

It is worth emphasizing that the sensitivity of the NECA system could be further enhanced by coupling with other cascade mechanisms. For example, we have demonstrated that the sensitivity could be improved by the "silver enhancement" technique (**Figure 7.7a**), which is widely used in bioanalysis.[46, 47] Herein, Ag nanospheres act as catalysts to reduce Ag^+ (from $AgNO_3$) to metallic Ag at room temperature in the presence of hydroquinone as a reducing agent. As shown by the SEM images in **Figure 7.7b**, the 20 nm Ag nanospheres were enlarged to ~50 nm during the silver enhancement process, with which the Ag content was greatly enriched. By coupling this technique to the NECA system, the LOD of the PSA assay was reduced to 0.031 $pg{\cdot}mL^{-1}$ as calculated on the basis of its calibration curve (**Figure 7.7c**). It can be concluded that, although the system has not yet been optimized for maximum Ag enrichment, an additional 5-fold enhancement in the sensitivity relative to the standard NECA assay could be achieved.

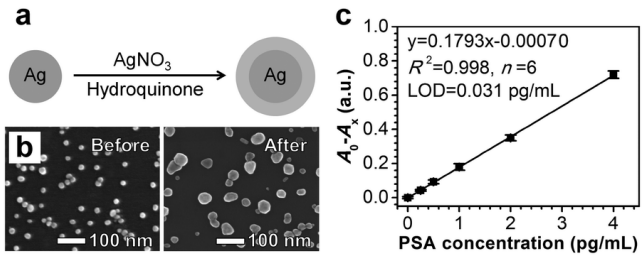

Figure 7.7 Silver enhancement technique coupled NECA assay. (a) Schematics showing the treatment of Ag nanospheres with silver enhancement; (b) SEM images of the 20 nm Ag nanospheres before and after silver enhancement; and (c) calibration curve of the silver enhancement technique-coupled NECA assay for PSA detection.

Finally, in order to demonstrate the potential use of the NECA assay in clinical scenarios, we applied it to detecting human serum samples spiked with the PSA standard at different concentrations in the range of 5-50 pg·mL^{-1}. As shown in **Table 7.1**, the analytical recoveries (defined as the amount measured as a percentage of the amount of PSA originally added to a sample[25]) for the five PSA spiked human serum samples were determined to be in the range of 92.46-104.31%. The coefficient of variation (n = 6) for all the samples was below 10.91%. We also benchmarked the detection against a commercial ELISA kit (Abcam plc., United Kingdom). As shown in **Figure 7.8**, the detection results from the NECA assay and the ELISA kit correlated very well with a correlation coefficient R^2 = 0.993. These results indicated that the performance of the NECA system was essentially not compromised by the complex matrices in human serum, suggesting the potential application of this technique in clinical diagnostics.

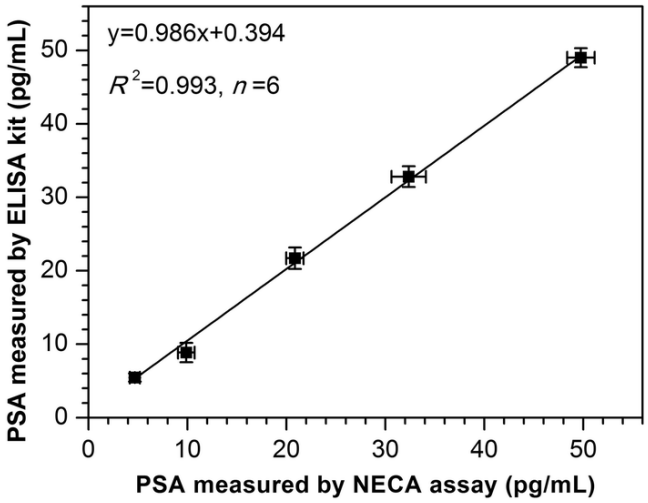

Figure 7.8 Correlation analysis between the NECA assay and a commercial ELISA kit (ab188389, Abcam plc.) in quantifying PSA from five PSA-spiked serum samples. The error bars indicate the standard deviations of six independent measurements.

Table 7.1 Analytical recoveries of the NECA assay in detecting PSA spiked human serum samples.

PSA amount spiked (pg/mL)	PSA amount measured (pg/mL)	Coefficient of variations (%, n = 6)	Recovery (%)
5	4.68	10.91	93.62
10	9.89	8.52	98.87
20	20.86	4.22	104.31
35	32.36	5.37	92.46
50	49.76	2.78	99.52

7.3 Conclusion

In conclusion, we have demonstrated a non-enzyme cascade signal amplification strategy for colorimetric assay of disease biomarkers with substantially enhanced sensitivity. This strategy was built by integrating two cascade processes – dissolution of nanoscale Ag particles to individual Ag^+ and generation of colored molecules catalyzed by Pt nanocubes as artificial peroxidases. To our knowledge, such a non-enzyme cascade amplification strategy has never been demonstrated before. Significantly, this technique is compatible with the instrument and procedures of existing biosensing technologies, making it straightforward to employ for clinical diagnostics. The concept of non-enzyme cascade signal amplification presented here may open up a new avenue for the development of more sensitive and reliable diagnostic technologies.

7.4 Materials and Experiment

7.4.1 Chemicals and Materials

Sodium hexachloroplatinate(IV) hexahydrate ($Na_2PtCl_6 \cdot 6H_2O$, 98%), potassium bromide (KBr, 99%), silver nitrate (AgNO3, ≥99.0%), hydroquinone (≥99%), polyvinylpyrrolidone (PVP, M.W. ≈ 55000), 3,3',5,5'-tetramethylbenzidine (TMB, >99%), hydrogen peroxide solution (wt=30% in H2O), citrate-capped Ag nanospheres of different sizes, human prostate-specific antigen (PSA, ≥99%), acetic acid (HOAc, ≥99.7%), sodium acetate (NaOAc, ≥99%), bovine serum albumin (BSA, ≥98%), tween 20, sodium chloride (NaCl, ≥99.5%), potassium chloride (KCl, ≥99%), sodium phosphate dibasic (Na_2HPO_4, ≥99%), potassium phosphate monobasic (KH_2PO_4, ≥99%), dimethylformamide (DMF), human serum, and sulfuric acid (H_2SO_4, 95-98%) were all obtained from Sigma-Aldrich. Ethylene glycol (EG) was from J. T. Baker. mPEG-SH (M.W. ≈ 5,000) was obtained from Laysan Bio, Inc. Rabbit anti- PSA polyclonal antibody (rabbit anti-PSA

pAb), mouse anti-PSA monoclonal antibody (mouse anti-PSA mAb), and commercial ELISA kit for PSA (product code: ab188389) were from Abcam plc. HRP-goat anti-mouse IgG conjugate and goat anti-mouse IgG were obtained from Thermo Fisher Scientific, Inc. 96-well microtiter plate (polystyrene, clear, flat bottom) was obtained from Celltreat Inc. All aqueous solutions were prepared using deionized (DI) water with a resistivity of 18.0 MΩ·cm.

7.4.2 Synthesis of PVP-Capped Pt Cubes

The synthesis of Pt nanocubes was the same as in **Chapter 5**. The concentration of final Pt nanocube suspension was estimated to be 334 nM (*e.g.*, 2.01×10^{14} particles/mL), according to the ICP-OES analysis and TEM imaging.

7.4.3 Demonstration of the Non-enzyme Cascade Amplification (NECA) System

50 μL aqueous suspensions of citrate-capped 20 nm Ag nanospheres with different particle concentrations were mixed with 50 μL of 0.1 M H_2O_2 in a cuvette. After incubation at 37 °C in an oven for 20 min, the etching solution was taken out to room temperature. Then, to the etching solution, 20 μL of PVP-capped 7.3 nm Pt nanocubes (100 pM, in DI water) and 100 μL of TMB substrate solution (*e.g.*, 4 M H_2O_2 and 1.6 mM TMB in 20 mM NaOAc/HOAc buffer, pH 4.0) were sequentially added. After incubation at room temperature for 20 min, the catalytic reaction was stopped by adding 20 μL of 2 M H_2SO_4, in which oxidized TMB was converted to yellow colored diimine with $\lambda_{max} \approx 450$ nm and $\varepsilon = 5.9\times10^4$ $M^{-1}\cdot cm^{-1}$. UV-vis spectra were then taken from the reaction solutions using a spectrophotometer.

7.4.4 Preparation of Ag Nanosphere-goat Anti-mouse IgG Conjugates

A 5 μL aliquot of goat anti-mouse IgG (1 mg/mL, correspond to the "secondary antibody" in **Figure 7.1**) was mixed with 10 μL of mPEG-SH (10 μM) at room temperature. Then, 1 mL of Ag nanospheres (0.185 mM in Ag element) was added to the mixture and incubated at room temperature for 20 min, followed by the addition of 100 μL of BSA (1 wt%) and incubation at room temperature for another 20 min. The final conjugates were purified by washing twice with 0.1 wt% BSA and stored in 10 mM phosphate buffered saline pH 7.4 (PBS) containing 10 wt% BSA and 0.05 wt% tween 20 at 4 °C for future use.

7.4.5 NECA Assay of PSA

In a standard NECA assay of PSA, 100 μL aliquots of rabbit anti-PSA pAb (5 μg/mL, in PBS, correspond to the "capture antibody" in **Figure 7.1**) was added to the wells of 96-well microtiter plate and incubated at 4 °C for 12 h. After being washed by washing buffer (PBS containing 0.05 wt% tween 20) for three times, the wells were blocked by 200 μL of blocking buffer (PBS containing 0.05 wt% tween 20 and 2 wt% BSA) and incubated at 37 °C for 1 h. Then, the wells were washed three times by washing buffer, followed by addition of 100 μL of PSA standards in dilution buffer (PBS containing 0.05 wt% tween 20 and 0.5 wt% BSA). After being shaken on a shaker at room temperature for 2 h, the wells were washed by washing buffer for three times. 100 μL of mouse anti-PSA mAb (2 μg/mL, in dilution buffer, correspond to the "detection antibody" in **Figure 7.1**) was added to the wells, followed by shaking at room temperature for 1 h. After the wells had been washed three times by washing buffer, 100 μL of Ag nanosphere-goat anti-mouse IgG conjugates (20 μg/mL in Ag elements) was added, followed by 1 h shaking at room temperature. After three times washing by washing buffer, 100 μL of H_2O_2 (0.05 M) was added to

the wells, followed by incubation at 37 °C for 20 min. Finally, 20 μL of Pt nanocubes (100 pM, in DI water) and 100 μL of TMB substrate solution (4 M H_2O_2 and 1.6 mM TMB in 20 mM NaOAc/HOAc buffer, pH 4.0) were sequentially added. After incubation at room temperature for 20 min, the reaction was stopped by adding 20 μL of 2 M H_2SO_4. The absorbance of each well at 450 nm was read using a microplate reader. PSA spiked human serum samples were measured by the same procedure for PSA standards as described above, except that the serum samples were pre-diluted 2 folds by dilution buffer prior to detection. Note that the original serum sample (from Sigma Aldrich) does not contain detectable PSA as determined by a commercial ELISA kit (Abcam plc., United Kingdom).

7.4.6 HRP ELISA of PSA

The detection principle and procedure of HRP ELISA was similar to those of NECA assay except that the color signal was generated from HRP. In brief, after the capture antibodies, PSA, and detection antibodies had been adsorbed on the 96-well microtiter plate (using the same procedure for NECA assay), 100 μL of HRP-goat anti-mouse IgG conjugates (1 μg/mL, in dilution buffer) was added to each well. The plate was shaken at room temperature for 1 h and then washed three times by washing buffer. 100 μL of TMB substrate for HRP ELISA (1 mM H_2O_2 and 0.8 mM TMB in 20 mM NaOAc/HOAc buffer solution, pH 4.0) was added to each well, followed by incubation at room temperature for 20 min. The reaction at the wells were finally stopped by 20 μL of 2 M H_2SO_4. The absorbance of each well at 450 nm was read using a microplate reader.

7.4.7 Silver Enhancement Technique-coupled NECA Assay of PSA

The procedure of silver enhancement technique-coupled NECA assay of PSA was same as that of above mentioned standard NECA assay except for the involvement of a silver enhancement process before the step of Ag particle etching by H_2O_2. The silver enhancement was conducted by adding 50 μL of $AgNO_3$ (0.1 mM, in DI water) and 50 μL of hydroquinone (0.1 mM, in DI water) to each well. After incubation at room temperature for 20 min, the wells were washed five times by DI water.

7.5 Characterizations

The UV-vis spectra were recorded using an Agilent Cary 60 UV-vis spectrophotometer. TEM images were taken using a JEOL microscope (JEM-2010) operated at 200 kV. Scanning electron microscopy (SEM) images were taken using a cold field emission high resolution scanning electron microscope (Hitachi S-4700) operated at 20 kV. To estimate particle concentrations, the Ag nanospheres and Pt nanocubes were dissolved to Ag and Pt ions by aqua regia. The concentrations of Ag and Pt ions were then determined using an inductively coupled plasma-optical emission spectroscopy (ICP-OES, PerkinElmer Optima 7000DV), which could be converted to the particle concentrations of Ag nanospheres and Pt nanocubes once the particle sizes and shapes had been resolved by TEM or SEM imaging. A microplate reader (PerkinElmer Victor 3 1420) was used to measure the absorbance at 450 nm for samples in microtiter plates. 37 °C-incubation was conducted in an oven (Precision Scientific, Inc.). Microtiter plates were shaken on a Corning LSE digital microplate shaker. A benchtop meter (Oakton pH 700) was used to measure the pH value of buffer solutions.

7.6 Reference

1. Giljohann, D. A.; Mirkin, C. A. *Nature*, **2009**, *462*, 461-464.
2. Turner, A. P. F. *Chem. Soc. Rev.* **2013**, *42*, 3184-3196.
3. Zhou, W.; Gao, X.; Liu, D.; Chen, X. *Chem. Rev*. **2015**, *115*, 10575-10636.
4. Kairdolf, B. A.; Qian, X.; Nie, S. *Anal. Chem*. **2017**, *89*, 1015-1031.
5. Zhang, C.; Yeh, H. C.; Kuroki, M. T.; Wang, T. *Nat. Mater*. **2005**, *4*, 826-831.
6. Zhang, L.; Guo, S.; Dong, S.; Wang, E. *Anal. Chem.* **2012**, *84*, 3568-3573.
7. Hu, R.; Liu, T.; Zhang, X.-B.; Huan, S.-Y.; Wu, C.; Fu, T.; Tan, W. *Anal. Chem.* **2014**, *86*, 5009-5016.
8. Yang, Z.; Liu, H.; Zong, C.; Yan, F.; Ju, H. *Anal. Chem.* **2009**, *81*, 5484-5489.
9. Akhavan-Tafti, H.; Binger, D. G.; Blackwood, J. J.; Chen, Y.; Creager, R. S.; de Silva, R.; Eickholt, R. A.; Gaibor, J. E.; Handley, R. S.; Kapsner, K. P. *J. Am. Chem. Soc*. **2013**, *135*, 4191-4194.
10. Zhang, Q.; Zhao, B.; Yan, J.; Song, S.; Min, R.; Fan, C. *Anal. Chem.* **2011**, *83*, 9191-9196.
11. Lee, J.-S.; Ulmann, P. A.; Han, M. S. Mirkin, C. A. *Nano Lett.* **2008**, *8*, 529-533.
12. Wignarajah, S.; Suaifan, G. A. R. Y.; Bizzarro, S.; Bikker, F. J.; Kaman, W. E.; M. Zourob, *Anal. Chem.* **2015**, *87*, 12161-12168.
13. Lu, D.; Wang, J.; Wang, L.; Du, D.; Timchalk, C.; Barry, R. C.; Lin, Y. *Adv. Funct. Mater.* **2011**, *21*, 4371-4378 .
14. Abellán-LIobergat, A.; Jeerapan, I.; Bandodkar, A.; Vidal, I.; Canals, A.; Wang, J.; Morallon, E. *Biosens. Bioelectron*. **2017**, *91*, 885-891.
15. Zhang, X.; Young, M. A.; Lyandres, O.; Van Duyne, R. P. *J. Am. Chem. Soc*. **2005**, *127*, 4484-4489.
16. Costas, C.; Lopez-Puente, V.; Bodelon, G.; González-Bello, C.; Perez-Juste, J.; Pastoriza-Santos, I.; Liz-Marzan, L. M. *ACS Nano* **2015**, *9*, 5567-5576.
17. Li, J.; Zhu, Z.; Zhu, B.; Ma, Y.; Lin, B.; Liu, R.; Song, Y.; Tu, S.; Yang, C. *Anal. Chem.* **2016**, *88*, 7828-7836.
18. Tabakman, S. M.; Lau, L.; Robinson, J. T.; Price, J.; Sherlock, S. P.; Wang, H.; Zhang, B.; Chen, Z.; Tangsombatvisit, S.; Jarrell, J. A.; Utz, P. J.; Dai, H. *Nat. Commun*. **2011**, *2*, 466.
19. De La Rica, R.; Stevens, M. M. *Nat. Nanotechnol*. **2012**, *7*, 821-824.

20. Lequin, R. M. *Clin. Chem*. **2005**, *51*, 2415-2418.
21. Cheng, C.-M.; Martinez, A. W.; Gong, J.; Mace, C. R.; Phillips, S. T.; Carrilho, E.; Mirica, K. A.; Whitesides, G. M. *Angew. Chem., Int. Ed*. **2010**, *49*, 4771-4774.
22. Wick, M. R. *Ann. Diagn. Pathol.* **2012**, *16*, 71-78.
23. Ambrosi, A.; Airo, F.; Merkoçi, A. *Anal. Chem*. **2010**, *82*, 1151-1156.
24. Lin, J.; Liu, Y.; Huo, J.; Zhang, A.; Pan, Y.; Bai, H.; Jiao, Z.; Fang, T.; Wang, X.; Cai, Y.; Wang, Q.; Zhang, Y.; Qian, X. *Anal. Chem.* **2013**, *85*, 6228-6232.
25. Ye, H.; Yang, K.; Tao, J.; Liu, Y.; Zhang, Q.; Habibi, S.; Nie, Z.; Xia, X. *ACS Nano*, **2017**, *11*, 2052-2059.
26. Zou, B.; Ma, Y.; Wu, H.; Zhou, G. *Angew. Chem., Int. Ed.* **2011**, *50*, 7395-7398.
27. Gao, Z.; Huo, L.; Xu, M.; Tang, D. *Sci. Rep*. **2014**, *4*, 3966.
28. Yin, J.; Xu, T.; Zhang, N.; Wang, H. *Anal. Chem.* **2016**, *88*, 7730-7737.
29. Kim, E.; Howes, P. D.; Crowder, S. W.; Stevens, M. M. *ACS Sens*. **2017**, *2*, 111-118.
30. Qiu, L.; Zhang, Y.; Liu, C.; Li, Z. *Chem. Commun*. **2017**, *53*, 2926-2929.
31. Wang, L.-J.; Ren, M.; Zhang, Q.; Tang, B.; Zhang, C.-Y. *Anal. Chem*. **2017**, *89*, 4488-4494.
32. Ge, L.; Wang, W.; Sun, X.; Hou, T.; Li, F. *Anal. Chem*. **2016**, *88*, 2212-2219.
33. Wei, H.; Wang, E. *Chem. Soc. Rev*. **2013**, *42*, 6060-6093.
34. Zhang, Q.; Cobley, C. M.; Zeng, J.; Wen, L.-P.; Chen, J.; Xia, Y. J. *Phys. Chem. C* **2010**, *114*, 6396-6400.
35. Ye, H.; Liu, Y.; Chhabra, A.; Lilla, E.; Xia, X. *ChemNanoMat* **2017**, *3*, 33-38.
36. Gao, Z.; Liu, G. G.; Ye, H.; Rauschendorfer, R.; Tang, D.; Xia, X. *Anal. Chem*. **2017**, *89*, 3622-3629.
37. Gao, L.; Zhuang, J.; Nie, L.; Zhang, J.; Zhang, Y.; Gu, N.; Wang, T.; Feng, J.; Yang, D.; Perrett, S. *Nat. Nanotechnol*. **2007**, *2*, 577-583.
38. Josephy, P. D.; Eling, T.; Mason, R. P. *J. Biol. Chem*. **1982**, *257*, 3669-3675.
39. Hermanson, G. T. *Bioconjugate Techniques*, Academic Press, San Diego, 2nd ed., **2008.**
40. Rissin, D. M.; Kan, C. W.; Campbell, T. G.; Howes, S. C.; Fournier, D. R.; Song, L.; Piech, T.; Patel, P. P.; Chang, L.; Rivnak, A. J.; Ferrell, E. P.; Randall, J. D.; Provuncher, G. K.; Walt, D. R.; Duffy, D. C. *Nat. Biotechnol*. **2010**, *28*, 595-599.

41. Laxman, B.; Morris, D. S.; Yu, J.; Siddiqui, J.; Cao, J.; Mehra, R.; Lonigro, R. J.; Tsodikov, A.; Wei, J. T.; Tomlins, S. A.; Chinnaiyan, A. M. *Cancer Res*. **2008**, *68*, 645-649.
42. Armbruster, D. A.; Tillman, M. D.; Hubbs, L. M. *Clin*. *Chem*. **1994**, *40*, 1233-1238.
43. Armbruster, D. A.; Pry, T. *Clin*. *Biochem*. *Rev*. **2008**, *29*, S49-S52.
44. Kaur, K.; Forrest, J. A. *Langmuir* **2012**, *28*, 2736-2744.
45. Ju, Q.; Noor, M. O.; Krull, U. J. *Analyst* **2016**, *141*, 2838-2860.
46. Gupta, S.; Huda, S.; Kilpatrick, P. K.; Velev, O. D. *Anal*. *Chem*. **2007**, *79*, 3810-3820 .
47. Taton, T. A.; Mirkin, C. A.; Letsinger, R. L. *Science* **2000**, *289*, 1757-1760.

CHAPTER 8 PLATINUM-DECORATED GOLD NANOPARTICLES WITH DUAL FUNCTIONALITIES FOR ULTRASENSITIVE COLORIMETRIC IN VITRO DIAGNOSTICS[a]

8.1 Introduction

In vitro diagnostic (IVD) tests are crucial for patients and physicians to make timely and optimal decisions for patient care and treatment.[1-3] Colorimetric IVD, among many other types of IVD technologies, has received increasing attention in recent years due to its simplicity and cost effectiveness.[4-10] The test results of colorimetric IVDs can be conveniently read out with the naked eyes and, if needed, quantified by an inexpensive and portable device.[11] In particular, these features make colorimetric IVDs extremely desirable for field work and point-of-care tests that are urgently needed, especially in resource-limited settings.

Au nanoparticles (AuNPs) as signal reporters have been widely used in colorimetric IVDs for decades because of their superior physicochemical properties.[3, 12] First, they offer highly intense color signals (red, in most cases) owing to an optical phenomenon called localized surface plasmon resonance (LSPR).[13-15] AuNPs of ~40 nm show an absorption cross-section 5 orders larger than ordinary organic dyes.[16] Second, they can be easily functionalized with biomolecules (*e.g.*, antibodies and DNAs) by means of simple thiol-gold chemistry and/or electrostatic interactions.[17-20] Third, they are made of an inert noble metal and thus are highly stable, enabling them to survive harsh environments. Moreover, they can be easily and reproducibly synthesized

[a]Reprinted with permission from *Nano Lett*. **2017**, *17*, 5572-5579

Haihang Ye contributed the conception and design of the related work, acquisition and interpretation of data, and preparation of the article.

in common chemical laboratories. The past few decades have witnessed a variety of AuNP-based IVD systems with home pregnancy test being one of the most familiar examples.[3, 21-24] Despite the simplicity and practicality, it remains a challenge to substantially enhance the sensitivity of AuNP-based colorimetric IVDs without adding complexity. Note that high detection sensitivity is critical to many important applications such as early detection of cancers and infectious diseases for which the concentrations of related biomarkers are very low.[25, 26] Because the detectable color signal in AuNP-based IVDs originates from the plasmonics of AuNPs, the detection sensitivity is essentially confined by the inherent plasmonic activity.

In this work, we report a novel strategy to circumvent such confinement of AuNP plasmonics and thus break through the detection limit barrier of associated colorimetric IVDs. Specifically, in this strategy conventional AuNPs are decorated with conformal, thin skins of Pt to form unique Au@Pt$_{n\mathrm{L}}$ core@shell NPs (**Figure 8.1a**). The number (*n*) of Pt atomic layers could be precisely controlled in the range of 1-10. We demonstrated that as long as the Pt shell is ultrathin (several atomic layers) the plasmonic property of the AuNP cores underneath Pt is well retained, making the resultant Au@Pt$_{n\mathrm{L}}$ NPs as red as the initial AuNPs (**Figure 8.1b**). On the other hand, Pt shells on the surface endow the Au@Pt$_{n\mathrm{L}}$ NPs with ultrahigh peroxidase-like catalytic activities, allowing them to rapidly generate blue-colored molecules by catalyzing the oxidation of TMB[27] by H_2O_2 in aqueous solution. It is worth mentioning that this catalytic reaction is extremely suitable for IVDs and has been widely used in commercial diagnostic kits mainly because (*i*) both TMB and H_2O_2 are cost-effective and nontoxic, (*ii*) the reaction can be conveniently conducted in aqueous system and at room temperature, and (*iii*) the blue-colored product [*e.g.*, oxidized TMB (oxTMB) with λ_{max} = 653 nm] has a large molar extinction coefficient.[27] Significantly, the intensity

of blue color from catalysis is orders of magnitude stronger than that of the intrinsic red color from plasmonics, ensuring an enhanced detection sensitivity. These dual functionalities, plasmonics and catalysis, of the Au@Pt_{nL} NPs make them particularly suitable for colorimetric IVDs. They can offer two different detection alternatives: one produced just by the red color of interior AuNPs (low-sensitivity mode) and the second more sensitive blue color produced by the Pt shell through catalysis (high-sensitivity mode), achieving an "on-demand" tuning of the detection performance. It should be pointed out that the low-sensitivity mode is faster and more convenient than the high-sensitivity mode because the latter involves an additional signal enhancement procedure (*e.g.,* 5 min TMB/H_2O_2 treatment process). In practical use, one will first perform the low-sensitivity mode. High-sensitivity mode is only needed when no signal is observed in low-sensitivity mode (for samples with low concentration of analytes or negative samples). Using lateral flow assay as a model IVD system, we demonstrated that the detection sensitivity could be enhanced by ~100 times as compared to conventional AuNPs as the benchmark.

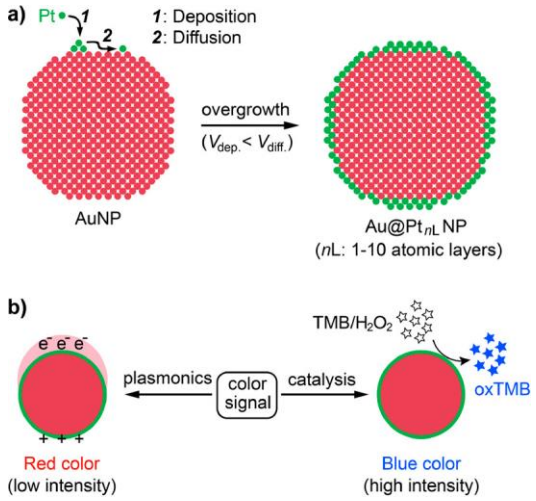

Figure 8.1 Schematics showing (a) the fabrication of Au@Pt$_{n\text{L}}$ NPs in which Pt atoms are deposited onto an AuNP to form a conformal, thin Pt shell with thicknesses of 1-10 atomic layers and (b) two types of color signal generated from Au@Pt$_{n\text{L}}$ NPs under different mechanisms. In (a), the rate of atom deposition is controlled to be slower than that of surface diffusion ($V_{\text{dep.}} < V_{\text{diff.}}$).

8.2 Results and Discussion

We started with the synthesis of Au@Pt$_{n\text{L}}$ NPs that was conducted using seed-mediated growth. In a standard synthesis, an aqueous solution of Na_2PtCl_6 as precursor to Pt was injected slowly (1.2 mL/h, with a syringe pump) into a mixture containing ~40 nm citrate-capped AuNPs with an overall spherical shape as the seeds, L-ascorbic acid as a reductant, and sodium citrate as a colloidal stabilizer, which had been preheated to 90 °C under magnetic stirring. We chose ~40 nm citrate-capped AuNPs as a model seed because they have been extensively used for various IVD systems.[28-31] As shown by the TEM images in **Figure S8.1** (Appendix F), the Au seeds displayed uniform spherical shapes and smooth surfaces. Most of them contained multiply twinned defects. Their average diameter was measured to be 40.2 nm by randomly analyzing 200 particles. **Figure 8.2a, b**, respectively, shows typical low- and high-magnification TEM images of

the Au@Pt$_{n\mathrm{L}}$ NPs prepared from a standard synthesis. It can be seen that the spherical shape, smooth surface, and twin structures of the Au seeds were well retained after Pt growth, implying the involvement of a layer-by-layer growth mode. The average edge length of the Au@Pt$_{n\mathrm{L}}$ NPs was measured to be 42.1 nm, which was 1.9 nm greater than that of the initial Au seeds. Therefore, on average, the thickness of the Pt shell deposited on the Au spherical seed was about 0.95 nm. **Figure 8.2c** shows a HAADF-STEM image of the same sample, from which the 3D spherical shape and smooth surface were more evident relative to the TEM images. The high-resolution TEM image of an individual particle (**Figure 8.2d**) reveals the continuous lattice fringes from Au core to Pt shell, indicating an epitaxial relationship between these two metals.

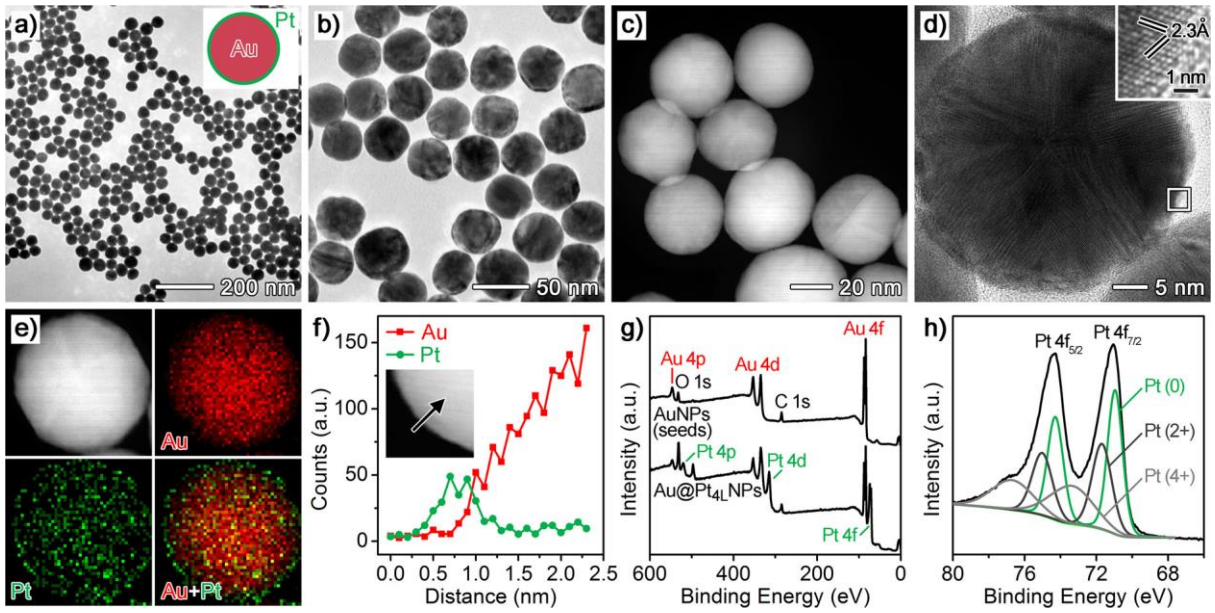

Figure 8.2 Morphological, structural, and compositional analyses of Au@Pt_{4L} NPs that were prepared from a standard synthesis. (a, b) TEM images at two different magnifications. (c) HAADF-STEM image. (d) High-resolution TEM image of an individual particle. Inset shows a magnified image of the region marked by a white box. (e) EDX mapping image of an individual particle (red = Au, green = Pt). (f) Line-scan EDX spectra of elemental Au and Pt that were recorded from an individual particle (inset) along a direction as indicated by the black arrow. (g) XPS survey spectra of the Au@Pt_{4L} NPs and initial AuNP seeds. (h) High-resolution XPS spectra of the Pt 4f region shown in (g).

Because Au and Pt have similar atomic masses and lattice constants, it is almost impossible to resolve Pt from Au via electron microscopy.[32] As such, the elemental distribution of Au and Pt in the sample was determined by energy-dispersive X-ray (EDX) mapping and line-scans analyses. From the EDX mapping image (**Figure 8.2e**), Au could only be observed in the interior (red) while Pt was distributed across the entire particle including the shell (green), suggesting an Au@Pt core@shell structure and the conformal coating of Pt on Au surface. The core@shell structure was further confirmed by the EDX line-scan profile recorded along a central axis direction of an individual sphere (**Figure 8.2f**), where the Pt trace dominated the shell region. To further confirm

Pt was conformally distributed on Au surfaces, those Au@Pt_{nL} NPs were etched with a chemical etchant of which strength is sufficiently strong to etch Au while too weak to react with Pt.[33] As shown by the TEM images in **Figure 8.3**, most of the Au@Pt_{nL} NPs were intact after etching. Only ~2% of them was converted to thin nanoshells with a hollow interior. This result suggested that conformal Pt overlayers existed in most of the Au@Pt_{nL} NPs, which prevented the Au cores from being etched. For a small portion of Au@Pt_{nL} NPs that were not fully covered by Pt, Au cores were etched away, leaving only nanoshells of Pt. The surface properties of the Au@Pt_{nL} NPs were determined by X-ray photoelectron spectroscopy (XPS). It can be seen that the XPS survey spectrum of the Au@Pt_{nL} NPs was similar to that of the initial Au seeds, except for the appearance of Pt characteristic peaks (**Figure 8.2g**). This observation suggests that the surface ligands on AuNPs remain unchanged after they had been coated with Pt, which ensured the simplicity of antibody functionalization as discussed later. The high-resolution spectra of the Pt 4f peaks (**Figure 8.2h**) revealed the existence of three chemical states for Pt species, where the $Pt^0$was dominant.

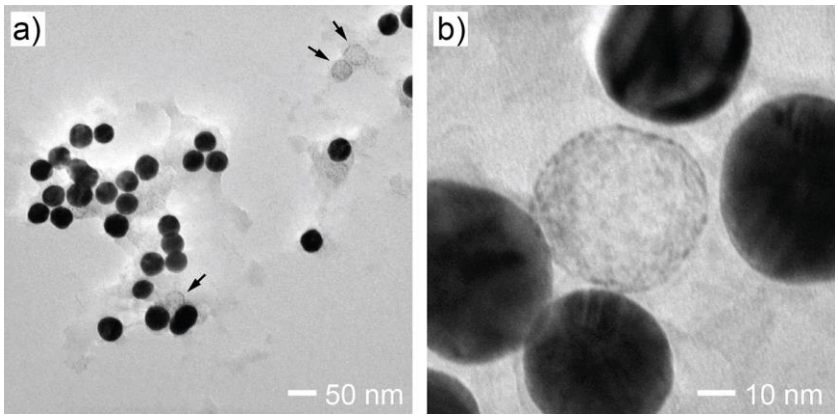

Figure 8.3 (a) Low- and (b) high-magnification TEM images of a sample that was prepared by etching the Au@Pt NPs shown in **Figure 8.2** with a CTAB solution containing I^- and Au^{3+} ions. In (a), black arrows indicate nanoshells with a hollow interior. By randomly analyzing ~500 particles under TEM, the statistical data showed that most of Au@Pt NPs were intact after etching. Only ~2% of them were converted to nanoshells.

To quantitatively determine the average number (*n*) of Pt atomic layers for the Au@Pt_{nL} NPs shown in **Figure 8.2**, the sample was subject to inductively coupled plasma-optical emission spectrometry (ICP-OES) analysis. The mass ratio of Au to Pt was measured to be 6.49:1. According to this ICP-OES data, the size of Au spherical seeds, and the densities of Au and Pt, the thickness of Pt shell was quantified to be 0.89 nm (see **Figure S8.2** in Appendix F for details), which is in good agreement with the value of 0.95 nm measured from the change to average diameter by TEM. In the following discussion, Pt shell thickness is referred to the data from ICP-OES because it averages over a much larger number of particles than TEM. Because a nanosphere of face-centered cubic structure tends to expose low-energy (111) surfaces,[34, 35] for rough estimation here we assume Pt layers are spaced by Pt{111} planes with the interplanar distance of ~0.23 nm.[36, 37] Thus, the average number of Pt atomic layers was ~4 for this sample, so is denoted as Au@Pt_{4L} NPs.

As demonstrated in our previous studies,[38-41] so long as the deposition of Pt on Au was directed to follow a layer-by-layer mode, the thickness of the Pt shells could be conveniently controlled with atomic precision by simply adjusting the amount of Pt precursor introduced to the synthesis. The key to induce and maintain such layer-by-layer mode was to ensure a slow atom deposition relative to surface diffusion ($V_{dep.} < V_{diff.}$, see **Figure 8.1a**) so the Pt adatoms could spread across the entire Au surface, resulting in the formation of a conformal and smooth Pt coating.[38] This argument was supported by our experimental result that Pt dendrites (**Figure 8.4**) instead of smooth shells were formed on Au seeds when the atom deposition rate was raised by increasing the injection rate of Pt precursor while all other conditions were kept unchanged. With this mechanistic understanding, we were able to finely tune the thickness of Pt shells from 1 to 10 atomic layers that were confirmed by both electron microscopy imaging and ICP-OES analysis (see **Table S8.1** in Appendix F). For example, Au@Pt_{2L} NPs (**Figure S8.3a** in Appendix F) and Au@Pt_{7L} NPs (**Figure S8.3b** in Appendix F), respectively, could be obtained by adjusting the amount of Pt precursor from 347 μL in a standard synthesis to 170 and 628 μL.

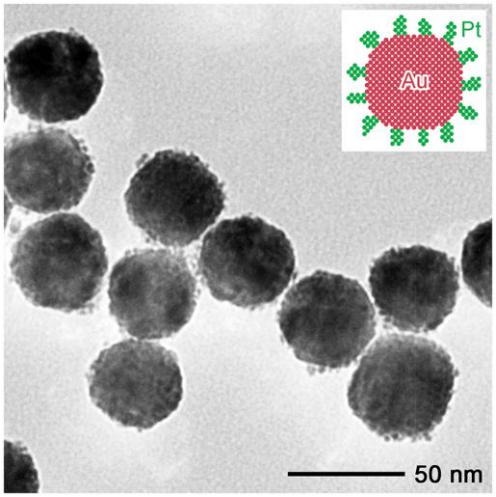

Figure 8.4 TEM image of Au-Pt bimetallic nanocrystals synthesized using the standard procedure for $Au@Pt_{4L}$ NPs except that the injection rate of Na_2PtCl_6 solution was increased from 1.2 to 120 mL/h. Inset shows a corresponding 2D atomic model.

We then evaluated the plasmonic properties of the $Au@Pt_{nL}$ NPs (n = 0-10). Here, $Au@Pt_{0L}$ NPs correspond to the initial AuNP seeds. **Figure 8.5a** compares the appearance of aqueous suspensions of $Au@Pt_{nL}$ NPs and initial Au seeds with the same particle concentration. An overall red color can be seen for all the samples, whereas the color intensity decreased with the increase of Pt atomic layers. **Figure 8.5b** shows the corresponding UV-vis spectra recorded from these samples. As the number (n) of Pt layers increased, the major LSPR peak at ~520 nm broadened, together with an intensity decrease. Compared to initial Au seeds, the extinction at 520 nm for the $Au@Pt_{nL}$ NPs was decreased by ~11% and ~15%, respectively, when n = 2 and 4 (see inset of **Figure 8.5b**). At n = 10, the decrease was enlarged to ~20%. Further increase of the Pt shell thickness led to the diminishment and eventual disappearance of the characteristic red color. For instance, the red color is barely detectable when the thickness of Pt shell reached 10 nm (about 44 Pt atomic layers, see **Figure S8.4** in Appendix F). These data demonstrate that the ultrathin coating of Pt (preferably several atomic layers) is critical to the retaining of plasmonic properties.

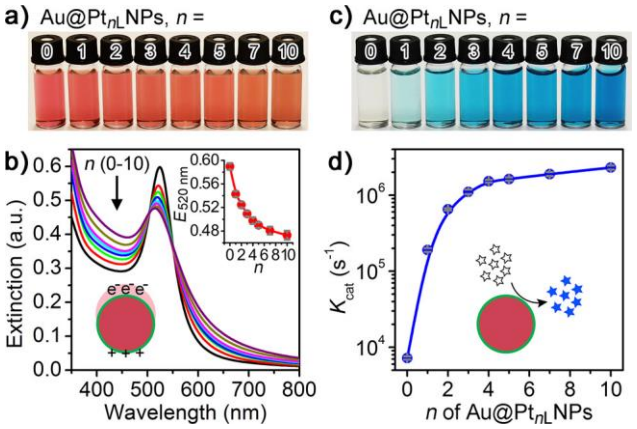

Figure 8.5 Plasmonic (a,b) and catalytic (c,d) properties of Au@Pt$_{nL}$ NPs, where n denotes the number of Pt atomic layers (n = 0 corresponds to the initial AuNP seeds shown in **Figure S8.1** in Appendix G). (a) A photograph taken from aqueous suspensions of Au@Pt$_{nL}$ NPs with the same particle concentration. (b) Corresponding UV-vis spectra recorded from the samples in (a). Inset shows a plot of extinction at 520 nm ($E_{520\ nm}$) against n. (c) A photograph taken from reaction solutions (*e.g.*, oxidation of TMB by H_2O_2) catalyzed by Au@Pt$_{nL}$ NPs of the same particle concentration. In all measurements, the reaction time was fixed at t = 3 min. The blue color was originated from the oxidized TMB as the product (λ_{max} = 653 nm). (d) A plot comparing the catalytic constant (K_{cat}) of different Au@Pt$_{nL}$ NPs. Error bars in (b, d) indicate the standard deviations of three independent measurements.

The peroxidase-like catalytic property of Au@Pt$_{nL}$ NPs was investigated with the oxidation of TMB by H_2O_2 being as a model catalytic reaction.[42-44] As shown in **Figure 8.5c**, Au@Pt$_{nL}$ NPs could rapidly generate a blue-colored product (*e.g.*, oxTMB) through the catalytic reaction. The intensity of blue color increased as the number (n) of Pt layers increased and became saturated at n = 4. In contrast, the initial Au seeds (n = 0) could barely catalyze the reaction (**Figure 8.5c**). To quantify the catalytic efficiency, catalytic constant (K_{cat}) was determined through the apparent steady-state kinetic assay, as shown in **Figure 8.6** for the sample of Au@Pt$_{4L}$ NPs.[42, 45] As summarized by **Figure 8.5d**, K_{cat} for the Au@Pt$_{nL}$ NPs ($n \geq 4$) reached the regime of

10^6 s^{-1}, which is several orders of magnitude higher than those of the initial AuNPs and natural peroxidases.[42]

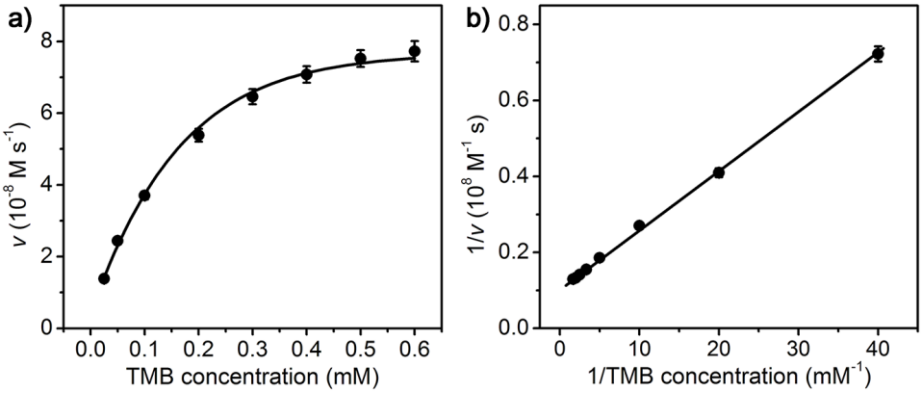

Figure 8.6 Kinetic assays of the Au@Pt_{4L} NPs as catalysts for the oxidation of TMB by H_2O_2. The initial reaction velocity (v) was measured in 0.2 M NaOAc/HOAc buffer pH 4.0, containing 2.0 M H_2O_2, 6.32×10^{-14} M Au@Pt_{4L} NPs, and TMB of different concentrations at room temperature. (a) Plot of v against TMB concentration; (b) Double-reciprocal plot generated from (a), with which the catalytic constant (K_{cat}) was determined. Error bars indicate the standard deviations of three independent measurements.

To better understand the relationship between the structure of Au@Pt_{nL} NPs and their plasmonic and catalytic properties, we conducted preliminary theoretical calculations. We first performed finite-difference time-domain (FDTD) simulations to investigate the extinction cross-section spectra of Au@Pt_{nL} NPs (n = 0-10).[46] The simulation results are shown in **Figure 8.7**. It can be seen that the AuNP seeds displayed a major LSPR peak at ~532 nm. When they were coated with Pt of different atomic layers (n), their LSPR peak gradually blue-shifted and broadened as n increased. The peak intensity decreased rapidly as n increased from 0 to 4. Thereafter (n = 5-10), the decrease of peak intensity slowed down. The overall trends of the changes in LSPR peak position, shape, and intensity agreed well with the experimental results shown in **Figure 8.5b**. In order to gain insight into the peroxidase-like catalytic activities of those Au@Pt_{nL} NPs, we

performed density functional theory (DFT) calculations to study the surface electronic structures of Pt overlayers on Au surface where the d-band center positions were derived. It is well documented that the d-band center of surface atoms of a transition-metal catalyst is a good measurement for its binding affinity toward adsorbates and therefore its catalytic activity.[47-50] **Figure 8.8** shows the partial density of state (PDOS) profiles of *5d* orbitals for the outmost atoms of Au(111) and Au@Pt$_{n\mathrm{L}}$(111) (n = 1-10) surfaces. It can be seen that the *d*-band of Au(111) surface was narrower and had a much lower density near the Fermi level compared to those of Au@Pt$_{n\mathrm{L}}$(111) surfaces. These results indicated that Au(111) was less catalytically active than Au@Pt$_{n\mathrm{L}}$(111) surfaces,[51, 52] which is in good agreement with the experimental results shown in **Figure 8.5c, d**. For the Au@Pt$_{n\mathrm{L}}$(111) surfaces with n = 1-10, significant change of d-band center positions was only observed when n increased from 1 to 3, as shown in **Figure 8.8b**, suggesting that the change of catalytic activity of Au@Pt$_{n\mathrm{L}}$(111) should be obvious in the range of n = 1-3.[47] This result is consistent with the experimental observations that the catalytic activity of Au@Pt$_{n\mathrm{L}}$ NPs drastically increased as n increased from 1 to 3 and tended to become saturated when $n \geq 4$ (**Figure 8.5d**).

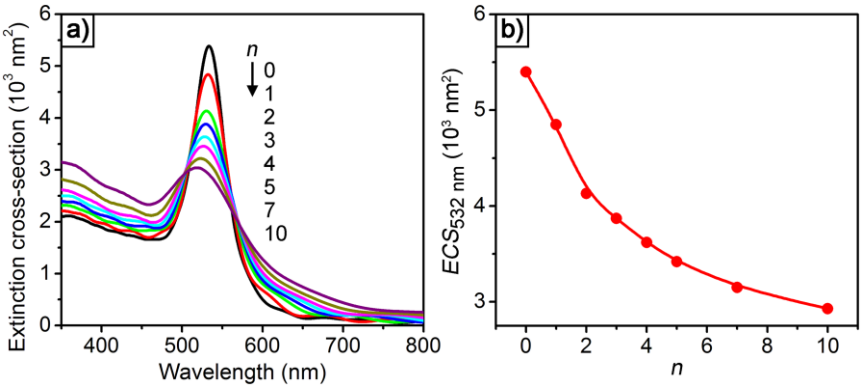

Figure 8.7 (a) FDTD-simulated extinction cross-section spectra of Au@Pt$_{n\mathrm{L}}$ NPs, where *n* denotes the number of Pt atomic layers (*n* = 0 denotes the initial AuNP seeds). (b) Plot of extinction cross-section at 532 nm ($ECS_{532\ nm}$) against *n*.

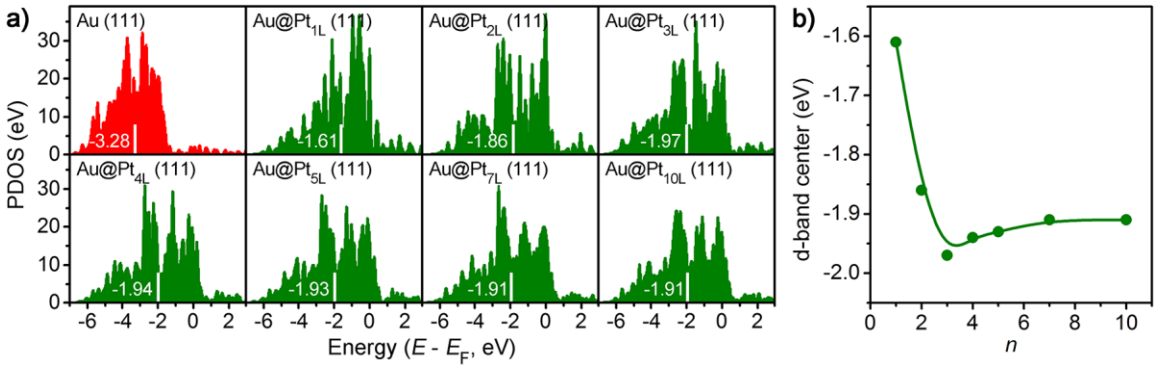

Figure 8.8 (a) Partial density of state (PDOS) profiles of *5d*-orbitals for the outmost atoms of Au(111) and Au@Pt$_{n\mathrm{L}}$(111) surfaces (*n* = 1-10). (b) Plot of *d*-band centers (relative to the Fermi level (E_F)) of Au@Pt$_{n\mathrm{L}}$(111) against *n*. Note the Fermi level is set as zero. In (a), the calculated *d*-band centers are marked with white lines.

It should be emphasized that even though Au@Pt core@shell nanostructures have been extensively reported in literature,[53-57] most of those studies did not precisely control over the surface structure and shell thickness at the atomic level. Particularly, in most cases the deposition of Pt on Au seeds was not maintained along a layer-by-layer mode during the entire course of growth.[40] As a result, Pt shells in the final products oftentimes took irregular morphologies. In the present work, Pt shells with a well-defined morphology and thickness of 1-10 atomic layers were

successfully coated on Au seeds, which allowed us to systematically investigate the structure–property relationships from both experimental and theoretical angles. We believe the insights from this study will serve as a strong foundation to inspire future work.

Because n = 4 for the Au@Pt_{nL} NPs well balanced the decrease of plasmonic activity and the increase of catalytic activity, the Au@Pt_{4L} NPs (**Figure 8.2**) were chosen for subsequent studies. It should be emphasized that the intensity of blue color from catalysis was significantly higher than that of the intrinsic red color from plasmonics. Specifically, the molar extinction coefficient of the 40.2 nm AuNPs was determined to be ~9.5×10^9 M^{-1} cm^{-1} (see **Figure S8.5** in Appendix F for details), which is consistent with literature reports on 40 nm AuNPs.[16, 58, 59] In contrast, the equivalent molar extinction coefficient (defined as the total light extinction of colored products catalyzed at t = 5 min) of the Au@Pt_{4L} NPs was calculated to be ~1.8×10^{13} $M^{-1}\cdot cm^{-1}$ (see **Figure S8.5** in Appendix F for details). To our knowledge, this value represents the record-high extinction efficiency among all types of nanoparticles with similar size. Taken together, the color signal of ~40 nm AuNPs could be enhanced by 3 orders of magnitude through a simple substrate treatment process (5 min, room temperature, and aqueous system), which forms the basis for exceptional detection sensitivity. Notably, this enhancement is expected to be more evident for AuNPs of smaller sizes since the molar extinction of AuNPs decreases at a fast rate proportional to the cube of particle radius.[60]

Finally, we applied the Au@Pt_{4L} NPs to lateral flow assay (LFA) of human PSA as a model cancer biomarker,[61] according to the principle shown in **Figure 8.9**. LFA is one of a handful of point-of-care techniques that can claim to have taken tests out of the laboratory.[62-65] AuNPs with tens of nanometers in size have been widely used in LFA as colorimetric labels for decades because

of their superior physicochemical properties.[22, 66] While creative research effort continues to be invested into the improvement in detection performance for AuNP-based LFAs, there is still an unmet need for a broadly applicable methodology to provide ultralow detection limits. A transformative idea to enhance the detection sensitivity of LFA is to amplify the plasmonics of AuNPs. The most commonly used strategy for plasmonics amplification is to assemble numerous AuNPs on larger-sized carrier particles. For example, Xu and co-workers decorated silica rods of several micrometers with AuNPs.[67] AuNPs ($\sim 10^4$) were assembled on a single silica rod. Owing to the increased AuNP density, the detection limit was lowered more than 10 times compared to conventional AuNP based LFA. Similarly, branched dendrimers as carriers also displayed enhanced color intensity.[68] Despite these demonstrations, this strategy is limited by the loading capacity of a carrier and the bulkiness of the AuNPs-carrier complexes, which inhibit the particles' migration within the strip thus exacerbating the steric effect for bioreceptor binding to analytes. Another notable strategy for plasmonics amplification is to enlarge the AuNPs on the test line through post gold or silver enhancement, in which the size and thus optical intensity of AuNPs is increased.[69-71] This strategy is troubled by using large amounts of highly toxic Au^{3+} or Ag^{+}. Both ions adversely affect the environment and have serious biological effects on human health.[72-74] Unless this issue can be addressed, it will be impractical to implement this method into LFAs, especially in nonlaboratory scenarios. Taken together, it remains a challenge to substantially enhance the sensitivity of AuNP-based LFAs that are presently confined by the inherent plasmonics of AuNPs.

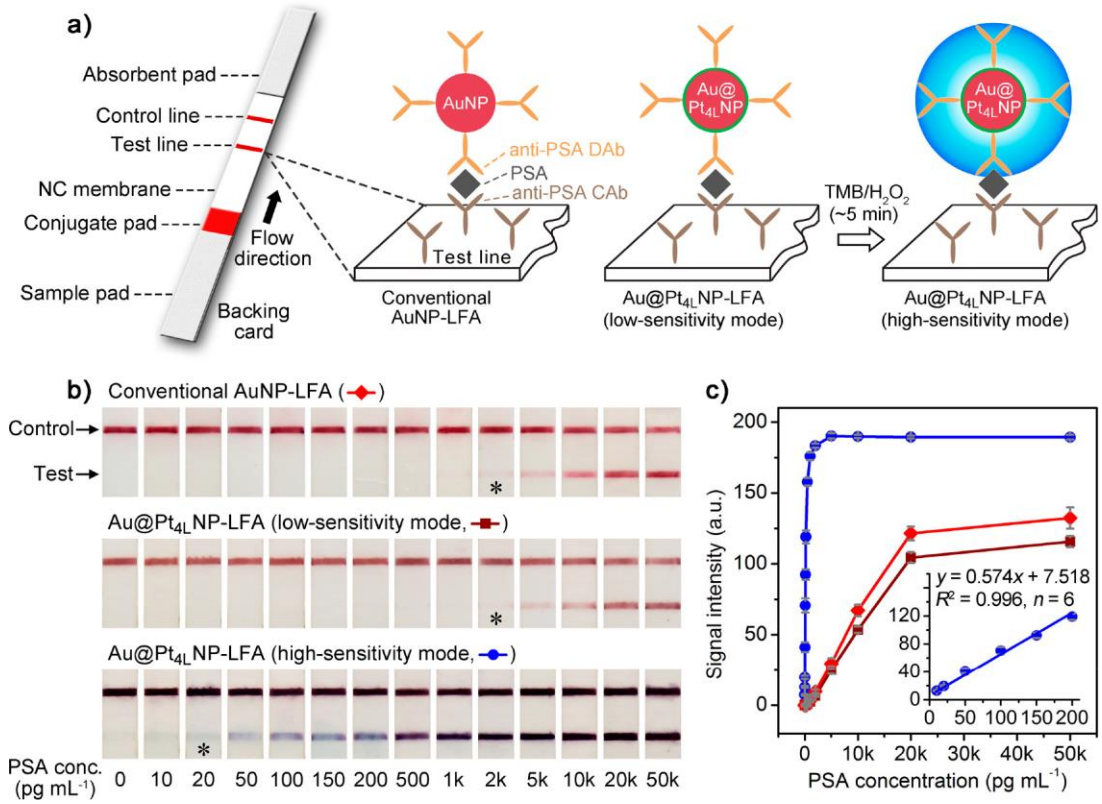

Figure 8.9 Detection of PSA with conventional AuNP-based LFA (AuNP-LFA) and Au@Pt_{4L} NP-based LFA (Au@Pt_{4L} NP-LFA). (a) Schematics showing the principles of AuNP-LFA and Au@Pt_{4L} NP-LFA at low- and high-sensitivity modes (see Section 8.4.10 for details about the preparation of LFAs). (b) Representative photographs taken from the LFAs of PSA standards. The asterisks (*) indicate detection limits by the naked eyes. (c) Corresponding calibration curves of the detection results shown in (b). Error bars indicate the standard deviations of six independent measurements. Inset shows the linear range region of the Au@Pt_{4L} NP-LFA at high-sensitivity mode.

For direct comparison, we benchmarked the performance of Au@Pt_{4L} NPs in LFA against initial ~40 nm AuNPs by using the same set of antibodies and materials. Procedures for the Au@Pt_{4L}NP- and AuNP-based LFAs were also kept the same except that an additional enhancement procedure (*e.g.*, TMB/H_2O_2 treatment) was involved in the "high-sensitivity" Au@Pt_{4L} NP-LFA (see **Figure 8.9a**). It is worth noting that Au@Pt_{4L} NPs could be easily

functionalized with antibodies through a simple incubation process that is usually used for conventional AuNPs (**Figure S8.6** in Appendix F for details).[75, 76] This facile antibody functionalization of Au@Pt_{4L}NPs could be ascribed to the existence of similar ligands on the surfaces as conventional AuNPs that had been demonstrated by the XPS data shown in **Figure 8.2g**.

PSA standards with various concentrations were monitored in test strips. The detection results were recorded with a digital camera (**Figure 8.9b**) and were subject to quantification using Adobe Photoshop software (**Figure 8.9c**). It can be seen that intensities of red bands at the test line region for both AuNP- and Au@Pt_{4L} NP-LFAs ("low-intensity mode") were almost the same. The naked eye detection limit was about 2 ng·mL^{-1} of PSA for both LFAs. This result suggests that the Au@Pt_{4L} NPs could be utilized in the same fashion as conventional AuNPs without the compromise of performance. For Au@Pt_{4L} NP-LFA at the "high-intensity mode", blue/purple lines could be resolved for strips applied with PSA standards of concentrations as low as 20 pg·mL^{-1}. It should be mentioned that a faint blue color was observed for the zero calibrator under high-sensitivity mode. This background signal may be caused by the nonspecific binding of a small amount of Au@Pt_{4L} NPs to the test line region, which were capable of catalyzing the formation of visible blue colored oxTMB molecules. **Figure 8.9c** compares the calibration curves of the three LFAs that were generated by plotting the color intensity at test line against the PSA concentration. In particular, a quality linear relationship (R^2 = 0.996) in the range of 10-200 pg·mL^{-1} PSA was observed for the "high-sensitivity" Au@Pt_{4L} NP-LFA (inset of **Figure 8.9c**). The detection limit, defined as the concentration corresponding to a signal that is 3 times the standard deviation above the zero calibrator,[77, 78] was calculated to be 3.1 pg·mL^{-1} for the "high-sensitivity" Au@Pt_{4L} NP-

LFA. It is worth pointing out that this detection limit is even lower than what could be achieved by commercial enzyme-linked immunosorbent assay (ELISA) kit (4.9 $pg{\cdot}mL^{-1}$, Abcam plc., United Kingdom, **Figure 8.10**), which involves complicated operation procedures and instruments. In comparison, the detection limits of the AuNP-LFA and "low-sensitivity" Au@Pt_{4L}NP-LFA were determined to be 272 and 322 $pg{\cdot}mL^{-1}$, respectively, based on their calibration curves (**Figure 8.9c**). These results demonstrated that Au@Pt_{4L} NP could enhance the sensitivity of conventional LFA by ~100 times, enabling it to rival the sensitivities of other sophisticated instrument-based IVD techniques (*e.g.*, ELISA). Such a significant enhancement in sensitivity is only paid by a simple 5 min substrate treatment process at room temperature. It should be mentioned that the magnitude of color signal enhancement by Au@Pt_{4L} NPs relative to conventional AuNPs in LFA test (~100 times, **Figure 8.9**) was lower than the case when Au@Pt_{4L}NPs were suspended in aqueous solution (~1,000 times, see **Figure 8.5** and **Figure S8.5** in Appendix F). Note in LFA test, Au@Pt_{4L} NPs were immobilized and accumulated on a solid phase (*e.g.,* nitrocellulose the membrane of test strip). Therefore, the relatively low signal enhancement in LFA test can be ascribed to the compromise of catalytic activity of Au@Pt_{4L} NPs that was caused by (*i*) the same nanocatalysts-medicated catalytic reaction in a solid-solution phase is generally less effective than in a solution phase[79] and (*ii*) the aggregation of Au@Pt_{4L} NPs in LFA test strips reduced the total surface area of active Pt surface.

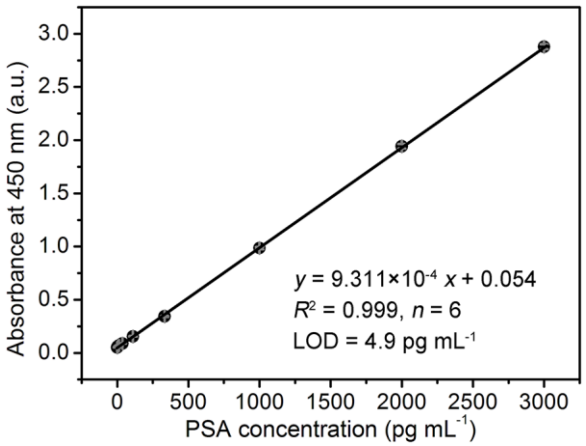

Figure 8.10 Calibration curve of a commercial PSA ELISA kit (Abcam plc., United Kingdom). Error bars indicate the standard deviations of six independent measurements. The limit of detection, defined as the concentration corresponding to a signal that is 3 times the standard deviation above the zero calibrator, was determined to be 4.9 pg·mL^{-1}.

We also compared the performance of Au@Pt$_{4L}$ NPs in LFA of PSA standards with those of Pt dendrites coated AuNPs (*e.g.*, the sample shown in **Figure 8.4**, which will be referred to as "Au@Pt$_{dendrite}$ NPs") and PtNPs (**Figure 8.11**) with similar sizes and the same surface ligands (*e.g.*, citrate). In the comparisons, all experimental conditions were kept unchanged except for the substitution of Au@Pt$_{4L}$ NPs with the same amount of Au@Pt$_{dendrite}$ NPs or PtNPs. As shown in **Figure 8.12**, the detection sensitivity of Au@Pt$_{dendrite}$ NP-LFA was comparable to that of Au@Pt$_{4L}$NP-LFA in both low- and high-sensitivity modes. PtNPs were synthesized according to a previously reported procedure with slight modifications.[80] As shown by the TEM image in **Figure 8.11**, the PtNPs displayed relatively irregular surface and broad size distribution compared to the Au@Pt$_{4L}$ NPs. **Figure 8.13** shows the performance of those PtNPs in LFA of PSA standards. It can be seen that the detection sensitivity of PtNP-LFA was similar to that of Au@Pt$_{4L}$ NP-based LFA under high-sensitivity mode. However, under low-sensitivity mode, its detection sensitivity was several times lower than Au@Pt$_{4L}$ NP-LFA. This difference can be

ascribed to the fact that Au@Pt_{4L} NPs with Au cores possess superior optical properties relative to the PtNPs of similar size.[81] It should be emphasized that the Au@Pt_{nL} NPs presented in this work are much more uniform in terms of size, shape, and elemental distribution than the Au@$Pt_{dendrite}$ NPs and PtNPs. Accordingly, they are expected to provide better detection reproducibility.[82] In addition, their properties (*e.g.*, plasmonic and catalytic activities) were well understood at the atomic level. Therefore, we believe the Au@Pt_{nL} NPs are more suitable for biosensing applications, providing sensitive and reliable tests.

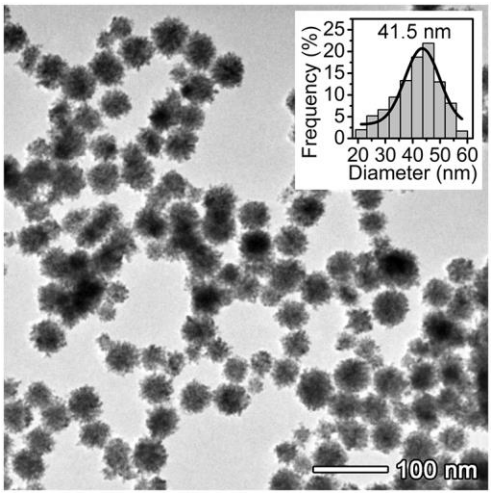

Figure 8.11 TEM image of citrate-capped Pt nanoparticles. Inset shows the distribution of diameter for this sample.

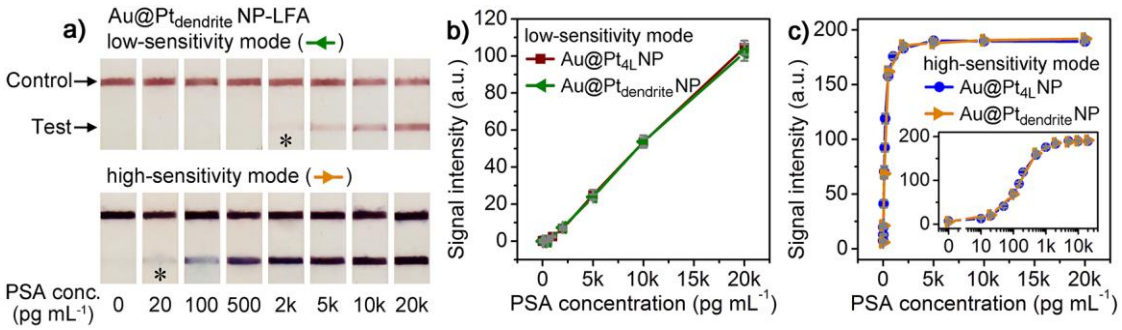

Figure 8.12 Comparison of the performance of Au@Pt$_{4L}$ NPs (**Figure 8.2**) and Au@Pt$_{dendrite}$ NPs (**Figure 8.4**) in LFA of PSA standards. (a) Representative photographs taken from the LFAs of PSA standards. The asterisks (*) indicate detection limits by the naked eyes; (b, c) Corresponding calibration curves of the detection results shown in (a). Error bars indicate the standard deviations of six independent measurements. In (b, c), the data of Au@Pt$_{4L}$ NP-LFA was retrieved from **Figure 8.9**.

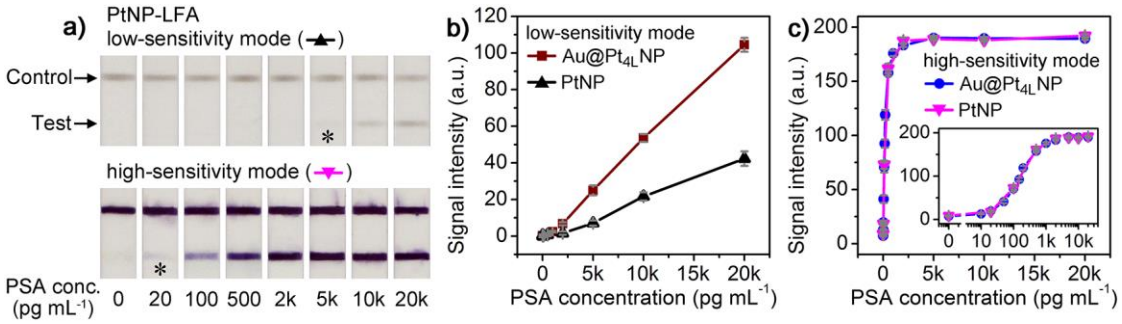

Figure 8.13 Comparison of the performance of Au@Pt$_{4L}$ NPs (**Figure 8.2**) and PtNPs (**Figure 8.11**) in LFA of PSA standards. (a) Representative photographs taken from the LFAs of PSA standards. The asterisks (*) indicate detection limits by the naked eyes; (b, c) Corresponding calibration curves of the detection results shown in (a). Error bars indicate the standard deviations of six independent measurements. In (b, c), the data of Au@Pt$_{4L}$ NP-LFA was retrieved from **Figure 8.9**.

To demonstrate the potential clinical use of the "high-sensitivity" Au@Pt$_{4L}$ NP-LFA, we applied it to quantifying PSA from human plasma samples (from a healthy female donor, provided by the UP-Health System-Portage, Houghton, Michigan, United States) that had been spiked with

PSA at concentrations of 20-160 pg·mL^{-1}. The detection was benchmarked against a commercial ELISA kit. As summarized in **Table 8.1**, the analytical recoveries for Au@Pt$_{4L}$ NP-LFA in analyzing the five PSA spiked human plasma samples were determined to be in the range of 94.5-106.6%. The coefficient of variation (n = 6) for all samples was below 7.3%. The detection results correlated well with the parallel tests by commercial ELISA kit with a correlation coefficient R^2 = 0.992 (see **Table 8.1** and **Figure 8.14**). These data demonstrated that the performance of Au@Pt$_{4L}$ NP-LFA was not influenced by the complex matrices in human plasma, suggesting the feasibility of the new LFA in analyzing clinical samples.

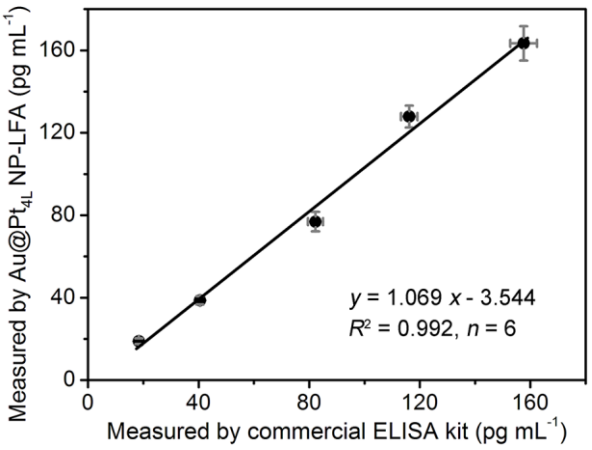

Figure 8.14 Correlation analysis between the Au@Pt$_{4L}$ NP-LFA and commercial ELISA kit in quantifying PSA from five PSA-spiked serum samples. Error bars indicate the standard deviations of six independent measurements.

Table 8.1 Performances of Au@Pt_{4L} NP-LFA (high-intensity mode) and a commercial ELISA kit (Abcam plc., United Kingdom) in detecting PSA-spiked human plasma samples

	PSA amount spiked ($pg \cdot mL^{-1}$)	**PSA amount measured ($pg \cdot mL^{-1}$)**	**coefficient of variations (%, *n* = 6)**	**recovery (%)**
Au@Pt_{4L}NP-LFA	20	18.9	7.3	94.5
	40	38.7	5.2	96.8
	80	76.9	6.2	96.1
	120	127.9	4.1	106.6
	160	163.4	5.1	102.1
commercial ELISA kit	20	18.4	3.6	92.0
	40	40.5	2.6	101.3
	80	82.3	3.3	102.9
	120	116.2	2.6	96.8
	160	157.6	3.1	98.5

8.3 Conclusion

In summary, we have demonstrated a dual-functional AuNPs (with both plasmonic and catalytic activities) for colorimetric in vitro diagnostics with substantially enhanced detection sensitivity. Such dual-functional AuNPs were engineered by coating conventional AuNPs with ultrathin Pt skins of sub-10 atomic layers (*e.g.*, Au@Pt NPs). The enhanced sensitivity is ascribed to the ultrahigh catalytic activity of the Au@Pt NPs that allows them to generate detectable color signal orders of magnitude stronger than the intrinsic color from plasmonics. Importantly, the Au@Pt NPs retain all the merits of conventional AuNPs, making it convenient and straightforward to employ them for clinical diagnostics.

8.4 Materials and Experiment

8.4.1 Chemicals and Materials

Gold(III) chloride trihydrate ($HAuCl_4 \cdot 3H_2O$, ≥99.9%), sodium citrate dihydrate (≥99%), L-ascorbic acid (AA, ≥99%), sodium hexachloroplatinate(IV) hexahydrate ($Na_2PtCl_6 \cdot 6H_2O$, 98%), hydrogen peroxide solution (30 wt% in H_2O), 3,3',5,5'-tetramethylbenzidine (TMB, >99%), TMB substrate solution for membranes, sodium acetate (NaOAc, ≥99%), acetic acid (HOAc, ≥99.7%), human prostate-specific antigen (PSA, ≥99%), bovine serum albumin (BSA, ≥98%), potassium phosphate monobasic (KH_2PO_4, ≥99%), sodium phosphate dibasic (Na_2HPO_4, ≥99%), potassium chloride (KCl, ≥99%), sodium chloride (NaCl, ≥99.5%), sodium azide (NaN_3, ≥99.5%), sodium carbonate (Na_2CO_3, ≥99.5%), sucrose (≥99.5%), cetyltrimethylammonium bromide (CTAB, ≥99%) and Tween 20 were all obtained from Sigma-Aldrich. Monoclonal mouse anti-human PSA capture antibody (referred to as "anti-PSA CAb"), monoclonal mouse anti-human PSA detection antibody (referred to as "anti-PSA DAb"), and human PSA enzyme-linked immunosorbent assay

(ELISA) kit (ab188389) were obtained from Abcam plc.. Polyclonal goat anti-mouse IgG antibody (referred to as "anti-mouse IgG") was obtained from Thermo Fisher Scientific, Inc. Nitrocellulose (NC) membrane, glass fiber membrane, and absorbent pad were obtained from GE Healthcare. Polyvinyl chloride (PVC) backing card was obtained from DCN Diagnostics. All aqueous solutions were prepared using deionized (DI) water with a resistivity of 18.0 MΩ·cm.

8.4.2 Preparation of ~15 nm Au Nanoparticles (AuNPs) To Be Used as Seeds for Preparing ~40 nm AuNPs

~15 nm AuNPs were synthesized using the classical Frens' method with minor modifications.S1 Briefly, 50 mL of $HAuCl_4$ aqueous solution (0.01%, w/v) was added to a 100-mL round-bottom flask equipped with a condenser and heated to boiling in an oil bath under magnetic stirring. Subsequently, 2 mL of sodium citrate aqueous solution (1%, w/v) was quickly added into the boiling solution with a pipet. The solution was kept boiling and stirring for 30 min until its color turned to red. After cool-down, the ~15 nm AuNPs as products were stored in dark at room temperature (~22 ^{o}C) for future use (~55 μg/mL in Au element).

8.4.3 Preparation of ~40 nm AuNPs To Be Used as Seeds for synthesizing Au@Pt$_{n\mathrm{L}}$ NPs

~40 nm AuNPs were synthesized according to a seed-mediated growth method with slight modifications, where above mentioned ~15 nm AuNPs were employed as the seeds. In brief, 1,700 μL of the ~15 nm AuNPs was diluted to 20 mL with DI water, and hosted in a 50-mL round-bottom flask at room temperature under magnetic stirring. Then, 10 mL of precursor aqueous solution containing 370 μL of $HAuCl_4$ aqueous solution (1%, w/v) and 10 mL of reductant aqueous solution containing 0.6 mL of AA aqueous solution (1%, w/v) plus 0.3 mL sodium citrate aqueous solution (1%, w/v) were injected separately to the flask at a rate of 12 mL/h using a syringe pump.

Right after the complete injection of the two solutions, the mixture was heated to boiling in an oil bath under magnetic stirring for 30 min. Finally, the ~40 nm AuNPs as products were cooled down to room temperature and stored in dark at room temperature for future use (8.06×10^{10} particles/mL or 1.34×10^{-10} M). Note all particle concentrations in this study were determined by the combination of ICP-OES analysis and TEM imaging. See the section "Characterizations" below for details.

8.4.4 Synthesis of Au@Pt$_{n\mathrm{L}}$ NPs

In a standard synthesis of Au@Pt4L NPs, 8.0 mL of the ~40 nm AuNPs and 3,653 μL DI water were hosted in a 25 mL three-neck flask and preheated to 90 ºC in an oil bath under magnetic stirring for 10 min. After the preheating, 347 μL of 1.0 mM Na_2PtCl_6 aqueous solution and 4.0 mL of 4.0 mM AA aqueous solution was injected separately into the flask at rates of 1.2 and 2.4 mL/h, respectively, using a syringe pump. The reaction was allowed to proceed for an additional 30 min after the complete injection of the Na_2PtCl_6 and AA solutions. Finally, the produced Au@Pt$_{4\mathrm{L}}$ NPs were cooled down to room temperature and stored in dark at room temperature for future use (3.80×10^{10} particles·mL^{-1} or 6.32×10^{-11} M). The procedures for synthesizing other Au@Pt$_{n\mathrm{L}}$ NPs (*n*: 1-10 Pt atomic layers) were similar to the standard procedure for Au@Pt$_{4\mathrm{L}}$ NPs except for the variations of reagents listed in **Table S8.1** (Appendix G).

8.4.5 Synthesis of ~40 nm Pt nanoparticles (PtNPs)

~40 nm PtNPs were synthesized according to a previously reported procedure with minor modifications. First, 100 μL of 0.4 M AA solution, 200 μL of 1% (w/v) sodium citrate aqueous solution, and 800 μL of 1.25 mM H_2PtCl_6 solution were added to a vial and mixed together. Then, the above mixture was incubated at 80 ℃ for 30 min. After being cooled down, the final products

(*e.g.,* ~40 nm PtNPs) were stored in dark at room temperature for future use (2.19×10^{11} particles·mL^{-1} or 3.64×10^{-10} M).

8.4.6 Steady-State Kinetic Assays

All the steady-state kinetic assays were performed at room temperature (~22 ºC) in cuvettes with a path length (*l*) of 1.0 cm by using 0.2 M NaOAc/HOAc buffer (pH 4.0) as the reaction buffer. Final particle concentrations of 6.32×10^{-14} M for all the Au@Pt$_{n\mathrm{L}}$ NPs and 6.70×10^{-12} M for the ~40 nm AuNPs were used for their corresponding kinetic measurements. The rest procedure for collection of V_{max} and K_m can be found in **Chapter 3**, **Section 3.4.4**.

8.4.7 FDTD Simulations

The finite-difference time-domain (FDTD) simulations were performed using FDTD Solutions 8.0 (Lumerical Solutions, Inc.) according to a previous report with minor modification.S7 During the FDTD simulations, an electromagnetic pulse with the wavelength range of 350-800 nm was launched into a box containing a target nanostructure. The targeted nanostructure was surrounded by a virtual boundary with an appropriate size. The nanostructure and its surrounding space were divided into 1-nm meshes. Finer meshes of 0.2 nm in size were added at nanostructure. The refractive index of the surrounding medium was set to be 1.33, which is the index of water. The nanostructures were modeled as a sphere, and the sizes of the nanostructures were set according to the average sizes measured from the TEM images. Typically, the diameter of the AuNPs (as the cores of Au@Pt*n*L NPs) was set to be 40.2 nm, and the Pt-shell thicknesses of the Au@Pt*n*L NPs were set to be 0.23 nm (*n* = 1), 0.46 nm (*n* = 2), 0.69 nm (*n* = 3), 0.92 nm (*n* = 4), 1.15 nm (*n* = 5), 1.61 nm (*n* = 7), and 2.30 nm (*n* = 10). For all simulations, the

dielectric function of gold and platinum was represented with the fitting from Babar and Palik's data, respectively.

8.4.8 DFT Calculations

All of the density functional theory (DFT) calculations were carried out using VASP codes. A projector augmented wave (PAW) pseudopotential was chosen to deal with the interaction between ion cores and valence electrons. The exchange-correlation effects between valence electrons were described by the Perdew-Burke-Ernzerhof (PBE) functional using the generalized gradient approximation (GGA). The Kohn-Sham wave functions for the valence electrons were expanded using a plane-wave basis set within an energy cutoff of 320 eV. The energy cutoff was increased to 400 eV to test for convergence, and the d-band centers were found to vary by less than 0.01 eV. The Monkhorst-Pack scheme K-points grid sampling was set as 4 × 4 × 1 for the irreducible Brillouinzone. The conjugate gradient (CG) scheme was chosen as the minimization algorithm. Its iterative process was considered to be converged when the force on the atoms was less than 0.01 eV/Å, the energy change per atom was less than 1×10^{-5} eV.

We first calculated the bulk crystal structure of Au and Pt, which gave the following lattice parameters: a = b = c = 4.1549 (Au) / 3.9665 (Pt) Å. This is in good agreement with the experimental parameters: a = b = c = 4.0783 (Au) / 3.9239 (Pt) Å. The Au(111) was simulated by the periodic (2 × 2) slab model. This model has 12 atomic layers. The slabs were separated by a 15 Å thick vacuum, which is sufficient to screen the self-interaction effects of the periodic boundary conditions. Au@Pt_{nL} NPs were modeled with different Pt monolayers (1, 2, 3, 4, 5, 7, 10) on the p (2 × 2) Au(111) slabs with the 12 atomic layers. The p (2 × 2) Pt(111) monolayers were constrained in the p (2 × 2) Au(111) surface. The atomic positions of the bottom six atomic

layers were fixed to simulate the bulk effects.

8.4.9 Preparation of Anti-PSA DAb Conjugated Au@Pt_{4L} NPs (Referred to as "Au@Pt_{4L} NP-Anti-PSA DAb Conjugates")

Au@Pt_{4L} NP-anti-PSA DAb conjugates were prepared according to the reported methods with minor modifications. In brief, 10 mL of the as-synthesized Au@Pt_{4L} NPs (6.32×10^{-11} M, in DI water) was initially adjusted to pH 9.0 using 0.1 M Na_2CO_3 aqueous solution under magnetic stirring. Then, 15 μL of anti-PSA detection antibody [2 $mg\cdot mL^{-1}$ in 10 mM phosphate buffered saline (PBS, pH 7.4) buffer] was added into the particle suspension. After incubation at room temperature for 30 min, the reaction solution was put in a refrigerator overnight at 4 ºC. Subsequently, 1 mL of blocking solution (10% BSA in PBS) was added to the reaction solution. After 1 h, the final products were collected by centrifugation, washed twice with PBS, and redispersed in 1 mL of PBS containing 5% sucrose, 5% BSA, 0.5% Tween 20, and 0.05% NaN_3 for future use.

The procedure for preparing the AuNP-anti-PSA DAb conjugates was the same as that for Au@Pt_{4L} NP-anti-PSA DAb conjugates except for the substitution of Au@Pt_{4L} NPs with ~40 nm AuNPs at the same particle concentration.

8.4.10 Preparation of Au@Pt_{4L} NP-LFA Test Strips

The LFA strips were prepared according to the reported procedure with minor modifications. A ZX1000 Dispensing Platform and a CM4000 Guillotine Cutter (BioDot Inc.) were used for the preparation. The Au@Pt_{4L} NP-LFA strips consist of five components: a sample pad, a conjugate pad, a NC membrane with a test line and a control line, an absorbent pad, and a PVC backing card (see Figure 8.4a). The absorbent pad and PVC backing card were utilized

without any pretreatment. The sample pad was prepared by dipping a glass fiber membrane into PBS containing 5% sucrose, 5% BSA, 0.5% Tween 20, and 0.05% NaN3, followed by drying out at room temperature for 4 h. The conjugate pad was prepared by dispensing the as-prepared Au@Pt_{4L} NP-anti-PSA DAb conjugates onto a glass fiber membrane at a speed of 25 μL/cm using a ZX1000 Dispensing Platform, followed by drying out at room temperature for 2 h. The NC membrane with the test and control lines was prepared by separately spotting anti-PSA CAb (1 $mg{\cdot}mL^{-1}$ in PBS containing 0.05% NaN_3, for the test line) and anti-mouse IgG (1 $mg{\cdot}mL^{-1}$ in PBS containing 0.05% NaN_3, for the control line) onto a NC membrane at a jetting rate of 1 μL/cm using a ZX1000 Dispensing Platform. The two lines were positioned at a 5.0 mm interval. Finally, the sample pad, conjugate pad, NC membrane, and absorbent pad were sequentially assembled onto the PVC backing card with an overlap between them of ~2 mm, and cut into strips with a wide of 4 mm. The prepared Au@Pt_{4L} NP-LFA strips were stored in refrigerator at -20 °C under dry condition for future use.

The procedure for preparing AuNP-LFA strips was the same as that for the Au@Pt_{4L} NP-LFA strips except for the substitution of Au@Pt_{4L} NP-anti-PSA DAb conjugates with AuNP-anti-PSA DAb conjugates at the same particle concentration.

8.4.11 Detection of PSA Using the Au@Pt_{4L} NP-LFA

100 μL PSA standards or human plasma samples were initially dispensed onto the sample pad of the Au@Pt_{4L} NP-LFA strips and kept at room temperature for ~10 min until the flow is stopped. Note that plasma was pre-diluted 2 folds by dilution buffer (1% BSA in PBS containing 0.05% Tween 20, PBST) prior to spiking of PSA and detection. Then, 100 μL of PBST was dispensed onto the sample pad and kept at room temperature for another ~10 min, in order to wash

away the excess Au@Pt_{4L} NP-anti-PSA DAb conjugates. The photographs of the strips were taken with a camera (the "low-sensitivity" mode). For the "high-sensitivity" mode, an additional TMB substrate treatment process was applied: substrate solution (a mixture containing 6 μL of TMB substrate solution for membranes, 2 μL of 1.0 M NaOAc/HOAc buffer, pH 4.0, and 2 μL 10 M H_2O_2) were dispensed onto the control and test lines of each strip. After 5 min incubation at room temperature, the photographs of the strips were taken. For quantitative analysis (Figure 8.4c), all the photographs were imported to a computer and converted to 8-bit grayscale images using Adobe Photoshop. The arithmetic mean of pixel intensity within the test line regions was read as the color signal intensity.

The procedure for the AuNP-LFA of PSA was the same as that for the "low-sensitivity" Au@Pt_{4L} NP-LFA of PSA except for the exclusion of the TMB substrate treatment process.

8.4.12 Detection of PSA Using a Commercial ELISA Kit

The detection was carried out according to the assay protocol provided by Abcam plc.. Briefly, 50 μL of PSA standards or human plasma samples were initially added into appropriate wells. Note that plasma was pre-diluted 2 folds by dilution buffer (1% BSA in PBST) prior to spiking of PSA and detection. Then, 50 μL of PSA Capture Antibody and 50 μL of PSA Detector Antibody were added into each well. After gently shaking at room temperature for 1 h, the wells were washed three times with Wash Buffer PT, followed by the addition of 100 μL of TMB Substrate. After 10 min incubation at room temperature, 100 μL of Stop Solution was added into each well. The absorbance of each well at 450 nm was read using a microplate reader.

8.5 Characterizations

The UV-vis spectra were recorded using an Agilent Cary 60 UV-vis spectrophotometer. The transmission electron microscope (TEM) images were taken using a JEOL JEM-2010 microscope operated at 200 kV. High-resolution TEM images, HAADF-STEM images, energy dispersive X-ray (EDX) mapping, and EDX line-scan profile were acquired using a double Cs-corrected JEOL ARM200F TEM at Brookhaven National Laboratory. The concentration of Au and Pt ions were determined using an inductively coupled plasma-optical emission spectroscopy (ICP-OES, PerkinElmer Optima 7000DV), which could be converted to the particle concentration of AuNPs and Au@Pt NPs once the particle sizes and shapes had been resolved by TEM imaging. The X-ray photoelectron spectroscopy (XPS) measurements were performed on a PHI Versa Probe III XPS system (ULVAC-PHI) using a monochromated Al Kα X-ray source (1486.6 eV). The LFA strips were prepared using a ZX1000 Dispensing Platform and a CM4000 Guillotine Cutter (BioDot Inc.). The absorbance of samples in microtiter plates was read using a PerkinElmer Victor 3 1420 Multilabel Plate Reader. Microtiter plates were shaken using a Corning LSE Digital Microplate Shaker. pH values of buffer solutions were measured using an Oakton pH 700 Benchtop Meter. Photographs of strips and samples in vials were taken using a Canon EOS Rebel T5 digital camera.

8.6 Reference

1. Gottlieb, S.; Woodcock, J. *Nat. Biotech.* **2006**, *24*, 927-929.
2. Giljohann, D. A.; Mirkin, C. A. *Nature* **2009**, *462*, 461-464.
3. Zhou, W.; Gao, X.; Liu, D.; Chen, X. *Chem. Rev.* **2015**, *115*, 10575-10636.
4. Elghanian, R.; Storhoff, J. J.; Mucic, R. C.; Letsinger, R. L.; Mirkin, C. A. *Science* **1997**, *277*, 1078-1081.

5. Li, H.; Rothberg, L. J. *J. Am. Chem. Soc.* **2004**, *126*, 10958-10961.
6. Cheng, C. M.; Martinez, A. W.; Gong, J.; Mace, C. R.; Phillips, S. T.; Carrilho, E.; Mirica, K. A.; Whitesides, G. M. *Angew. Chem., Int. Ed.* **2010**, *49*, 4771-4774.
7. Qu, W.; Liu, Y.; Liu, D.; Wang, Z.; Jiang, X. *Angew. Chem., Int. Ed.* **2011**, *50*, 3442-3445.
8. Zhu, Z.; Wu, C.; Liu, H.; Zou, Y.; Zhang, X.; Kang, H.; Yang, C. J.; Tan, W. *Angew. Chem., Int. Ed.* **2010**, *49*, 1052-1056.
9. De La Rica, R.; Stevens, M. M. *Nat. Nanotechnol.* **2012**, *7*, 821-824.
10. Fu, X.; Chen, L.; Choo, J. *Anal. Chem.* **2017**, *89*, 124-137.
11. Martinez, A. W.; Phillips, S. T.; Carrilho, E.; Thomas III, S. W.; Sindi, H.; Whitesides, G. M. *Anal. Chem.* **2008**, *80*, 3699-3707.
12. Huang, X.; El-Sayed, M. A. *J. Adv. Res.* **2010**, *1*, 13-28.
13. Eustis, S.; El-Sayed, M. A. *Chem. Soc. Rev.* **2006**, *35*, 209-217.
14. Willets, K. A.; Van Duyne, R. P. *Annu. Rev. Phys. Chem.* **2007**, *58*, 267-297.
15. Mayer, K. M.; Hafner, J. H. *Chem. Rev.* **2011**, *111*, 3828-3857.
16. Jain, P. K.; Lee, K. S.; El-Sayed, I. H.; El-Sayed, M. A. *J. Phys. Chem. B* **2006**, *110*, 7238-7248.
17. Love, J. C.; Estroff, L. A.; Kriebel, J. K.; Nuzzo, R. G.; Whitesides, G. M. *Chem. Rev.* **2005**, *105*, 1103-1170.
18. Cao-Milán, R.; Liz-Marzán, L. M. *Expert Opin. Drug Delivery* **2014**, *11*, 741-752.
19. Kumar, S.; Aaron, J.; Sokolov, K. *Nat. Protoc.* **2008**, *3*, 314-320.
20. Sokolov, K.; Follen, M.; Aaron, J.; Pavlova, I.; Malpica, A.; Lotan, R.; Richards-Kortum, R. *Cancer Res.* **2003**, *63*, 1999-2004.
21. Saha, K.; Agasti, S. S.; Kim, C.; Li, X.; Rotello, V. M. *Chem. Rev.* **2012**, *112*, 2739-2779.
22. Posthuma-Trumpie, G. A.; Korf, J.; van Amerongen, A. *Anal. Bioanal. Chem.* **2009**, *393*, 569-582.
23. Huang, X.; Jain, P. K.; El-Sayed, I. H.; El-Sayed, M. A. *Nanomedicine* **2007**, *2*, 681-693.
24. Sun, J.; Xianyu, Y.; Jiang, X. *Chem. Soc. Rev.* **2014**, *43*, 6239-6253.
25. Perfézou, M.; Turner, A.; Merkoçi, A. *Chem. Soc. Rev.* **2012**, *41*, 2606-2622.
26. Wu, L.; Qu, X. *Chem. Soc. Rev.* **2015**, *44*, 2963-2997.
27. Josephy, P. D.; Eling, T.; Mason, R. P. *J. Biol. Chem.* **1982**, *257*, 3669-3675.

28. Ching, K. H. Lateral Flow Immunoassay. In *ELISA: Methods and Protocols*, Hnasko, R. Ed. Springer New York: New York, NY, 2015; 127-137.
29. Choi, D. H.; Lee, S. K.; Oh, Y. K.; Bae, B. W.; Lee, S. D.; Kim, S.; Shin, Y.-B.; Kim, M.-G. *Biosens. Bioelectron.* **2010**, *25*, 1999-2002.
30. Nath, N.; Chilkoti, A. *Anal. Chem.* **2004**, *76*, 5370-5378.
31. Liu, X.; Wang, Y.; Chen, P.; McCadden, A.; Palaniappan, A.; Zhang, J.; Liedberg, B. *ACS Sens.* **2016**, *1*, 1416-1422.
32. Bian, T.; Zhang, H.; Jiang, Y.; Jin, C.; Wu, J.; Yang, H.; Yang, D. *Nano Lett.* **2015**, *15*, 7808-7815.
33. Jiang, H.-J.; Ham, S.; Acapulco, J. A.; Song, Y.; Hong, S.; Shuford, K. L.; Park. S. *J. Am. Chem. Soc.* **2014**, *136*, 17674-17680.
34. Xia, Y.; Xiong, Y.; Lim, B.; Skrabalak, S. E. *Angew. Chem., Int. Ed.* **2009**, *48*, 60-103.
35. Xia, Y.; Gilroy, K. D.; Peng, H.-C.; Xia, X. *Angew. Chem., Int. Ed.* **2017**, *56*, 60-95.
36. Song, H.; Kim, F.; Connor, S.; Somorjai, G. A.; Yang, P. *J. Phys. Chem. B* **2005**, *109*, 188-193.
37. Jiang, K.; Zhao, D.; Guo, S.; Zhang, X.; Zhu, X.; Guo, J.; Lu, G.; Huang, X. *Sci. Adv.* **2017**, *3*, e1601705.
38. Xia, X.; Xie, S.; Liu, M.; Peng, H.-C.; Lu, N.; Wang, J.; Kim, M. J.; Xia, Y. *Proc. Natl. Acad. Sci. U.S.A.* **2013**, *110*, 6669-6673.
39. Xia, X.; Figueroa-Cosme, L.; Tao, J.; Peng, H.-C.; Niu, G.; Zhu, Y.; Xia, Y. *J. Am. Chem. Soc.* **2014**, *136*, 10878-10881.
40. Xia, Y.; Xia, X.; Peng, H.-C. *J. Am. Chem. Soc.* **2015**, *137*, 7947-7966.
41. Ye, H.; Wang, Q.; Catalano, M.; Lu, N.; Vermeylen, J.; Kim, M. J.; Liu, Y.; Sun, Y.; Xia, X. *Nano Lett.* **2016**, *16*, 2812-2817.
42. Gao, L.; Zhuang, J.; Nie, L.; Zhang, J.; Zhang, Y.; Gu, N.; Wang, T.; Feng, J.; Yang, D.; Perrett, S. *Nat. Nanotechnol.* **2007**, *2*, 577-583.
43. Xia, X.; Zhang, J.; Lu, N.; Kim, M. J.; Ghale, K.; Xu, Y.; McKenzie, E.; Liu, J.; Ye, H. *ACS Nano* **2015**, *9*, 9994-10004.
44. Porter, D.; Bright, H. *J. Biol. Chem.* **1983**, *258*, 9913-9924.
45. Wei, H.; Wang, E. *Chem. Soc. Rev.* **2013**, *42*, 6060-6093.

46. Jiang, R.; Chen, H.; Shao, L.; Li, Q.; Wang, J. *Adv. Mater.* **2012**, *24*, OP200-OP207.
47. Nørskov, J. K.; Bligaard, T.; Hvolbæk, B.; Abild-Pedersen, F.; Chorkendorff, I.; Christensen, C. H. *Chem. Soc. Rev.* **2008**, *37*, 2163-2171.
48. Greeley, J.; Nørskov, J. K.; Mavrikakis, M. *Annu. Rev. Phys. Chem.* **2002**, *53*, 319-348.
49. Zhang, J.; Vukmirovic, M. B.; Xu, Y.; Mavrikakis, M.; Adzic, R. R. *Angew. Chem., Int. Ed.* **2005**, *44*, 2132-2135.
50. Nørskov, J. K.; Bligaard, T.; Rossmeisl, J.; Christensen, C. H. *Nat. Chem.* **2009**, *1*, 37-46.
51. Sholl, D. S.; Steckel, J. A. *Density Functional Theory: A Practical Introduction*; John Wiley & Sons, Inc.: Hoboken, NJ, **2009**.
52. Mirkin, M. V.; Amemiya, S. *Nanoelectrochemistry*; CRC Press: Boca Raton, FL, **2014**.
53. Xie, W.; Herrmann, C.; Kömpe, K.; Haase, M.; Schlücker, S. *J. Am. Chem. Soc.* **2011**, *133*, 19302-19305.
54. Kang, S. W.; Lee, Y. W.; Park, Y.; Choi, B.-S.; Hong, J. W.; Park, K.-H.; Han, S. W. *ACS Nano* **2013**, *7*, 7945-7955.
55. Guo, S.; Li, J.; Dong, S.; Wang, E. *J. Phys. Chem. C* **2010**, *114*, 15337-15342.
56. Fu, Q.; Wu, Z.; Du, D.; Zhu, C.; Lin, Y.; Tang, Y. *ACS Sens.* **2017**, *2*, 789-795.
57. Varadea, D.; Haraguchi, K. *Chem. Commun.* **2014**, *50*, 3014-3017.
58. Haiss, W.; Thanh, N. T. K.; Aveyard, J.; Fernig, D. G. *Anal. Chem.* **2007**, *79*, 4215-4221.
59. Liu, X.; Atwater, M.; Wang, J.; Huo, Q. *Colloids Surf. B* **2007**, *58*, 3-7.
60. Yang, X.; Yang, M.; Pang, B.; Vara, M.; Xia, Y. *Chem. Rev.* **2015**, *115*, 10410-10488.
61. Lilja, H.; Ulmert, D.; Vickers, A. J. *Nat. Rev. Cancer* **2008**, *8*, 268-278.
62. Weigl, B.; Domingo, G.; LaBarre, P.; Gerlach, J. *Lab Chip* **2008**, *8*, 1999-2014.
63. Yager, P.; Domingo, G. J.; Gerdes, J. *Annu. Rev. Biomed. Eng.* **2008**, *10*, 107-144.
64. McNerney, R.; Daley, P. *Nat. Rev. Microbiol.* **2011**, *9*, 204-213.
65. Gubala, V.; Harris, L. F.; Ricco, A. J.; Tan, M. X.; Williams, D. E. *Anal. Chem.* **2012**, *84*, 487-515.
66. Quesada-González, D.; Merkoçi, A. *Biosens. Bioelectron.* **2015**, *73*, 47-63.
67. Xu, H.; Chen, J.; Birrenkott, J.; Zhao, J. X.; Takalkar, S.; Baryeh, K.; Liu, G. *Anal. Chem.* **2014**, *86*, 7351-7359.
68. Shen, G.; Xu, H.; Gurung, A. S.; Yang, Y.; Liu, G. *Anal. Sci.* **2013**, *29*, 799-804.

69. Horton, J. K.; Swinburne, S.; O'Sullivan, M. J. *J. Immunol. Methods* **1991**, *140*, 131-134.
70. Yang, W.; Li, X. B.; Liu, G. W.; Zhang, B. B.; Zhang, Y.; Kong, T.; Tang, J. J.; Li, D. N.; Wang, Z. *Biosens. Bioelectron.* **2011**, *26*, 3710-3713.
71. Fu, E.; Liang, T.; Houghtaling, J.; Ramachandran, S.; Ramsey, S. A.; Lutz, B.; Yager, P. *Anal. Chem.* **2011**, *83*, 7941-7946.
72. Kumar, M.; Kumar, R.; Bhalla, V. *Org. Lett.* **2010**, *13*, 366-369.
73. Miao, P.; Ning, L.; Li, X. *Anal. Chem.* **2013**, *85*, 7966-7970.
74. Park, J.; Choi, S.; Kim, T. I.; Kim, T. *Analyst* **2012**, *137*, 4411-4414.
75. Hermanson, G. T. *Bioconjugate Techniques*, 2nd ed.; Academic Press: San Diego, 2008.
76. Beesley, J. E. *Colloidal gold: A new perspective for cytochemical marking*; Oxford University Press: Oxford, **1989**.
77. Armbruster, D. A.; Tillman, M. D.; Hubbs, L. M. *Clin. Chem.* **1994**, *40*, 1233-1238.
78. Armbruster, D. A.; Pry, T. *Clin. Biochem. Rev.* **2008**, *29*, S49-S52.
79. Serp, P.; Philippot, K. *Nanomaterials in Catalysis*; John Wiley & Sons, Inc., **2013**.
80. Zhu, Z.; Guan, Z.; Liu, D.; Jia, S.; Li, J.; Lei, Z.; Lin, S.; Ji, T.; Tian, Z.; Yang, C. *Angew. Chem., Int. Ed.* **2015**, *54*, 10448-10453.
81. Rycenga, M.; Cobley, C. M.; Zeng, J.; Li, W.; Moran, C. H.; Zhang, Q.; Qin, D.; Xia, Y. *Chem. Rev.* **2011**, *111*, 3669-3712.
82. Lim, D.-K.; Jeon, K.-S.; Hwang, J.-H.; Kim, H.; Kwon, S.; Suh, Y. D.; Nam, J.-M. *Nat. Nanotechnol.* **2011**, *6*, 452-460.

APPENDIX A LIST OF COPYRIGH PERMISSIONS

1. Of Figure 1.2 a, Ref. 21

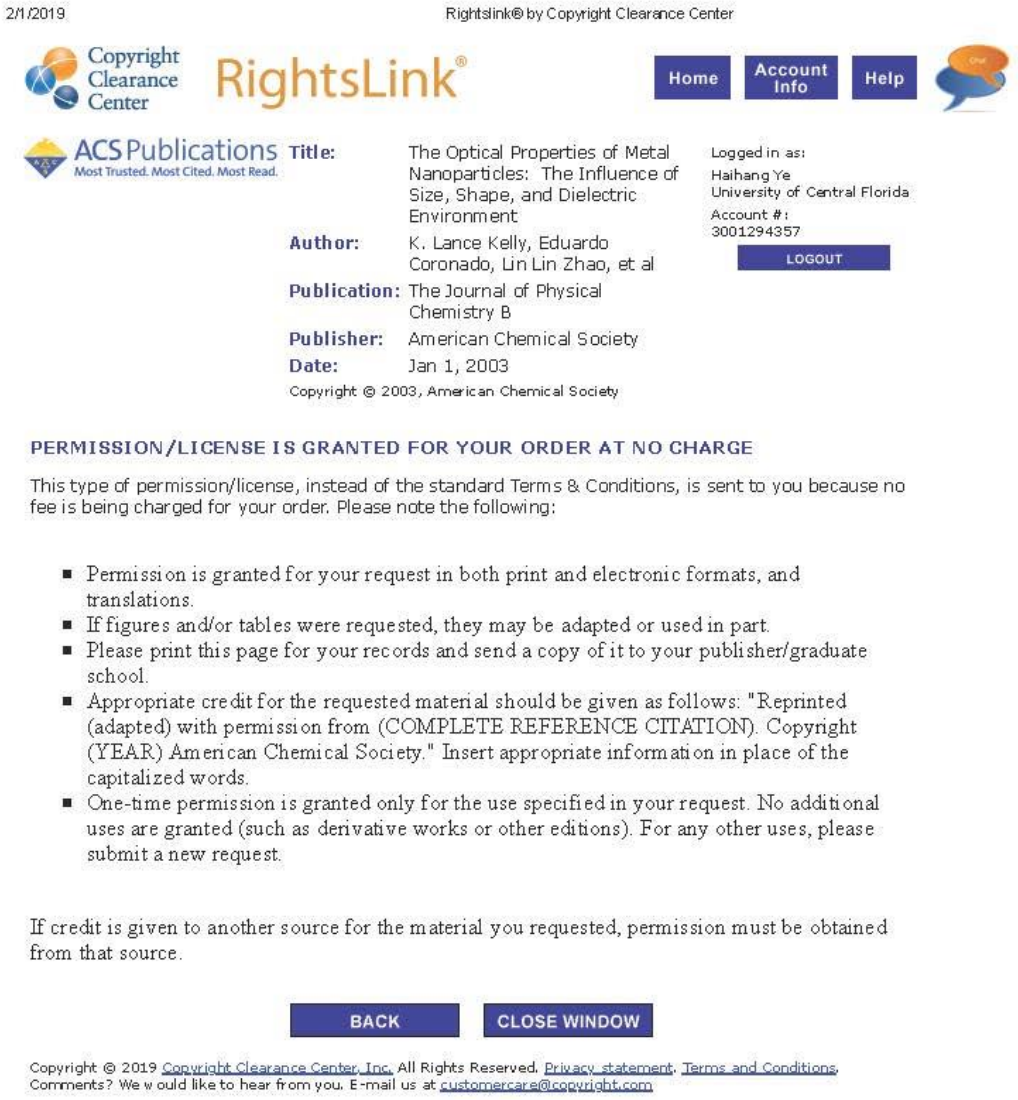

2/1/2019 Rightslink® by Copyright Clearance Center

Copyright Clearance Center RightsLink®

Home | Account Info | Help

ACS Publications Most Trusted. Most Cited. Most Read.

Title: The Optical Properties of Metal Nanoparticles: The Influence of Size, Shape, and Dielectric Environment

Author: K. Lance Kelly, Eduardo Coronado, Lin Lin Zhao, et al

Publication: The Journal of Physical Chemistry B

Publisher: American Chemical Society

Date: Jan 1, 2003

Copyright © 2003, American Chemical Society

Logged in as:
Haihang Ye
University of Central Florida
Account #:
3001294357

LOGOUT

PERMISSION/LICENSE IS GRANTED FOR YOUR ORDER AT NO CHARGE

This type of permission/license, instead of the standard Terms & Conditions, is sent to you because no fee is being charged for your order. Please note the following:

- Permission is granted for your request in both print and electronic formats, and translations.
- If figures and/or tables were requested, they may be adapted or used in part.
- Please print this page for your records and send a copy of it to your publisher/graduate school.
- Appropriate credit for the requested material should be given as follows: "Reprinted (adapted) with permission from (COMPLETE REFERENCE CITATION). Copyright (YEAR) American Chemical Society." Insert appropriate information in place of the capitalized words.
- One-time permission is granted only for the use specified in your request. No additional uses are granted (such as derivative works or other editions). For any other uses, please submit a new request.

If credit is given to another source for the material you requested, permission must be obtained from that source.

BACK CLOSE WINDOW

Copyright © 2019 Copyright Clearance Center, Inc. All Rights Reserved. Privacy statement. Terms and Conditions.
Comments? We would like to hear from you. E-mail us at customercare@copyright.com

2. Of Figure 1.2 b, Ref 22

OSA Open Access License for OSA-Formatted Journal Article PDFs

3. Of Figure 1.2 c, Ref. 23

United States
Attn: University of Central Florida

Total 0.00 USD

Terms and Conditions

Springer Nature Terms and Conditions for RightsLink Permissions

Springer Nature Customer Service Centre GmbH (the Licensor) hereby grants you a non-exclusive, world-wide licence to reproduce the material and for the purpose and requirements specified in the attached copy of your order form, and for no other use, subject to the conditions below:

1. The Licensor warrants that it has, to the best of its knowledge, the rights to license reuse of this material. However, you should ensure that the material you are requesting is original to the Licensor and does not carry the copyright of another entity (as credited in the published version).

   If the credit line on any part of the material you have requested indicates that it was reprinted or adapted with permission from another source, then you should also seek permission from that source to reuse the material.

2. Where **print only** permission has been granted for a fee, separate permission must be obtained for any additional electronic re-use.

3. Permission granted **free of charge** for material in print is also usually granted for any electronic version of that work, provided that the material is incidental to your work as a whole and that the electronic version is essentially equivalent to, or substitutes for, the print version.

4. A licence for 'post on a website' is valid for 12 months from the licence date. This licence does not cover use of full text articles on websites.

5. Where **'reuse in a dissertation/thesis'** has been selected the following terms apply: Print rights of the final author's accepted manuscript (for clarity, NOT the published version) for up to 100 copies, electronic rights for use only on a personal website or institutional repository as defined by the Sherpa guideline (www.sherpa.ac.uk/romeo/).

6. Permission granted for books and journals is granted for the lifetime of the first edition and does not apply to second and subsequent editions (except where the first edition permission was granted free of charge or for signatories to the STM Permissions Guidelines http://www.stm-assoc.org/copyright-legal-affairs/permissions/permissions-guidelines/), and does not apply for editions in other languages unless additional translation rights have been granted separately in the licence.

7. Rights for additional components such as custom editions and derivatives require additional permission and may be subject to an additional fee. Please apply to Journalpermissions@springernature.com/bookpermissions@springernature.com for these rights.

8. The Licensor's permission must be acknowledged next to the licensed material in print. In electronic form, this acknowledgement must be visible at the same time as the figures/tables/illustrations or abstract, and must be hyperlinked to the journal/book's homepage. Our required acknowledgement format is in the Appendix below.

9. Use of the material for incidental promotional use, minor editing privileges (this does not include cropping, adapting, omitting material or any other changes that affect the meaning, intention or moral rights of the author) and copies for the disabled are permitted under this licence.

10. Minor adaptations of single figures (changes of format, colour and style) do not require the Licensor's approval. However, the adaptation should be credited as shown in Appendix below.

SPRINGER NATURE LICENSE TERMS AND CONDITIONS

Feb 01, 2019

This Agreement between University of Central Florida -- Haihang Ye ("You") and Springer Nature ("Springer Nature") consists of your license details and the terms and conditions provided by Springer Nature and Copyright Clearance Center.

License Number	4520391272598
License date	Feb 01, 2019
Licensed Content Publisher	Springer Nature
Licensed Content Publication	Nature Photonics
Licensed Content Title	Nano-optics from sensing to waveguiding
Licensed Content Author	Surbhi Lal, Stephan Link, Naomi J. Halas
Licensed Content Date	Nov 1, 2007
Licensed Content Volume	1
Licensed Content Issue	11
Type of Use	Thesis/Dissertation
Requestor type	non-commercial (non-profit)
Format	print and electronic
Portion	figures/tables/illustrations
Number of figures/tables/illustrations	1
High-res required	no
Will you be translating?	no
Circulation/distribution	<501
Author of this Springer Nature content	no
Title	Engineered Noble-metal Nanostructures for Biosensing Applications
Institution name	University of Central Florida
Expected presentation date	Mar 2019
Order reference number	23
Portions	Figure 1
Requestor Location	University of Central Florida Department of Chemistry 4000 Central Florida Blvd ORLANDO, FL 32816 United States Attn: University of Central Florida
Billing Type	Invoice
Billing Address	University of Central Florida Department of Chemistry 4000 Central Florida Blvd ORLANDO, FL 32816

4. Of Figure 1.3 a, b

2019 Mail - Haihang Ye - Outlook

Re: Request permission for re-use the images on website

'Amanda Madsen' <customer.service@nanocomposix.com>
Fri 2/1/2019 2:01 PM
To: Haihang Ye <yehaihang@Knights.ucf.edu>

Dear Haihang,

Thank you for your request. Yes, you may feel free to use the requested images, provided that you reference nanoComposix accordingly.

Best of luck with your thesis! If you're willing to share it with us once complete, we are always exited to see how our images and materials are being used.

Please let me know if there's anything else that I can help you with.

Kind regards,
Amanda

Amanda Madsen
Sales Support
Accounts Receivable
nanoComposix Logo
nanoComposix, Inc.
4878 Ronson Ct, Suite K
San Diego, CA 92111
nanocomposix.com
info@nanocomposix.com
Tel: (858) 565-4227 × 113
Fax: (619) 330-2556

Watch our recent webinars! *New:* The Upcoming Revolution in Lateral Flow Diagnostics
Subscribe to our newsletter for updates about new products and upcoming webinars. Click here.

On Feb 01, 2019 at 01:54PM PST Haihang Ye <yehaihang@knights.ucf.edu> wrote:

> Hello,
>
> I'm a graduate student at the University of Central Florida. I wonder if I can use the following images on your website for my thesis? Thanks.
>
> [cid:2e12d419-90a3-4b36-be1a-fbce9f74d45b][cid:a9c99aee-37be-45d8-87cc-4ed0231a240e]
>
> Best,
> Haihang
> --
> Haihang (Alex) Ye
> Ph.D. Candidate
> Department of Chemistry

https://outlook.office.com/mail/inbox/id/AAQkADZhYWMyYTk0LWZkNTEtNGMwZS04NzRiLTE0MDg2MmU0OWM3YwAQAJNxNjiptqJNgQ8pnw1F9tU...

5. Of Figure 1.3 c, Ref. 16

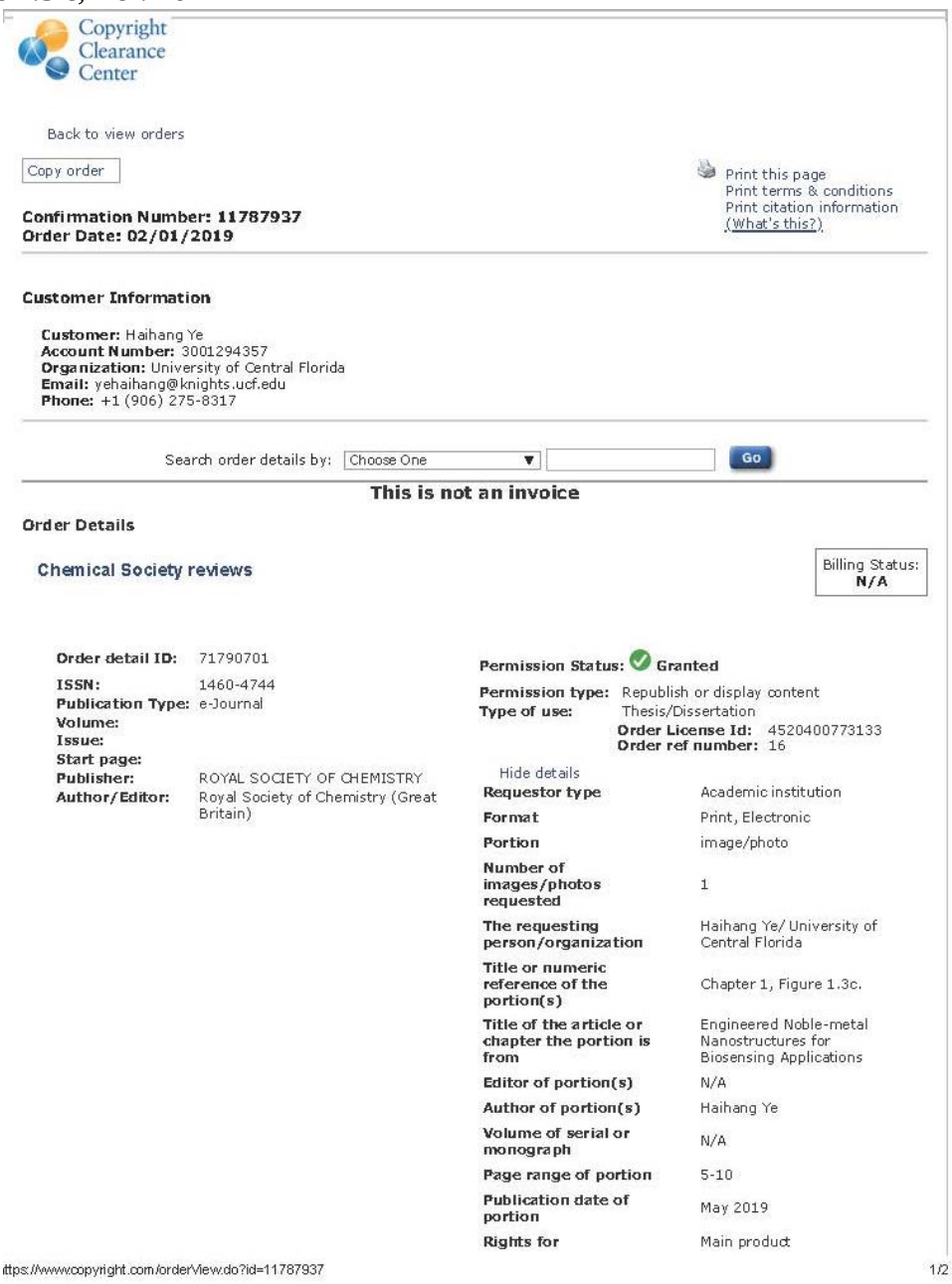

Copyright Clearance Center

Back to view orders

Copy order

Print this page
Print terms & conditions
Print citation information
(What's this?)

Confirmation Number: 11787937
Order Date: 02/01/2019

Customer Information

Customer: Haihang Ye
Account Number: 3001294357
Organization: University of Central Florida
Email: yehaihang@knights.ucf.edu
Phone: +1 (906) 275-8317

Search order details by: Choose One Go

This is not an invoice

Order Details

Chemical Society reviews

Billing Status: **N/A**

Order detail ID:	71790701
ISSN:	1460-4744
Publication Type:	e-Journal
Volume:	
Issue:	
Start page:	
Publisher:	ROYAL SOCIETY OF CHEMISTRY
Author/Editor:	Royal Society of Chemistry (Great Britain)

Permission Status: Granted

Permission type: Republish or display content
Type of use: Thesis/Dissertation
Order License Id: 4520400773133
Order ref number: 16

Hide details

Requestor type	Academic institution
Format	Print, Electronic
Portion	image/photo
Number of images/photos requested	1
The requesting person/organization	Haihang Ye/ University of Central Florida
Title or numeric reference of the portion(s)	Chapter 1, Figure 1.3c.
Title of the article or chapter the portion is from	Engineered Noble-metal Nanostructures for Biosensing Applications
Editor of portion(s)	N/A
Author of portion(s)	Haihang Ye
Volume of serial or monograph	N/A
Page range of portion	5-10
Publication date of portion	May 2019
Rights for	Main product

https://www.copyright.com/orderView.do?id=11787937 1/2

Duration of use	Life of current edition
Creation of copies for the disabled	no
With minor editing privileges	yes
For distribution to	Worldwide
In the following language(s)	Original language of publication
With incidental promotional use	no
Lifetime unit quantity of new product	Up to 499
Title	Engineered Noble-metal Nanostructures for Biosensing Applications
Institution name	University of Central Florida
Expected presentation date	Mar 2019
Order reference number	16

Note: This item was invoiced separately through our **RightsLink service.** More info **$ 0.00**

Total order items: 1 **Order Total: $0.00**

6. Of Figure 1.4, Ref. 32

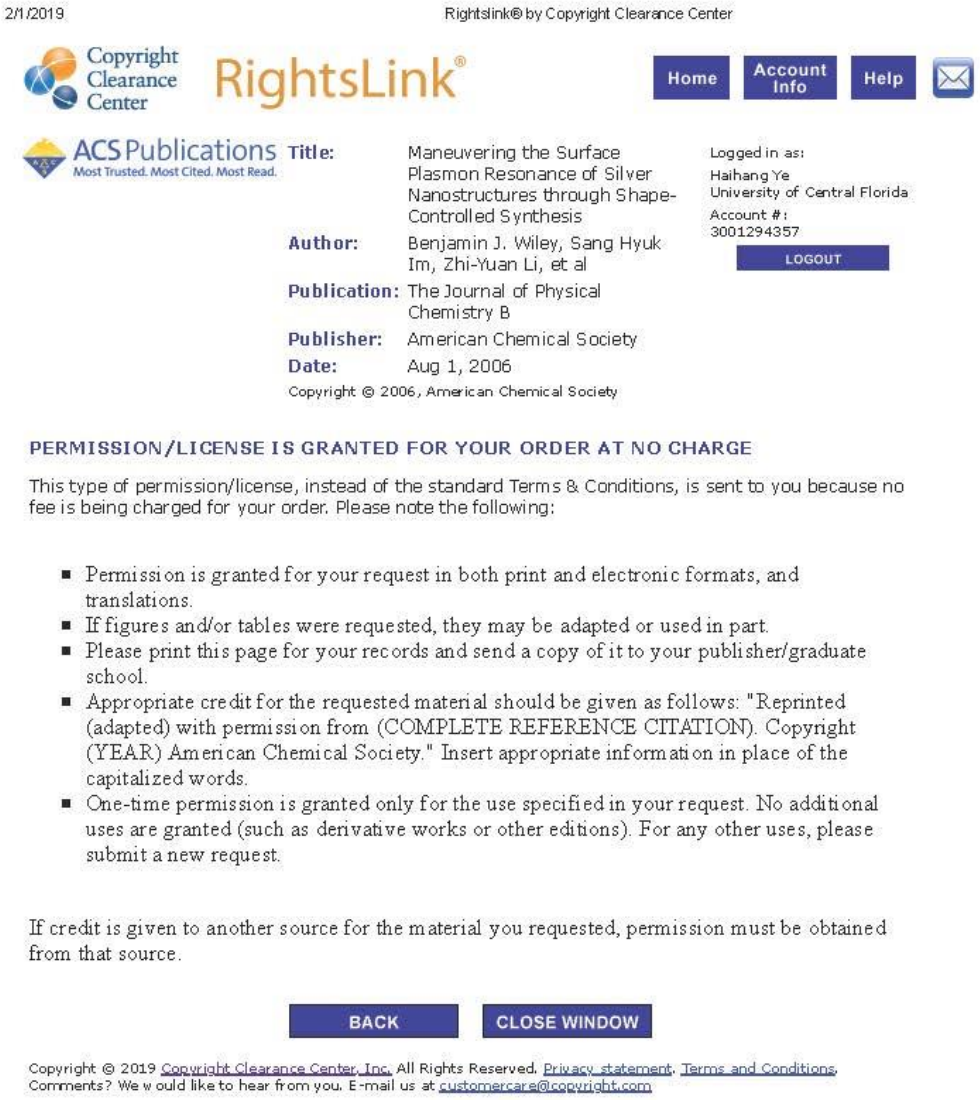

2/1/2019 Rightslink® by Copyright Clearance Center

Copyright Clearance Center RightsLink® Home Account Info Help

ACS Publications Most Trusted. Most Cited. Most Read.

Title: Maneuvering the Surface Plasmon Resonance of Silver Nanostructures through Shape-Controlled Synthesis

Author: Benjamin J. Wiley, Sang Hyuk Im, Zhi-Yuan Li, et al

Publication: The Journal of Physical Chemistry B

Publisher: American Chemical Society

Date: Aug 1, 2006

Copyright © 2006, American Chemical Society

Logged in as: Haihang Ye University of Central Florida Account #: 3001294357 LOGOUT

PERMISSION/LICENSE IS GRANTED FOR YOUR ORDER AT NO CHARGE

This type of permission/license, instead of the standard Terms & Conditions, is sent to you because no fee is being charged for your order. Please note the following:

- Permission is granted for your request in both print and electronic formats, and translations.
- If figures and/or tables were requested, they may be adapted or used in part.
- Please print this page for your records and send a copy of it to your publisher/graduate school.
- Appropriate credit for the requested material should be given as follows: "Reprinted (adapted) with permission from (COMPLETE REFERENCE CITATION). Copyright (YEAR) American Chemical Society." Insert appropriate information in place of the capitalized words.
- One-time permission is granted only for the use specified in your request. No additional uses are granted (such as derivative works or other editions). For any other uses, please submit a new request.

If credit is given to another source for the material you requested, permission must be obtained from that source.

BACK CLOSE WINDOW

Copyright © 2019 Copyright Clearance Center, Inc. All Rights Reserved. Privacy statement. Terms and Conditions. Comments? We would like to hear from you. E-mail us at customercare@copyright.com

7. Of Figure 1.5, Ref. 38

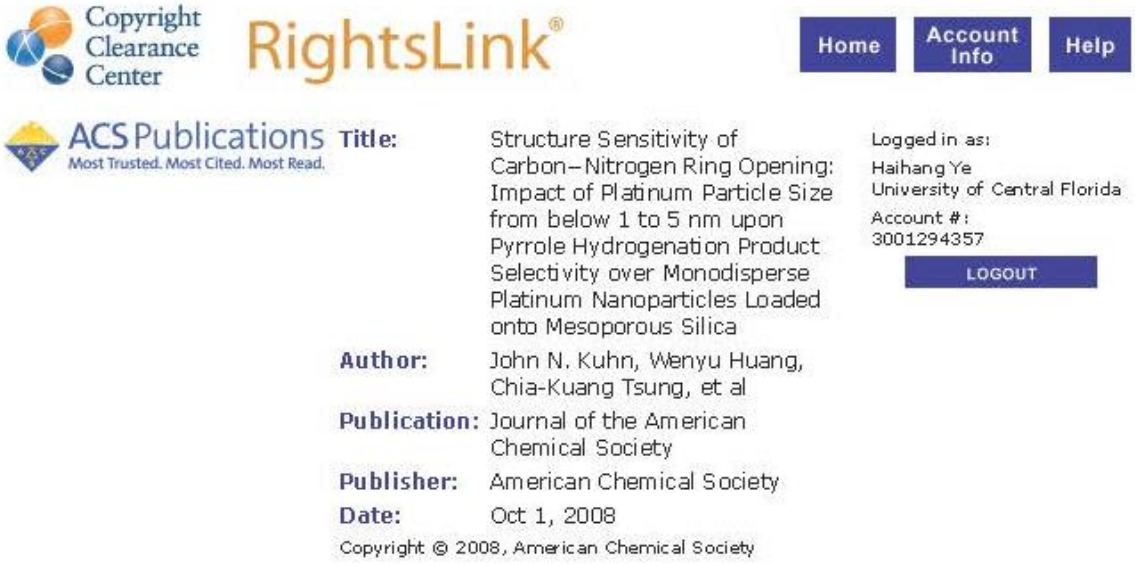

Copyright Clearance Center RightsLink®

Home | Account Info | Help

ACS Publications Most Trusted. Most Cited. Most Read.

Title: Structure Sensitivity of Carbon–Nitrogen Ring Opening: Impact of Platinum Particle Size from below 1 to 5 nm upon Pyrrole Hydrogenation Product Selectivity over Monodisperse Platinum Nanoparticles Loaded onto Mesoporous Silica

Author: John N. Kuhn, Wenyu Huang, Chia-Kuang Tsung, et al

Publication: Journal of the American Chemical Society

Publisher: American Chemical Society

Date: Oct 1, 2008

Copyright © 2008, American Chemical Society

Logged in as:
Haihang Ye
University of Central Florida
Account #:
3001294357

LOGOUT

PERMISSION/LICENSE IS GRANTED FOR YOUR ORDER AT NO CHARGE

This type of permission/license, instead of the standard Terms & Conditions, is sent to you because no fee is being charged for your order. Please note the following:

- Permission is granted for your request in both print and electronic formats, and translations.
- If figures and/or tables were requested, they may be adapted or used in part.
- Please print this page for your records and send a copy of it to your publisher/graduate school.
- Appropriate credit for the requested material should be given as follows: "Reprinted (adapted) with permission from (COMPLETE REFERENCE CITATION). Copyright (YEAR) American Chemical Society." Insert appropriate information in place of the capitalized words.
- One-time permission is granted only for the use specified in your request. No additional uses are granted (such as derivative works or other editions). For any other uses, please submit a new request.

If credit is given to another source for the material you requested, permission must be obtained from that source.

BACK | CLOSE WINDOW

8. Of Figure 1.6, Ref. 39

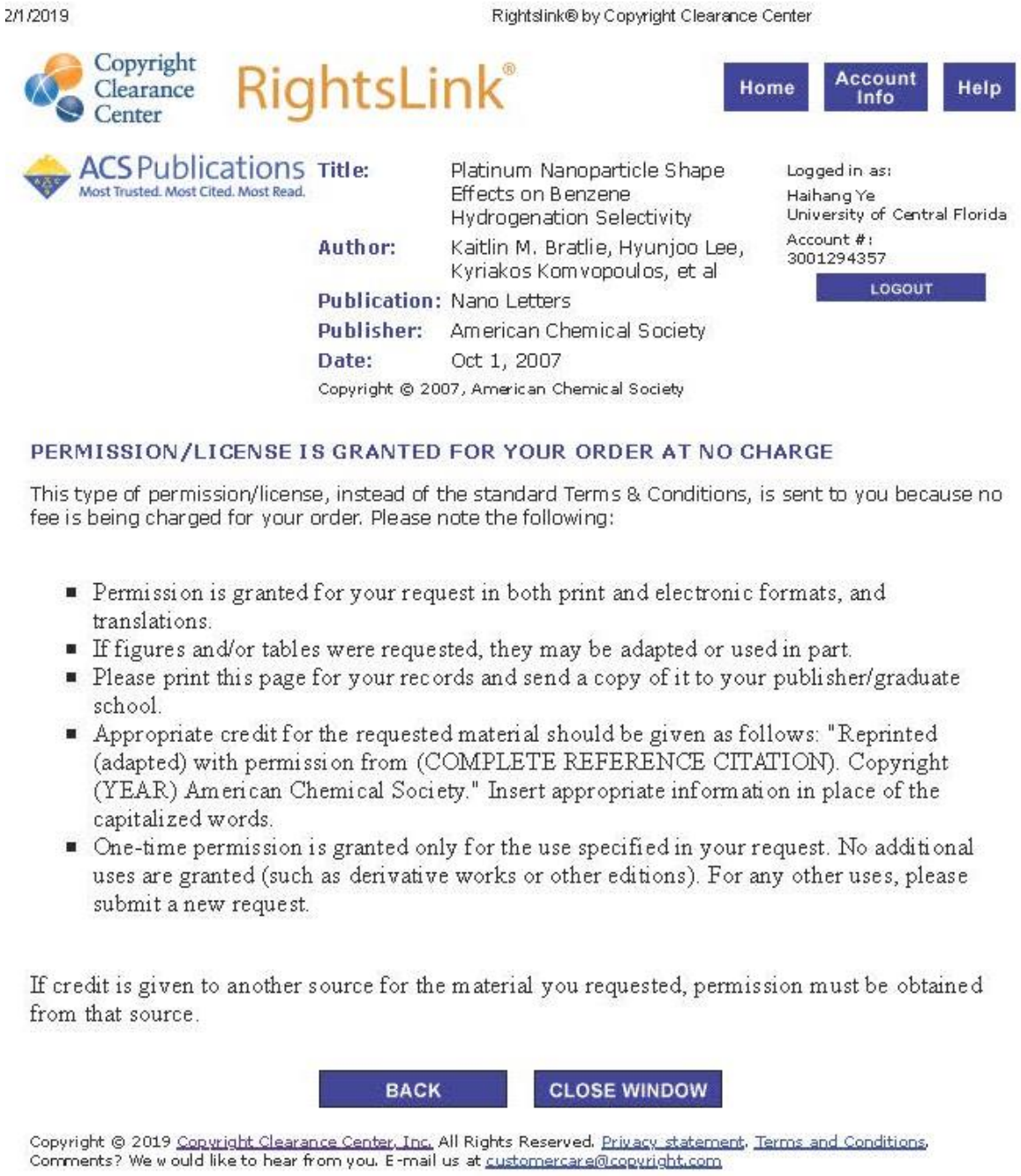

2/1/2019 Rightslink® by Copyright Clearance Center

Copyright Clearance Center RightsLink®

Home | Account Info | Help

ACS Publications Most Trusted. Most Cited. Most Read.

Title: Platinum Nanoparticle Shape Effects on Benzene Hydrogenation Selectivity

Author: Kaitlin M. Bratlie, Hyunjoo Lee, Kyriakos Komvopoulos, et al

Publication: Nano Letters

Publisher: American Chemical Society

Date: Oct 1, 2007

Copyright © 2007, American Chemical Society

Logged in as:
Haihang Ye
University of Central Florida
Account #:
3001294357

LOGOUT

PERMISSION/LICENSE IS GRANTED FOR YOUR ORDER AT NO CHARGE

This type of permission/license, instead of the standard Terms & Conditions, is sent to you because no fee is being charged for your order. Please note the following:

- Permission is granted for your request in both print and electronic formats, and translations.
- If figures and/or tables were requested, they may be adapted or used in part.
- Please print this page for your records and send a copy of it to your publisher/graduate school.
- Appropriate credit for the requested material should be given as follows: "Reprinted (adapted) with permission from (COMPLETE REFERENCE CITATION). Copyright (YEAR) American Chemical Society." Insert appropriate information in place of the capitalized words.
- One-time permission is granted only for the use specified in your request. No additional uses are granted (such as derivative works or other editions). For any other uses, please submit a new request.

If credit is given to another source for the material you requested, permission must be obtained from that source.

BACK | CLOSE WINDOW

Copyright © 2019 Copyright Clearance Center, Inc. All Rights Reserved. Privacy statement. Terms and Conditions.
Comments? We would like to hear from you. E-mail us at customercare@copyright.com

9. Of Figure 1.7, Ref. 40

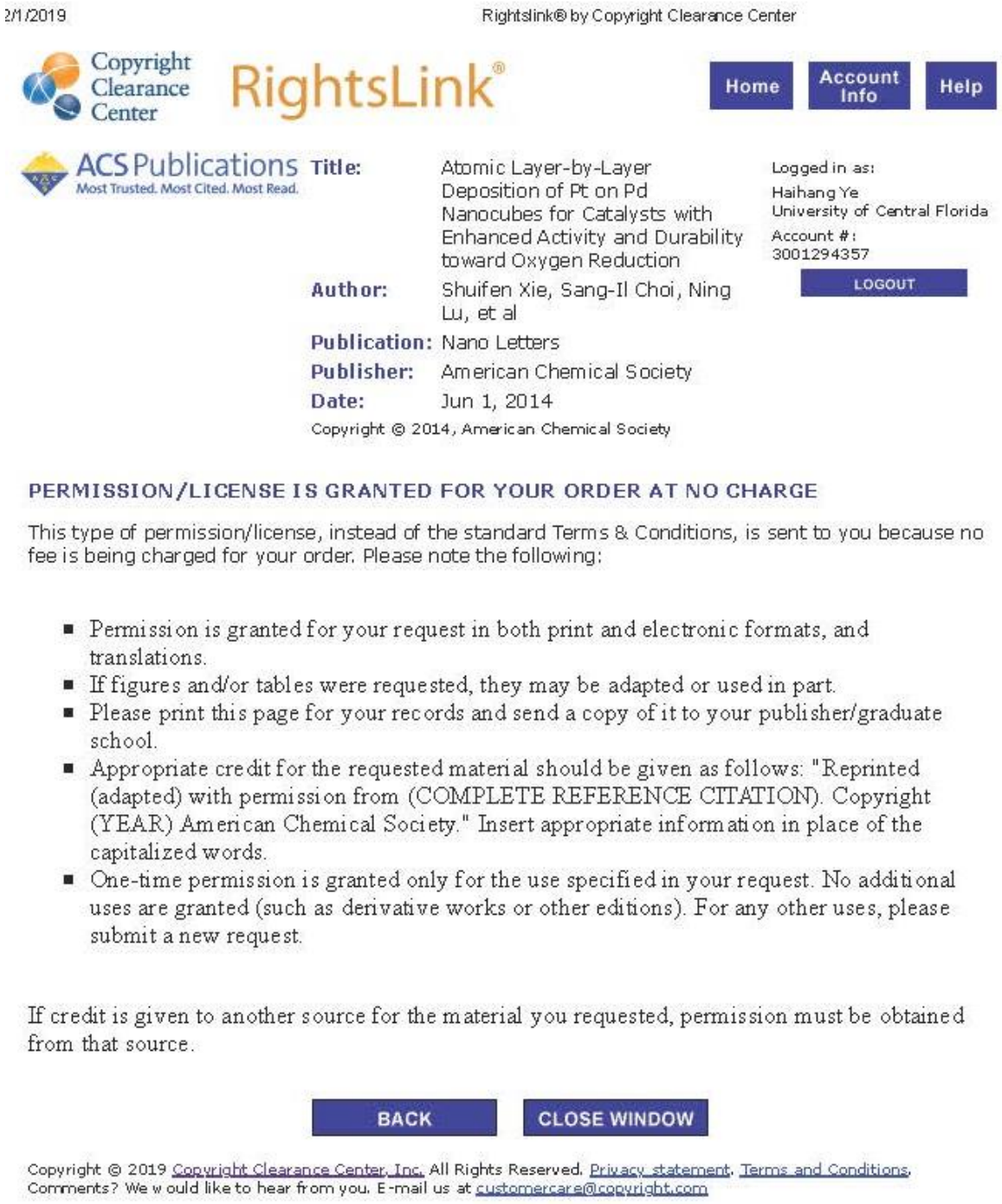

2/1/2019 Rightslink® by Copyright Clearance Center

Copyright Clearance Center RightsLink®

Home | Account Info | Help

ACS Publications Most Trusted. Most Cited. Most Read.

Title: Atomic Layer-by-Layer Deposition of Pt on Pd Nanocubes for Catalysts with Enhanced Activity and Durability toward Oxygen Reduction

Author: Shuifen Xie, Sang-Il Choi, Ning Lu, et al

Publication: Nano Letters

Publisher: American Chemical Society

Date: Jun 1, 2014

Copyright © 2014, American Chemical Society

Logged in as:
Haihang Ye
University of Central Florida
Account #:
3001294357

LOGOUT

PERMISSION/LICENSE IS GRANTED FOR YOUR ORDER AT NO CHARGE

This type of permission/license, instead of the standard Terms & Conditions, is sent to you because no fee is being charged for your order. Please note the following:

- Permission is granted for your request in both print and electronic formats, and translations.
- If figures and/or tables were requested, they may be adapted or used in part.
- Please print this page for your records and send a copy of it to your publisher/graduate school.
- Appropriate credit for the requested material should be given as follows: "Reprinted (adapted) with permission from (COMPLETE REFERENCE CITATION). Copyright (YEAR) American Chemical Society." Insert appropriate information in place of the capitalized words.
- One-time permission is granted only for the use specified in your request. No additional uses are granted (such as derivative works or other editions). For any other uses, please submit a new request.

If credit is given to another source for the material you requested, permission must be obtained from that source.

BACK | CLOSE WINDOW

Copyright © 2019 Copyright Clearance Center, Inc. All Rights Reserved. Privacy statement. Terms and Conditions.
Comments? We would like to hear from you. E-mail us at customercare@copyright.com

10. Of Figure 1.8, Ref. 41

Copyright Clearance Center RightsLink®

Home | Account Info | Help

Science AAAS

Title:	Platinum-based nanocages with subnanometer-thick walls and well-defined, controllable facets
Author:	Lei Zhang,Luke T. Roling,Xue Wang,Madeline Vara,Miaofang Chi,Jingyue Liu,Sang-Il Choi,Jinho Park,Jeffrey A. Herron,Zhaoxiong Xie,Manos Mavrikakis,Younan Xia
Publication:	Science
Publisher:	The American Association for the Advancement of Science
Date:	Jul 24, 2015

Logged in as:
Haihang Ye
University of Central Florida
Account #:
3001294357
LOGOUT

Order Completed

Thank you for your order.

This Agreement between University of Central Florida -- Haihang Ye ("You") and The American Association for the Advancement of Science ("The American Association for the Advancement of Science") consists of your license details and the terms and conditions provided by The American Association for the Advancement of Science and Copyright Clearance Center.

Your confirmation email will contain your order number for future reference.

printable details

License Number	4520410166366
License date	Feb 01, 2019
Licensed Content Publisher	The American Association for the Advancement of Science
Licensed Content Publication	Science
Licensed Content Title	Platinum-based nanocages with subnanometer-thick walls and well-defined, controllable facets
Licensed Content Author	Lei Zhang,Luke T. Roling,Xue Wang,Madeline Vara,Miaofang Chi,Jingyue Liu,Sang-Il Choi,Jinho Park,Jeffrey A. Herron,Zhaoxiong Xie,Manos Mavrikakis,Younan Xia
Licensed Content Date	Jul 24, 2015
Licensed Content Volume	349
Licensed Content Issue	6246
Volume number	349
Issue number	6246
Type of Use	Thesis / Dissertation
Requestor type	Scientist/individual at a research institution
Format	Print and electronic
Portion	Figure
Number of figures/tables	3
Order reference number	
Title of your thesis / dissertation	Engineered Noble-metal Nanostructures for Biosensing Applications
Expected completion date	Mar 2019

Estimated size(pages)	1
Requestor Location	University of Central Florida Department of Chemistry 4000 Central Florida Blvd ORLANDO, FL 32816 United States Attn: University of Central Florida
Billing Type	Invoice
Billing address	University of Central Florida Department of Chemistry 4000 Central Florida Blvd ORLANDO, FL 32816 United States Attn: University of Central Florida
Total	0.00 USD

ORDER MORE CLOSE WINDOW

11. Of Table 1.1, Ref 48

Step 3: Order Confirmation

Thank you for your order! A confirmation for your order will be sent to your account email address. If you have questions about your order, you can call us 24 hrs/day, M-F at +1.855.239.3415 Toll Free, or write to us at info@copyright.com. This is not an invoice.

Confirmation Number: 11792277
Order Date: 02/19/2019

If you paid by credit card, your order will be finalized and your card will be charged within 24 hours. If you choose to be invoiced, you can change or cancel your order until the invoice is generated.

Payment Information

Haihang Ye
University of Central Florida
yehaihang@knights.ucf.edu
+1 (906) 275-8317
Payment Method: n/a

Order Details

Nanozymes: Next Wave of Artificial Enzymes

Order detail ID:	71817286
Order License Id:	4532640765975
ISBN:	9783662530665
Publication Type:	Book
Publisher:	Springer Berlin Heidelberg
Author/Editor:	Wang, Xiaoyu ; et al

Permission Status: **Granted**

Permission type: Republish or display content
Type of use: Thesis/Dissertation

Hide details

Requestor type	Academic institution
Format	Print, Electronic
Portion	chart/graph/table/figure
Number of charts/graphs/tables/figures	1
The requesting person/organization	Haihang Ye/ University of Central Florida
Title or numeric reference of the portion(s)	Chapter 1, Table 1.1
Title of the article or chapter the portion is from	GENERAL INTRODUCTION
Editor of portion(s)	N/A
Author of portion(s)	Haihang Ye
Volume of serial or monograph	N/A
Page range of portion	15-20
Publication date of portion	May 2019

Rights for	Main product
Duration of use	Current edition and up to 5 years
Creation of copies for the disabled	no
With minor editing privileges	no
For distribution to	Worldwide
In the following language(s)	Original language of publication
With incidental promotional use	no
Lifetime unit quantity of new product	Up to 499
Title	Engineered Noble-metal Nanostructures for Biosensing Applications
Institution name	University of Central Florida
Expected presentation date	Mar 2019

12. Of Section 1.2.1 and Section 1.3

Copyright Clearance Center RightsLink®

Home | Account Info | Help

ACS Publications
Most Trusted. Most Cited. Most Read.

Title:	Engineered Noble-Metal Nanostructures for in Vitro Diagnostics
Author:	Zheng Xi, Haihang Ye, Xiaohu Xia
Publication:	Chemistry of Materials
Publisher:	American Chemical Society
Date:	Dec 1, 2018

Copyright © 2018, American Chemical Society

Logged in as:
Haihang Ye
University of Central Florida
Account #:
3001294357
LOGOUT

PERMISSION/LICENSE IS GRANTED FOR YOUR ORDER AT NO CHARGE

This type of permission/license, instead of the standard Terms & Conditions, is sent to you because no fee is being charged for your order. Please note the following:

- Permission is granted for your request in both print and electronic formats, and translations.
- If figures and/or tables were requested, they may be adapted or used in part.
- Please print this page for your records and send a copy of it to your publisher/graduate school.
- Appropriate credit for the requested material should be given as follows: "Reprinted (adapted) with permission from (COMPLETE REFERENCE CITATION). Copyright (YEAR) American Chemical Society." Insert appropriate information in place of the capitalized words.
- One-time permission is granted only for the use specified in your request. No additional uses are granted (such as derivative works or other editions). For any other uses, please submit a new request.

BACK | CLOSE WINDOW

13. Of Figure 1.10, Ref. 129

Copyright Clearance Center RightsLink®

Home | Account Info | Help

ACS Publications
Most Trusted. Most Cited. Most Read.

Title: Enhancing Sensitivity of Surface Plasmon Resonance Biosensors by Functionalized Gold Nanoparticles: Size Matters

Author: Tomáš Špringer, Maria Laura Ermini, Barbora Špačková, et al

Publication: Analytical Chemistry

Publisher: American Chemical Society

Date: Oct 1, 2014

Copyright © 2014, American Chemical Society

Logged in as:
Haihang Ye
University of Central Florida
Account #:
3001294357

LOGOUT

PERMISSION/LICENSE IS GRANTED FOR YOUR ORDER AT NO CHARGE

This type of permission/license, instead of the standard Terms & Conditions, is sent to you because no fee is being charged for your order. Please note the following:

- Permission is granted for your request in both print and electronic formats, and translations.
- If figures and/or tables were requested, they may be adapted or used in part.
- Please print this page for your records and send a copy of it to your publisher/graduate school.
- Appropriate credit for the requested material should be given as follows: "Reprinted (adapted) with permission from (COMPLETE REFERENCE CITATION). Copyright (YEAR) American Chemical Society." Insert appropriate information in place of the capitalized words.
- One-time permission is granted only for the use specified in your request. No additional uses are granted (such as derivative works or other editions). For any other uses, please submit a new request.

If credit is given to another source for the material you requested, permission must be obtained from that source.

BACK | CLOSE WINDOW

14. Of Figure 1.11, Ref. 132

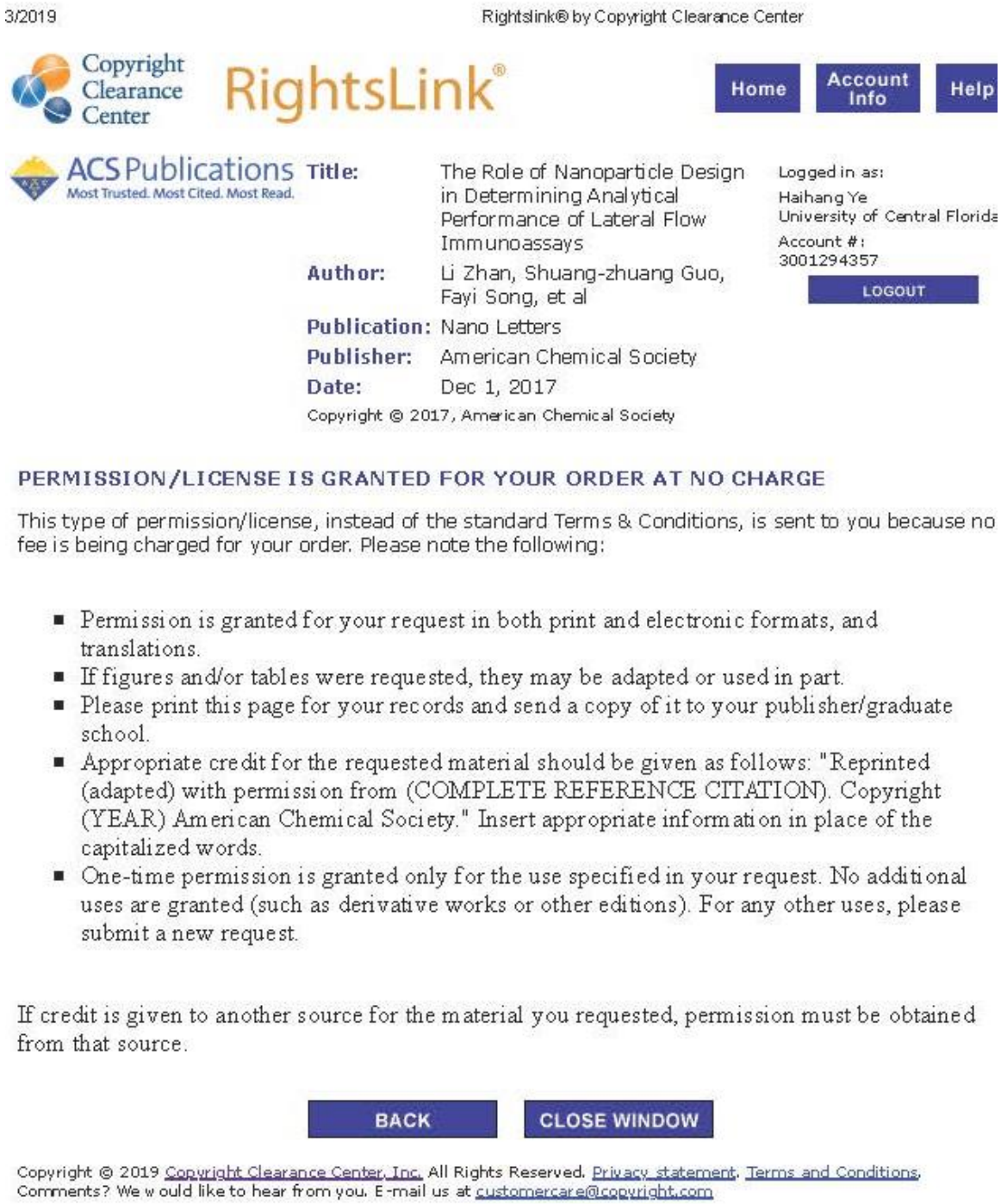

3/2019 Rightslink® by Copyright Clearance Center

Copyright Clearance Center RightsLink®

Home | Account Info | Help

ACS Publications Most Trusted. Most Cited. Most Read.

Title: The Role of Nanoparticle Design in Determining Analytical Performance of Lateral Flow Immunoassays

Author: Li Zhan, Shuang-zhuang Guo, Fayi Song, et al

Publication: Nano Letters

Publisher: American Chemical Society

Date: Dec 1, 2017

Copyright © 2017, American Chemical Society

Logged in as:
Haihang Ye
University of Central Florida
Account #:
3001294357

LOGOUT

PERMISSION/LICENSE IS GRANTED FOR YOUR ORDER AT NO CHARGE

This type of permission/license, instead of the standard Terms & Conditions, is sent to you because no fee is being charged for your order. Please note the following:

- Permission is granted for your request in both print and electronic formats, and translations.
- If figures and/or tables were requested, they may be adapted or used in part.
- Please print this page for your records and send a copy of it to your publisher/graduate school.
- Appropriate credit for the requested material should be given as follows: "Reprinted (adapted) with permission from (COMPLETE REFERENCE CITATION). Copyright (YEAR) American Chemical Society." Insert appropriate information in place of the capitalized words.
- One-time permission is granted only for the use specified in your request. No additional uses are granted (such as derivative works or other editions). For any other uses, please submit a new request.

If credit is given to another source for the material you requested, permission must be obtained from that source.

BACK | CLOSE WINDOW

Copyright © 2019 Copyright Clearance Center, Inc. All Rights Reserved. Privacy statement. Terms and Conditions.
Comments? We would like to hear from you. E-mail us at customercare@copyright.com

15. Of Figure 1.12, Ref. 139

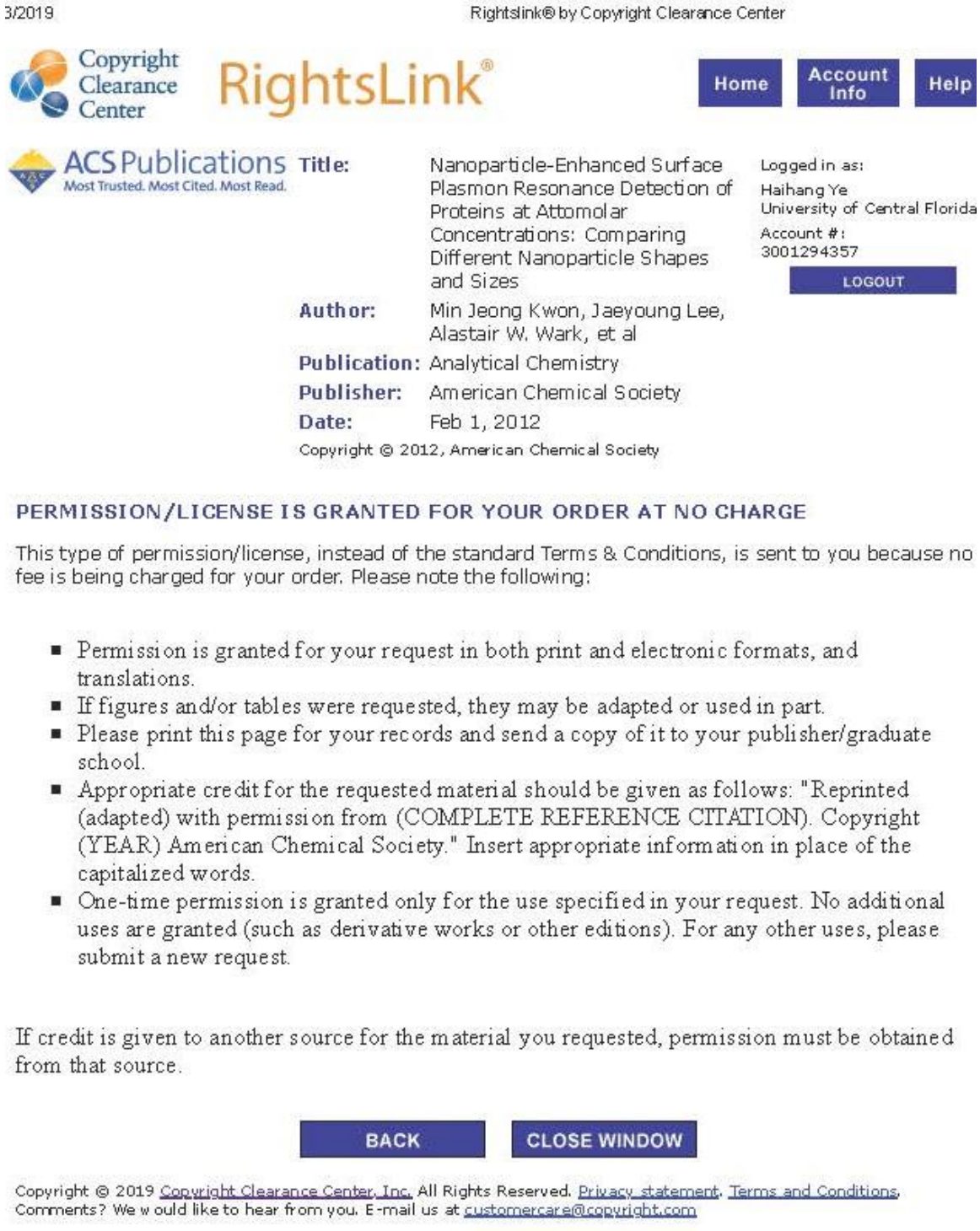

3/2019 Rightslink® by Copyright Clearance Center

Copyright Clearance Center RightsLink®

Home | Account Info | Help

ACS Publications Most Trusted. Most Cited. Most Read.

Title: Nanoparticle-Enhanced Surface Plasmon Resonance Detection of Proteins at Attomolar Concentrations: Comparing Different Nanoparticle Shapes and Sizes

Author: Min Jeong Kwon, Jaeyoung Lee, Alastair W. Wark, et al

Publication: Analytical Chemistry

Publisher: American Chemical Society

Date: Feb 1, 2012

Copyright © 2012, American Chemical Society

Logged in as:
Haihang Ye
University of Central Florida
Account #:
3001294357

LOGOUT

PERMISSION/LICENSE IS GRANTED FOR YOUR ORDER AT NO CHARGE

This type of permission/license, instead of the standard Terms & Conditions, is sent to you because no fee is being charged for your order. Please note the following:

- Permission is granted for your request in both print and electronic formats, and translations.
- If figures and/or tables were requested, they may be adapted or used in part.
- Please print this page for your records and send a copy of it to your publisher/graduate school.
- Appropriate credit for the requested material should be given as follows: "Reprinted (adapted) with permission from (COMPLETE REFERENCE CITATION). Copyright (YEAR) American Chemical Society." Insert appropriate information in place of the capitalized words.
- One-time permission is granted only for the use specified in your request. No additional uses are granted (such as derivative works or other editions). For any other uses, please submit a new request.

If credit is given to another source for the material you requested, permission must be obtained from that source.

BACK | CLOSE WINDOW

Copyright © 2019 Copyright Clearance Center, Inc. All Rights Reserved. Privacy statement. Terms and Conditions.
Comments? We would like to hear from you. E-mail us at customercare@copyright.com

16. Of Figure 1.13, Ref. 146

Copyright Clearance Center RightsLink®

Home | Account Info | Help

ACS Publications
Most Trusted. Most Cited. Most Read.

Title: Facet Energy versus Enzyme-like Activities: The Unexpected Protection of Palladium Nanocrystals against Oxidative Damage

Author: Cuicui Ge, Ge Fang, Xiaomei Shen, et al

Publication: ACS Nano

Publisher: American Chemical Society

Date: Nov 1, 2016

Copyright © 2016, American Chemical Society

Logged in as:
Haihang Ye
University of Central Florida
Account #:
3001294357

LOGOUT

PERMISSION/LICENSE IS GRANTED FOR YOUR ORDER AT NO CHARGE

This type of permission/license, instead of the standard Terms & Conditions, is sent to you because no fee is being charged for your order. Please note the following:

- Permission is granted for your request in both print and electronic formats, and translations.
- If figures and/or tables were requested, they may be adapted or used in part.
- Please print this page for your records and send a copy of it to your publisher/graduate school.
- Appropriate credit for the requested material should be given as follows: "Reprinted (adapted) with permission from (COMPLETE REFERENCE CITATION). Copyright (YEAR) American Chemical Society." Insert appropriate information in place of the capitalized words.
- One-time permission is granted only for the use specified in your request. No additional uses are granted (such as derivative works or other editions). For any other uses, please submit a new request.

If credit is given to another source for the material you requested, permission must be obtained from that source.

BACK | CLOSE WINDOW

17. Of Figure 1.14, Ref. 66

/3/2019 Rightslink® by Copyright Clearance Center

Copyright Clearance Center RightsLink®

Home | Account Info | Help

ACS Publications Most Trusted. Most Cited. Most Read.

Title: Pd–Ir Core–Shell Nanocubes: A Type of Highly Efficient and Versatile Peroxidase Mimic

Author: Xiaohu Xia, Jingtuo Zhang, Ning Lu, et al

Publication: ACS Nano

Publisher: American Chemical Society

Date: Oct 1, 2015

Copyright © 2015, American Chemical Society

Logged in as:
Haihang Ye
University of Central Florida
Account #:
3001294357
LOGOUT

PERMISSION/LICENSE IS GRANTED FOR YOUR ORDER AT NO CHARGE

This type of permission/license, instead of the standard Terms & Conditions, is sent to you because no fee is being charged for your order. Please note the following:

- Permission is granted for your request in both print and electronic formats, and translations.
- If figures and/or tables were requested, they may be adapted or used in part.
- Please print this page for your records and send a copy of it to your publisher/graduate school.
- Appropriate credit for the requested material should be given as follows: "Reprinted (adapted) with permission from (COMPLETE REFERENCE CITATION). Copyright (YEAR) American Chemical Society." Insert appropriate information in place of the capitalized words.
- One-time permission is granted only for the use specified in your request. No additional uses are granted (such as derivative works or other editions). For any other uses, please submit a new request.

If credit is given to another source for the material you requested, permission must be obtained from that source.

BACK CLOSE WINDOW

Copyright © 2019 Copyright Clearance Center, Inc. All Rights Reserved. Privacy statement. Terms and Conditions.
Comments? We would like to hear from you. E-mail us at customercare@copyright.com

18. Of Figure 1.15, Ref. 165

19. Of Figure 1.16 a, b, Ref. 172

Regarding Incident 2534160 Request copyright permission

support@services.acs.org
Sun 2/3/2019 6:08 PM
To: Haihang Ye <yehaihang@Knights.ucf.edu>

ACS Chemistry for Life®

Dear Dr. Haihang Ye,

Thank you for contacting ACS Publications Support.

Your permission request is granted and there is no fee for this reuse. In your planned reuse, you must cite the ACS article as the source, add this direct link <https://pubs.acs.org/doi/10.1021/acsphotonics.5b00667>, and include a notice to readers that further permissions related to the material excerpted should be directed to the ACS.

Should you need further assistance, please let us know.

Sincerely,

Noemi D. Cabalza
ACS Customer Services & Information
Website: https://help.acs.org/

Incident Information:

Incident #: 2534160
Date Created: 2019-02-03T22:53:12
Priority: 3
Customer: Haihang Ye
Title: Request copyright permission
Description: Hello,

I'm writing to request copyright permission for the article below:

https://pubs.acs.org/doi/10.1021/ja502890c

I would like to reuse the figure 1 and figure 5 for my thesis, entitled "Engineered Noble-metal Nanostructures for Biosensing Applications".

Thanks.

Best,
Haihang
--
Haihang (Alex) Ye
Ph.D. Candidate
Department of Chemistry
University of Central Florida

20. Of Figure 1.16 c, Ref. 173

Regarding Incident 2538942 Request copyright permission

support@services.acs.org
Tue 2/5/2019 9:46 PM
To: Haihang Ye <yehaihang@Knights.ucf.edu>

ACS Chemistry for Life®

Dear Dr. Ye:

Thank you for contacting ACS Publications Support.

Your permission request is granted and there is no fee for this reuse. In your planned reuse, you must cite the ACS article as the source, add this direct link (https://pubs.acs.org/doi/10.1021/ja502890c) and include a notice to readers that further permissions related to the material excerpted should be directed to the ACS.

I hope this information helped. Please let me know if I can be of further assistance.

Sincerely,

Kryxie J. Ramirez
ACS Customer Services & Information
https://help.acs.org/

Incident Information:

Incident #: 2538942
Date Created: 2019-02-06T07:27:17
Priority: 3
Customer: Haihang Ye
Title: Request copyright permission
Description: Hello,

I'm writing to request copyright permission for the article below:

https://pubs.acs.org/doi/10.1021/ja502890c

Fully Alloyed Ag/Au Nanospheres: Combining the Plasmonic Property of Ag with the Stability of Au - Journal of the American Chemical Society (ACS Publications) - pubs.acs.org

ACS AuthorChoice - This is an open access article published under an ACS AuthorChoice License, which permits copying and redistribution of the article or any adaptations for non-commercial purposes.

pubs.acs.org

I would like to reuse the figure 1 and figure 5 for my thesis, entitled "Engineered Noble-metal Nanostructures for Biosensing Applications".

Thanks.

Best,

21. Of Chapter 2

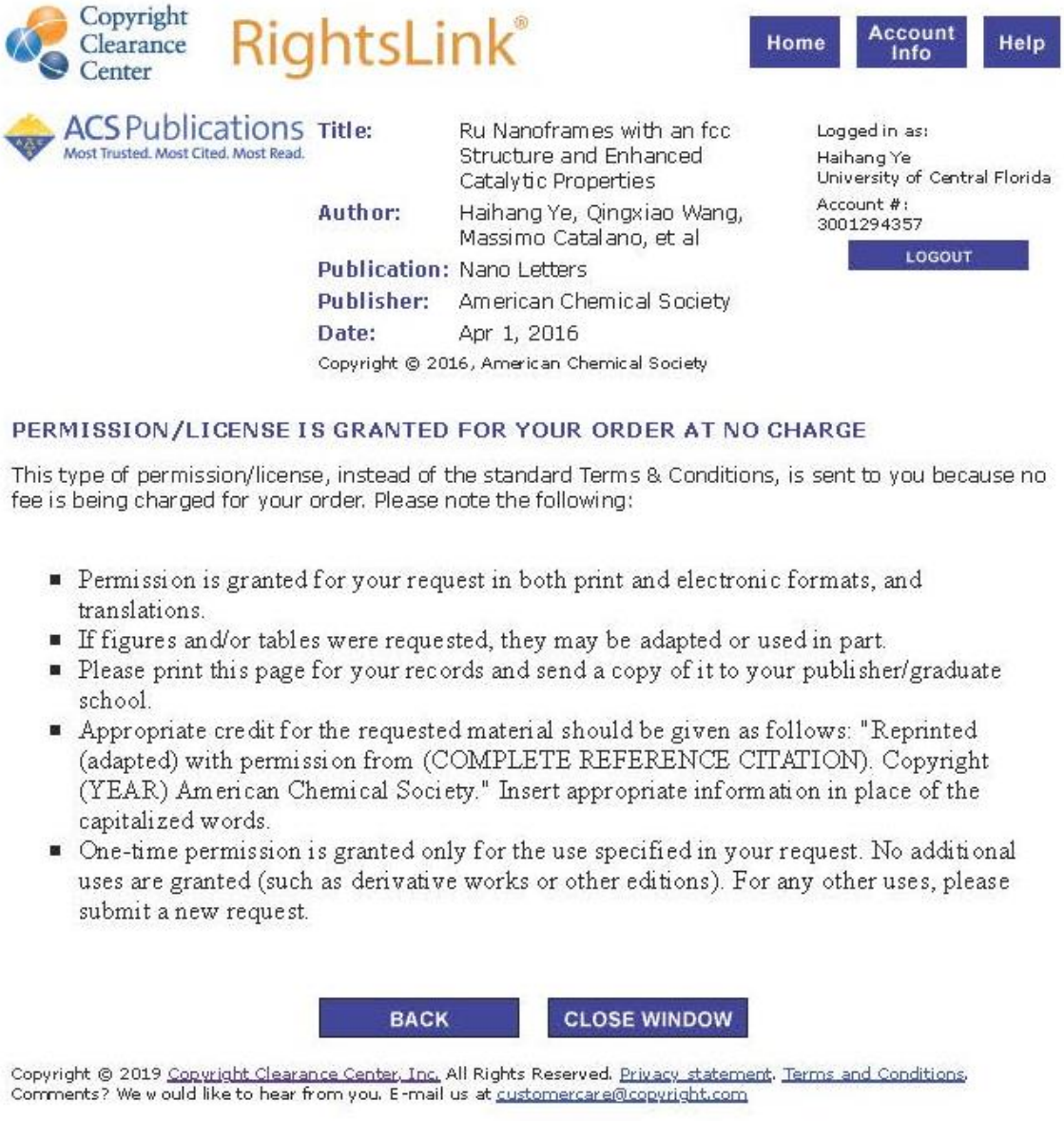

Copyright Clearance Center RightsLink®

Home | Account Info | Help

ACS Publications
Most Trusted. Most Cited. Most Read.

Title: Ru Nanoframes with an fcc Structure and Enhanced Catalytic Properties

Author: Haihang Ye, Qingxiao Wang, Massimo Catalano, et al

Publication: Nano Letters

Publisher: American Chemical Society

Date: Apr 1, 2016

Copyright © 2016, American Chemical Society

Logged in as:
Haihang Ye
University of Central Florida
Account #:
3001294357

LOGOUT

PERMISSION/LICENSE IS GRANTED FOR YOUR ORDER AT NO CHARGE

This type of permission/license, instead of the standard Terms & Conditions, is sent to you because no fee is being charged for your order. Please note the following:

- Permission is granted for your request in both print and electronic formats, and translations.
- If figures and/or tables were requested, they may be adapted or used in part.
- Please print this page for your records and send a copy of it to your publisher/graduate school.
- Appropriate credit for the requested material should be given as follows: "Reprinted (adapted) with permission from (COMPLETE REFERENCE CITATION). Copyright (YEAR) American Chemical Society." Insert appropriate information in place of the capitalized words.
- One-time permission is granted only for the use specified in your request. No additional uses are granted (such as derivative works or other editions). For any other uses, please submit a new request.

BACK | CLOSE WINDOW

Copyright © 2019 Copyright Clearance Center, Inc. All Rights Reserved. Privacy statement. Terms and Conditions.
Comments? We would like to hear from you. E-mail us at customercare@copyright.com

22. Of Chapter 3

23. Of Chapter 4

Copyright Clearance Center RightsLink®

Home | Account Info | Help

ACS Publications
Most Trusted. Most Cited. Most Read.

Title: An Enzyme-Free Signal Amplification Technique for Ultrasensitive Colorimetric Assay of Disease Biomarkers

Author: Haihang Ye, Kuikun Yang, Jing Tao, et al

Publication: ACS Nano

Publisher: American Chemical Society

Date: Feb 1, 2017

Copyright © 2017, American Chemical Society

Logged in as:
Haihang Ye
University of Central Florida
Account #:
3001294357

LOGOUT

PERMISSION/LICENSE IS GRANTED FOR YOUR ORDER AT NO CHARGE

This type of permission/license, instead of the standard Terms & Conditions, is sent to you because no fee is being charged for your order. Please note the following:

- Permission is granted for your request in both print and electronic formats, and translations.
- If figures and/or tables were requested, they may be adapted or used in part.
- Please print this page for your records and send a copy of it to your publisher/graduate school.
- Appropriate credit for the requested material should be given as follows: "Reprinted (adapted) with permission from (COMPLETE REFERENCE CITATION). Copyright (YEAR) American Chemical Society." Insert appropriate information in place of the capitalized words.
- One-time permission is granted only for the use specified in your request. No additional uses are granted (such as derivative works or other editions). For any other uses, please submit a new request.

BACK | CLOSE WINDOW

Copyright © 2019 Copyright Clearance Center, Inc. All Rights Reserved. Privacy statement. Terms and Conditions.
Comments? We would like to hear from you. E-mail us at customercare@copyright.com

24. Of Chapter 5

Order Completed

Thank you for your order.

This Agreement between University of Central Florida -- Haihang Ye ("You") and John Wiley and Sons ("John Wiley and Sons") consists of your license details and the terms and conditions provided by John Wiley and Sons and Copyright Clearance Center.

Your confirmation email will contain your order number for future reference.

printable details

License Number	4522721397792
License date	Feb 05, 2019
Licensed Content Publisher	John Wiley and Sons
Licensed Content Publication	ChemNanoMat
Licensed Content Title	Polyvinylpyrrolidone (PVP)-Capped Pt Nanocubes with Superior Peroxidase-Like Activity
Licensed Content Author	Haihang Ye, Yuzi Liu, Ashima Chhabra, et al
Licensed Content Date	Dec 21, 2016
Licensed Content Volume	3
Licensed Content Issue	1
Licensed Content Pages	6
Type of use	Dissertation/Thesis
Requestor type	Author of this Wiley article
Format	Print and electronic
Portion	Full article
Will you be translating?	No
Title of your thesis / dissertation	Engineered Noble-metal Nanostructures for Biosensing Applications
Expected completion date	Mar 2019
Expected size (number of pages)	1
Requestor Location	University of Central Florida Department of Chemistry 4000 Central Florida Blvd ORLANDO, FL 32816 United States Attn: University of Central Florida
Publisher Tax ID	EU826007151

25. Of Chapter 6

Copyright Clearance Center RightsLink®

Home | Account Info | Help

ACS Publications
Most Trusted. Most Cited. Most Read.

Title: Facile Colorimetric Detection of Silver Ions with Picomolar Sensitivity

Author: Zhuangqiang Gao, Grace G. Liu, Haihang Ye, et al

Publication: Analytical Chemistry

Publisher: American Chemical Society

Date: Mar 1, 2017

Copyright © 2017, American Chemical Society

Logged in as:
Haihang Ye
University of Central Florida
Account #:
3001294357

LOGOUT

PERMISSION/LICENSE IS GRANTED FOR YOUR ORDER AT NO CHARGE

This type of permission/license, instead of the standard Terms & Conditions, is sent to you because no fee is being charged for your order. Please note the following:

- Permission is granted for your request in both print and electronic formats, and translations.
- If figures and/or tables were requested, they may be adapted or used in part.
- Please print this page for your records and send a copy of it to your publisher/graduate school.
- Appropriate credit for the requested material should be given as follows: "Reprinted (adapted) with permission from (COMPLETE REFERENCE CITATION). Copyright (YEAR) American Chemical Society." Insert appropriate information in place of the capitalized words.
- One-time permission is granted only for the use specified in your request. No additional uses are granted (such as derivative works or other editions). For any other uses, please submit a new request.

BACK | CLOSE WINDOW

26. Of Chapter 7

Author reusing their own work published by the Royal Society of Chemistry

You do not need to request permission to reuse your own figures, diagrams, etc, that were originally published in a Royal Society of Chemistry publication. However, permission should be requested for use of the whole article or chapter except if reusing it in a thesis. If you are including an article or book chapter published by us in your thesis please ensure that your co-authors are aware of this.

Reuse of material that was published originally by the Royal Society of Chemistry must be accompanied by the appropriate acknowledgement of the publication. The form of the acknowledgement is dependent on the journal in which it was published originally, as detailed in 'Acknowledgements'.

27. Of Chapter 8

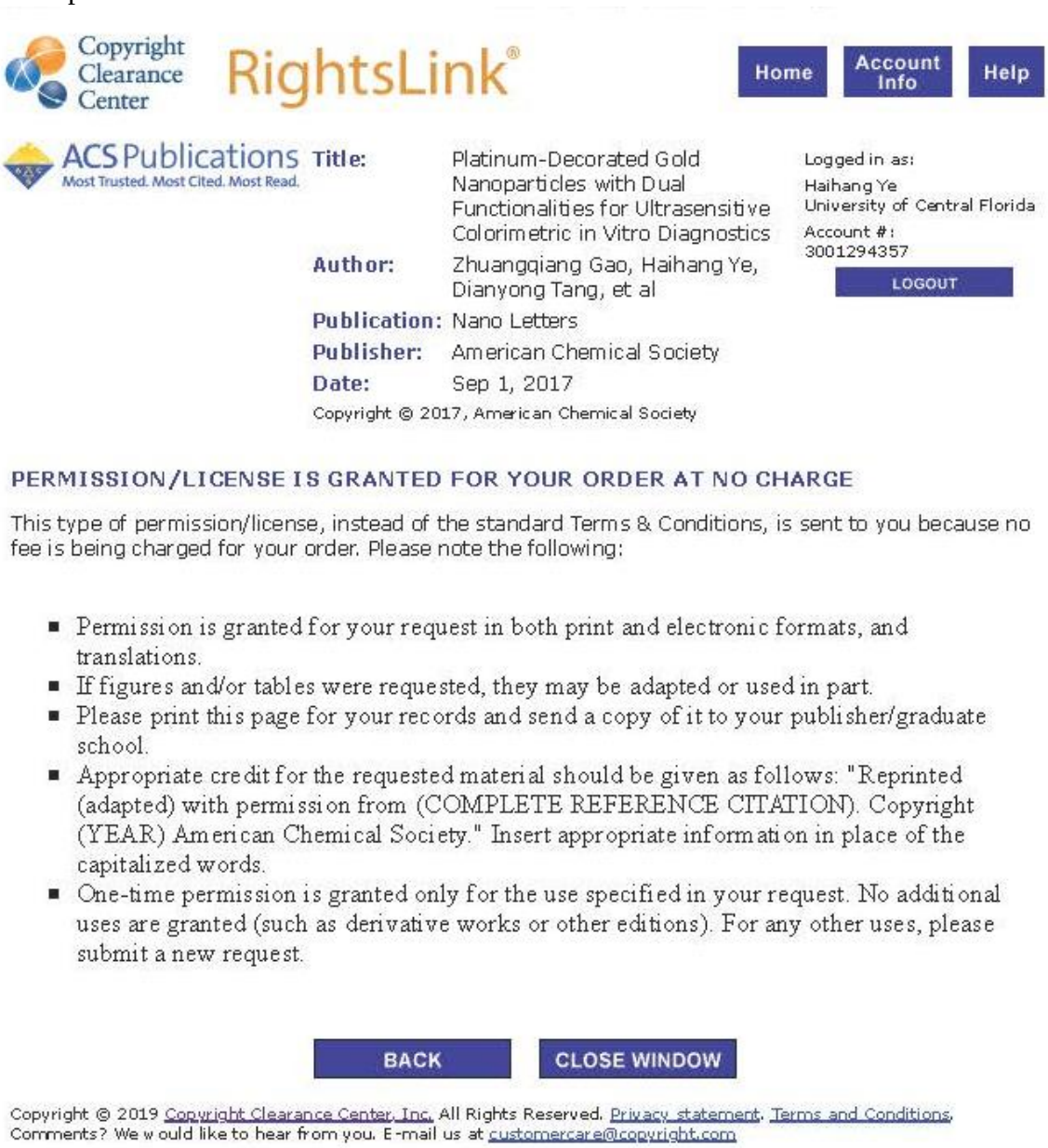

Copyright Clearance Center RightsLink®

Home | Account Info | Help

ACS Publications
Most Trusted. Most Cited. Most Read.

Title: Platinum-Decorated Gold Nanoparticles with Dual Functionalities for Ultrasensitive Colorimetric in Vitro Diagnostics

Author: Zhuangqiang Gao, Haihang Ye, Dianyong Tang, et al

Publication: Nano Letters

Publisher: American Chemical Society

Date: Sep 1, 2017

Copyright © 2017, American Chemical Society

Logged in as:
Haihang Ye
University of Central Florida
Account #:
3001294357

LOGOUT

PERMISSION/LICENSE IS GRANTED FOR YOUR ORDER AT NO CHARGE

This type of permission/license, instead of the standard Terms & Conditions, is sent to you because no fee is being charged for your order. Please note the following:

- Permission is granted for your request in both print and electronic formats, and translations.
- If figures and/or tables were requested, they may be adapted or used in part.
- Please print this page for your records and send a copy of it to your publisher/graduate school.
- Appropriate credit for the requested material should be given as follows: "Reprinted (adapted) with permission from (COMPLETE REFERENCE CITATION). Copyright (YEAR) American Chemical Society." Insert appropriate information in place of the capitalized words.
- One-time permission is granted only for the use specified in your request. No additional uses are granted (such as derivative works or other editions). For any other uses, please submit a new request.

BACK | CLOSE WINDOW

Copyright © 2019 Copyright Clearance Center, Inc. All Rights Reserved. Privacy statement. Terms and Conditions.
Comments? We would like to hear from you. E-mail us at customercare@copyright.com

APPENDIX B ADDITIONAL INFORMATION FOR CHAPTER 2

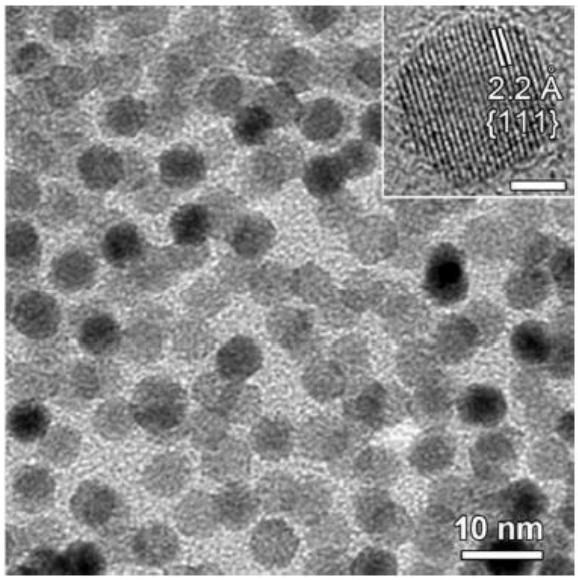

Figure S2.1 TEM image of Pd truncated octahedra with an overall spherical shape and an average size of 5.6 nm that served as seeds for the preparation of Pd-Ru core-frame octahedra and subsequent Ru NFs. The inset shows a HRTEM image recorded from an individual particle orientated along <110> direction.

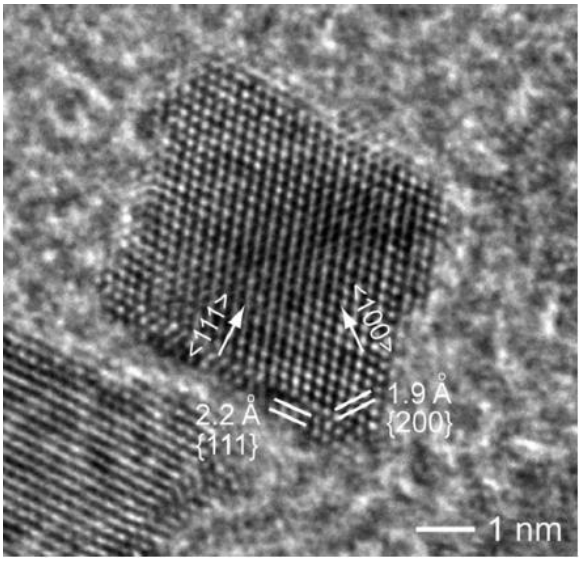

Figure S2.2 HRTEM image of an individual Pd-Ru core-frame octahedron orientated along <110> direction.

.

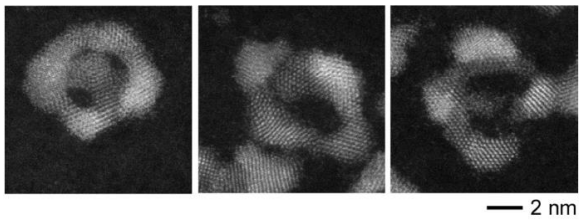

Figure S2.3 Representative HAADF-STEM images of individual Ru NFs showing the imperfect octahedral shape of the sample.

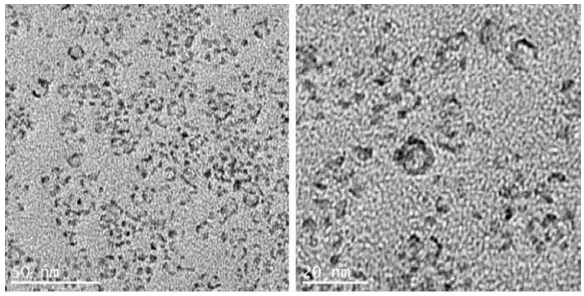

Figure S2.4 TEM images of the sample prepared using the same procedure for the Ru NFs shown in **Figure 2.6** except for the reduction of Ru precursor by 50%.

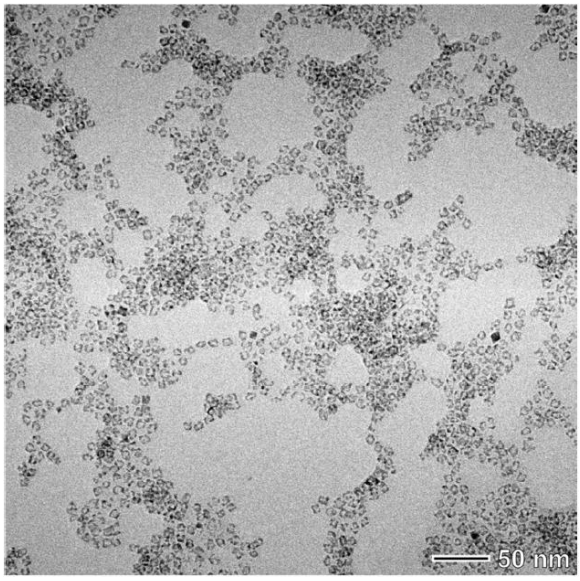

Figure S2.5 Additional TEM image of the Ru NFs at a lower magnification relative to the images shown in **Figure 2.6**.

APPENDIX C ADDITIONAL INFORMATION FOR CHAPTER 4

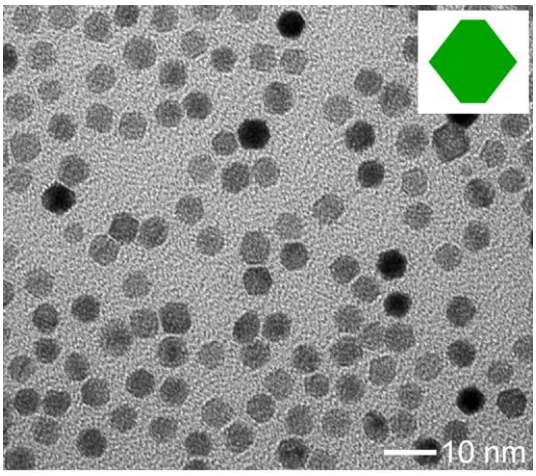

Figure S4.1 TEM image of Pd truncated octahedra with an average size of 5.6 nm that served as seeds for the preparation of Pd-Ir NPs. The inset is a 2D schematic model of the sample.

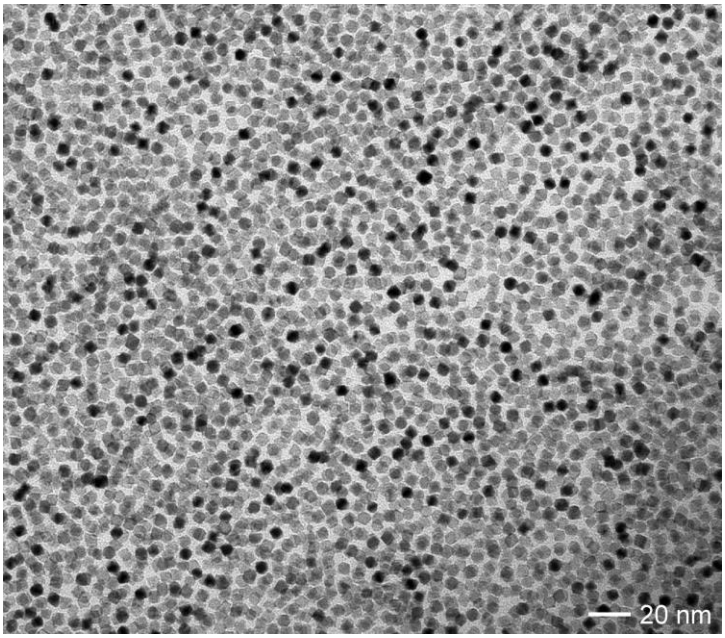

Figure S4.2 Low magnification TEM image of Pd-Ir NPs shown in **Figure 4.2b**.

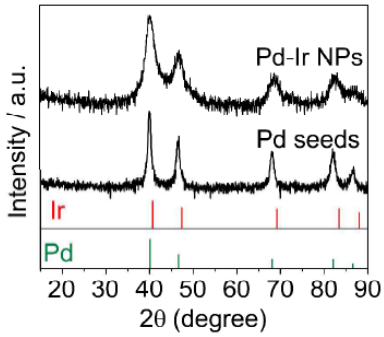

Figure S4.3 XRD patterns of the Pd seeds (**Figure S4.1**) and Pd-Ir NPs (**Figure 4.1**). Red bars: JCPDS no. 06-0598 (*fcc* Ir). Green bars: JCPDS no. 05-0681 (*fcc* Pd).

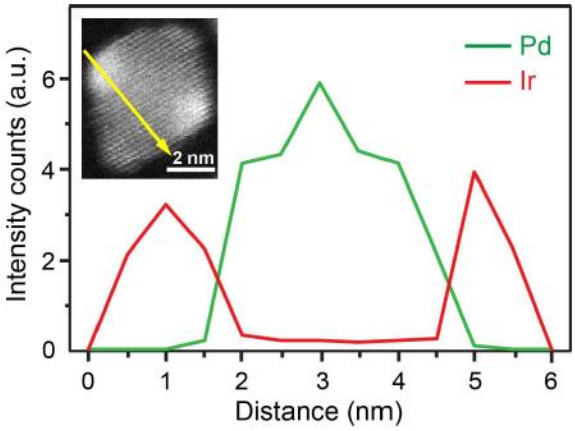

Figure S4.4 Line-scan EDX spectra of elemental Pd and Ir that were recorded along a corner-to edge direction of the individual Pd-Ir NP shown in the inset.

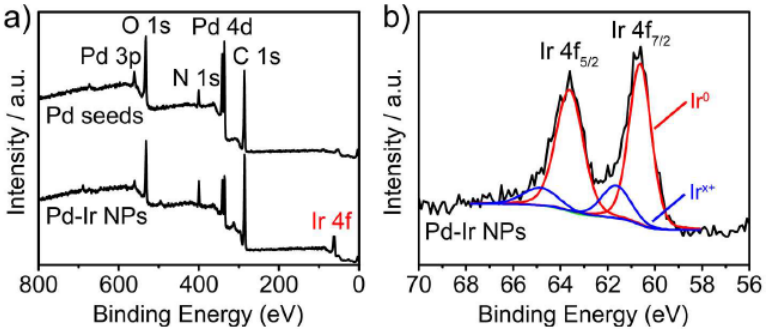

Figure S4.5 XPS analyses of the initial Pd seeds (Figure S1) and Pd-Ir NPs (**Figure 4.1**). (a) XPS survey spectra, in which the Ir 4f peak of the Pd-Ir NPs was labeled in red. (b) High-resolution XPS spectra of the Ir 4f region.

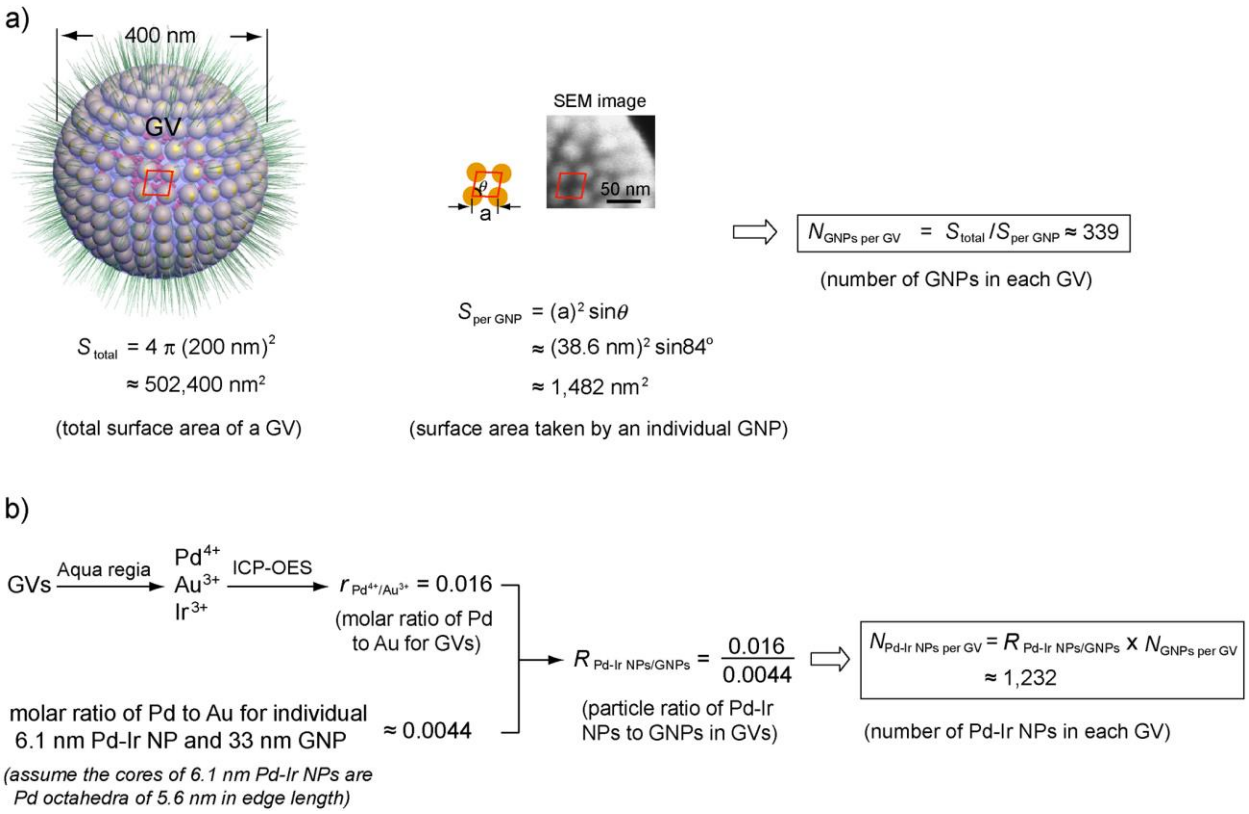

Figure S4.6 Schematics showing the rough estimation of a) the average number of GNPs in each GV ($N_{\text{GNPs per GV}}$) and b) the average number of Pd-Ir NPs in each GV ($N_{\text{Pd-Ir NPs per GV}}$). A SEM image of GV is integrated to a).

APPENDIX D ADDITIONAL INFORMATION FOR CHAPTER 5

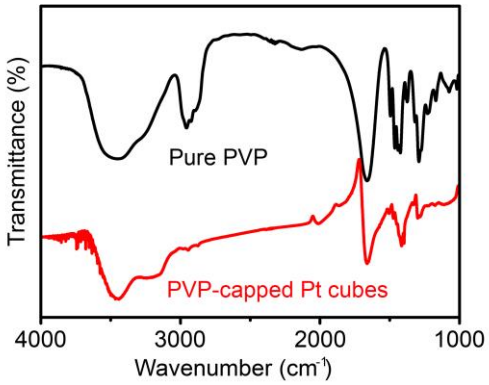

Figure S5.1 FTIR spectra of pure PVP_{55} powder and dried PVP_{55}-capped Pt cubes shown in **Figure 5.1**.

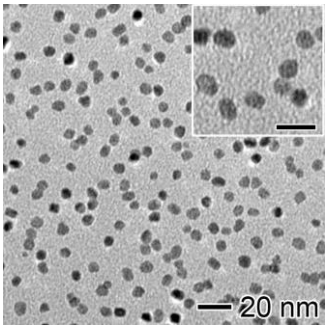

Figure S5.2 TEM image of Pt nanocrystals that was prepared using the standard procedure for PVP_{55}-capped Pt cubes shown in **Figure 5.1**, except for the absence of KBr. Scale bar in inset is 10 nm.

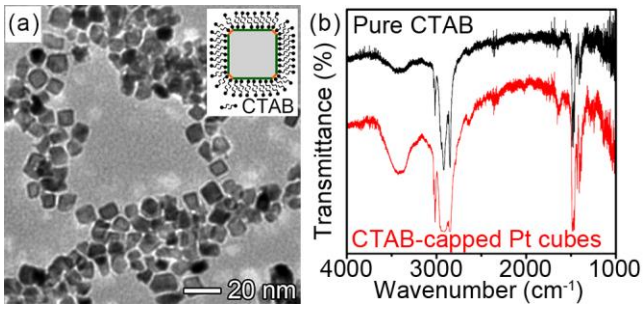

Figure S5.3 CTAB-capped Pt cubes that were synthesized using a previously reported protocol with minor modification. (a) TEM image, and (b) FTIR spectra taken from the CTAB-capped cubes and pure CTAB powder as reference. Inset in (A) shows a model of the cube, in which the bilayer of CTAB on the surface is highlighted.

Table S5.1 Comparison of kinetic parameters of various peroxidase mimics toward the oxidation of TMB by H_2O_2.

Catalysts	Size (nm)	[*E*] (M)	K_m (M)	V_{max} (Ms^{-1})	K_{cat} (s^{-1})	$K_{cat\text{-}specific}$ ($s^{-1}nm^{-2}$)	Ref
PVP_{55}-Pt cubes	8.16	2.9×10^{-13}	8.1×10^{-4}	2.76×10^{-7}	9.53×10^{5}	2.38×10^{3}	This work
PVP_{55}-Pt cubes	6.45	5.9×10^{-13}	6.6×10^{-4}	3.86×10^{-7}	6.54×10^{5}	2.62×10^{3}	This work
PVP_{55}-Pt spheres	4.30	4.0×10^{-13}	7.1×10^{-4}	5.12×10^{-7}	1.28×10^{5}	2.2×10^{3}	This work
Fe_3O_4 particles	300 (diameter)	1.1×10^{-12}	9.8×10^{-5}	3.4×10^{-8}	3.0×10^{4}	0.11	1
Pd cubes	18 (edge length)	1.4×10^{-12}	5.4×10^{-5}	9.7×10^{-8}	6.9×10^{4}	35	2
Pd-Ir cubes	19.2 (edge length)	3.4×10^{-14}	1.3×10^{-4}	6.5×10^{-8}	1.9×10^{6}	8.6×10^{2}	2
Ir particles	1.5 (diameter)	2.0×10^{-9}	2.0×10^{-5}	1.1×10^{-7}	56	7.8	3
Ft-Pt particles	1.87 (diameter)	4.2×10^{-8}	2.2×10^{-4}	3.2×10^{-4}	7.6×10^{3}	6.8×10^{2}	4
MnO_2 particles	4.5 (diameter)	3.0×10^{-8}	4.0×10^{-5}	5.8×10^{-6}	1.9×10^{2}	3.0	5
Co_3O_4 cubes	20 (edge length)	3.4×10^{-10}	1.0×10^{-4}	6.3×10^{-8}	1.8×10^{2}	7.2×10^{-2}	6
Graphene oxide[a]	1 (thickness)	1.2×10^{-9}	2.4×10^{-5}	3.5×10^{-8}	29	3.7×10^{-4}	7
Fe_2O_3 particle	~10 (diameter)	3.1×10^{-10}	3.1×10^{-4}	1.1×10^{-6}	3.4×10^{3}	11	8
Carbon nanodots[b]	2.1 (diameter)	1.5×10^{-7}	3.9×10^{-5}	3.6×10^{-8}	0.24	1.7×10^{-2}	9
PtPd-Fe_3O_4 particle	~12 (diameter)	3.9×10^{-9}	-	9.4×10^{-8}	24	5.3×10^{-3}	10
Au@Pt rods	~30×70 (width×length)	1.3×10^{-11}	2.7×10^{-5}	1.8×10^{-7}	1.4×10^{4}	2.1	11
Au@Pd particles	~20 (diameter)	9.6×10^{-11}	1.7×10^{-4}	2.0×10^{-6}	2.1×10^{4}	17	12

[a]Estimated from the mass concentration (40 μg/mL) and the hypothesis that each particle is an ideal disc with size of 100×1 nm (diameter × thickness).

[b]Estimated from the mass concentration (1 μg/mL).

References

1. Gao, L.; Zhuang, J.; Nie, L.; Zhang, J.; Zhang, Y.; Gu, N.; Wang, T.; Feng, J.; Yang, D.; Perrett, S.; Yan, X. *Nat. Nanotechnol.* **2007**, *2*, 577-583.
2. Xia, X.; Zhang, J.; Lu, N.; Kim, M. J.; Ghale, K.; Xu, Y.; McKenzie, E.; Liu, J.; Ye, H. *ACS Nano* **2015**, *9*, 9994-10004.
3. Su, H.; Liu, D.; Zhao, M.; Hu, W.; Xue, S.; Cao, Q.; Le, X.; Ji, L.; Mao, Z. *ACS Appl. Mater. Inter.* **2015**, *7*, 8233-8242.
4. Fan, J.; Yin, J.; Ning, B.; Wu, X.; Hu, Y.; Ferrari, M.; Anderson, G. J.; Wei, J.; Zhao, Y.; Nie, G. *Biomaterials* **2011**, *32*, 1611-1618.
5. Liu, X.; Wang, Q.; Zhao, H.; Zhang, L.; Su, Y.; Lv, Y. *Analyst* **2012**, *137*, 4552-4558.
6. Mu, J.; Wang, Y.; Zhao, M.; Zhang, L. *Chem. Commun.* **2012**, *48*, 2540-2542.
7. Song, Y.; Qu, K.; Zhao, C.; Ren, J.; Qu, X. *Adv. Mater.* **2010**, *22*, 2206-2210.
8. Zhang, X.; Gong, S.; Zhang, Y.; Yang, T.; Wang, C.; Gu, N. *J. Mater. Chem.* **2010**, *20*, 5110-5116.
9. Shi, W.; Wang, Q.; Long, Y.; Cheng, Z.; Chen, S.; Zheng, H.; Huang, Y. *Chem. Commun.* **2011**, *47*, 6695-6697.
10. Sun, X.; Guo, S.; Liu, Y.; Sun, S. *Nano Lett.* **2012**, *12*, 4859-4863.
11. He, W.; Liu, Y.; Yuan, J.; Yin, J.; Wu, X.; Hu, X.; Zhang, K.; Liu, J.; Chen, C.; Ji, Y.; Guo, Y. *Biomaterials* **2011**, *32*, 1139-1147.
12. Gao, Z.; Hou, L.; Xu, M.; Tang, D. *Sci. Rep.* **2014**, *4*, 3966.

APPENDIX E ADDITIONAL INFORMATION FOR CHAPTER 6

Table S6.1 Comparison of analytical performances of various fluorescent methods and the colorimetric method developed in this work in detecting Ag^+.

Method	Detection probes	LOD (nM)	Assay time (min)
Fluorescent methods	DNA + Ru complex + quantum dots	100	40
	CdTe quantum dots	50	N/A
	DNA-based fluorogenic probe	32	10
	Silver DNAzyme	24.9	30
	DNA-Ag nanoclusters	10	N/A
	MoS_2 nanosheets	10	10
	Cytidine-stabilized gold nanocluster	10	N/A
	MnO_2 nanosheet + DNA	9.1	45
	Graphene oxide + fluorescent DNA probe	5	7
	Fluorescent DNA probe	5	2
	ZnO/CdS@SiO_2 core/shell nanocomposites	3.3	N/A
	2-Aminopurine-modified DNA homopolymers	3	10
	Carbon nanoribbons	1.73	30
	nano-graphite-DNA hybrid + DNase I	0.3	135
	i-Motif DNA + Cyanine dye	0.25	0.17
Colorimetric method	PVP-capped Pt cubes	0.08	6

APPENDIX F ADDITIONAL INFORMATION FOR CHAPTER 8

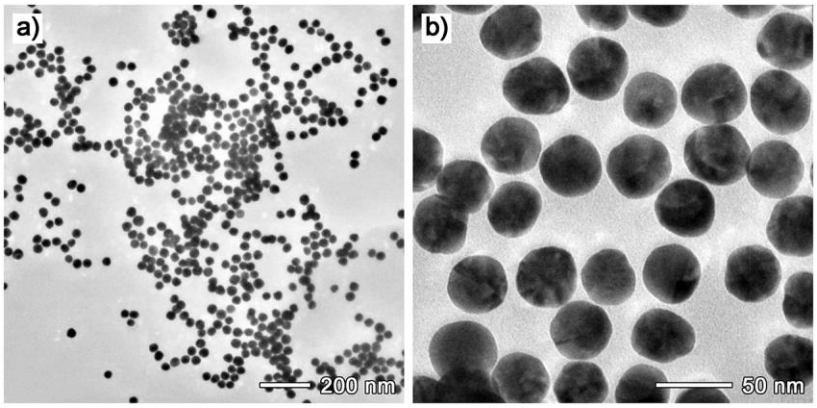

Figure S8.1 (a) Low- and (b) high-magnification TEM images of AuNPs with an average diameter of 40.2 nm that served as seeds for the preparation of Au@Pt_{nL} NPs.

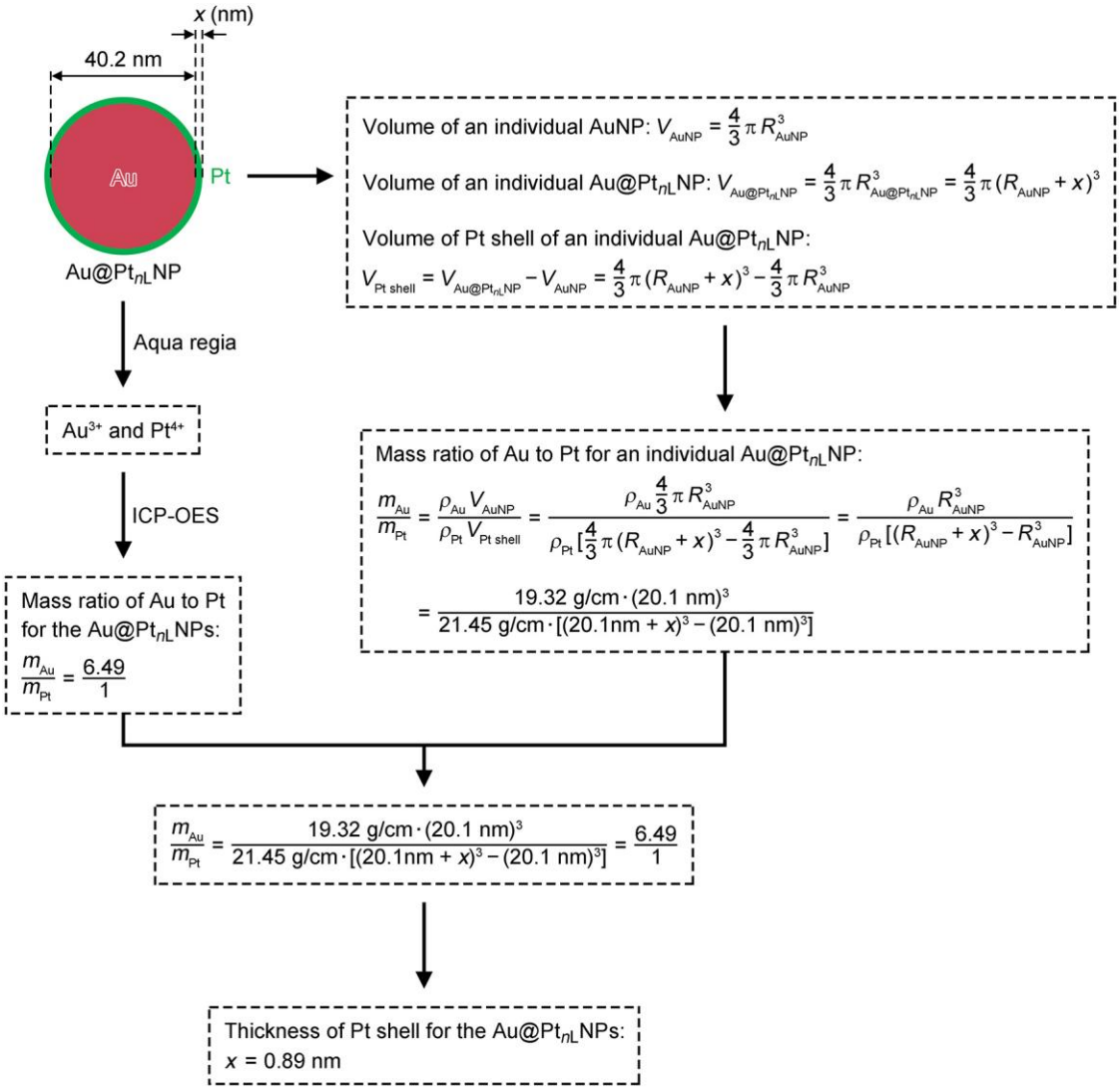

Figure S8.2 Schematic showing the estimation of Pt shell thickness (x nm) for the Au@Pt$_{nL}$ NPs shown in **Figure 8.2**.

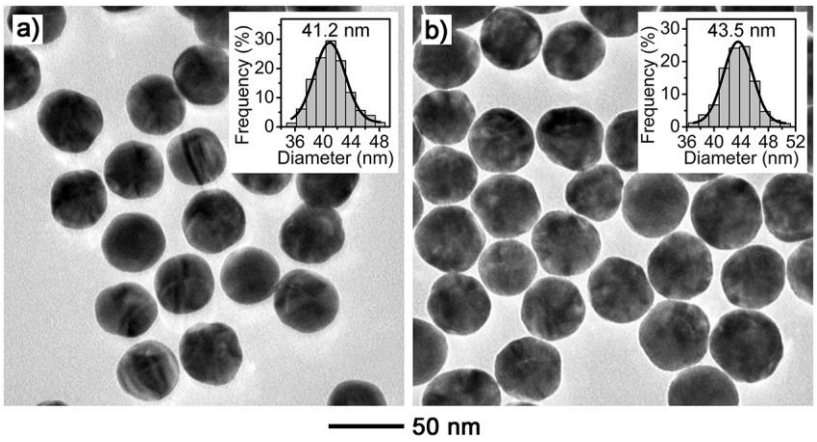

Figure S8.3 TEM images of (a) Au@Pt_{2L} NPs and (b) Au@Pt_{7L} NPs that were synthesized using the standard procedure for Au@Pt_{4L}NPs except that the total volume of Na_2PtCl_6 solution was adjusted from 347 µL to 170 and 628 µL, respectively. The number of Pt atomic layers was determined by ICP-OES. Insets show the distributions of diameter for both samples.

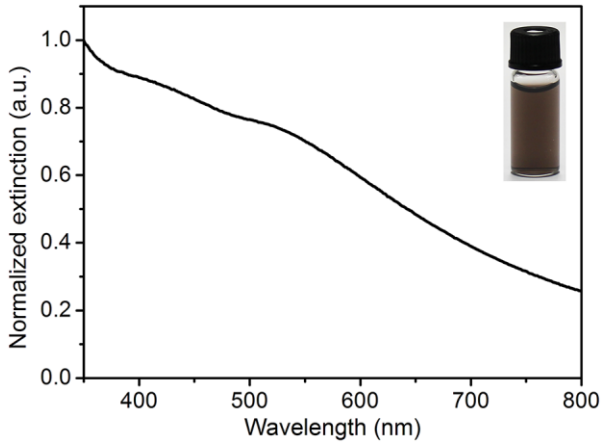

Figure S8.4 Normalized UV-vis spectrum taken from an aqueous suspension of Au@Pt NPs with Pt thickness of ~10 nm. Inset shows a photograph of corresponding sample hosted in a glass vial.

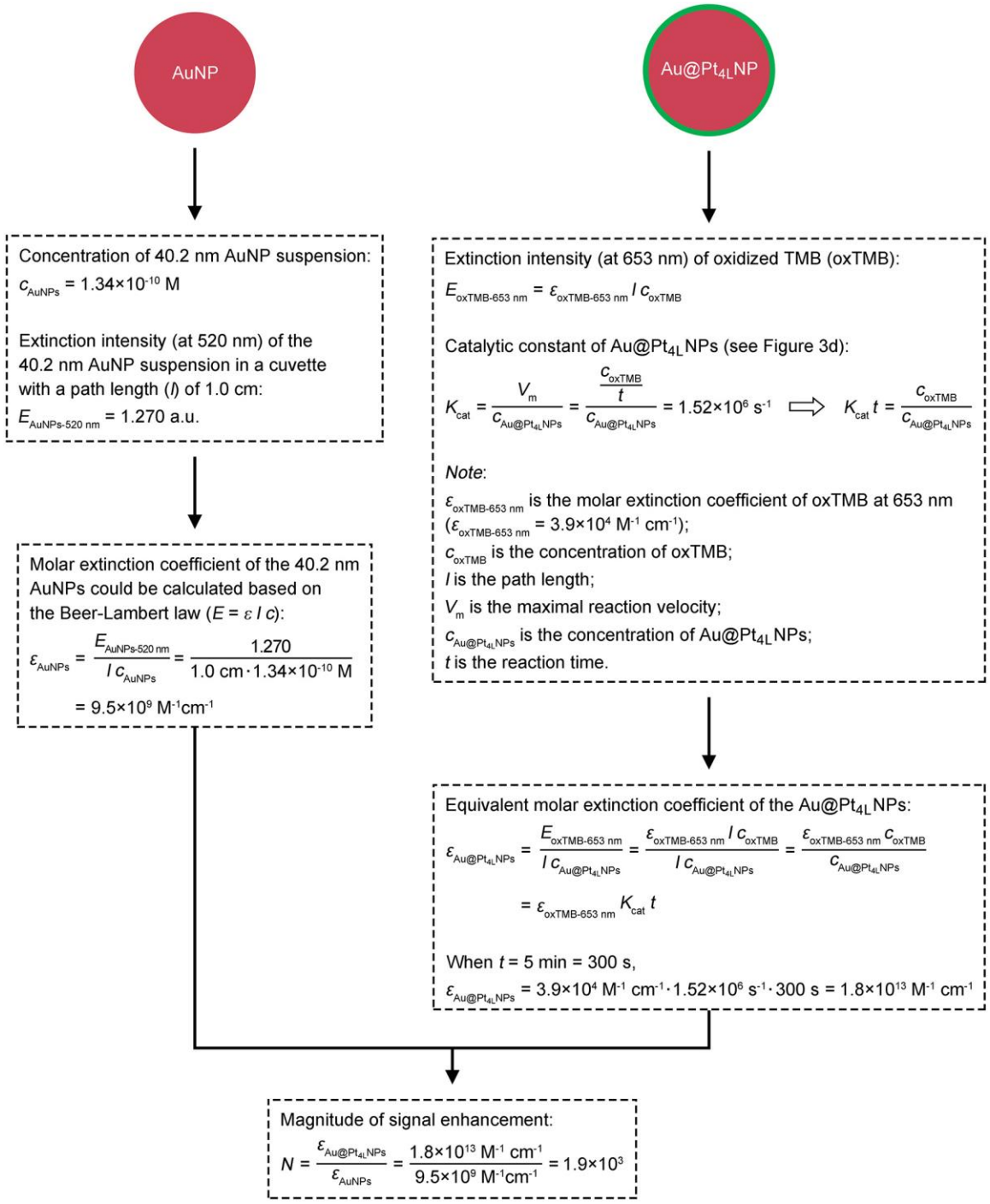

Figure S8.5 Schematics illustrating the estimation of molar extinction coefficients for the 40.2 nm AuNPs (ε_{AuNPs}) and Au@Pt$_{4L}$NPs ($\varepsilon_{Au@Pt4LNPs}$), as well as the magnitude of signal enhancement (N). Here, the $\varepsilon_{Au@Pt4LNPs}$ is referred to as the equivalent molar extinction coefficient, which is defined as the total light extinction of colored products (*e.g.*, oxTMB) catalyzed at t = 5 min.

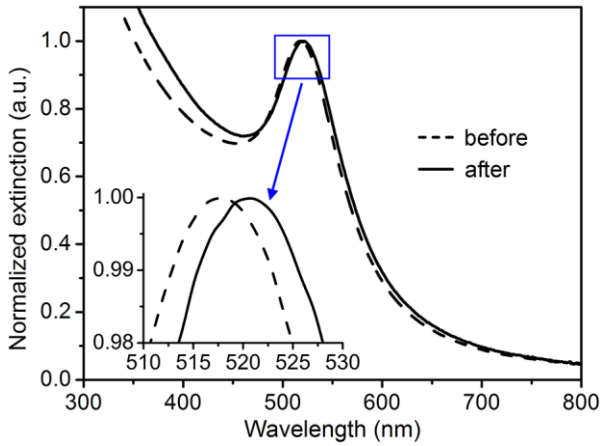

Figure S8.6 Normalized UV-vis spectra of Au@Pt_{4L} NPs before (dashed) and after (solid) they had been incubated with mouse anti-PSA monoclonal detection antibodies. The red shift of major peak implies the successful conjugation of antibodies on Au@Pt_{4L} NP.

Table S8.1 The dosages of reagents for the synthesis of various Au@Pt_{nL} NPs (*n*: 1-10 Pt atomic layers).

Number (*n*) of Pt atomic layers	Volume of AuNPs (mL)	Volume of DI H_2O (μL)	Volume of 1.0 mM Na_2PtCl_6 solution (μL)	Volume of 4.0 mM AA solution (mL)
1	8.0	3,916	84	4.0
2	8.0	3,830	170	4.0
3	8.0	3,743	257	4.0
4	8.0	3,653	347	4.0
5	8.0	3,562	438	4.0
7	8.0	3,372	628	4.0
10	8.0	3,073	927	4.0

APPENDIX G LIST OF PUBLICATIONS AND CONFERENCE PROCEEDING

Publication Record

21. **Ye**, **H**.; Xi, Z.; Magloire, K.; Xia. X. Noble-metal Nanostructures as Highly Efficient Peroxidase Mimics. Under review by *ChemNanoMat*.

20. **Ye**, **H**.; Xia. X. Enhancing the Sensitivity of Colorimetric Lateral Flow Assay (CLFA) through Signal Amplification Techniques. *Journal of Materials Chemistry B*, 2018, **6**, 7102-7111.

19. Xi, Z.; **Ye**, **H**.; Xia. X. Engineered Noble-metal Nanostructures for *In Vitro* Diagnostics. *Chem. Mater* **2018**, *30*, 8391–8414.

18. Wan, S.; Wang, Q.; **Ye**, **H**.; Kim, M. J.; Xia, X. Pd-Ru Bimetallic Nanocrystals with a Porous Structure and Their Enhanced Catalytic Properties. *Particle and Particle System Characterization*, **2018**, *35*, 1700386.

17. **Ye**, **H**.; Yang, K.; Tao, J.; Liu, Y.; Zhang, Q.; Habibi, S.; Nie, Z.; Xia, X. An Enzyme-Free Signal Amplification Technique for Ultrasensitive Colorimetric Assay of Disease Biomarkers. *ACS Nano*, **2017**, *11*, 2052-2059.

16. **Ye**, **H**.; Liu, Y.; Chhabra, A.; Lilla, E.; Xia, X. Polyvinylpyrrolidone (PVP)-Capped Pt Nanocubes with Superior Peroxidase-Like Activity. *ChemNanoMat*, **2017**, *3*, 33-38. (It was highlighted as a **back cover**)

15. Gao, Z.; **Ye**, **H**.; Tang, D.; Tao, J.; Habibi, S.; Minerick, A.; Tang, D.; Xia, X. Platinum Decorated Gold Nanoparticles with Dual Functionalities for Ultrasensitive Colorimetric *in Vitro* Diagnostics. *Nano Letters*, **2017**, *17*, 5572-5579.(It was highlighted by the NSF Science 360 News as a top story)

14. Li, J.; Gao, Z.; **Ye**, **H**.; Wan, S.; Pierce, M.; Tang, D.; Xia, X. A Non-Enzyme Cascade Amplification Strategy for Colorimetric Assay of Disease Biomarkers. *Chemical Communications*, **2017**, *53*, 9055-9058. (**Cover feature**. It was also highlighted as a **hot article**)

13. Gao, Z.; Liu, G. G.; **Ye**, **H**.; Rauschendorfer, R.; Tang, D.; Xia, X. Facile Colorimetric Detection of Silver Ions with Picomolar Sensitivity. *Analytical Chemistry*, **2017**, *89*, 3622-3629.

12. **Ye**, **H**.; Mohar, J.; Wang, Q.; Catalano, M.; Kim, M. J.; Xia, X. Peroxidase-Like Properties of Ruthenium Nanoframes. *Science Bulletin*, 2016, *61*, 1739-1745. (**Cover feature**)

11. **Ye**, **H**.; Wang, Q.; Catalano, M.; Lu, N.; Vermeylen, J.; Kim, M. J.; Liu, Y.; Sun, Y.; Xia, X. Ru Nanoframes with an *fcc* Structure and Enhanced Catalytic Properties. *Nano Letters*, **2016**, *16*, 2812-2817. (It was **highlighted** by C&EN News in the issue of March 28, 2016 and DOE Office of Science on April 4, 2016)

10. Xia, X.; Zhang, J.; Lu, N.; Kim, M. J.; Ghale, K.; Xu, Y.; McKenzie, E.; Liu, J.; **Ye, H.** Pd-Ir Core-Shell Nanocubes: A Type of Highly Efficient and Versatile Peroxidase Mimic, *ACS Nano*, **2015**, *9*, 9994-10004.(It was reported by Michigan Tech News, MedicalResearch.com, and highlighted by DOE Office of Sciences and many other news media)

9. Zhu, D.; Tang, A.; **Ye**, **H**.; Wang, M.; Yang, C.; Teng, F. Tunable Near-Infrared Localized Surface Plasmon Resonances of Djurleite Nanocrystals: Effects of Size, Shape, Surface-Ligands and Oxygen Exposure Time. *Journal of Materials Chemistry C*, **2015**, *3*, 6686-6691.

8. Tang, A.; Hu, Z.; Yin, Z.; **Ye**, **H**.; Yang, C.; Teng, F. One-Pot Synthesis of CuInS2 Nanocrystals Using Different Anions to Engineer Their Morphology and Crystal Phase. *Dalton Transactions*, **2015**, *44*, 9251-9259.

7. **Ye**, **H**.; Tang, A.; Yang, C.; Li, K.; Hou, Y.; Teng, F. Synthesis of $Cu_{2-x}S$ Nanocrystals Induced by Foreign Metal Ions: Phase and Morphology Transformation and Localized Surface Plasmon Resonance. *CrystEngComm*, **2014**,*16*, 8684-8690. (It was **highlighted** as inside front cover)

6. **Ye**, **H.**; Tang, A.; Hou, Y.; Yang, C.; Teng, F. Tunable Near-Infrared Localized Surface Plasmon Resonances of Heterostructured $Cu_{1.94}S$-ZnS Nanocrystals. *Optical Materials Express*, **2014**, *4*, 220-226.

5. Li, X.; Tang, A.; Guan, L.; **Ye**, **H**.; Hou, Y.; Dong, G.; Yang, Z.; Teng, F. Effects of Alkanethiols Chain Length on the Synthesis of $Cu_{2-x}S$ Nanocrystals: Phase, Morphology, Plasmonic Properties and Electrical conductivity. *RSC Advances*, **2014**, *97*,54547-54553.

4. Yin, Z.; Hu, Z.; **Ye**, **H**.; Teng, F.; Yang, C.; Tang, A. One-Pot Controllable Synthesis of Wurtzite $CuInS_2$ Nanoplates. *Applied Surface Science*, **2014**, *307*, 489-494.

3. **Ye**, **H**.; Tang, A.; Huang, L.; Wang, Y.; Yang, C.; Hou, Y.; Peng, H.; Zhang, F.; Teng, F. Facile One-Step Synthesis and Transformation of Cu(I)-Doped Zinc Sulfide Nanocrystals to $Cu_{1.94}S$-ZnS Heterostructured Nanocrystals. *Langmuir*, **2013**, *29*, 8728-8735.

2. Tang, A.; Wang, Y.; **Ye**, **H.**; Zhou, C.; Yang, C.; Li, X.; Peng, H.; Zhang, F.; Hou, Y.; Teng, F. Controllable Synthesis of Silver and Silver Sulfide Nanocrystals via Selective Cleavage of Chemical Bonds. *Nanotechnology*, **2013**, *24*, 355602. (**Cover feature**)

1. Wang, Y.; Tang, A.; Li, K.; Yang, C.; Wang, M.; **Ye**, **H.**; Hou, Y.; Teng, F. Shape-Controlled Synthesis of PbS Nanocrystals via a Simple One-Step Process. *Langmuir*, **2012**, *28*, 16436-16443.

Conference Proceeding

1. Engineering Dual-function Gold-Platinum Nanoparticles for Ultrasensitive Colorimetric *in Vitro* Diagnostics. 2019 Graduate Research Forum, University of Central Florida, Orlando, FL, USA, April 2019. (Poster)

2. Engineering Ru Nanoframes with *fcc* Crystal Structure and Enhanced Catalytic Activities. Division of Colloid and Surface, 254th American Chemistry Society (ACS) National Meeting, Washington, DC, USA, August 2017. (Outstanding Student Poster Award)

3. Facile Synthesis of Polyvinylpyrrolidone (PVP)-Capped Pt Nanocubes with Superior Peroxidase-Like Activity. UPLS of ACS Student Research Symposium, Northern Michigan University, Marquette, MI, USA, April 2017. (Poster)

4. Controllable Synthesis of Cu-Zn-S-based Semiconductor Nanocrystals. 4thChinaNano, Beijing, China. September 2013. (Poster)